Manipulation of Three-Dimensional Turbulent Wakes for Aerodynamic Drag Reduction

Yann Haffner

THÈSE

Pour l'obtention du grade de

DOCTEUR DE L'ÉCOLE NATIONALE SUPÉRIEURE DE MÉCANIQUE ET D'AÉROTECHNIQUE

(Diplôme National - Arrêté du 25 Mai 2016)

École Doctorale : Sciences et Ingénierie en Matériaux, Mécanique, Energétique

Secteur de Recherche : MÉCANIQUE DES MILIEUX FLUIDES

Présentée par

Yann HAFFNER

Manipulation of three-dimensional turbulent wakes for aerodynamic drag reduction

Directeur de thèse : **M. Jacques BORÉE**

Co-encadrant : **M. Thomas CASTELAIN**

Soutenue le 29 Juin 2020 devant la Commission d'Examen

JURY

Holger Babinsky	Professor, University of Cambridge, Cambridge (UK)	Reviewer
Louis N. Cattafesta	Professor, Florida State University, Tallahassee (USA)	Reviewer
Caroline Braud	Chargée de recherche CNRS, Centrale Nantes, Nantes	
Olivier Cadot	Professor, University of Liverpool, Liverpool (UK)	
Fabien Harambat	Ingénieur-Docteur, Groupe PSA, Vélizy-Villacoublay	
Andreas Spohn	Maître de Conférences, Institut PPRIME, Poitiers	
Jacques Borée	Professeur, Institut PPRIME, Poitiers	
Thomas Castelain	Maître de conférences, Université Lyon 1, Lyon	

"*In der Kürze steckt die Würze*"

— Un aérodynamicien allemand citant *Hamlet*, SHAKESPEARE
(oder GOETHE vielleicht...).

Remerciements

C'est certainement la page la plus facile à rédiger de ce manuscrit (avec la première de courverture qui était déjà pré-remplie par l'école doctorale). Certainement parce que les mots viennent assez naturellement pour remercier des personnes qui ont tellement apporté à ce travail de thèse et à moi aussi. Je doute que ce soit possible de faire ça correctement en une ou deux pages, mais je vais essayer pour m'en tenir au principe de la page précédente et ne pas contrarier *mein Lieblingsaerodynamiker...*

Tout d'abord, Thomas. Je sais que ça n'a pas été évident de travailler souvent ensemble à cause de la distance, mais ta contribution est comme un iceberg : immense même si on n'en voit qu'une petite partie. J'ai vraiment apprécié travailler avec toi et ta grande minutie à questionner le plus petit des détails pour nous faire toujours prendre des décisions réfléchies et mesurées et finir par avancer dans une bonne direction malgré l'adversité expérimentale. Humainement, c'est là où moi et mon caractère de cochon trop impulsif avons le plus appris... Tu es certainement une des personnes les plus attentionnées que j'ai pu rencontrer et je sais que tu aurais aimé t'investir encore d'avantage. Mais tout ce que tu m'as apporté de manière continuelle pendant ces trois ans (et demi) se reflète partout dans tout ce travail, quand bien même tu as pu remettre en question (complètement à tort) ton apport scientifique sur certaines parties.

Pour venir à bout d'un long et tumultueux périple, il faut toujours se parer du meilleur des guides. Jacques, je ne te remercierai jamais assez de t'être autant investi avec ton enthousiasme et ta pédagogie légendaires. Les débuts ont été un peu chaotiques, la deuxième partie de thèse aura été extraordinaire. J'ai adoré tout ton enthousiasme à rebondir sur mes idées un peu bancales parfois et à partager ton savoir avec un plaisir communicatif (cf l'introduction du chapitre 5 pour un exemple parlant...). J'ai au fur et à mesure de l'avancement de ce travail pris de plus en plus de plaisir à travailler sur toutes ces idées –un peu trop parfois (au point que certains ont pu croire que je dormais dans ce bureau...)–, et c'est en grande partie grâce à ton travail pour mettre en valeur ce que j'ai essayé de faire. Je pense qu'humainement je ne pouvais pas espérer un meilleur endroit pour faire ma thèse, et c'est bien parce que l'ambiance au sein de ce labo est passionnante et m'a permis d'être entouré de personnes extraordinaires et inspirantes comme toi.

Und jetzt muss ich die Sprache Goethes benützen um dir zu bedanken Andreas. Ich bin sehr stolz darauf, dass ich mit dir arbeiten können habe, obwohl ich manchmal gequetscht ware zwichen den Aerodynamiker und den 'Turbulenz-Mann' (ich zitiere hier kein Name...). Alles sieht so spannend aus wenn man lernt mit deinem Blick zu gucken und es gibt kein besserer Lehrer um Forschung zu schätzen. Ich weiss nicht, ob ich dieses Arbeit zu einem guten Ende bringen hätte ohne allen deinen freundlichen Ratschläge, und deswegen hoffe ich auch, dass ich noch viel von dir lernen kann.

La qualité d'un travail expérimental est d'abord lié à l'entourage technique du doctorant qui n'est pas plus habile qu'un bambin lorsqu'il commence sa thèse. J'ai eu la chance de travailler avec la plus fine des équipes ici et je leur dois une fière chandelle. Sans vous Jean-Marc et François et votre travail formidable, je pense que j'en aurais eu pour quelques années de plus et quelques cheveux de moins (en même temps certains diraient que ce serait pas plus mal...). Merci à Patrick et Romain pour les montages optiques aux petits oignons qui sont une part importante de ce travail, et à Janick pour avoir 'mis un coup de pression'. Et merci aux artistes de l'atelier Mathieu, Bastien et Olivier.

J'ai également eu la chance de collaborer avec de très nombreuses personnes dans le cadre du projet ANR Activ_Road, et je vous suis tous vraiment reconnaissant pour tous les échanges et ce que j'ai pu apprendre à vos côtés : Kévin, Marc, Patricia, Sylvie, Fabien (merci de t'être beaucoup

investi pour que je vois quelque chose qui ressemble à une voiture dans la soufflerie et pas seulement un gros cube chelou), Eric, Laurent.

Bien sûr, tout ce travail n'aurait pas la même allure sans l'ambiance géniale orchestrée par toute l'équipe de collègues-amis du labo (sorry guys, I'm not translating it in English, it will be your French holiday homework) : Christophe (2* au guide Michelin et critique en pâtisserie averti), Yifei et Ruiying, Armando (grazie per i giri da bici ma spero che adesso non ti perderai nel bosco perchè ti aspetto per aprire la focacceria), Ksenia, Di (really ??), Gabriel, Clément(s), Muhittin, Catherine, Florian.

I also want to thank the members of my thesis committee for investing part of their time on this piece of research. Lou Cattafesta and Holger Babinsky for accepting the role of reviewer and making insightful suggestions on my work. Olivier Cadot pour avoir présidé le jury et Caroline Braud. The interest and curiosity that you have all shown for this work is an honor and a pleasure.

Èndlisch mùss ich á unbedìngt mine Familie bedònke. Ich hätt gàr nìx gemacht ohne mi Momme ùn mi Papi und binn sehr glìcklisch, dass se immer dò sinn far mich. Ich binn zefriede, dass Litt toll wìe eìsch stolz ùff mich sinn.

Et merci à celle qui m'a longtemps accompagné sur ce chemin trop tortueux.

Et puis un dessin vaut bien plus que des mots pour exprimer tout ce que vous m'avez apporté.

Yann

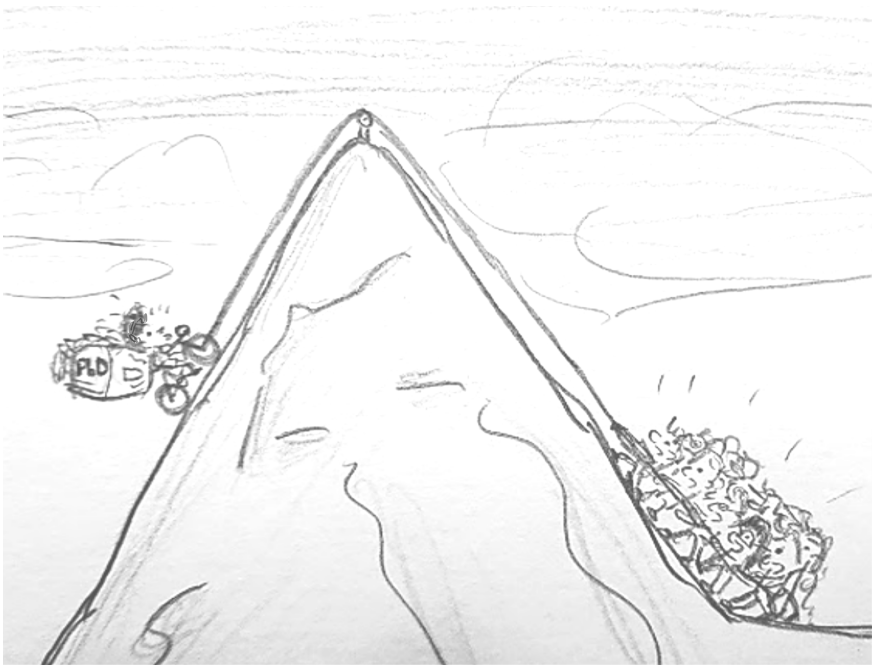

Contents

Chapter 1

An introduction about bluff body wakes

An introduction is proposed to present the frame of this work. Industrial and societal contexts are first illustrated. A review of the flow past bluff bodies is presented with a focus on the peculiar dynamics of the wake and the problem of aerodynamic drag generation. From then on, various passive and active flow control methodologies with aiming at manipulating the drag of bluff bodies are discussed. This leads finally to the presentation of the main problematics tackled by this work and how the remainder of the manuscript addresses these issues.

Contents

1.1 Industrial context

The problematic of transportation and its environmental impact has been considered as one of the major societal stakes in the recent years. A wide part of our society functioning is highly dependent on transportation for both the movement of people and the exchanges of goods. Currently in France, more than 85 % of the volume of transport of people is ensured by road transports amongst which 80 % is due to the sole personal vehicles. In the same time, ground transportation of goods is massively dominated by road vehicles with almost 90 % of the total amount of exchanges in question. With an estimated 15-20 % of global CO2 emissions attributed to transport, amongst which around 75 % just for road vehicles, road transport is a key problematic from the environmental point-of-view.[1] The reduction of road vehicles greenhouse gases emissions represents thus a key lever to tackle the problem of climate change. The emissions of the median car were around 130 g_{CO2} km^{-1} in 2015 with a target of 95 g_{CO2} km^{-1} by 2021. Conversely, strict regulatory norms are also imposed for heavy trucks emissions. Strong levers must accordingly be identified to allow for these drastic reductions in pollutant emissions to be achieved.

Th main levers existing to reach these emission norms are the optimization of the propulsion system (ranging from improving the efficiency of combustion engines to developing electric propulsion systems and renewable-energy-powered vehicles), the reduction of vehicle's mass and the reduction of the drag force experienced by vehicles. This drag force is the addition of two main contributions : the solid friction due to the contact of the vehicle with the surface of the road, and the aerodynamic drag resulting from the resisting force imposed by the air-stream on the vehicle. The aerodynamic drag of a vehicle is characterized by a normalized coefficient C_D which lies around 0.3 and 0.6 (or SC_D around 0.45 and 4.5 by taking into account the frontal surface of the vehicle S) respectively for current cars and trucks. For these typical values of SC_D, above 60 to 90 km h^{-1} the aerodynamic drag becomes the major contributor to the drag force (Hucho & Sovran, 1993). With most of the road freight occurring above these speeds on trunk roads and highways, the reduction of aerodynamic drag is a promising lever to regulate greenhouse gases emissions. More generally, around 30 % of the emissions and gas consumption of cars is due to aerodynamic drag.

Nevertheless, the problem of aerodynamic drag reduction remains quite complex, which is particularly illustrated by the stagnation in average C_D for cars over the past 20 years. Indeed, the optimization of the drag coefficient of a car or a heavy truck is only one amongst many aspects for the conception of a vehicle. Moreover, many of these aspects are contradictory to a minimal C_D and privileged by manufacturers on security or transport efficiency grounds : useful load and other functional aspects, thermal management of the vehicle, aerodynamic stability or crash safety, etc. Figure 1.1 gives a striking illustration of this tricky problematic. The problem of aerodynamic drag-optimality of vehicles has been solved a long time ago[2] : the two cars presented in figure 1.1(a,b) (a personal car *Schlörwagen* imagined in Göttingen, and a Mercedes-Benz race-car which

[1] Most of the figures cited here are extracted from the 2019 report of the *Ministère de la Transition Ecologique et Durable* on transport. *Chiffres clés du transport – Edition 2019*, C. Sarron & P. Serre.

[2] The problem of aerodynamic drag-optimality refers here to the problem of finding the shape with the lowest drag in subsonic flow for a given cross-sectional area or a given volume.

Figure 1.1: Typical old drag-optimized (a,b) and modern functionality-optimized (c,d) vehicle shapes illustrating the fundamental problem of vehicle aerodynamics being a trade-off between aerodynamic drag efficiency, aerodynamic stability and useful space. (a) *Schlörwagen* (1936). (b) Mercedes-Benz W125 Stromlinien (1938). (c) Volvo VNL (2017). (d) Peugeot 2008 (2019).

held the land speed record in the late 1930's) are over 80 years old, nevertheless they had a C_D below 0.15, a value which is not even approached by the current cars. Indeed, nowadays, vehicle manufacturers are favouring functionality and thus vehicles with the highest possible useful load as a priority. This imposes a more-or-less common shape for all current vehicles roughly derived from a parallelepiped geometry as illustrated in figure 1.1(c,d). Aerodynamic drag considerations are only taken into account afterwards and the aerodynamic optimization is done with minor changes on the geometry (roof inclination or additional rear spoilers for instance). Such sharp and bluff geometries are the source of an important drag generation especially because of the near-wake of the vehicle responsible on its own for 30 to 50 % of the total aerodynamic drag for heavy-trucks and cars respectively. As a consequence, radical solutions have to be sought to control the flow behind vehicles and achieve noticeable aerodynamic drag reductions.

In this industrial context, the present work aims at improving the comprehension of aerodynamic drag generation in the wake past vehicles, as well as providing flow control strategies leading to important aerodynamic drag reductions. The next sections will give a detailed picture of bluff body wakes and a review of efficient drag-reducing flow control strategies.

1.2 A picture of bluff body wakes

We first propose a global view of bluff body wakes in order to describe the main features characterizing these flows.

The complexity of wakes lying in the variety of scales, dynamics and features, figure 1.2 gathers a representative ensemble of wake flows visualizations drawing these essential features. To introduce all the different aspects, wake flows are organized depending on the two main parameters accounting for flow peculiarities: the complexity of the bluff body geometry (ranging from simple bi-dimensional geometries to complex three-dimensional real geometries) and the Reynolds number of the flow $Re = U_0 D/\nu$ where U_0 is the free-stream velocity, D the characteristic cross-flow length scale of the geometry and ν the kinematic viscosity of the fluid.

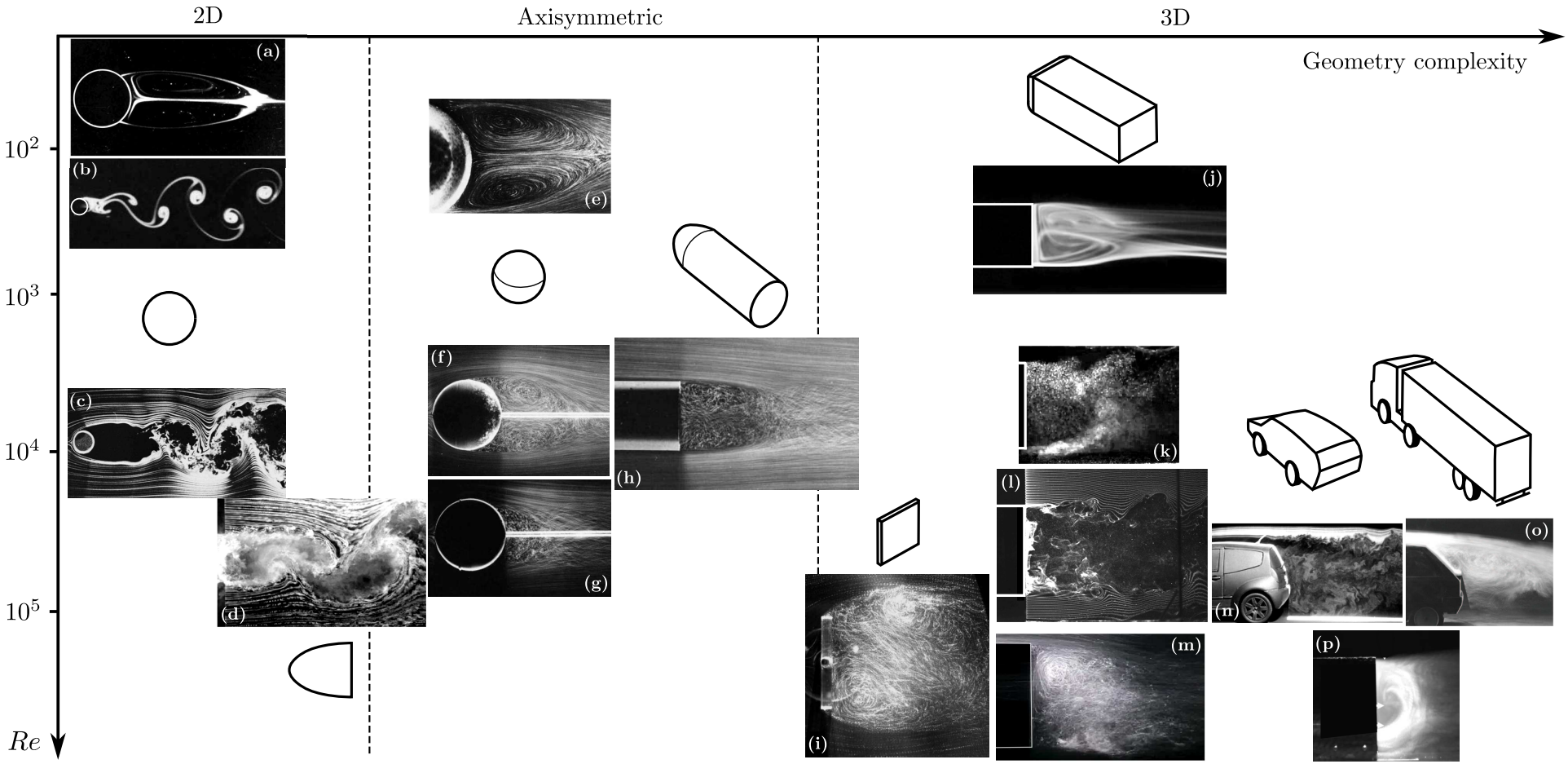

Figure 1.2: A global picture of bluff body flows. Flow visualizations are ranked by increasing Re vertically and geometry complexity horizontally. (a,b) Circular cylinder wake at $Re = 41$ and $Re = 105$ (Taneda, 1956*b*). (c) Circular cylinder at $Re = 10^4$ (Van Dyke, 1982). (d) Wake of a D-shaped cylinder at $Re = 4.6 \times 10^4$ (Li *et al.*, 2015). (e) Laminar sphere wake at $Re = 118$ (Taneda, 1956*a*). (f,g) Turbulent sphere wake at $Re = 1.5 \times 10^4$ and 3×10^4 (Van Dyke, 1982). (h) Wake of an axisymmetric bullet-shaped body at $Re = 10^4$ (Van Dyke, 1982). (i) Flat plate normal to the flow at $Re = 2.64 \times 10^5$ (Cadot, 2016). Wake of an Ahmed body in ground effect at $Re = 365$ (j) (Grandemange *et al.*, 2012), $Re = 9 \times 10^3$ (k,l) (private communication with A. Spohn and D. Barros) and $Re = 2.16 \times 10^5$ (m) (Cadot *et al.*, 2015). Wakes past different real cars (n,o) (Beaudoin, 2004; Grandemange, 2013) and real heavy truck (p) (Lo & Kontis, 2017).

A striking common feature of all these flows, despite the different types of geometries and the degree of complexity of the flow, is the presence of flow separation leading to a large recirculating flow region just behind the body. This flow separation can be of two different nature depending on the geometry, which gives a first distinction among bluff bodies. Flow separation of the boundary layer around the body is triggered either by an adverse pressure gradient related to the curvature of a smooth geometry (circular cylinder, sphere, figure 1.2(a-c,e-g)), or by the presence of salient edges in the geometry (truncated cylinder, bullet-shaped body, normal flat-plate, figure 1.2(d,h,i-p)). For the latter, the bluff body geometry is termed as blunt and the salient edge sets the location of an inertial flow separation. This separated flow region leads to a set of different dynamics on a broad range of spatial and time scales which becomes broader as Re is increased and which can be seen in the visualizations. These dynamics are represented on the sketch in figure 1.3(a) and can be summed up as follows :

- The separation of the boundary-layer leads to the release of concentrated vorticity in the wake and forms free shear layers separating the high-momentum free-stream flow from the low-momentum wake. This flow configuration leads to initial convective instability of the vortex sheet called the Kelvin-Helmholtz instability (denoted KH on figure 1.3(a)), and to the rolling of the shear surface leading to the periodic formation of vortices (see figure 1.12(a) for an example). The development of the shear layer is responsible for a complex mixing process between the two flow regions of different momentum which governs the formation of the wake and of the recirculation region. These coherent dynamics occur essentially on short spatial and time scales compared to the rest of coherent dynamics of the wake. Depending on the initial state of the separating boundary layer (either laminar or turbulent) the Kelvin-Helmholtz periodic rolling covers a range of time-scales centered on $St_\theta = f\theta/U_0 \sim 0.016$ or 0.025 related to the momentum thickness θ of the shear layer (Michalke, 1965; Dimotakis & Brown, 1976; Ho & Huerre, 1984; Morris & Foss, 2003). The contribution of this initial shear layer development to the entrainment of external fluid into the recirculating region (Philip & Marusic, 2012) and its formation has lately been tackled by a couple of studies (Trip & Fransson, 2017; Stella *et al.*, 2017) but there remains a lot of open questions on the topic.

- The recirculating flow (denoted RF in figure 1.3(a)) fed by the entrainment of external flow through the shear layer (Gerrard, 1966) is of low pressure which is responsible for most of the aerodynamic drag of these bluff body geometries as discussed in the previous section. This low pressure region will be one of the main focus of the work presented in this manuscript. As can be seen from figure 1.2(i,j,k,m,p), this recirculating region can exhibit a large degree of asymmetry in certain cases which can have a fundamental impact on the aerodynamic forces balance. This important aspect of the bluff body wakes dynamics will be thoroughly presented in the forthcoming sections.

- The development of the shear layers of opposite sign in vorticity surrounding the recirculating flow leads to a further interaction amongst them. This interaction results in an anti-symmetric instability characterized by the periodic shedding (denoted VS in figure 1.3(a)) of large-scale vortices which is quite clear in figure 1.2(b-d). This global instability involves scales which are generally one order of magnitude greater than the Kelvin-Helmholtz instability of the shear layers and are scaled by the geometry such as $St_D \sim 0.2$ (Provansal *et al.*, 1987; Williamson, 1996; Zdravkovich, 1997). These dynamics have a more or less pronounced impact on the wake and the aerodynamic drag of the bluff bodies depending on its initial geometry and thus has important consequences for the control of such flows. These aspect will be further discussed in the following sections.

Now that a general picture of the flow past bluff bodies has been drawn, we can focus in more detail on the different features presented and discuss their relation to the drag generation problem. For that, we follow the organization of figure 1.2 by discussing flows around bodies of increasing geometry complexity which will naturally reveal an increasing flow complexity.

1.2.1 Bi-dimensional geometries

One of the most investigated bluff body flows remains the cylinder flow, especially its circular section version. This flow has received particular attention both to investigate its dynamics and to model the wake flow. As such, it represents a strong starting point to move up to more complex three-dimensional geometries.

Most of the dynamics of the cylinder wake are dominated by the shedding at $St_{\mathcal{W}_r} \sim 0.2$ of large-scale vortices resulting from the strong interaction between the two opposite shear layers over a certain Reynolds number ($Re = 47$ for the circular cylinder instance) [3]. Here $\mathcal{W}_r$ is the cross-flow characteristic dimension of the mean wake (as sketched on figure 1.3(b)), an estimation of the distance separating both shear layers which governs the scaling of the vortex shedding frequency. These shed vortices are of quite strong vorticity intensity and an important contributor to the low pressure in the recirculating region. They even keep a strong coherence at higher Re, way above $O(10^3)$ where the wake becomes turbulent (Roshko, 1961)(see flows from figure 1.2(c,d)). Therefore, their dynamics significantly affects the drag of this bluff body and they play a key role in the mean properties of this flow. In this sense, the model of Gerrard (1966) established that the formation of the recirculation region results from an equilibrium between the reversed flow and the flow entrained across the shear layers. As a result, the mean length of the recirculating region $\mathcal{L}_r$ can be viewed as a direct consequence of the shear layer activity and the formation of the von Kármán vortices produced by the vortex shedding. This conceptual model introduces thus an important correlation between a feature of the mean recirculation region, the recirculation length, and the drag of the bluff body.

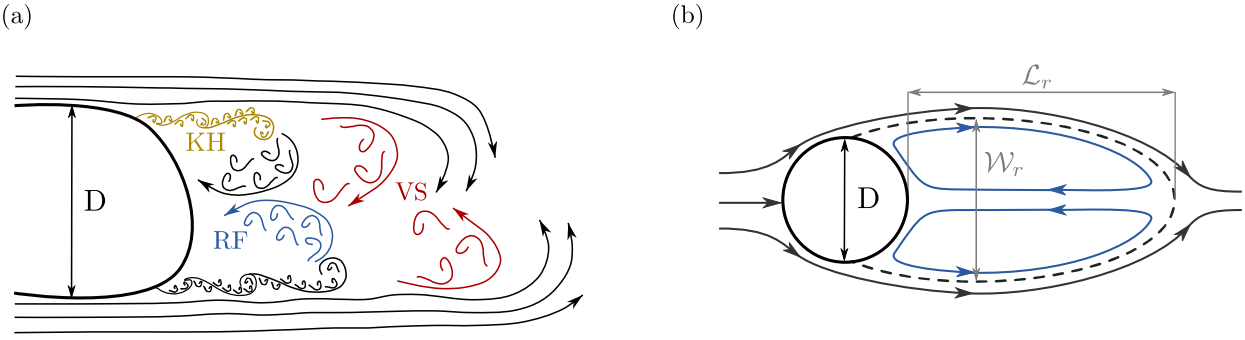

Figure 1.3: Main features of the wake flow past a bluff body. (a) From a dynamical point of view (adapted from Barros (2015)). (b) From a mean flow point of view (adapted from Grandemange *et al.* (2013*b*)).

These concepts of recirculating region balance are at the root of many works focusing on modelling the wake of bluff bodies to provide an analytical description of this flow and of its drag. Kirchhoff (1869) and Brillouin (1910) are the first to provide a model of the wake of a 2D bluff body, decades after the statement of D'Alembert's paradox (D'Alembert, 1752) on the nil drag of any body in an inviscid flow. These first model known as free-streamline theory had as a starting point a wake of infinite length $\mathcal{L}_r = \infty$ at free-stream pressure p_0 (or equivalently a pressure coefficient[4] $C_p = 0$) separated from the potential free-stream flow by singular streamlines. Nevertheless, this model is known to poorly predict the drag of bluff bodies for two main linked reasons. For one thing, the free-stream pressure in the wake is a very rough approximation as negative values of C_p are encountered in such wakes, thus strongly underestimating the drag. For another, as argued by Batchelor (1956), the infinite length of the recirculation region is not admissible from a physical point-of-view. Following this, the model can be made more realistic by imposing a finite length

[3] The presence of vortex shedding is mainly independent of the shape of the cylinder's cross-section as exemplified on the circular and D-shaped cylinders in figure 1.2(b,c) and (d).

[4] The pressure coefficient C_p in a flow at free-stream velocity U_0 and free-stream pressure p_0 is defined as

$$C_p = \frac{p - p_0}{\frac{1}{2}\rho U_0^2}$$

where p is the pressure in the flow and ρ the density of the fluid.

$\mathcal{L}_r$ or conversely imposing the pressure coefficient on the base of the bluff body C_{pb}, and imposing the separation points in the case of a smooth bluff body as the circular cylinder. The important shortcomings of these models (Roshko, 1954, 1955; Parkinson & Jandall, 1970) come then from the fact that the model requires empirical input (C_{pb} or L_r) to estimate the drag. Further work from Sychev *et al.* (1998) proposed that the Kirchhoff wake is the limit when $Re \to \infty$ where minimal drag is obtained. Recent efforts from Yeung & Parkinson (2000) or Steiros & Hultmark (2018) incorporating flow momentum balance considerations in the free-streamline theory to circumvent the need for empirical input led to the formulation of self-contained models to convincingly predict the drag of normal flat plates in the case of laminar steady flows.

Sychev *et al.* (1998) further developed the model proposition of Batchelor (1956) of a closed wake with rotational recirculating motion inside, similarly to the sketch in figure 1.3(b), with similar momentum balance considerations. However, this model only provides asymptotic behaviour of the wake more than a practical view of it allowing drag estimations. Nevertheless, it provides key arguments on the relation between the drag, the pressure at the base of the bluff body and the main features of the recirculating wake. In the same idea, Roshko (1993) or Balachandar *et al.* (1997) also built on the momentum balance on the free-streamline to provide qualitative relations between the mean recirculation region and the drag and base pressure of any 2D bluff body flow :

- The concept of wake bluffness introduced by Roshko (1955) relating the width of the recirculating region $\mathcal{W}_r$ to the width of the body D has an important influence on the drag. The greater the ratio $\mathcal{W}_r/D$, the greater the drag (and the lower the base pressure). This empirical result appears quite clearly when considering the higher drag of a normal flat plate compared to a circular cylinder or a D-shaped cylinder because of the flow separation normal to the free-stream in the former case. The importance of the flow separation orientation is also revealed through the example of the drag crisis of the circular cylinder. Around $Re \sim 2 \times 10^5$, the point of flow separation moves downstream because of the transition to a turbulent boundary layer, which results in a thinner wake (see figure 1.2(f,g)) and meanwhile a drag coefficient decreasing from 1.2 to 0.4 (Zdravkovich, 1997).

- In the case of blunt geometries, where the bluffness is fixed $\mathcal{W}_r = D$, the length of the recirculation region highly influences the drag. The shorter $\mathcal{L}_r$, the higher the drag (and the lower the base pressure).

These two aspects can also be formalized in a common approach by looking at the ratio $\mathcal{L}_r/\mathcal{W}_r$ as it was done by Sychev *et al.* (1998). These qualitative relations between the properties of the mean recirculation region and the base pressure and drag of 2D bluff bodies are valuable not only for the understanding of these wake flows but also as guidelines to design pertinent flow control techniques for reducing the drag.

1.2.2 Axisymmetric geometries

When increasing one step further the degree of complexity of the geometry, one finds bluff bodies presenting a natural axisymmetry. Three canonical axisymmetric geometries are of great interest to describe the specificities of this type of flow : the sphere for smooth geometries, and the normal disk and the bullet-shaped body for blunt geometries (see figure 1.2(e-h)).

For the case of the sphere, despite the axisymmetry of the geometry the flow loses its axisymmetry property for low values of Re. In this sense, the wake flow of a sphere differs remarkably from the previously seen cylinder wake. At $Re \sim 210$ the axisymmetry is lost and the flow selects a simple plane of symmetry as shown in figure 1.4(b) (Thompson *et al.*, 2001; Pier, 2008; Fabre *et al.*, 2008). This bifurcation occurs before a second transition analogous to the 2D case of the cylinder where vortex shedding starts to occur above $Re \sim 280$. An interesting consequence of this loss of axisymmetry of the wake flow is the additional drag generated by the only-planar-symmetric flow. Indeed, the theoretical study by Pier (2008) manages to compute the unstable axisymmetric flow of the sphere at Re above the first bifurcation and thus propose a fair estimate of the influence of symmetry on the drag of the sphere. The main result from the study, the evolution of the drag coefficient of the sphere C_D with Re of the different stable and unstable flow configurations, is reproduced in figure 1.4(a). Around 6 to 7 % of the total drag of the sphere is ascribed to the loss

of axisymmetry in favour of planar-symmetry, which represents a quite important amount. In the same time, only an additional ~ 1.5 % is related to the onset of vortex shedding, suggesting its relatively weaker influence in the three-dimensional wake of the sphere compared to the analogous 2D cylinder wake. Very similar scenarios can be drawn for the case of the normal disk (Natarajan & Acrivos, 1993; Meliga *et al.*, 2009) or the bullet-shaped body (Sevilla & Martínez-Bazán, 2004; Bohorquez *et al.*, 2011), which generalizes the behaviour of the wake flow past axisymmetric bluff bodies.

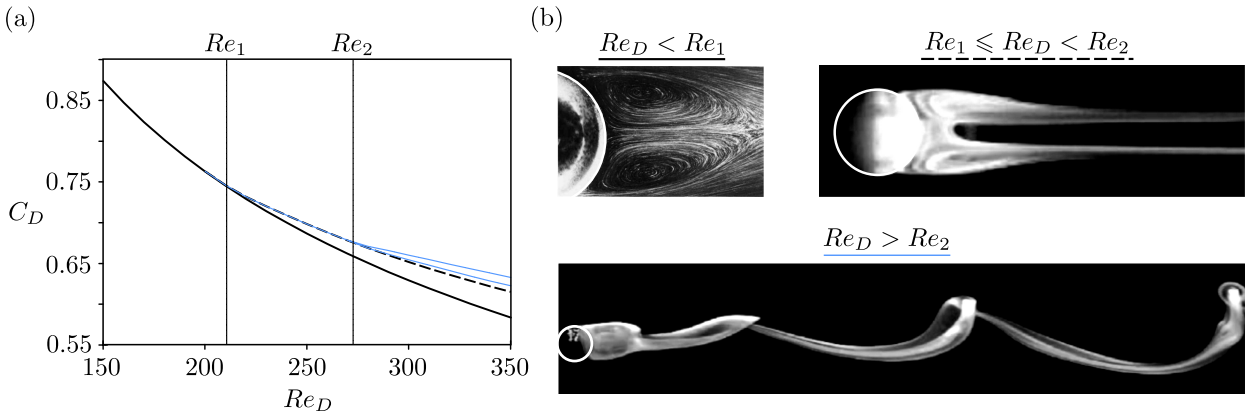

Figure 1.4: Bifurcation scenario in the wake of a sphere at low Re and its relation to drag. (a) Drag of the sphere depending on the flow regime from Pier (2008) : steady axisymmetric (thick black line), steady planar symmetric (dashed line) and unsteady planar symmetric (thin blue lines delimiting maxima and minima). (b) Flow visualization of each flow regime in its stable Re domain from Taneda (1956*a*), Thompson *et al.* (2001) and Chrust *et al.* (2013) respectively.

Interestingly, when further increasing the Reynolds number to the turbulent regime, the axisymmetry of the sphere and the bullet-shaped body are restored in a statistical sense according to recent experiments by Grandemange *et al.* (2014*a*) and Rigas *et al.* (2014) performed respectively for the sphere at $Re = 2 \times 10^4$ and the bullet-shaped body at $Re = 2 \times 10^5$. Actually, at these high Re, a planar symmetry is still observed in the large-scale organization of the wake but only in the instantaneous sense. This plane of symmetry rotates randomly over very long time scales 100 times slower than the vortex shedding dynamics, and the azimuthal orientation of the plane θ_W explores equiprobably all the orientations as shown in figure 1.5(a). However, once the axisymmetry of the geometry is perturbed, as in the study of Grandemange *et al.* (2014*a*) which mimics the presence of side holding wires on the sphere, the statistical axisymmetry is broken and the instantaneous plane of symmetry explores preferentially positions θ_W the most distant from the perturbations positions (*ie* π for a $m = 1$ perturbation at $\theta_W = 0$ or $\pm\pi/2$ for a $m = 2$ perturbation at $\theta_W = 0$ and π as shown in figure 1.5(b)). Similar sensitivity to perturbations has also been evidenced for the bullet-shaped body by Gentile *et al.* (2017) in the turbulent regime. In this study, a small misalignment of the body's axis with the free-stream flow (less than 1 deg.) results in a complete locking of the position of the symmetry plane of the wake flow, underlining the high sensitivity of these loss of symmetries to small perturbations. In an effort of modelisation, Rigas *et al.* (2015) showed that the diffusive dynamics of the wake orientation of the bullet-shaped body are stochastically well captured by a simple non-linear Langevin equation describing the position of the base pressure barycenter. The persistence of this instantaneous axisymmetry-breaking of the wake has thus important consequences on the drag of these bodies as shown analogously in the laminar regime, and should constitute a strong lever for drag reduction. Nevertheless, these low frequency dynamics of the wake in the turbulent regime are not retrieved for the case of the normal disk according to Boujo & Cadot (2019) where the axisymmetry is not instantaneously broken whereas the axisymmetry was broken in the laminar regime. This observation suggests that the orientation of the flow separation at the base (normal to the free-stream for the disk, tangential for the bullet-shaped body) has a strong influence of these dynamics.

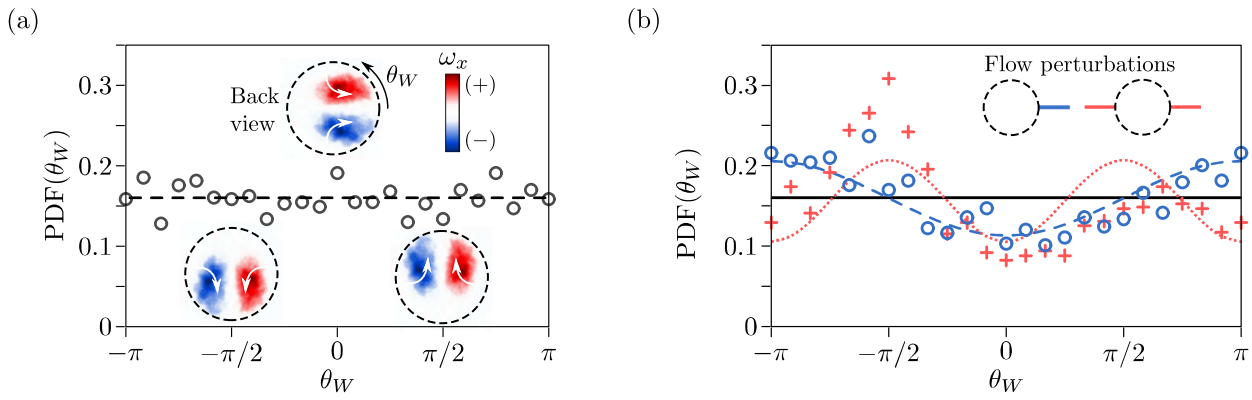

Figure 1.5: Azimuthal random rotation of the plane of symmetry of the sphere wake at higher $Re = 2 \times 10^4$ adapted from Grandemange *et al.* (2014*a*). (a) Probability density function (pdf) of the orientation of the plane of symmetry of the wake θ_W deduced from the position of the momentum deficit barycenter. Longitudinal vorticity fields ω_x in a cross-stream plane in the wake show three specific orientations $\theta_W = 0$ and $\pm\pi/2$. (b) Perturbation of the statistical axisymmetry of the wake by control cylinders placed in the wake. $m = 1$ perturbation in blue and $m = 2$ in red.

1.2.3 From three-dimensional geometries to real vehicles

The last step of complexity among the simplified bluff body geometries is the flow behind fully three-dimensional blunt geometries. There are two basic prototype flow for these bluff bodies with again a difference in flow complexity. The complexity is influenced by two main features. For one thing, the sharpness of the upstream-facing side of the geometry and its streamwise aspect ratio[5] strongly influence the development of the flow in the wake. Indeed, the wake flow past simple cubes (Klotz *et al.*, 2014) and stream-facing rectangular plates (Marquet & Larsson, 2015) is characterized by a strong coupling between the front separation and the main features of the wake, especially for the cube where the flow separating at the front edge interacts with the wake. A second degree of complexity comes from the presence of a ground – as is necessary to properly mimic road vehicles – which removes an additional symmetry plane of the geometry.

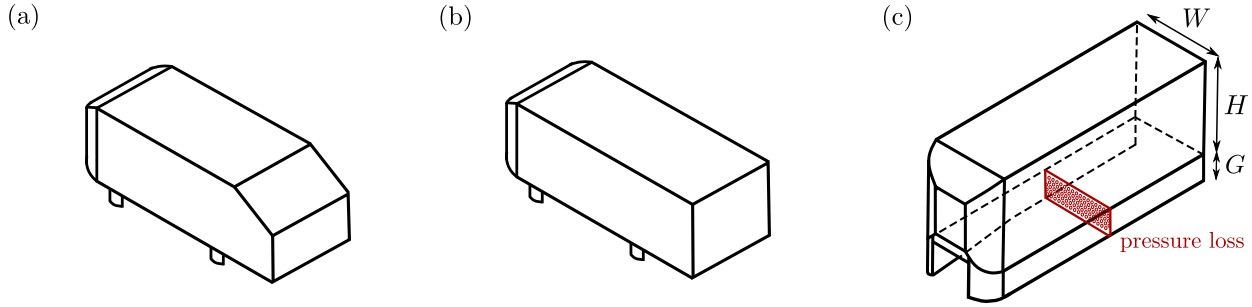

Figure 1.6: Simplified ground vehicles. (a) Original slanted Ahmed body introduced by Morel (1978) and Ahmed *et al.* (1984) representative of hatch-back vehicles. (b) Square-back Ahmed body. (c) Heavy-truck model introduced by Szmigiel (2017) and Castelain *et al.* (2018). The underbody is closed by skirts and crossed by drilled plates to alter the momentum of the underbody flow and be more representative of heavy-trucks flows.

Among these fully three-dimensional geometries, one has received particular attention both from a fundamental and industrial point-of-view for its pertinence as a simplified model of ground vehicles. The Ahmed body shown in its original rear-slanted version and its squareback version in figure 1.6(a,b) was introduced and popularized by the studies of Morel (1978) and Ahmed *et al.* (1984). Its main advantage over the simpler geometries discussed in the previous paragraph is the increased streamwise aspect ratio and smooth front surface allowing for a decoupling between the

[5]Here meaning the ratio between the characteristic streamwise length and cross-stream dimension of the geometry.

wake and the rest of the body and an interesting representativeness of its flow features compared to real vehicles[6]. While the slanted version of the model still receives academic attention mainly to study the large-scale streamwise vortices developing over the edges of the slant (Zhang *et al.*, 2015, 2018), recently the main focus was granted to the square-back version both for the richness of the wake dynamics (related to what was shown for less-complex geometries previously) and its representativeness of plethora of current geometries of ground vehicles (compact and urban cars, mini-vans and commercial vehicles, etc.). Recently, the specificities of the flow past lorries has also been accounted for by a specific, more representative, model geometry – depicted in figure 1.6(b) introduced by Szmigiel (2017) and Castelain *et al.* (2018) and derived from the square-back Ahmed body. Additional side skirts and pressure losses system in the underbody put a strong emphasis on the state of the underbody flow and its influence on the wake to be close to actual lorries.

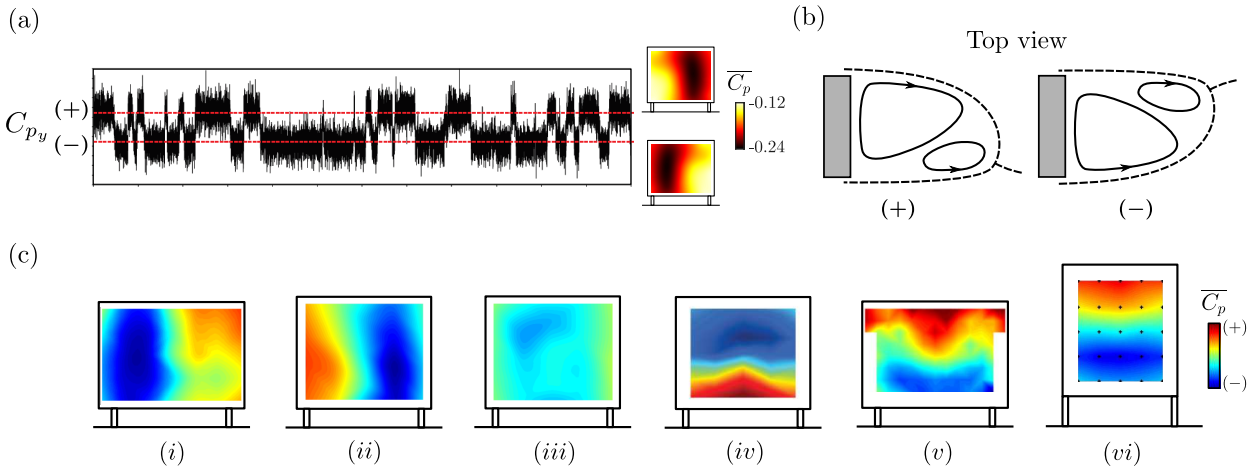

Figure 1.7: Asymmetries of the wake of the square-back Ahmed body. (a) Simplified description of the lateral bi-stability phenomenon. The wake switches randomly on long time-scales between two asymmetric states (+) and (−) corresponding to a positive and negative lateral pressure gradient on the base of the model C_{p_y}. The associated base pressure distribution of each state is also given. (b) Corresponding mean wake structure for each asymmetric state. (c) Mean base pressure distribution from various references in the literature presenting different lateral and vertical asymmetries : $(i-v)$ are square-back Ahmed bodies and (vi) the simplified heavy-truck model depicted in figure 1.6. (i) Grandemange *et al.* (2013*b*), $H/W = 0.74$, only state (−) is shown. (ii, iii) Bonnavion (2018), $H/W = 0.83$, state (+) only and full mean base pressure. (iv) Barros (2015), $H/W = 0.83$. (v) Eulalie (2014), $H/W = 0.74$. (vi) Szmigiel (2017), $H/W = 1.25$.

Even if the streamwise aspect ratio of the Ahmed body[7] is quite larger than the stream-facing flat plate or the cube (length to height ratio L/H is of O(3)) separation and reattachment of the flow just after the rounded front can importantly influence the flow conditions at the rear separation line and thus the dynamics in the wake at a second order[8] (Spohn & Gilliéron, 2002; Courtine, 2006).

The wake dynamics of the Ahmed body are in the continuity of the previously discussed peculiar features of the wake of simpler geometries. Grandemange *et al.* (2012) experimentally and then Evstafyeva *et al.* (2017) numerically showed how the laminar flow past an Ahmed body follows a first steady symmetry-breaking bifurcation similar to the one observed in the wake of the sphere or the bullet-shaped body. In the case of the small aspect ratio of the base of the model $H/W < 1$,

[6]The slanted Ahmed body with moderate slant angles is an interesting simplification of fastback vehicles, while the peculiar case of the square-back Ahmed body is more representative of many current squareback vehicles.

[7]In the rest of this manuscript we refer to the square-back Ahmed body simply as Ahmed body as from now on it will be the main focus of this work.

[8]This aspect is briefly qualitatively discussed by Barros (2015). Actually the presence or not of a front separation and reattachment on the Ahmed body can notably influence the characteristics of the boundary layer at rear separation and then the activity in the shear layers. Nevertheless, the wake dynamics are only weakly altered and the main features of the wake remain similar from a qualitative point-of-view.

this first bifurcation breaks the last plane of symmetry of the model and the wake is permanently deviated on one side. Nevertheless, when moving to higher turbulent Reynolds numbers, the large-scale dynamics of the wake become quite more complex compared to the cases of the sphere and the bullet-shaped body. This is due to the geometry having only two planes of symmetry[9] which has important influence on the symmetry-breaking behaviour observed. The aspect ratio of the base H/W and the ground clearance G have a strong influence to determine the evolution of the symmetry-breaking instability in the turbulent regime. For the original Ahmed body setup ($H/W = 0.74$ and $G/H = 0.17$ in Morel (1978); Ahmed *et al.* (1984)), Grandemange *et al.* (2013*c*) showed how, analogously to the sphere and the bullet-shaped body, the turbulent regime restore the vertical symmetry of the setup in a statistical sense but with an instantaneous asymmetry. Given the symmetry properties of the geometry, the instantaneous asymmetry of the wake manifests as a lateral asymmetry and random side reversals of the wake to statistically restore the symmetry. This behaviour called bi-stability, summed up in figure 1.7(a,b), is characterized by a random flipping motion of the wake from one side to the other with a characteristic residence time of $O(10^3 H/U_0)$ in an asymmetric state. When reversing the aspect ratio of the base ($H/W > 1$), the bi-stability occurs in the vertical direction under the condition the ground clearance is sufficiently high not to influence too much the flow. Grandemange *et al.* (2013*a*) has drawn a landscape of this bi-stable feature of the wake in the parameter plane $(H/W, G)$ which was also numerically assessed by Dalla Longa *et al.* (2019) for the original Ahmed body and its inverted stream-normal aspect ratio version. This exchange of instability direction depending on the stream-normal aspect ratio of the geometry is quite reminiscent of the linear stability study of Marquet & Larsson (2015) for stream-normal flat plates in the laminar regime where the symmetry-breaking instability aligns depending on the stream-normal aspect ratio of the plate.

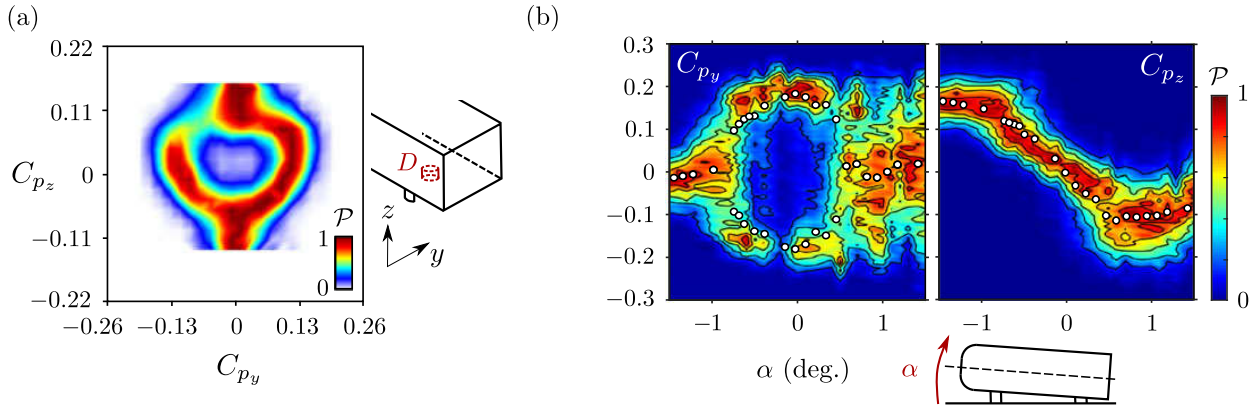

Figure 1.8: Bifurcation scenario of the turbulent Ahmed body wake at $Re = O(10^5)$. The asymmetry of the wake is quantified by the lateral C_{p_y} and vertical C_{p_z} pressure gradient on the base of the model. (a) Pdf $\mathcal{P}(C_{p_y}, C_{p_z})$ where C_{p_z} is fixed by the introduction of cylindrical perturbations of diameter D in the underbody (adapted from Barros *et al.* (2017)). (b) Pdfs $\mathcal{P}(\beta, C_{p_y})$ and $\mathcal{P}(\beta, C_{p_z})$ obtained by changing the pitch angle α of the model (adapted from Bonnavion & Cadot (2018)). The white circles denote the most probable values.

Nevertheless, these symmetry-breaking dynamics in the wake of the Ahmed body appear to be highly sensitive to small flow perturbations. This is made clear from the important discrepancy shown throughout the literature in the mean symmetry of the wake flow of Ahmed bodies with very similar aspect ratios H/W and similar ground clearance G/H, of which several representative examples are given in figure 1.7(c). Different mean wakes are observed exhibiting either lateral bi-modality or permanent vertical asymmetry. Two recent studies investigated in detail this feature and provide more insight into the symmetry-breaking instability for this particular fully 3D geometry. Barros *et al.* (2017) showed how small geometric perturbations in the underbody (typically cylinders of diameter one to two order of magnitude smaller than H) strongly affect the asym-

[9] Actually, the Ahmed body itself has two planes of symmetry. Nevertheless, as it is placed in ground proximity and mounted on supports in experimental studies, the horizontal plane of symmetry of the geometry does not strictly remain a plane of symmetry.

metry direction of the wake. The study drew a complete bifurcation scenario as shown in figure 1.8(a) suggesting a competition between vertical and lateral asymmetries with an evolution from purely lateral bi-stable asymmetries[10] to purely vertical permanent asymmetries depending on the size of the perturbation. Bonnavion & Cadot (2018) further formalized this sensitivity study by looking at the influence of small changes on the wake asymmetries of the pitch angle of the Ahmed body as shown in figure 1.8(b), the yaw angle (as done by Cadot *et al.* (2015) also), the ground clearance or the stream-normal aspect ratio of the body. The work provides a description of the symmetry-breaking instability as an analogous to the axisymmetric case of the sphere and the bullet-shaped body discussed previously with two specific modifications : an elliptic modulation of the degree of asymmetry due to the aspect ratio H/W of the body, and an alignment of the admissible asymmetry orientations on the two plane of symmetry of the geometry[11] which echoes the sensitivity study of the sphere wake from Grandemange *et al.* (2014*a*).

Even if these recent works give important insight in the behaviour of the symmetry-breaking instability in the wakes of three-dimensional blunt bodies, there is still an important open question concerning what triggers this symmetry-breaking and its advanced relation to drag generation. Grandemange *et al.* (2014*a*) and Castelain *et al.* (2018) showed how changes in ground clearance and underbody flow can highly modify the wake flow and affect the generation of base drag. These answers would give valuable insight in efficient methods to control these wakes with an aim of drag reduction.

1.3 Manipulation of bluff blunt bodies wakes

Now that the main features of the wake flow past bluff bodies have been extensively presented and their link to the generation of drag discussed, we review in this section the most important flow control techniques successful at reducing drag and the main challenges these techniques are facing. The focus is put on the control of flow past blunt bodies as this will be the interest of the rest of this manuscript.

According to Choi *et al.* (2008), control techniques can be separated in two main categories : passive flow control techniques do not require an additional external energy input to function whereas active flow control techniques do. Here this distinction will be followed for our review of wake flow control techniques. Lately, another distinction has also appeared among active flow control techniques relating to the presence or not of a feedback loop to provide information of the state of the system to the control system. A simplified description of the main control techniques which have proved to be successful at reducing the drag of blunt bodies is provided in figures 1.9 and 1.10 for passive and active flow control techniques respectively.

Precursory works by Roshko (1955) and Bearman (1965) on 2D blunt bodies have shown how the control of the vortex shedding dynamics in the wake was a very strong lever for drag reduction. Using splitter plates with length of order $O(D)$ in the middle of the wake, they both showed how the interaction between the opposite shear layers could be prevented. This results in vortex shedding dynamics appearing only farther downstream and thus an increased length of the recirculating region and associated base pressure recovery at the base of the cylinder (as has been discussed previously). As an example, in Bearman (1965), splitter plates lead to a 50% base pressure recovery on a parallelepiped cylinder at $Re = O(10^5)$. The length of the recirculation region and the base pressure thus obtained are close to the ones in the wake of three-dimensional geometries as the Ahmed body. Other notable works on drag reduction by controlling the vortex shedding are based on the introduction of three-dimensional perturbations such as small tabs as in Park *et al.* (2006) for a D-shaped cylinder (see also the review by Choi *et al.* (2014)). Here the vortex shedding dynamics are weakened by the loss of their spanwise coherence due to the 3D flow perturbations. Albeit less efficient than splitter plates in drag reduction –around one-third of base pressure recovery is obtained–, these tabs represent geometrical modifications which are far less important. Using active flow control methods, these geometrical modifications can be almost

[10] Meaning with nil or only residual vertical asymmetry.

[11] Here $\theta_W = 0, \pm\pi/2$ or π are the possible asymmetry orientations if we refer to the notations of the case of the sphere in figure 1.5.

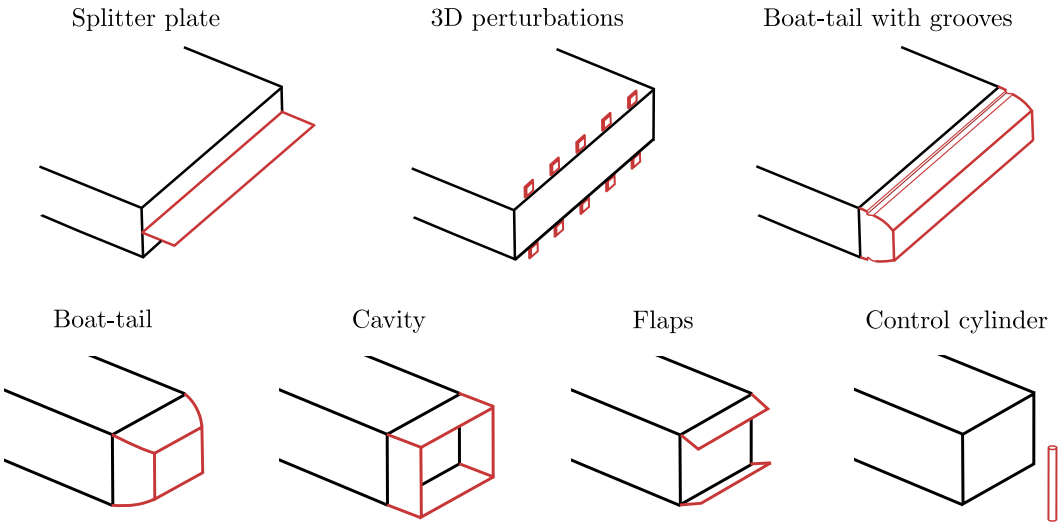

Figure 1.9: Representative passive flow control devices leading to successful drag reduction on 2D and 3D geometries. Some of the figures are inspired by Choi *et al.* (2008) and Choi *et al.* (2014). Detailed description and references are provided in the text.

completely avoided. Pastoor *et al.* (2006) used synthetic jets at the edges of a D-shaped cylinder to force the wake at low frequencies around the vortex-shedding. Coupled to a feedback loop giving information about the phase of the vortex-shedding cycle, they managed to desynchronize both shear layers and thus prevent vortex-shedding and elongate the recirculation region –as with splitter plates– leading to 15% drag reduction.

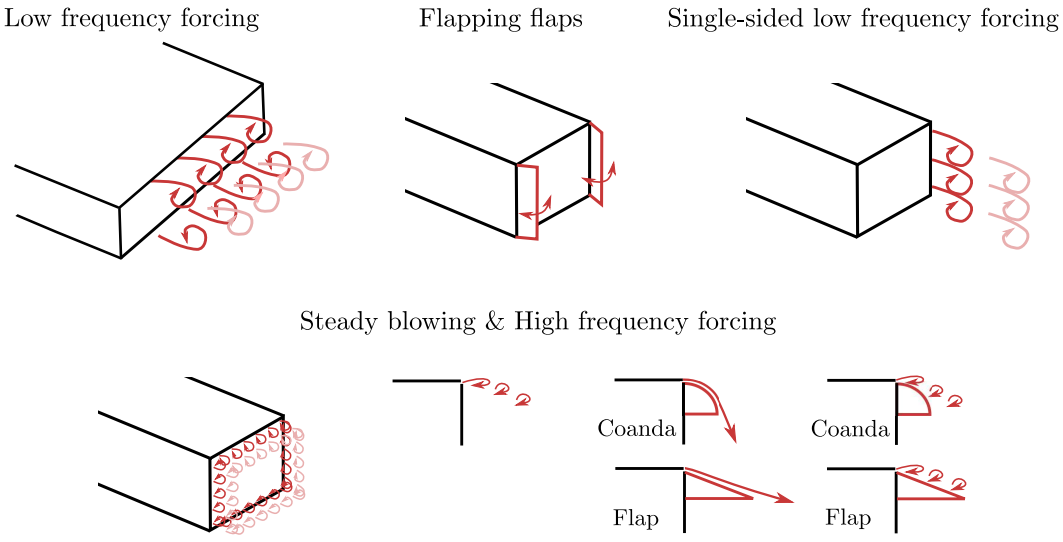

Figure 1.10: Representative active flow control techniques leading to successful drag reduction on 2D and 3D geometries. Some of the figures are inspired by Barros (2015). Detailed description and references are provided in the text.

Unfortunately, these methods are specific to nominally to 2D geometries, and for three 3D blunt bodies where vortex shedding has only a week signature on the drag they fail to give results in terms of drag reduction (Brackston *et al.*, 2018). Efficient drag reduction strategies in the wake of 3D blunt bodies are mostly based on different mechanisms building either on decreasing the bluffness of the wake or controlling its symmetry-breaking dynamics. To decrease the bluffness of the wake, one of the most efficient strategies is to act on the flow orientation at separation to force an inwards deflection. Passively, this is achieved by the use of straight or curved boat-tails (from the old studies of Maull & Hoole (1967), Mair (1969) or Wong & Mair (1983) to more recent

investigations by Lorite-Díez *et al.* (2017), Lorite-Díez *et al.* (2018), Bonnavion & Cadot (2018) or Bonnavion & Cadot (2019)) or inwards-oriented flaps around the base of the model (Grandemange *et al.* (2013*c*), de la Cruz *et al.* (2017*a*), Szmigiel (2017)). The performances in drag reduction are highly dependent on the length and the inclination angle of the boat-tails or flaps. Usually lengths of order between 0.15 and 0.5H and inclination angles around 10 deg are needed to obtain significant drag reductions of 5 to 10 %. However, above a critical angle[12], an important loss of efficiency occurs due to the detachment of the flow from the boat-tail or flap surface and can even lead to drag increase. Recent studies from Mariotti *et al.* (2017) and Mariotti *et al.* (2019) proved that the use of contoured grooves at a fixed position on the boat-tail could lead to improved drag reductions at higher inclination angles. The boundary layer can remain further attached due to the local relaxation of the no-slip boundary condition at the groove location.

Another aim to circumvent the flow detachment for important inclination angles is to resort to active flow control by employing small-scale jets in the vicinity of the surface. The main advantage lies in the possibility of employing even higher inclination angles compared to passive techniques and also reducing the size of the flaps or boat-tails used so that they remain one to two orders of magnitude smaller than H. Many of the early studies were devoted to steady blowing over small flaps of curved surfaces (Freund & Mungal, 1994; Englar, 2001; Rouméas *et al.*, 2009; Pfeiffer & King, 2018) to take advantage of the Coanda effect for the flow deviation (Kadosch, 1958; Wille & Fernholz, 1965). The main shortcoming of such a technique lies in the high power expenses due to the important mass flow rates involved in the steady blowing.

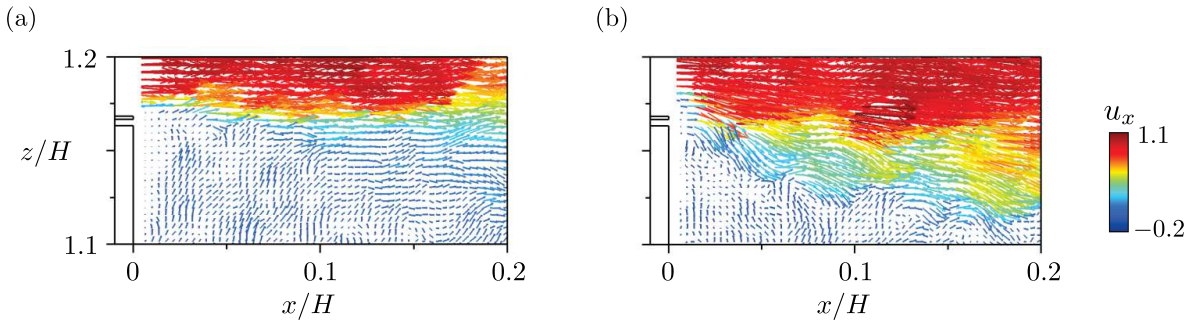

Figure 1.11: Fluidic boat-tail effect obtained with high-frequency forcing around the base of the Ahmed body from Barros *et al.* (2016*b*). Velocity field colored by the streamwise velocity u_x in the vicinity of an edge of the base for the unforced flow (a) and the flow forced at $St_H \sim 12$ (b).

To alleviate the energetic cost, unsteady blowing has proven to be an adequate solution. The last decade has been a really active period for research on this topic. Studies on the bullet-shaped body (Qubain, 2009; Oxlade *et al.*, 2015) and on square-back 3D geometries (Barros *et al.*, 2014; Cabitza, 2015; Barros *et al.*, 2016*b*) have shown how unsteady blowing could lead to substantial drag reductions of order 10 % even without the presence of flaps or curved surface in the vicinity of the jets. This results from the fluidic boat-tailing effect occurring when forcing at high frequencies, typically above the shear layer frequency, as exemplified in figure 1.11 from the study of Barros *et al.* (2016*b*). This flow deviation is the consequence of an accumulation of circulation from the pulsed blowing below the trailing-edge of the body. Rouméas *et al.* (2009) has shown the importance of the jets' inclination in the occurrence of this deviation effect for a steady blowing case and concluded that an inwards angle of 45 deg was the most efficient in terms of drag reduction. The addition of a flap or a curved surface below the jet further enhances this deviation effect as shown by Chaligné *et al.* (2013), Chaligné (2013), Schmidt *et al.* (2015), Barros *et al.* (2016*b*) or Szmigiel (2017). Additionally, as shown by Oxlade *et al.* (2015) and Barros *et al.* (2016*b*), this kind of active flow control strategy also leads to a stabilization of the shear layers surrounding the recirculating region of the wake and thus a lowered entrainment rate of flow momentum inside the wake. As discussed previously, this effect thus plays a role in elongating the recirculation region which is beneficial for drag. This stabilizing effect appears very clearly in the experiments of Parezanovic

[12] A typical value for this critical angle is around 15 deg. but it is sensitive to upstream flow conditions such as the boundary layer characteristics upstream the flap or the turbulence intensity.

et al. (2015) on forcing a canonical free-shear layer with pulsed jets shown in figure 1.12.

Conversely, when forcing this canonical free-shear layer at frequencies close to the most amplified frequency of the shear layer, its growth is noticeably increased. In the case of a blunt body wake, such an effect has important consequences on the flow entrainment rate as it is highly increased. Qubain (2009), Oxlade *et al.* (2015) and Barros *et al.* (2016*b*) showed how this led to an important drag increase in the wake of a 3D blunt body. Nevertheless, in peculiar cases such an increase in entrainment by forcing the shear layer can be used in a beneficial way in terms of drag. The study of Li *et al.* (2019) focused on the Ahmed body in slight yaw conditions with an important static lateral asymmetry of the wake. By forcing the wake only on the leeward side of the base at high frequency, the fluidic boat-tailing resulted in a 6 % drag decrease without any influence on the wake asymmetry. When modulating this forcing with a low frequency ($St_H \sim O(1)$), the increase flow entrainment was able to re-symmetrize the wake in addition to the boat-tailing and give a slightly increased drag reduction in line with our previous discussion on asymmetry-related drag.

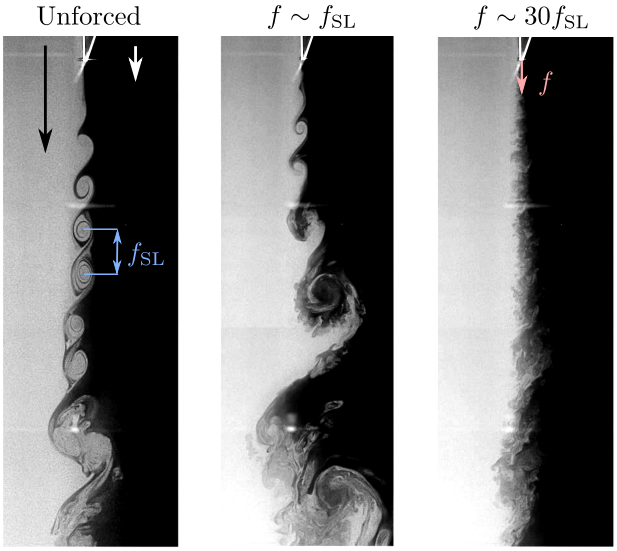

Figure 1.12: Flow visualization of the development of a free shear layer originating from a laminar boundary layer from Parezanovic *et al.* (2015). The unforced flow is characterized by coherent structures forming at a characteristic frequency f_{SL}. Forcing the flow at $f \sim f_{\mathrm{SL}}$ using micro-jet actuators promotes the formation of these structures and their pairing. Forcing the flow at higher frequency $f \sim 30 f_{\mathrm{SL}}$ results in the disappearing of these structures and stabilization of the free shear layer.

This low frequency flow control strategy was also used in order to mitigate the lateral bi-stable dynamics in the wake of the Ahmed body. Li *et al.* (2016) used a simple closed-loop opposition control scheme with pulsed jets on both sides of the base in order to force the wake on either side depending on the lateral position of the wake deduced from the lateral base pressure gradient. A mean symmetrization was achieved with a wake meandering around the completely symmetric state as described in figure 1.13. However, it came only with an associated 2 % pressure drag decrease due to the increased turbulent activity in the shear layers and thus a slightly reduced length of the recirculation region. Moreover, the side-alternating control promotes the vortex shedding dynamics in the wake resulting in a detrimental impact on the drag. Similarly, Brackston *et al.* (2016) with oscillating side flaps and Plumejeau *et al.* (2019) also with pulsed jets have shown similar mixed 2 % drag reduction using similar feedback control with linear control methods. To mitigate the lateral bi-stable dynamics, only passive control methods have proven to be satisfyingly efficient in terms of associated drag reductions. Grandemange *et al.* (2014*a*) mitigated the instability using a small vertical control cylinder localized in the middle of the wake with an associated base pressure recovery of around 5 %. The studies of Evrard *et al.* (2016) and Lucas *et al.* (2017) (also confirmed by Bonnavion (2018)) have shown how a cavity placed at the base of the Ahmed body could completely eliminate the symmetry-breaking leading to lateral bi-stability provided

that the cavity is long enough (around $0.3H$)[13]. The associated drag reduction is around 9 % but also includes the drag reduction related to the artificial increase in the length of the recirculation region by the cavity. Nevertheless, both control techniques are quite invasive in terms of geometrical modifications, and even unpractical to arrange on a real configuration for the control cylinder.

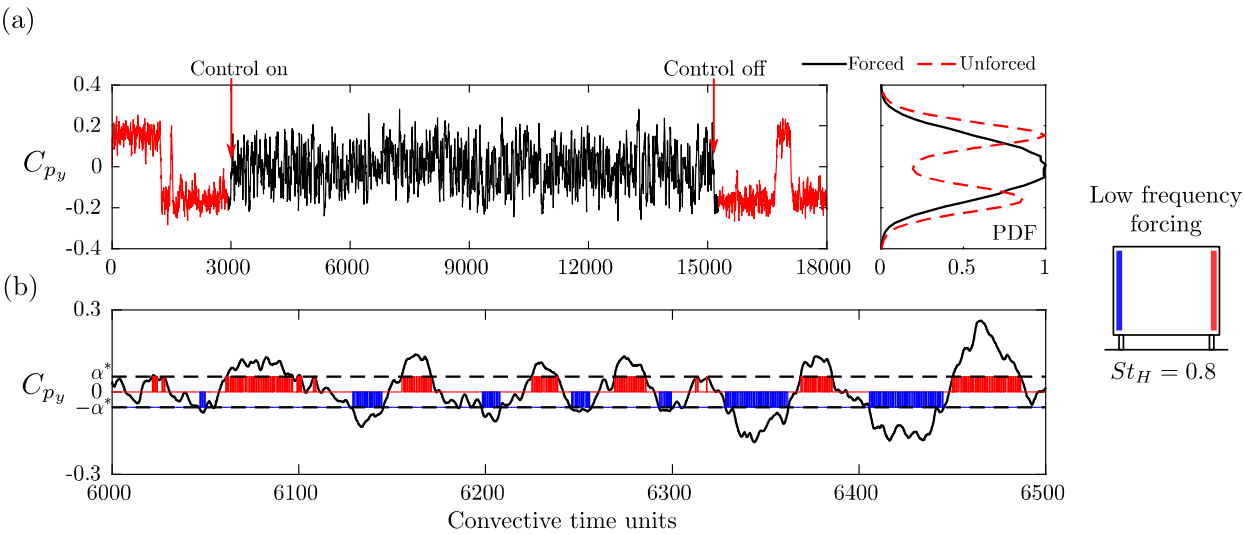

Figure 1.13: Closed-loop control of lateral bi-stability in the wake of an Ahmed body (adapted from Li *et al.* (2016). Forcing is provided by pulsed jets at low frequency ($St_H = 0.8$) from the lateral edges of the base. The forced edge is chosen based on the detection of the sign of the lateral pressure gradient at the base of the model C_{p_y} as shown in (b). This control strategy leads to a relative symmetrisation of the wake (see (a)), but the associated drag reduction is quite small (less than 2 %) because of the enhancement of the shear layer activity by the low frequency forcing.

1.4 Objectives and outline of the thesis

Based on this brief review on bluff body wakes and their control for drag reduction, a couple of main problematics are tackled in this work focused on the flow past square-back Ahmed body.

- An important aspect of the wake past three-dimensional blunt bodies is the presence large-scale asymmetries very sensitive to small changes in flow or geometry characteristics. A further investigation about these asymmetries and the wake reversals possibly occurring would allow for a deeper understanding of the related drag generation mechanisms and their physical origin. Additionally, this would also provide valuable insights on the strategies aiming at controlling these asymmetries. In general, a simplified description and modelling of the main drag sources in these wakes would be of great value as 3D wakes past blunt bodies are still far from being well understood.

- The efficient control of this wake flow for drag reduction remains a challenge, mostly because of the important geometrical constraints imposed for road vehicles applications and the complexity of the flow. Consequently, flow control techniques with minimal geometrical changes must be developed to tackle the problem of drag reduction. The use of pulsed jet forcing of the wake goes in this sense, but despite the significant contributions of Chaligné (2013), Oxlade *et al.* (2015) and Barros *et al.* (2016*b*) on these aspects, there is still a lack in a more advanced description of the flow mechanisms involved in drag reduction and the effect of forcing on the wake. In this sense, scaling laws of the drag generation mechanism itself and also of the flow control mechanisms would be valuable for application at the industrial scale or generalization to the ubiquitous problem of separated flows. In general, it would help improving the robustness of such flow control strategies.

[13] de la Cruz *et al.* (2017*b*) analogously showed a symmetrization and a 5 % base pressure recovery using similar ventilated cavities on the bullet-shaped body, just communicating with the wake through a perimetric slit.

- As far as road vehicles are concerned, variability in real flow conditions manifested by changes in velocity, cross-wind conditions, vehicle alignment due to its dynamics, etc. need to be taken into account. This aspect can be linked with the more fundamental problem of the high sensitivity of the asymmetries in the wake past 3D blunt bodies. In this sense, flow control strategies developed should have strong adaptivity and robustness properties. A set of different control strategies building on the different drag generating mechanisms in the wake of 3D blunt bodies would be valuable in order to answer this problematic. As an example, the recent work of Li *et al.* (2019) goes in this direction by developing control strategies adapted to changes in yaw angle of the Ahmed body.

To address these problematics, the present manuscript is organized as follows.

After the review provided in this introductory chapter, Chapter 2 gives a description of the experimental methods used to perform all the investigations gathered in the rest of the manuscript. The focus is put on describing the model setup in the wind-tunnel, the pulsed-jet system used for forcing of the Ahmed-body wake in particular detail and the main measurement and analysis techniques.

In Chapter 3, a brief description of the natural, unforced flow pas the square-back Ahmed body is given in terms of mean and dynamical features. This chapter will serve to introduce the main concepts used throughout the remainder of the manuscript.

The Chapter 4 is devoted to the investigation of the large-scale asymmetries present in the wake. Asymmetries of the natural flow are perturbed and modified using different means combining passive flow disturbances, changes in yaw angle and wake forcing. A detailed study of the wake reversals occurring in bi-stable configurations of the wake is attempted. The main focus of the chapter is to relate the asymmetries and reversals to drag changes and to provide a fine description of the mechanisms involved in drag generation by these particular features of the wake.

The effects on the wake of high-frequency forcing coupled to small flush-mounted curved surfaces are discussed in Chapter 5. We propose a fine description of a peculiar unsteady Coanda effect involved in the drag reduction observed. For this, an extensive set of experiments involving variations of the main parameters of the problem (forcing frequency and amplitude, size of the curved surfaces, Reynolds number) is used as a starting point to provide scaling laws of the peculiar unsteady Coanda effect. A flow model is also derived to describe the phenomenon and its effects on the wake and the drag.

Chapter 6 focuses on a further application of the high-frequency forcing coupled to curved surfaces in the presence of large-scale asymmetries. Localized forcing around the base is used in order to interact with different asymmetries fixed using passive flow disturbances. The different outcomes in terms of drag are presented and discussed to relate drag changes to the influence of forcing on the asymmetries. This particular forcing can be viewed as an active flap and we present the possible outlooks in terms of adaptivity and robustness. An extension is proposed to discuss more generally the implications between wake asymmetries and drag.

Finally, we summarize the main findings in Chapter 7 by providing a general synthesis of this work. We also provide the main outlooks stemming from this work by discussing the main questions raised by the study.

Chapter 2

Experimental methods

In this chapter, details about the experimental setup and the measurement techniques used in this study are given. A careful description of the main aspects involved in the different experiments is attempted before exploiting the results in the following chapters. First, aspects of the model setup and the forcing apparatus are detailed in order to provide a framework for the experiments performed. Then, the different measurements techniques used are presented and discussed, with an emphasis on their complementarity in the aim of accurately describing the bluff body wake flow.

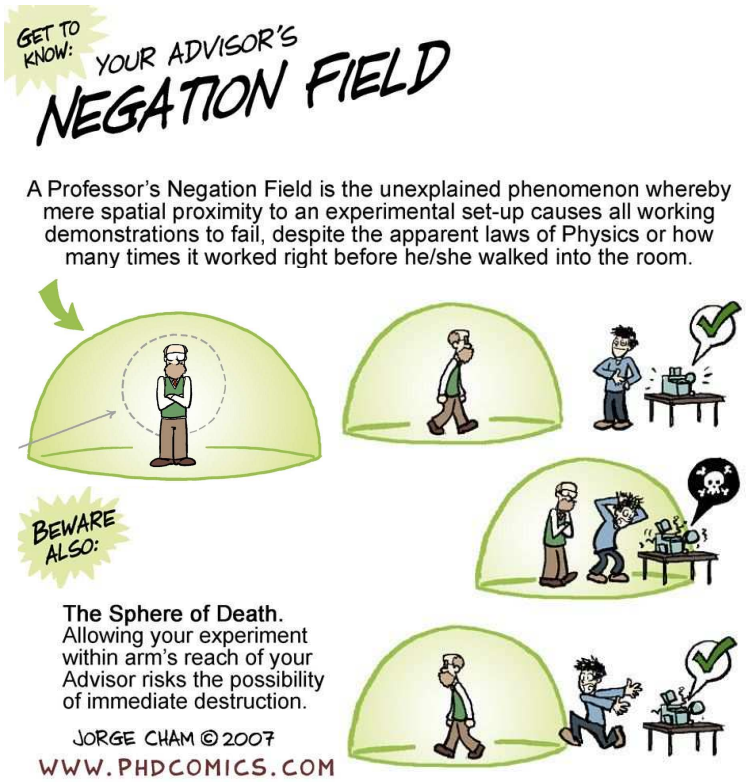

Contents

2.1 Model geometry

The three-dimensional blunt body studied in the present work is similar to the square-back Ahmed body discussed in the Introduction. It is a rectangular-sectioned geometry with a rounded front surface in order to prevent massive flow separation at the front of the model. This geometry simplifies the shape of a commercial blunt vehicle. Figure 2.1 pictures the model's geometry and its main characteristics.

The main geometric characteristics of the model are gathered in table 2.1. The height $H = 0.3$ m, the width $W = 0.36$ m and the length $L = 1$ m of the geometry are slightly different from the original square-back Ahmed body introduced in Ahmed *et al.* (1984). The differences are mainly threefold :

- The aspect ratio of the base $H/W = 0.83$ is slightly higher, more representative of current blunt vehicles' shape.
- The front surface of the model is rounded with a non-constant radius leading to a smoother curvature transition with the flat side surfaces. This is aimed at minimizing the flow detachment just after the rounded front surface and limit its impact on the downstream wake flow (Spohn & Gilliéron, 2002; Courtine, 2006). [1]
- NACA 0024 profiled supports are used under the model to limit the blockage in the underbody and flow perturbations.

The conception of the model is such that the front surface, the base and the four side surfaces are independently removable to facilitate the access to the interior of the body.

2.2 Experiments setup

2.2.1 Wind-tunnel facility

The experiments are performed inside the working section of a subsonic close-loop wind-tunnel (*Soufflerie S620*, ENSMA, Poitiers, France). Figure 2.2 depicts a global view of the facility showing the relative positions of the test section, the fan and the flow conditioning grids. A convergence

[1] This specific front geometry results from a numerical optimization of the basic Ahmed body. Lattice-Boltzmann method simulations have been performed with commercial software *Powerflow* by F. Oger and F. Harambat at PSA Group to ensure the complete flow attachment with this final front geometry at $Re_H = 6 \times 10^5$. Further experimental evidence of flow attachment over the investigated range of Re_H is given in Chapter 3.

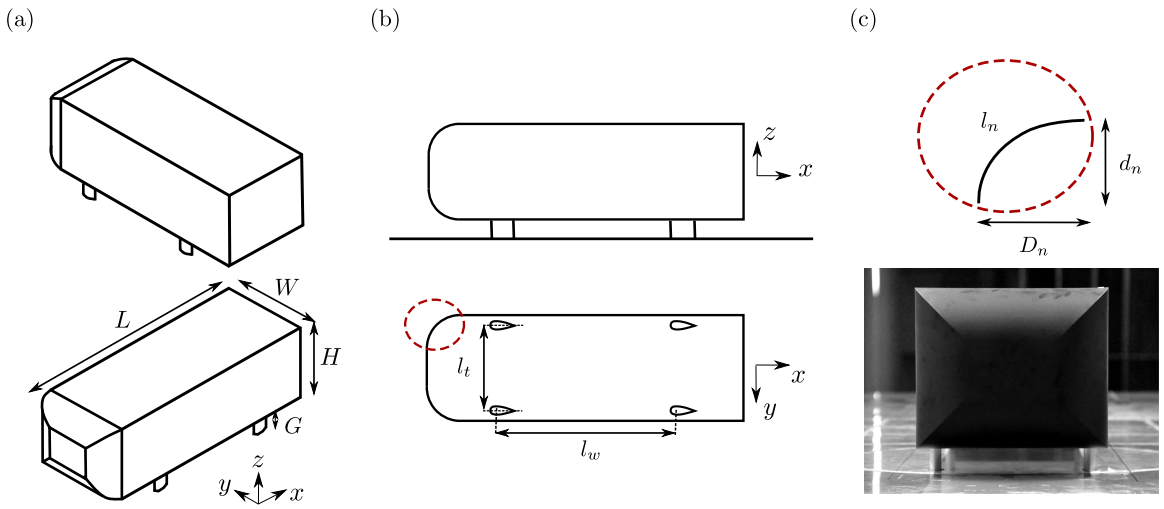

Figure 2.1: Description of the modified Ahmed body (Ahmed *et al.*, 1984) used in the present experiments. (a) Front and rear iso-views of the model with the main length scales of the geometry. (b) Lateral and bottom views with the detail of the supporting feet. (c) Detail of the modified nose geometry.

Parameter	Symbol	Value [m]
Height	H	0.3
Width	W	0.36
Length	L	1
Ground clearance	G	0.05
Track	l_t	0.535
Wheelbase	l_w	0.292
Nose x-radius	D_n	0.12
Nose y, z-radius	d_n	0.1
Nose arc length	l_n	0.176

Table 2.1: Main characteristics of the blunt body used in this study. All the geometric parameters are explicited in figure 2.1.

ratio of 7:1 links the grids and the entrance of the test section whose area is 6.2 m^2 (2.4 m wide $\times$ 2.6 m high). Maximum operating velocity in the test section allowed by the facility is 60 m s^{-1} and flow stability in the wind-tunnel is ensured for velocities greater than 5 m s^{-1}. The turbulence intensity of the flow entering the test section is of the order of 0.5 % at most operating conditions and a good flow homogeneity is achieved in the whole cross-section of the test section.

2.2.2 Model setup in the test section

The model is placed on a raised floor inside the test section in order to control the floor boundary layer characteristics upstream the model. This floor is a flat-plate with an elliptical leading edge spanning the whole width of the test section. The raised floor is ended by a flap with an adjustable incidence angle which aims at controlling the streamwise pressure gradient over the floor. The model is directly linked by its four profiled supports to the aerodynamic balance which is supported by a *Newport RV350-BPE* turntable integrated in the raised floor. This turntable allows for rotating displacements in yaw around the z-axis with precision of 0.001°. All pneumatic and electrical supplies pass through the four profiled supports of the model and extend to the bottom of the test section surrounded by fairings. An overview of the entire setup in the test section is provided in figure 2.3. The reference frame is defined as $(Oxyz)$ with an origin arbitrarily placed on the raised floor at the intersection between the vertical symmetry plane and the base section plane of the model, and axes respectively associated with streamwise, spanwise and wall-normal directions.

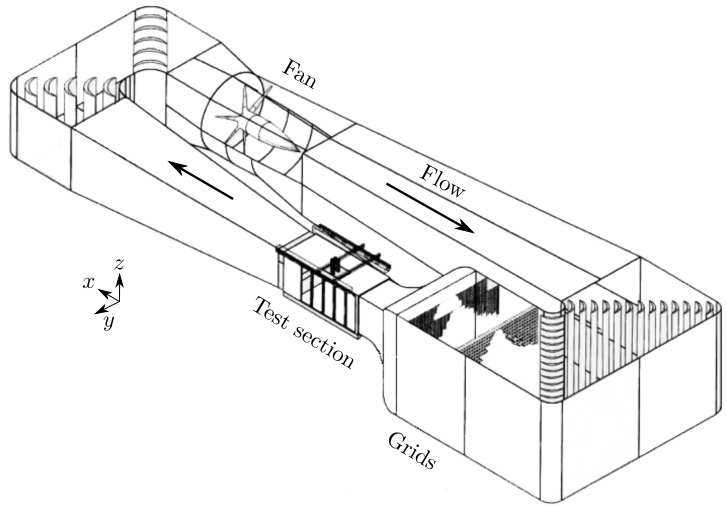

Figure 2.2: Global description of the wind-tunnel facility used in the experiments.

Configuration	δ_{99} [mm]	δ^* [mm]	θ [mm]	δ^*/θ	δ_{99}/G
Without model	9.2	1.69	1.07	1.57	0.18
With model	8.7	1.36	0.91	1.49	0.17

Table 2.2: Main characteristics of the boundary layer developing on the raised floor upstream of the model at $x/H = -4.5$ for $U_0 = 25$ m s^{-1}

During the mounting of the setup, attention was paid to the whole system composed of the raised floor and the model. This ensemble generates lift due the differences between the underflow-overflow mass fluxes, resulting in a possible deviation of the upstream flow and a streamwise pressure gradient establishing over the raised floor. These may affect the flow past the blunt body model. To overcome this coupling problem, the flap angle α is adjusted in order to balance the pressure distributions measured by 10 pressure taps along the upper and lower sides of the raised floor upstream of the model. This procedure, repeated at the beginning of each experimental campaign after mounting the model on the raised floor, enables an excellent repeatability between the experiments. The blockage ratio of the model's frontal surface with respect to the test section area above the raised floor is 2.3 %. Thanks to this low value, no blockage corrections are performed (Apelt, 1982).

The test section is equipped with a reference Pitot tube installed over the model allowing to monitor both the static pressure p_0 and the free-stream velocity U_0. This free-stream velocity is maintained in the test section with an incertitude of ± 0.1 m s^{-1}. Additionally, the temperature T_0 is monitored using another sensor located next to the reference Pitot tube. This enables the calculation of the density ρ with an uncertainty of ± 0.001 kg m^{-3}. In this study, the free-stream velocity is varied between 15 and 40 m s^{-1} which corresponds to Reynolds numbers $Re_H = \rho U_0 H/\mu$ varying between $(2.98 \pm 0.02) \times 10^5$ and $(7.96 \pm 0.01) \times 10^5$.

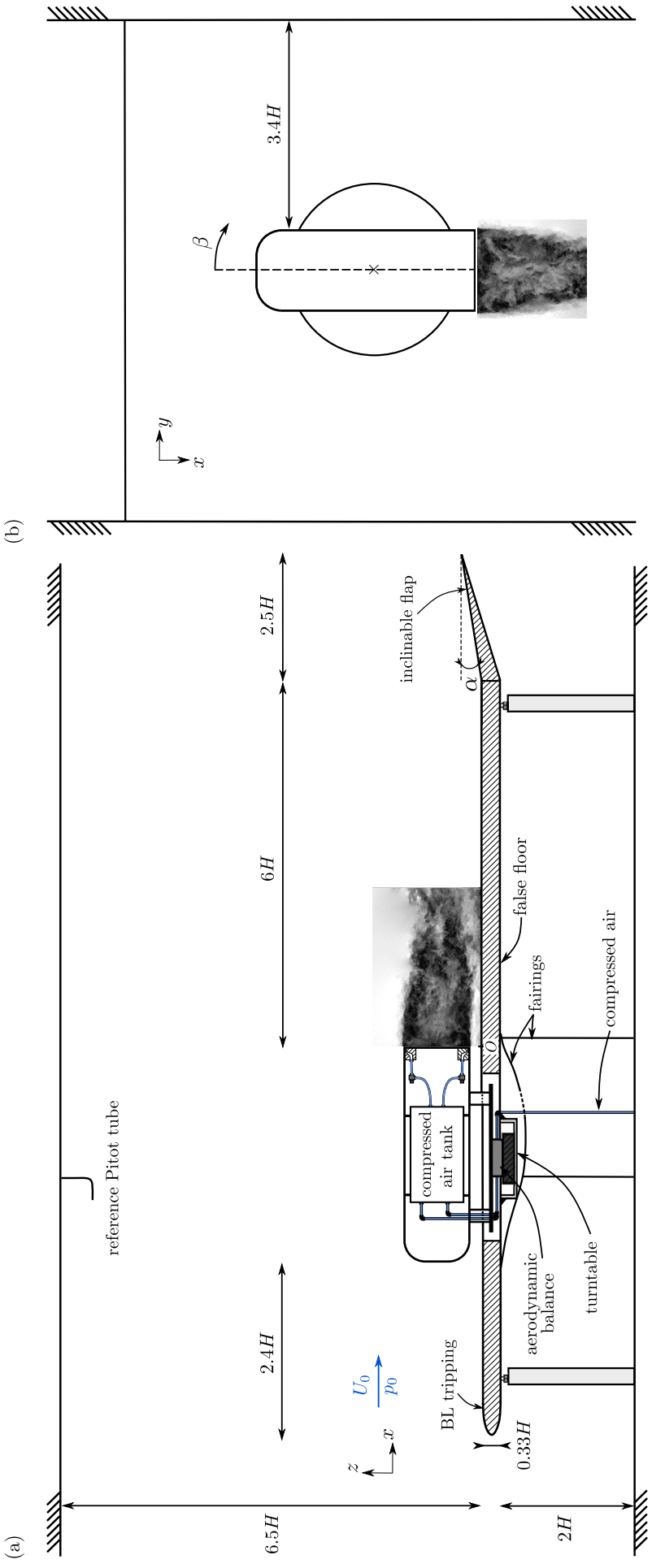

Figure 2.3: Global setup in the test section of the wind-tunnel. (a) Lateral view detailing the mounting of the model on the raised floor. (b) Top view of the model on the raised floor.

As the blunt body model is in ground proximity, the boundary layer developing on the raised floor upstream of the model has been characterized. A flattened Pitot probe was used to measure the time-averaged streamwise velocity in the boundary layer upstream the model's position in presence and absence of the model. Table 2.2 gathers the main characteristics of the boundary layer in terms of thickness (total thickness δ_{99}, displacement thickness δ^* and momentum thickness θ). The boundary layer is tripped with a 10-mm wide strip of 250 μm-grain-sized carborundum just after the elliptic leading edge in order to fix the transition point and get a developed turbulent boundary layer upstream of the model. According to the measured shape factor δ^*/θ between 1.5 and 1.6, the boundary layer with or without the presence of the model can be considered as turbulent. The total thickness of the boundary layer represents around $1/6^{\text{th}}$ of the basic ground clearance $G = 50$ mm used in the majority of the experiments. Thickness values are slightly lower for the boundary layer in presence of the model, which can be attributed to flow acceleration effects when approaching the front of the blunt body.

2.3 Pulsed-jet forcing system

The wake is forced using a system of pulsed jets emitted near the edges of the blunt body's base. In this section, we detail the system and finely characterize the forcing conditions used in the experiments.

2.3.1 System setup

The pulsed jets used for forcing are generated using an electro-pneumatic system comprising an ensemble of solenoid valves and diffusers. Pulsed jets are one of several alternatives used in the flow control community (Cattafesta & Sheplak (2011) provides an overview of the existing approaches) leading to the creation to a time-varying non-zero net mass and momentum flow.

A global picture of the forcing system is provided in figure 2.4. The system consists in a duct flow driven by a pressure difference between the upstream compressed air tank and the atmospheric pressure (or local wake pressure when a free-stream flow is present) at the exit of the diffusers. Solenoid valves located in-between allow for a time modulation of this pressure-driven flow. Compressed air of relative pressure p_i up to 5 bar is provided by a 12-L tank located inside the model (figure 2.4(a)) supplied by the global compressed air supply through three 12-mm diameter tubes passing through the supports of the model. The capacity of this tank has been chosen so that pressure variations are minimized when a mass flow is authorized by the solenoid valves. The pressure p_i inside the tank is regulated by a PID feedback controller and a flow regulator placed upstream with an instantaneous error of less than ± 0.02 bar. A series of 14 high-speed solenoid valves *SMC SX11F-AJ* are linked by flexible tubes (4 mm in diameter and 250 mm in length) to the tank. These solenoid valves are linked downstream to 26 slits of width 40 mm and thickness $h = 1$ mm positioned 0.5 mm below the edges of the model's base (7 slits along the top and bottom edges, 6 along the left and right edges). The separation between two consecutive slits is 4 mm. A sketch of one slit is provided in figure 2.4(b). Each solenoid valve feeds two slits through a succession of a Y-junction, flexible tubing of length 135 mm and diameter 5.5 mm and a carefully designed diffuser ending with the slit (figure 2.4(c)). Design of the diffuser has been chosen so that the flow is tangential to the free-stream at the exit and so that flow separation is prevented which minimizes the pressure loss across the duct. The total curvilinear equivalent length of the junction between the solenoid valve and the slit is $L_{\text{eq}} = 250$ mm. This value is of practical importance as it dictates the acoustic resonator behaviour of the system and influences the velocity of the pulsed jets at the exit. This is further discussed in §2.3.2. An in-house designed electronic system [2] allows for the control of the opening and closing of the solenoid valves at forcing frequencies f ranging from 0 (steady) to 1050 Hz (or equivalently for forcing time-scales T as low as 9.5×10^{-4} s). The command signal to the solenoid valves is composed of ON and OFF states leading to a 0-5 V square wave signal characterized by a duty-cycle d_c corresponding to the portion

[2] The whole electronic control system has been designed by the colleagues from Laboratoire Ampère at INSA Lyon.

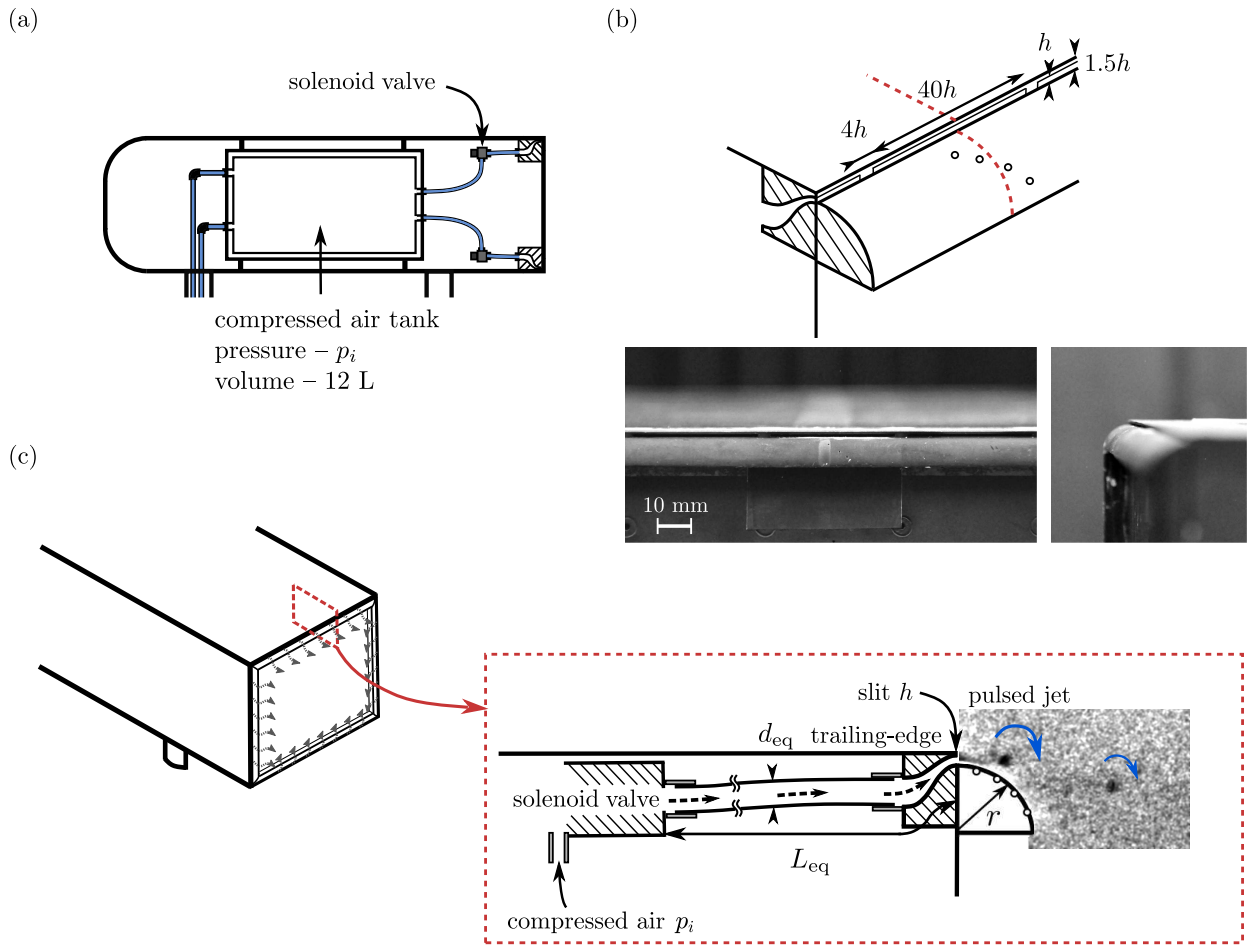

Figure 2.4: Pulsed jets system used for forcing. (a) Global arrangement of the system. (b) Detail arrangement of one solenoid valve, tubing system and curved surface generating the pulsed jets. The inserted picture from the small PIV FOV visualizes small scale vortical structures forming at the exit of the slit. (c) Detailed description of the slit geometry. The position of the additional pressure taps on the curved surface are also shown.

of time during which the solenoid valve remains open during a cycle. For the remainder and in all experiments presented, the duty-cycle d_c of the command signal to the solenoid valves is fixed at 50 %. The power command unit provides then the current intensity needed by the solenoid valves to open and close. This current signal basically consists in an overshoot in current at 1.5 A to open the solenoid valve followed by a constant current of 0.5 A to maintain it open. Because of the mechanical design of the solenoid valves, the pressure forces from the compressed air tank on the valves are helping the closing but preventing the opening movement. As a consequence, a frequency-dependent minimal input pressure p_i is needed to insure the good closing of the solenoid valves. Power consumption of the solenoid valves and their mechanical inertia limit their using at a maximal frequency of $f = 1050$ Hz for a given duty-cycle $d_c = 50\%$. Higher actuation frequencies would not guarantee the proper closing of the valve in the time of a cycle.

Additionally, curved surfaces are mounted flush to the slits as sketched on figure 2.4(b,c) in order to introduce a Coanda effect (Kadosch, 1958; Wille & Fernholz, 1965) as discussed in the Introduction. These curved surfaces span the whole edges at the base of the blunt body and are characterized by their curvature radius r. Radii of relatively small dimensions $r/H = \{5, 7, 9, 16\}$ are investigated in the frame of this study as they represent only a really small geometric change which would be accordance with industrial design requirements. These curved surfaces are carefully moulded using a rigid epoxy resin and are mounted flush to the slits using double-faced adhesive tape. Alignment with the slits is done visually and the error is estimated to be less than 0.1 mm.

2.3.2 Characterization of the forcing conditions in quiescent environment

In order to quantitatively characterize the forcing conditions provided by these solenoid valves, we describe in this section an ensemble of velocity measurements taken at the exit of a slit. Both the relative input pressure p_i and the frequency f are varied in order to depict the forcing conditions chosen for the experiments. A first step is to describe the forcing conditions at the exit of a slit in a quiescent environment, ie without a free-stream flow.

Measurements are performed using hot-wire anemometry (HWA) at the exit of a slit of the blunt body. A *Dantec Dynamics 55P11* single-wire probe (5 μm diameter and 1.25 mm long) is operated in constant temperature anemometry by a *StreamlinePro Anemometer System* at a sampling frequency of 50 kHz. Calibration of the probe was performed on a dedicated in-house automatic calibrator system for velocities covering the entire range of velocities found at the exit of the slit. Care was taken to repeat a calibration at the start and end of each experiment. The probe was visually placed on the y centerline of the exit section (within the $x = 0$ plane) of a slit with an estimated 0.1 mm error in x position, as sketched on figure 2.5. The z position of the probe was refined for each case by looking for the position at which the exit velocity of the pulsed jet V_j was maximal with a precision of 0.05 mm.

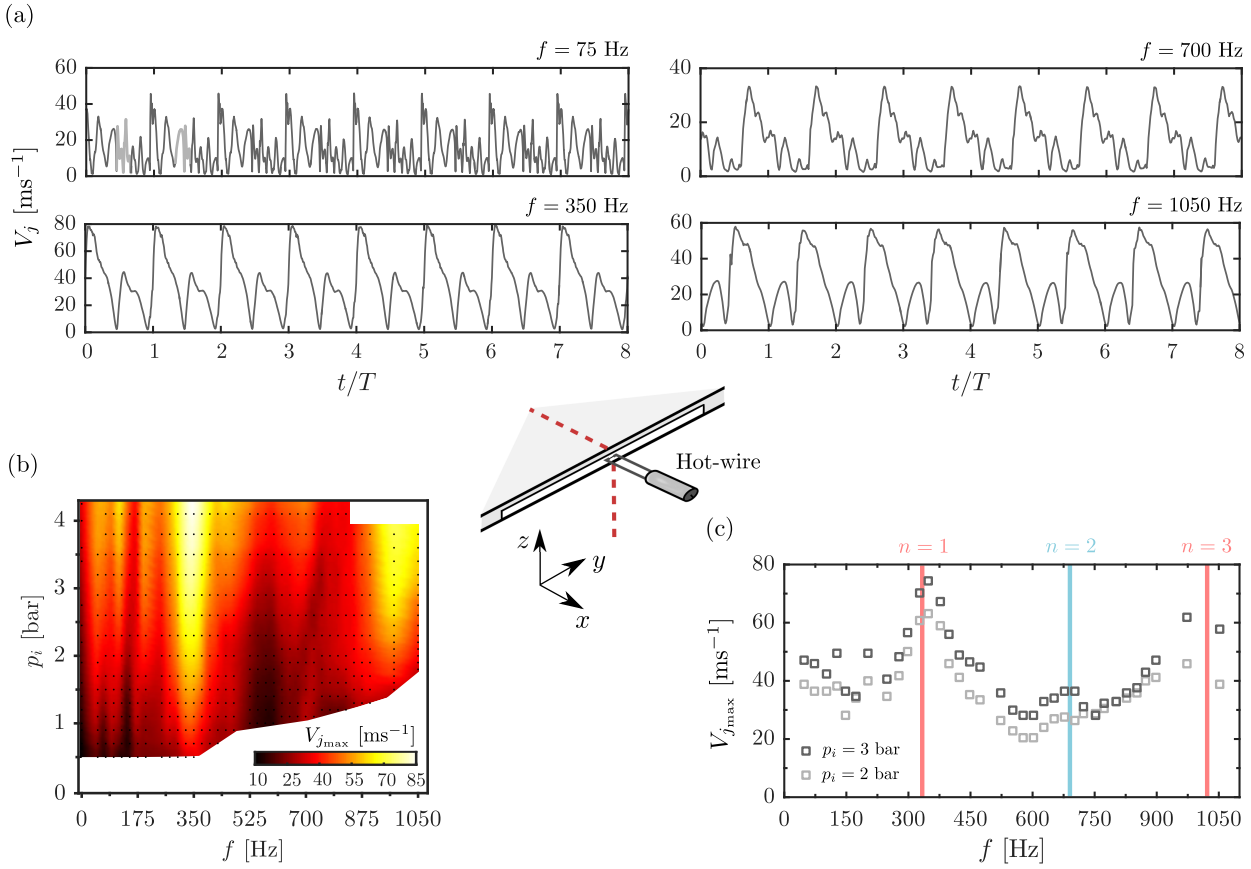

Figure 2.5: Hot-wire anemometry characterization of the pulsed jet velocity at the slit exit. (a) Time-series of the pulsed jet velocity V_j for different forcing frequencies $f = 75$, 350, 700 and 1050 Hz at $p_i = 2.5$ bar. (b) Evolution of the peak velocity $V_{j_{\max}}$ in the parameter space (f, p_i). Black dots indicate the measurement points. (c) Frequency response of the peak velocity of the pulsed-jet apparatus at two different input pressures $p_i = 2$ and 3 bar. Colored vertical lines indicate the three first harmonics of acoustic resonance in the closed-end/opened-end tube model from equation 2.2.

The time evolution of V_j for different forcing frequencies are presented in figure 2.5(a) at a given input pressure $p_i = 2.5$ bar. It is obvious that profiles are quite different depending on the forcing frequency. At $f = 350$ and 1050 Hz, V_j presents a very simple pattern comprising two marked peaks with an almost perfect triangular shape meaning that the forcing operates almost at constant acceleration and deceleration dV_j/dt during the rise and drop in velocity. On the

contrary, V_j profiles are more complex at other forcing frequencies not directly in the vicinity of the two previous frequencies. An example is provided with the profiles at $f = 75$ and 700 Hz showing a multitude of velocity peaks with a quite more complex pattern. The solenoid valves with the peculiar tubing arrangement are responsible for these qualitative differences in exit velocity profiles. Indeed, the acoustic behaviour of this duct flow has an important effect on the flow itself and the pulsed jet formation at the exit of the slit. To further argument this point, we investigate the evolution of the peak velocity $V_{j_{\max}}$ in the (f, p_i) parameter space in figure 2.5(b,c). The peak velocity is defined as the maximal velocity in the velocity profile phase-averaged over the forcing cycle :

$$V_{j_{\max}} = \max_t \langle V_j(t) \rangle_f \tag{2.1}$$

where $\langle \cdot \rangle_f$ denotes a phase-average relative to the forcing cycle. Figure 2.5(b,c) shows the frequency-resonant behaviour of the present forcing setup with two clear peaks in $V_{j_{\max}}$ around $f \sim 350$ and 1000 Hz at which the peak exit velocity is almost doubled compared to non-resonant frequencies. Following Michard *et al.* (2017), this behaviour can be retrieved by a simple acoustic model of the setup. As the solenoid valve is the seat of a chocked flow, the duct linking the solenoid valve to the exit slit can be seen as a simple duct closed on the solenoid valve side and opened on the slit side. For a simple closed-open cylindrical duct of length L and diameter d, acoustic resonance occurs at frequencies

$$f_n = \frac{nc}{4L} = nf_0, \quad n \in 2\mathbb{N} + 1, \tag{2.2}$$

where c is the sound celerity, while anti-resonance occurs at even multiples of the fundamental f_0 (Kinsler *et al.*, 1999). When evaluating the relation 2.2 with the equivalent curvilinear length between the solenoid valve and the slit $L_{\text{eq}} = 250$ mm and an equivalent diameter $d_{\text{eq}} = 5.5$ mm simply chosen as the tubing diameter, we obtain values of $f_1 \sim 340$ Hz, $f_2 \sim 680$ Hz and $f_3 \sim 1020$ Hz which are indicated in figure 2.5(c). The agreement between the predictions of the resonance and anti-resonance frequencies and the HWA measurements is quite satisfying. Not only this acoustic resonant behaviour accelerates the flow at the exit of the slit –which is quite important from an energetic point-of-view–, it also allows for simple triangular pattern for the V_j profile where acceleration and deceleration effects are straightforwardly interpretable in terms of flow physics. For these reasons, we choose in the experiments to focus on forcing frequencies f close to the first to resonant frequencies f_1 and f_3 of the forcing apparatus, hence the choice of two main forcing frequencies investigated in this work $f = 350$ and 1050Hz (which is the highest accessible frequency for our forcing apparatus). To insure the robustness of the results for the highest frequency forcing, we also chose a forcing frequency $f = 975$Hz close enough to the first odd harmonic f_3 but with sufficient margin compared to the limit of the forcing apparatus.

Planar particle image velocimetry (PIV) is used to further investigate the formation of pulsed jets at these particular forcing frequencies. Some results are presented in figure 2.6 for forcing at $f \sim f_1 \sim 350$ Hz and $p_i = 2.5$ bar. A phase-averaged description of the small-scale flow dynamics is performed with a sufficient spatial resolution ($\sim 0.12h$). The out-of-plane phase-averaged vorticity dynamics described in figure 2.6(a) shows the development of a symmetric 2D vortex pair due to the high aspect ratio of the slit geometry qualitatively very similar to the axisymmetric vortex rings described by Gharib *et al.* (1998). The late times of the formation of the vortex ring ($t/T \sim 0.13$) are the seat of an instability of the trailing jet resulting in the apparition of secondary vortex heads. This is reminiscent of the vortex rings at large stroke numbers $L_0 = \int_0^T V_j(t)dt$ investigated by Gharib *et al.* (1998), Smith & Glezer (1998) or Glezer & Amitay (2002). Interestingly, around $t/T \sim 0.6$ the vorticity released at each side of the slit changes sign compared to the first half of the forcing cycle. This is characteristic of an aspiration phase with reversed velocities and flow ingested back in the slits. This observation is confirmed by the streamwise velocity field u_x in figure 2.6(b,c) where quite important reversed flow is observed in the vicinity of the slit exit. As HWA is not sensitive to the streamwise direction of the flow, the PIV can be used to correct the sign of the HWA measurements. The secondary velocity peak observed in HWA measurements in figure 2.5(a) is actually an aspiration phase of negative velocity V_j and when the sign of V_j is reversed in this phase HWA and PIV measurements agree quite well. Similar observations are made around the second resonance frequency $f_3 \sim 1$ kHz, and the HWA are thus accordingly corrected for the aspiration phase.

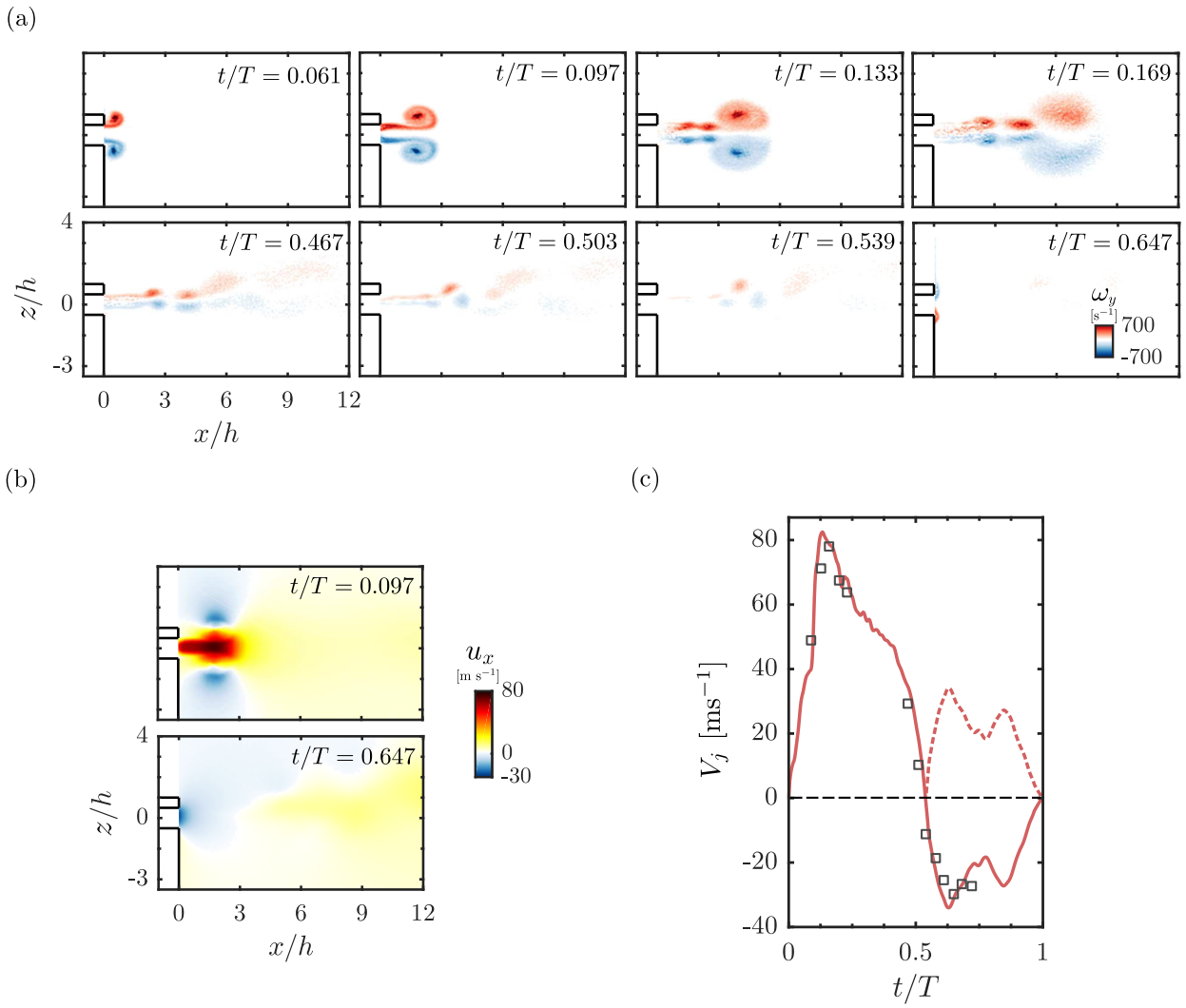

Figure 2.6: Characteristics of the formation of the pulsed jets in a quiescent environment at $f = 350$ Hz and $p_i = 2.5$ bar. Phase-averaged evolution of (a) the spanwise vorticity field ω_y at reduced times $t/T = \{0.061, 0.097, 0.133, 0.169, 0.467, 0.503, 0.539, 0.647\}$ and (b) the streamwise velocity field u_x at $t/T = \{0.097, 0.647\}$. (c) Time evolution of u_x at the exit of the slit measured by PIV (black squares) and V_j measured by HWA (red line) over a forcing period. Original HWA data where the velocity direction is misinterpreted is shown by a dashed line and the corrected profile after sign inversion by a continuous line.

Using this correction method, a fine characterization of the forcing conditions can be done as presented in figure 2.7. The phase-averaged velocity profiles V_j in figure 2.7(a) show very similar triangular patterns with almost constant acceleration and deceleration phases amongst the three frequencies of interest $f = 350, 975$ and 1050 Hz. For the first two frequencies the acceleration phase until the maximal velocity is reached ($t/T < 0.2$) is rather independent from the input pressure p_i, only an important $V_{j_{\max}}$ dependence on p_i exists. Only for $f = 1050$ Hz (and more mildly for $f = 975$ Hz) this observation does not hold anymore at the lowest input pressures where the acceleration phase is slightly extended and the theoretical duty-cycle of 50% not respected anymore. This is explained by the low p_i not favouring the closing of the solenoid valve and leading to increased effective duty-cycle. These very low p_i barely sufficient for the proper functioning of the solenoid valves are not further presented in the rest of the manuscript.

Finally, an important aspect of the forcing conditions is their homogeneity along the edges of the base of the blunt body. Indeed, as discussed in the Introduction, large-scale asymmetries are a peculiar feature of this type of blunt body flow, and as a consequence a satisfactory forcing homogeneity has to be insured in order to clearly interact with these asymmetries. Homogeneity is checked by HWA measurements at the center of each of the 26 exit slits. An example of the

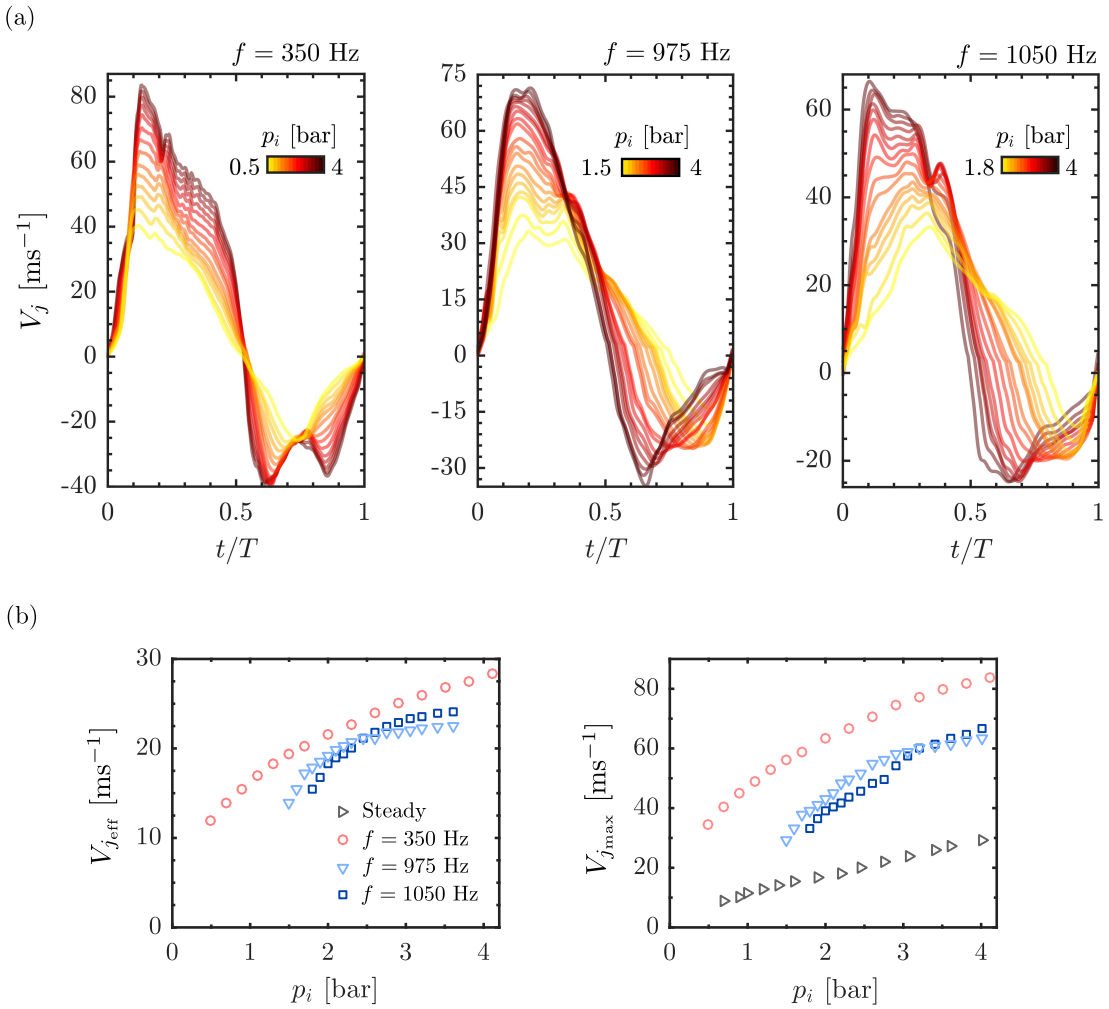

Figure 2.7: Detailed exit velocity characteristics at the forcing frequencies of interest in the frame of this study f = Steady, 350, 975 and 1050 Hz. (a) Corrected phase-averaged pulsed jet velocity profiles with different input pressures p_i at f = 350, 975 and 1050 Hz. (b) Evolution of effective $V_{j_{\text{eff}}} = \sqrt{\overline{V_j^2}}$ and peak $V_{j_{\max}}$ velocities with p_i. For the steady forcing case, the time-averaged jet velocity is shown.

similarity of the velocity profiles at f = 1050 Hz is shown in figure 2.8(a). A satisfactory similarity is achieved, albeit the slightly higher discrepancies between slits during the very opening phase ($t/T < 0.1$) and the aspiration phase ($t/T \sim 0.8$) of the solenoid valves. The deviation of the peak velocity $V_{j_{\max}}$ from the slits-averaged $\langle V_{j_{\max}} \rangle$ one is given in figure 2.8(b). This deviation is for all the slits less than $\pm 5\%$ for all the forcing conditions of interest. Steady forcing shows even better homogeneity, suggesting that the inhomogeneities mainly come from functioning discrepancies between the solenoid valves.

2.3.3 Interaction of the forcing with a free-stream flow

As the forcing interacts with a free-stream and a wake flow in our experiments, a forcing amplitude coefficient to characterize the injected momentum can be defined by

$$C_\mu = d_c \frac{S_j V_{j_{\max}}^2}{S U_0^2} \tag{2.3}$$

where S_j is the total section of the slits, $V_{j_{\max}}$ the peak velocity of the pulsed jets and $S = HW$ the section of the model. d_c is here the effective duty-cycle of the forcing based on the HWA measurements. This amplitude coefficient definition based on the peak velocity is chosen in order to more fairly compare unsteady and steady forcing and because, as we will see in Chapter 5,

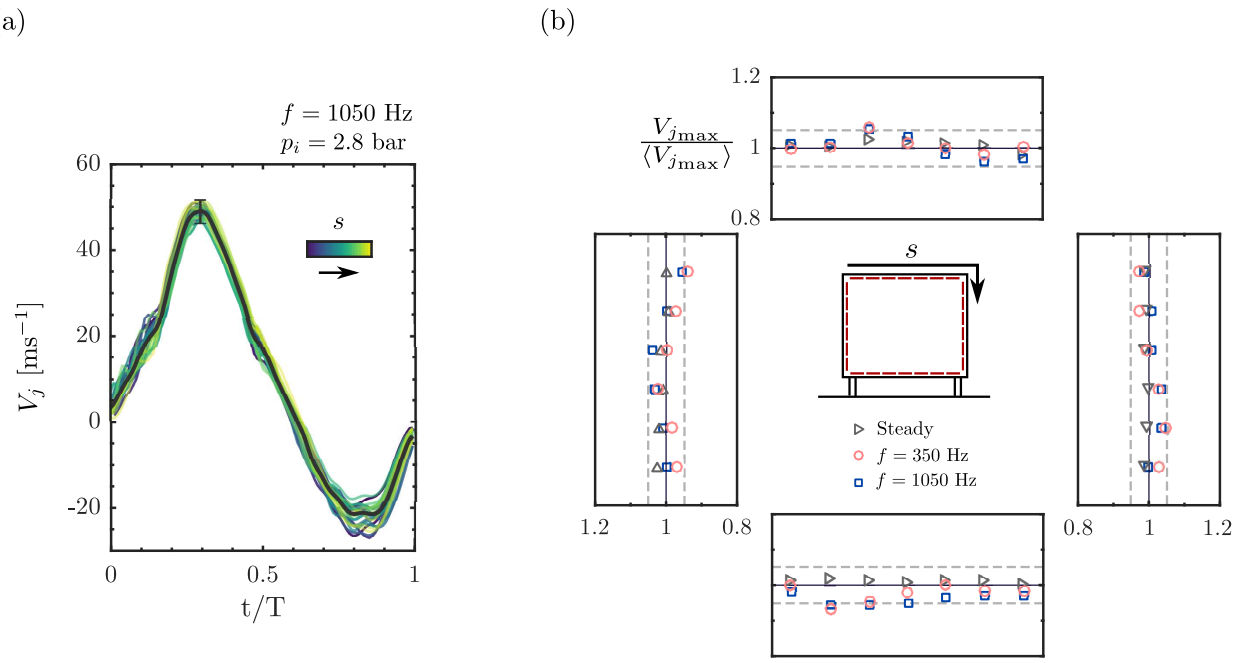

Figure 2.8: Spatial homogeneity of the forcing. (a) Corrected phase-averaged velocity profiles at each slit center for forcing at $f = 1050$ Hz and $p_i = 2.8$ bar. The coordinate s denotes the position of the slit from the top left slit in clockwise direction (as indicated on (b)). The black line is the phase-averaged velocity profile averaged between all the slits and the error bar indicates $\pm 5\%$ of the peak velocity. (b) Homogeneity of the peak velocity $V_{j_{\max}}$ at all slits for different forcing frequencies f = steady, 350 and 1050 Hz at $p_i = 2.8$ bar. Peak velocities are shown relative to the average peak velocity between all slits $\langle V_{j_{\max}}\rangle$. Gray dashed lines indicate $\pm 5\%$ deviation from this average peak velocity.

the peak velocity has a key role in the interaction mechanisms between the pulsed jets and the wake flow. Similar definition was chosen in the study of Oxlade *et al.* (2015) for instance. Others definitions exist, mainly based on the root-mean square velocity of the forcing $V_{j_{\text{eff}}} = \sqrt{\overline{V_j^2}}$ which accounts for all the momentum injected in the flow by the pulsed jets and used in the study of Barros *et al.* (2016*b*) for instance. Nevertheless, as shown in figure 2.7(b,c), the mapping between p_i and $V_{j_{\text{eff}}}$ or$V_{j_{\max}}$ is qualitatively very similar.

We will show in the following chapters that two characteristic time scales have to be defined in order to analyse the interaction of the pulsed jets with the curved surfaces and the consequences on the evolution of the global drag force. On one hand, the sudden rise of the jet velocity imposes a time scale on the flow at separation. This time scale t_a is defined as

$$t_a = \frac{V_j(t')}{\left[\frac{dV_j}{dt}\right](t')} \tag{2.4}$$

where $t' = \underset{t}{\text{argmax}}(dV_j/dt)$ is the time of maximal jet acceleration. The typical values of t_a and $t_a f$ for the three forcing frequencies investigated are gathered in table 2.3. These values are rather constant over the range of p_i studied except at low p_i for $f = 975$ Hz and especially for $f = 1050$ Hz due to the solenoid valve closing dynamics evoked previously. For the remainder, forcing is only performed at p_i sufficient to guarantee a good opening of the valves at high frequencies[3] We will show in chapter 5 that the rate of variation of V_j characterized by t_a has indeed a great influence on the coherent structures generated during the forcing. t_a will be called jet acceleration time scale or simply acceleration time scale in what follows. As a side remark, one can notice that $t_a/2$ is the time scale of injection of vorticity by the jet in the flow because the instantaneous flux of vorticity is equal to $V_j^2/2$. As the acceleration phase is rather linear, another estimation of this

[3]This means $p_i \geqslant 2$ bar for $f = 1050$ Hz and $p_i \geqslant 1.8$ bar for $f = 975$ Hz.

Frequency [Hz]	t_a [s^{-1}]	$t_a f$ [–]
350	1.43×10^{-4}	0.05
975	5.84×10^{-5}	0.057
1050	5.05×10^{-4}	0.053

Table 2.3: Characteristic dimensional t_a and non-dimensional $t_a f$ acceleration time of the pulsed jet velocity used for forcing. This time-scale represents a fair estimation of the acceleration imposed by the pulsed jets. An average estimation of t_a is provided over the whole range of inlet pressure p_i investigated as its dependence on p_i is weak (t_a is not evolving by more than 10% over the range of p_i investigated).

acceleration time scale is obtained from the time at which the blowing velocity is maximal, called thereafter peaking time. From a physical viewpoint, this time-scale may also be interpreted as

$$t_p = \frac{V_{j_{\max}}}{\langle \frac{dV_j}{dt} \rangle_{[0;t_p]}} \tag{2.5}$$

where $\langle \cdot \rangle_{[0;t_p]}$ denotes a time-average over the time horizon $[0; t_p]$. In practice, t_p is evaluated as the time of maximum blowing velocity over one actuation cycle and is used to model the coherent structures dynamics. In Chapter 5 this time-scale is also used by convenience to model the coherent structures dynamics. Similarly to $t_a f$, $t_p f$ has a rather constant value when varying p_i and for the three different forcing frequencies, which is around 0.13.

A second time scale is of course the period $T = 1/f$ of the signal. We will show that T has to be compared to characteristic convective time scales in order to quantify the influence of the periodicity of the generation of these structures on the flow over the curved surfaces.

As the forcing is interacting with the free-stream flow (the turbulent boundary layer separating from the model) in our experiments, pulsed jets dynamics are also influenced. Numerous studies focused on the interaction of pulsed jets formation and dynamics in presence of a co-flow (Krueger *et al.*, 2003, 2006) or a cross-flow (Sau & Mahesh, 2008; Manesh, 2013; Buren *et al.*, 2016).

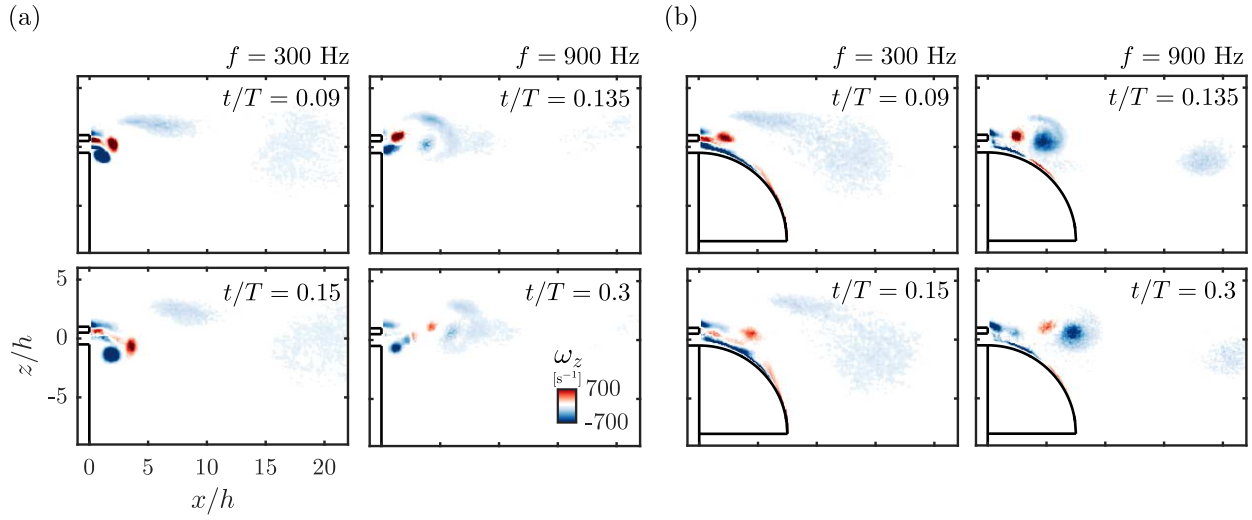

Figure 2.9: Characteristics of the formation of the pulsed jets in presence of a co-flow at $U_0 = 25$ m s^{-1} for $f = 300$ Hz $p_i = 1.8$ bar and $f = 900$ Hz at $p_i = 2.5$ bar, with (a) and without (b) the presence of a flush-mounted curved surface of radius $r/h = 7$. Phase-averaged evolution the spanwise vorticity field ω_y.

Experiments have been performed in which the same pulsed jets are generated in presence of a turbulent boundary layer separating at the salient edge over the slit. The free-stream flow was set at $U_0 = 25$ m s^{-1} and figure 2.9 presents the vorticity dynamics for two cases forced at frequencies near f_1 and f_3 with $V_{j_{\max}}/U_0 \sim 1.6$. A pair of counter-rotating vortical structures is still formed as in the quiescent environment case, but the pair is tilted downstream because of the presence of the free-stream flow above the slit. Qualitatively, the dynamics are quite similar between both frequencies.

When adding a curved surface flush to the slit, the complexity of the pulsed jet dynamics is further increased. Even though a pair of counter-rotating vortical structures is still observed it no longer has the same physical origin as in absence of a curved surface [4]. With a curved surface of radius $r/h = 7$, the vortical structures appear in an inverted fashion. Moreover, only at the higher frequency the negative vortical structure keeps a strong coherence whereas at the lower frequency the vorticity is way more diffused. These peculiar dynamics will be of capital importance in analyzing the effect of the pulsed jet and curved surfaces on the separating boundary layer and on the drag variation of the blunt body flow in Chapter 5.

2.4 Measurement techniques

The main measurements techniques used to characterize the flow in this study are presented in detail in this section. In particular, focus is put on their complementarity for an extensive study of the blunt body flow.

2.4.1 Pressure measurements

To perform surface pressure measurements on the model, two different systems have been used. First, a 64-channel *Pressure Systems ESP-DTC-64HD* pressure scanner with a ±1 kPa range is used to perform static pressure measurements sampled at 200 Hz. The pressure scanner is linked to 1-mm diameter pressure tappings around the model (35 taps on the base, the rest around the model as indicated in figure 2.10(a)) by 80-cm long vinyl tubes. This tubbing leads to a cut-off frequency around 50 Hz for the measurements meaning that the pressure scanner is only used for time-averaged measurements.

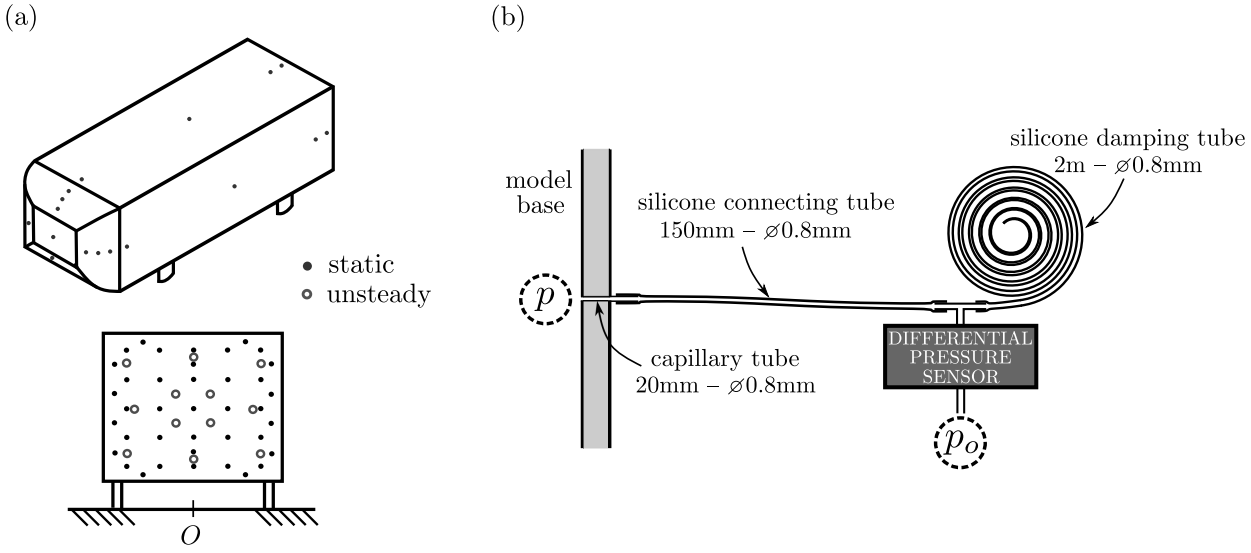

Figure 2.10: Pressure measurement apparatus. (a) Position of the pressure taps around the model (left) and on the base (right). Pressure taps linked to the pressure scanner are shown by the black dots and those linked to the differential pressure sensors for time-resolved measurements by gray circles. (b) Detail of the connection between the pressure taps and the differential pressure sensors.

In addition, 12 differential pressure sensors *SensorTechnics HCLA 02X5DB* (range ±250 Pa) and 4 *SensorTechnics HCLA 12X5DB* (range ±1250 Pa) are linked respectively to pressure taps on the base (2.10(a)) and on the top curved surface (2.4(b)). If pressure taps on the base are of similar diameter to those linked to the pressure scanner, the ones on the curved surface are reduced to a diameter of 0.7 mm in order to reduce the influence on the curvature of the surface. A specific tubbing system described in figure 2.10(b) is employed for these sensors with a reduced total length of 25 cm between the tap and the sensor, and an additional bifurcation towards a

[4] The physical origin of these two coherent structures is assessed and modelled in Chapter 5.

2-m long continuation tube before each sensor. These continuation tubes are successfully used to damp the pressure oscillations inside the tubing system as they have been used in a couple of other works (Ruiz *et al.* (2009), Beaudet (2014), Barros (2015), Li *et al.* (2017)). In order to perform time-resolved measurements, a frequency response calibration of each tap-sensor couple has been performed on a dedicated bench against a reference *B&K 1/4-inch* microphone. The results of the frequency response function (FRF) and the impulse response are shown in figure 2.11. As the sensitivity of the reference microphone is not fully satisfying in the low frequency region (typically below ~ 20 Hz), the FRF is corrected in this region with a constant sensitivity and a linear phase down to the known values of mean sensitivity of the sensors. Such a setup for the sensors has a first-order low-pass filter behaviour. According to figure 2.11(c), the time-delay of the sensors and their mounting is of order 1.5 ms. With the obtained frequency and impulse response functions, the measurements of each sensor are a posteriori corrected either in the frequency or time domain to obtain measurements with 2 kHz bandwidth. The latter is sufficient to resolve all the time-scales of interest related both to the unforced and forced wakes.

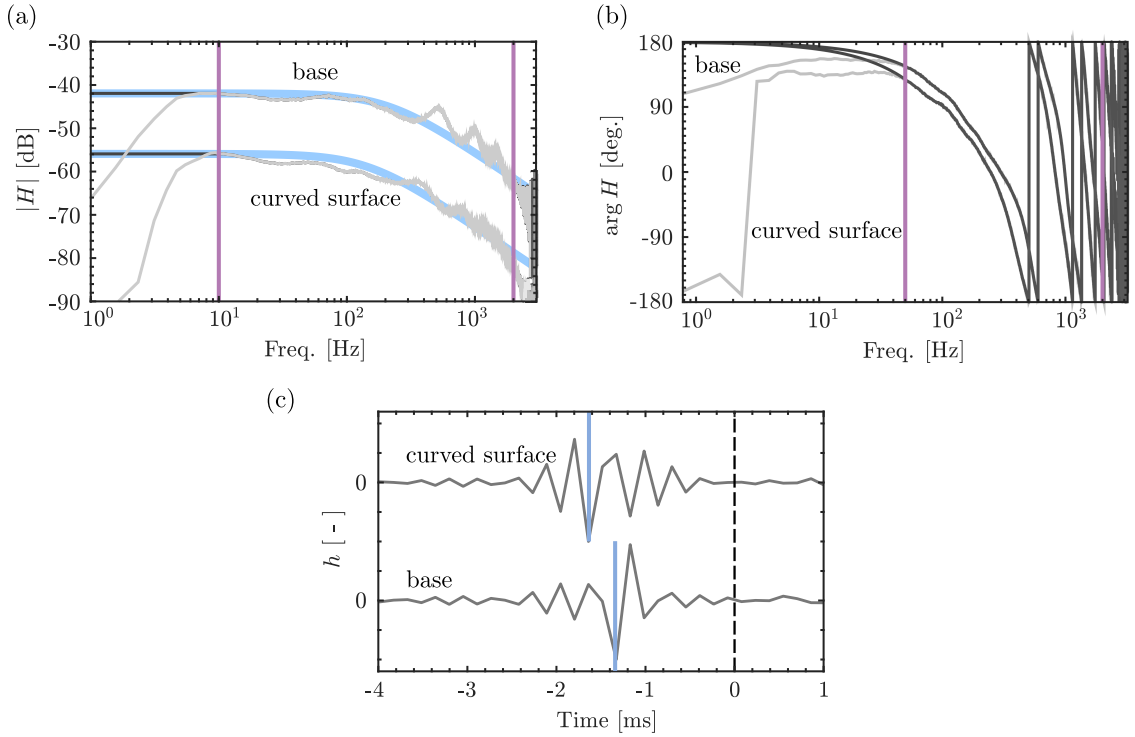

Figure 2.11: Calibration of the differential pressure sensors for time-resolved measurements. (a) Modulus $|H|$ and (b) phase $\arg H$ of the frequency response function (FRF) of the differential pressure sensors for both the taps located on the base and on the curved surfaces. Light gray lines are the raw FRF and dark gray lines the FRF corrected in the low frequency region where the reference microphone has a loss of sensitivity. Thick blue lines are a first-order low pass filter fit. Pink vertical lines denote the lowest frequency where the reference microphone has a reliable response and the highest frequency resolved by the differential pressure sensors. (c) Impulse response function h of the differential pressure sensors. Vertical blue lines represent the time delay due to the whole apparatus.

Measurement incertitude lies respectively below ± 1.5 Pa and ± 0.7 Pa (3.2 Pa for the measurements on the curved surfaces) for the two systems, which represents less than $\pm 2\%$ and $\pm 1\%$ of the averaged mean pressure at the base. Pressure measurements are expressed in terms of the pressure coefficient C_p defined as

$$C_p = \frac{p - p_0}{0.5\rho U_0^2} \tag{2.6}$$

The reference pressure p_0 is taken at the location $x/H = -2$ over the model thanks to a Pitot tube at the ceiling of the test section. For each configuration studied in this work, pressure measurements are performed over a time window of at least $t = 120$s (10^4 convective time units H/U_0

	ESP-DTC Pressure scanner	HCLA differential pressure sensors
Range /Pa	±1000	±250 (base) or ±1250 (curved surface)
Accuracy /Pa	±1.5	±0.7 or ±3.2
$/\%\overline{C_{pb}}$	±2	±1 or ±4.3
Correction	No	Yes, a posteriori
Bandwidth /Hz	∼ 50	2000
Acquisition frequency /Hz	200	1000 (long acquisitions) or 4000 (short acquisitions)
Acquisition length /s	600 to 900 (unforced) or 120 to 240 (forced)	360 to 480 (unforced) or 120 (forced)
$/(H/U_0)$	5 to 7.5×10^4 or 1 to 2×10^4	3 to 4×10^4 or 1×10^4
Maximal measurements repetitions	2 or 6	2 or 6

Table 2.4: Summary of the main pressure measurements characteristics. A reference $U_0 = 25$ m s^{-1} is taken for the different estimations.

at $U_0 = 25\text{ms}^{-1}$). As the unforced flow behind our model presents a lateral bi-modal behaviour on long time scales of order $O(10^3 H/U_0)$ (Grandemange *et al.*, 2013*b*) which persists when global forcing all around the base of the model is applied, this time window is not sufficient to obtain complete statistical convergence. Nevertheless, due to the important number of configurations studied involving all the parameter sweeps in this work presented in Chapter 5, this time window was considered as satisfactory to keep a reasonable experiment duration. Indeed, care was taken for the repeatability of the results by reproducing a couple of parameter sweeps, and for all the configurations investigated with PIV the measurements were repeated during the PIV acquisitions for a duration of $t = 240s$ for 1 to 5 times for the cases where phase-locked measurements were taken. For the configurations involving phase-locked PIV, it leads to a total acquisition time of $t = 1320$s (110000 convective time units at $U_0 = 25\text{ms}^{-1}$) which is sufficient to achieve satisfactory statistical convergence. All these characteristics are summed up in table 2.4.

2.4.2 Aerodynamic balance

To quantify the aerodynamic efforts on the blunt body model, a 6-component aerodynamic balance (*Kistler 9129AA* piezoelectric sensors and *Kistler 5080A* charge amplifier) is used. As sketched on figure 2.3(a), the link between the model and the balance is insured by a 20-mm thick steel plate on which the model's support are fixed. Attention was paid to the stiffness of the ensemble and its dynamic behaviour so that aerodynamic measurements are not perturbed by any mechanical and structural deformations. A rigid 50-mm thick steel base insures the stability on one side of the balance sensors to that deformations only related to aerodynamic efforts on the model are taken into account.

The balance has been in-house calibrated using known masses and a system of pulley applying pure forces, pure moments or a combination of both on the balance. A whole volume including the expected application point of the aerodynamics forces of the model has been covered for calibration by using various level arms length for moments. Total measurement incertitude is less than 0.6 % of the full scale range which is adapted to each configuration studied depending on the expected aerodynamic forces. This represents less than 1% incertitude on the mean drag force F_x for instance. Aerodynamic forces measurements are expressed as non-dimensional aerodynamic coefficients

$$C_i = \frac{F_i}{0.5\rho S U_0^2}, \quad i \in \{x, y, z\}. \tag{2.7}$$

Measurements are performed at an acquisition rate of 200 Hz. As no corrections are implemented to isolate aerodynamic forces from inertia forces, only the time-averaged forces are investigated from these measurements. In consequence, a 10-Hz low-pass filter is applied to the balance signals by the acquisition system in order to limit high-frequency noise.

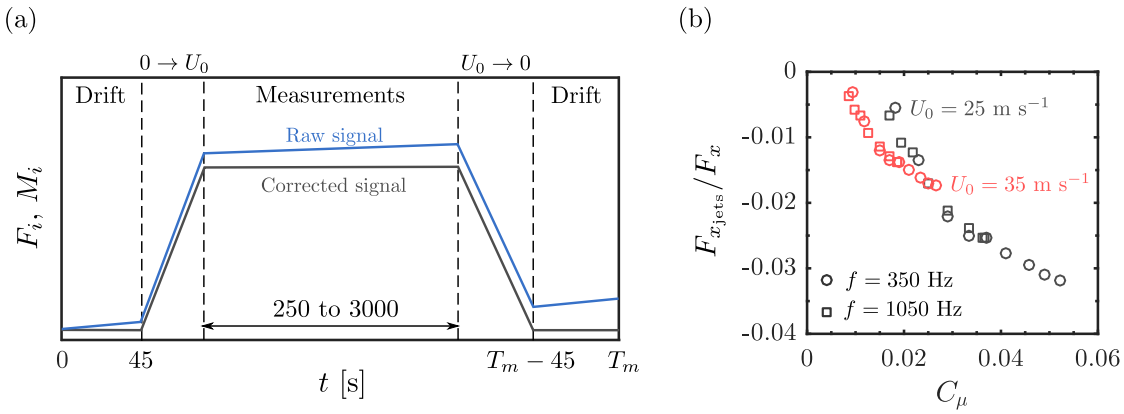

Figure 2.12: Characteristics of the aerodynamic balance measurements. (a) Procedure used for performing experiments and correcting for the drift of the balance's sensors. (b) Typical ratio between the thrust produced by the pulsed jets and the total drag force measured when forcing in quiescent wind-tunnel conditions. The total drag force measured comes from unforced measurements at the corresponding free-stream velocity.

In order to compensate for the drift of the piezoelectric sensors composing the aerodynamic balance, all the measurements are performed following a similar procedure described in figure 2.12(a) where the first and last 45 s of each run is dedicated to the sole balance measurements in quiescent wind-tunnel conditions allowing to estimate the linear drift of the sensors. As this drift rate does not exceed 2 N h^{-1} ($\sim 20\%$ of typical full scale range at $U_0 = 25$ m s^{-1}), several different configurations are gathered in the same run for the forcing experiments in order to perform runs of maximal length ~ 45 minutes.

The pulsed jets system used for forcing induces a small thrust which is included in the drag force measurement F_x. In order to evaluate the contribution of the pulsed jets thrust to the measured drag, each forcing is also tested at quiescent free-stream conditions. Results are gathered in figure 2.12(b) for the case of forcing on all the edges of the base. It is found for example at $U_0 = 25\text{ms}^{-1}$ the thrust contribution $F_{x_{\text{jets}}}$ to the measured drag F_x is less than 3 % at $U_0 = 25$ m s^{-1} and less than 1.8 % at $U_0 = 35$ m s^{-1}.

Measurements were performed with a protocol similar to the pressure measurements as they were done at the same time, leading to similar conclusions concerning their statistical convergence discussed in the previous paragraph.

2.4.3 Particle image velocimetry

Particle image velocimetry (PIV) is performed in the near-wake of the model to gain insight in the flow structure. Three different PIV setups are used to scrutinize in detail different and complementary aspects of the wake. The fields of view (FOV) investigated and an example of instantaneous velocity field realization are shown in figure 2.13, and the main characteristics of each setup are provided in table 2.5.

A large FOV covering the whole recirculation region in the wake in the vertical plane of symmetry of the model (plane $y = 0$) is imaged by a *LaVision Imager LX* 16 *Mpx* equipped with a *Zeiss Makro-Planar ZF 50 mm* objective. The laser light sheet of 1 mm thickness is provided by a *Quantel EverGreen* 2 × 200 *mJ* laser. The flow is seeded from downstream the raised floor by atomization of mineral oil producing 1-μm diameter particles, which is common to all PIV setups discussed in this work. A total of 1000 to 2500 image pairs are acquired at a rate of 4 Hz for each configuration studied, which is satisfactory for convergence of first and second order statistics. Image pairs are processed with Davis 8.4 with a final interrogation window of 16 × 16 pixels and overlap of 50 % leading to a velocity vector each 1.1 mm. Further detail about the spatial resolution are provided in table 2.5. The results from this setup are used throughout the whole manuscript.

A second smaller FOV is localized in the same plane but covering only the beginning of the top shear layer until $x/H \sim 0.3$. The setup is similar as for the larger FOV except for the

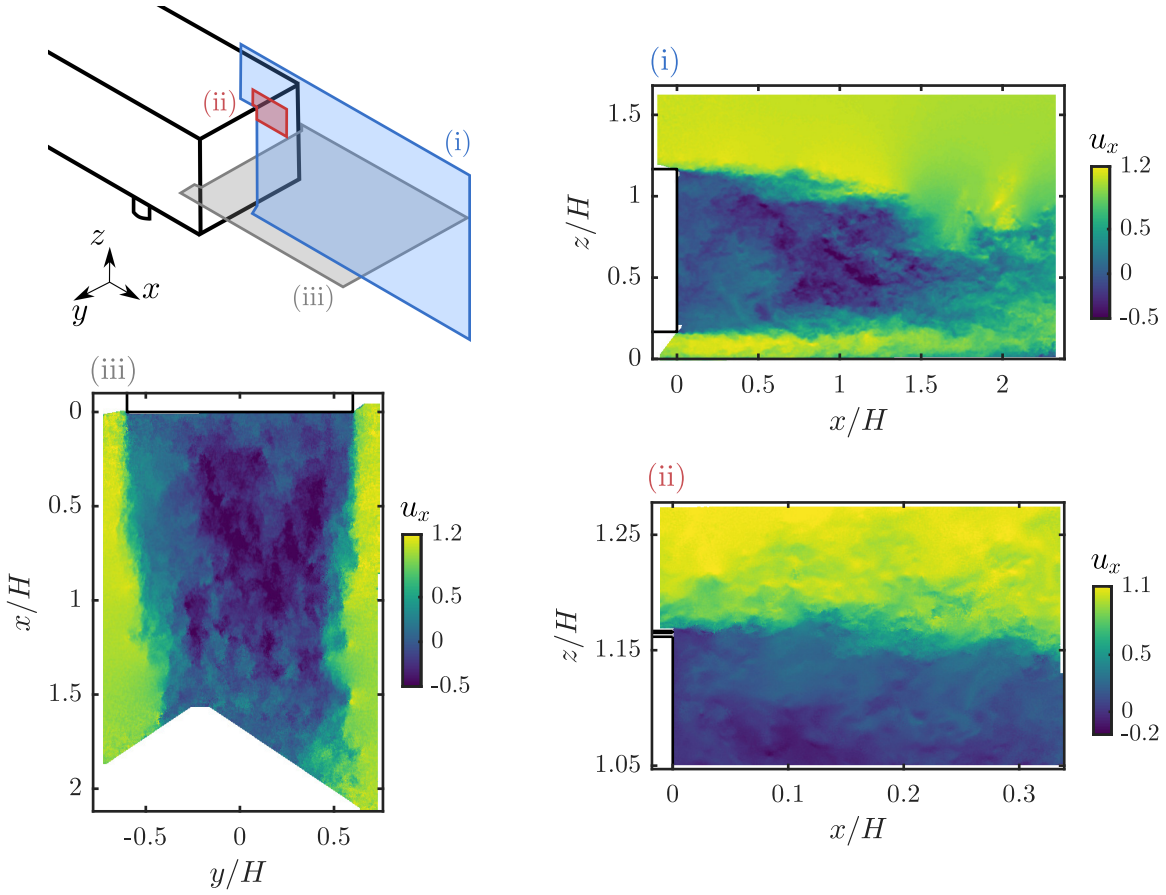

Figure 2.13: Fields of view investigated with PIV. The upper left schematic positions the three FOVs. For each, an example of instantaneous realization of the streamwise velocity u_x is given.

objective used being a *Nikkon AF Micro-Nikkor 200 mm* coupled to a 2×-teleconverter. This high magnification setup allows to resolve the small scale coherent structures of the forcing interacting with the separating boundary layer with a vector field pitch of 0.15 mm. For this FOV, although the pulsed jets are not directly seeded, the aspiration phase of the forcing (discussed in detail in §2.3) allows for the presence of particles in the flow coming from the jets when the forcing is used, which leads to satisfactory seeding of the flow. Additional phase-locked measurements using as the reference the command signal of the forcing system are performed for the small FOV. In this case, 1000 image pairs are acquired for each phase, and each pulsing period is split in 7 to 13 phases. Finally, specific surface treatment is used on the curved surfaces by coating them with a fine layer of oil ($\sim 10\ \mu$m) in order to limit the influence of laser light reflections near the surface. Two additional steps are used in the processing of image pairs : a sliding minimum subtraction in order to eliminate residual laser light reflections near the curved surface, and an image translation to correct for the small displacements of the model due to relative flexibility of the aerodynamic balance which can result in 2-3 pixels displacement on this high magnification factor PIV setup. This setup is used in Chapter 5.

Finally, a third setup is associated to a large FOV spanning the whole recirculating wake in the horizontal plane of symmetry of the model (plane $z/H = 0.67$). For this FOV, time-resolved PIV is deployed to investigate transient dynamics of the wake in Chapter 4. A *Phantom VEO4K 990* camera coupled to a *Sigma DG Macro 105 mm* objective is used to image this FOV in a double-frame mode at a frequency of 500 Hz. In order to have sufficient illumination of the PIV plane, two lasers *Continuum Terra PIV* 2×30 *mJ* and *Quantronix Darwin Duo* 18 *mJ* are synchronously fired from each side of the test section. For this setup, care is taken to resolve both temporally and spatially the most important scales in the wake. The frame rate is sufficient to resolve the smallest time-scales associated to the initial shear layer instability after separation of the turbulent boundary layer. This time-scale is estimated to be $T_\theta = St_\theta U_0/\theta \sim 230$ Hz, where

	Large FOV (i)	Detailed FOV (ii)	Large FOV (iii)
Plan	$y = 0$	$y = 0$	$z = 0.67H$
Field of view $/H^2$	2.3×1.6	0.32×0.21	1.8×1.3
Laser	Quantel Evergreen 2×200 mJ	Quantel Evergreen 2×200 mJ	Continuum Terra PIV 2×30 mJ + Quantronix Darwin Duo 18 mJ
Camera	LaVision Imager LX 16 Mpx	LaVision Imager LX 16 Mpx	Phantom VEO4K 990
Objective	Zeiss Makro-Planar ZF 50 mm	Nikkon AF Micro-Nikkor 200 mm + Kenko N-AF Teleplus 2×-teleconverter	Sigma DG Macro 105 mm
Magnification	0.04	0.5	0.055
Sensor size /px^2	4900×3300	4900×3300	4096×2300 (cropped at 3300×2300)
Pixel size /μm	7.4	7.4	6.75
U_0 /m s^{-1}	25, 35	25, 35	25
Δt /μs	70, 50	9, 6.5	60
IW /px	16×16	16×16	12×12
Overlap /%	50	50	50
Spatial resolution $/H$	7.5×10^{-3}	1×10^{-3}	6.5×10^{-3}
$/h$	–	0.33	–
$/\theta$	0.95	0.14	0.8
Time resolution /s	0.25	0.25	2×10^{-3}
$/T_\theta$	–	–	0.45
Maximum uncertainty[5] /m s^{-1}	0.2	0.2	0.25
Number of samples	1000 to 2500 (unforced), 1000 (forced)	1000 (random and phase-averaged)	2000 to 2800
Measurement time /s	250 to 625	250	4 to 5.6

Table 2.5: Summary of the main PIV parameters for all the experiments discussed in this study. The different PIV setup and field of view are denoted according to figure 2.13. The boundary layer momentum thickness θ used for the estimation of the spatial and temporal resolutions is the one obtained from the hot-wire anemometry measurements at $(x, y, z)/H = (0, 0, 1.167)$.

θ is the boundary layer momentum thickness at separation from the model (see Chapter 3) and $St_\theta \sim 0.022$ is the initial most amplified time-scale in a turbulent shear layer according to Zaman & Hussain (1981). Similarly the final interrogation window of 12×12 pixels and overlap of 50 % leads to a velocity vector each 1 mm which is less than half of θ at separation. A total of 17 forced and unforced transient wake reversals discussed in the Introduction each between 2000 and 2800 image pairs have been acquired using this setup representing 4 to 5.6 s for each realization.

2.4.4 Pressure from PIV

The method used in this study to reconstruct the mean pressure field $\overline{C_p}$ from the PIV measurements is directly derived from the one proposed by Oxlade (2013) with adjustments on the integration algorithm to improve the efficiency of the method.

Direct integration of the mean 2D momentum equations is performed where we neglect the viscous terms as we focus on a high Reynolds number turbulent wake flow. Hence the 2D equations

used for mean pressure coefficient $\overline{C_p}$ integration :

$$-\frac{1}{\rho}\frac{\partial \overline{p}}{\partial x} = \overline{U_x}\frac{\partial \overline{U_x}}{\partial x} + \overline{U_z}\frac{\partial \overline{U_z}}{\partial z} + \frac{\partial \overline{u'_x u'_x}}{\partial x} + \frac{\partial \overline{u'_x u'_z}}{\partial z}, \tag{2.8a}$$

$$-\frac{1}{\rho}\frac{\partial \overline{p}}{\partial z} = \overline{U_x}\frac{\partial \overline{U_z}}{\partial x} + \overline{U_z}\frac{\partial \overline{U_z}}{\partial z} + \frac{\partial \overline{u'_x u'_z}}{\partial x} + \frac{\partial \overline{u'_z u'_z}}{\partial z} \tag{2.8b}$$

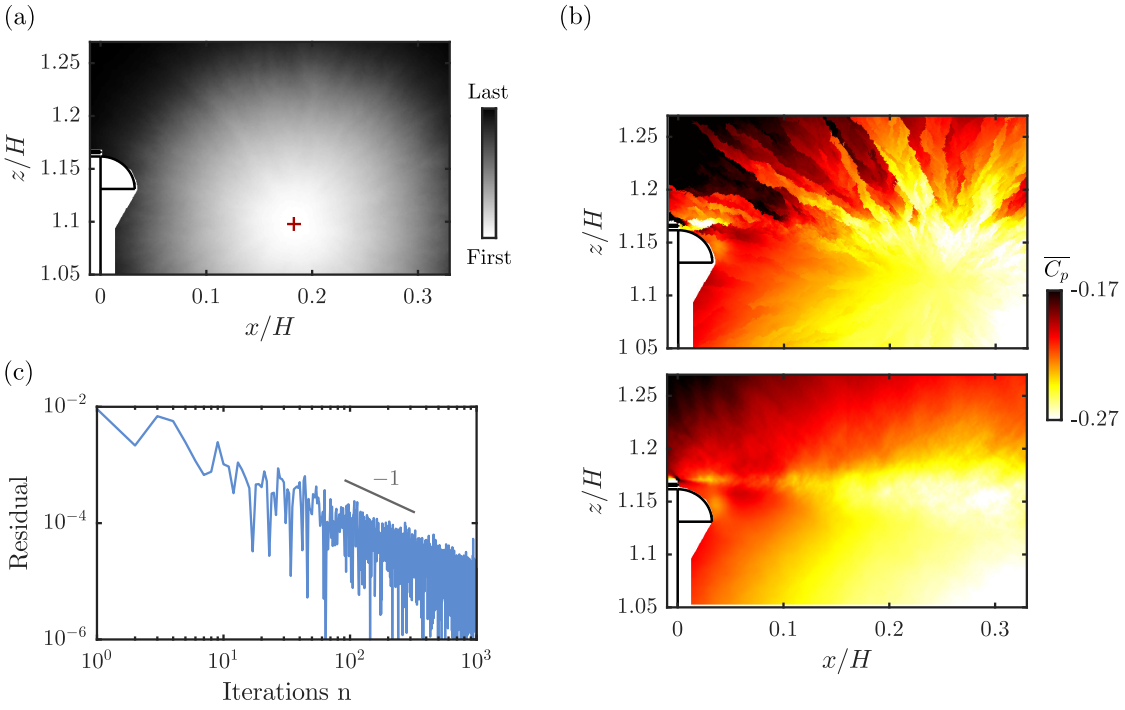

Figure 2.14: Detail of the pressure field reconstruction from PIV technique. (a) Progression of the integration algorithm. Red cross marks the integration path start. (b) Pressure field obtained after a single iteration. (c) Convergence of the reconstructed pressure. The different aspects are examplified on the small FOV (ii) of the unforced flow.

The direct integration procedure is described as follows :

1. A point $N_k = (i, j)$ is randomly chosen in the domain and a random integration path m_k is generated from this origin. Every point in the domain is given an order corresponding to its place in the path. The random path algorithm ensures each point of the domain appears once and only once in the path. The pressure coefficient is initialized $\overline{C_{p_k}}(m_k) = 0$ at the origin of the path.

2. The pressure is integrated to the next point $k+1$ in the path according to the order given by the previously generated path and using a 2D trapezoidal rule :

$$\overline{C_{p_{k+1}}}(m_k) = \overline{C_{p_k}}(m_k) + \frac{\Delta x}{2}\left(\frac{\partial \overline{C_{p_{k+1}}}}{\partial x} + \frac{\partial \overline{C_{p_k}}}{\partial x}\right) + \frac{\Delta y}{2}\left(\frac{\partial \overline{C_{p_{k+1}}}}{\partial y} + \frac{\partial \overline{C_{p_k}}}{\partial y}\right) \tag{2.9}$$

3. The following point in the path is taken and steps 2. and 3. are repeated until all the domain is solved.

4. Step 1. and the rest of the procedure is repeated with a different origin and different path until statistical convergence is reached for the estimation of $\overline{C_p}$.

The convergence criterion used is based on the residual average pressure in the domain $\langle \overline{C_p}_{k+1} - \overline{C_p}_k \rangle$ and around 1000 iterations are necessary to reach satisfactory convergence with a residual being decreased by almost 4 orders of magnitude. The different steps of the method are illustrated in figure 2.14. Advantage of generating a complete random integration path is to be able to transform the whole problem in the resolution of a big linear system leading to important speed up of the method. Besides, as all the random integration path are completely independent, it would be an easy task to optimize the computation using a GPU implementation (Wang *et al.*, 2019).

Finally the integration constant C is determined from using as a boundary condition BC Bernoulli's law on a streamline located in the potential flow region outside the wake where hypotheses linked to Bernoulli's law are satisfied :

$$C = \left(\overline{\mathbf{u}}^2_{\mathrm{BC}} - 1\right) + \overline{C_p}_{\mathrm{BC}} \tag{2.10}$$

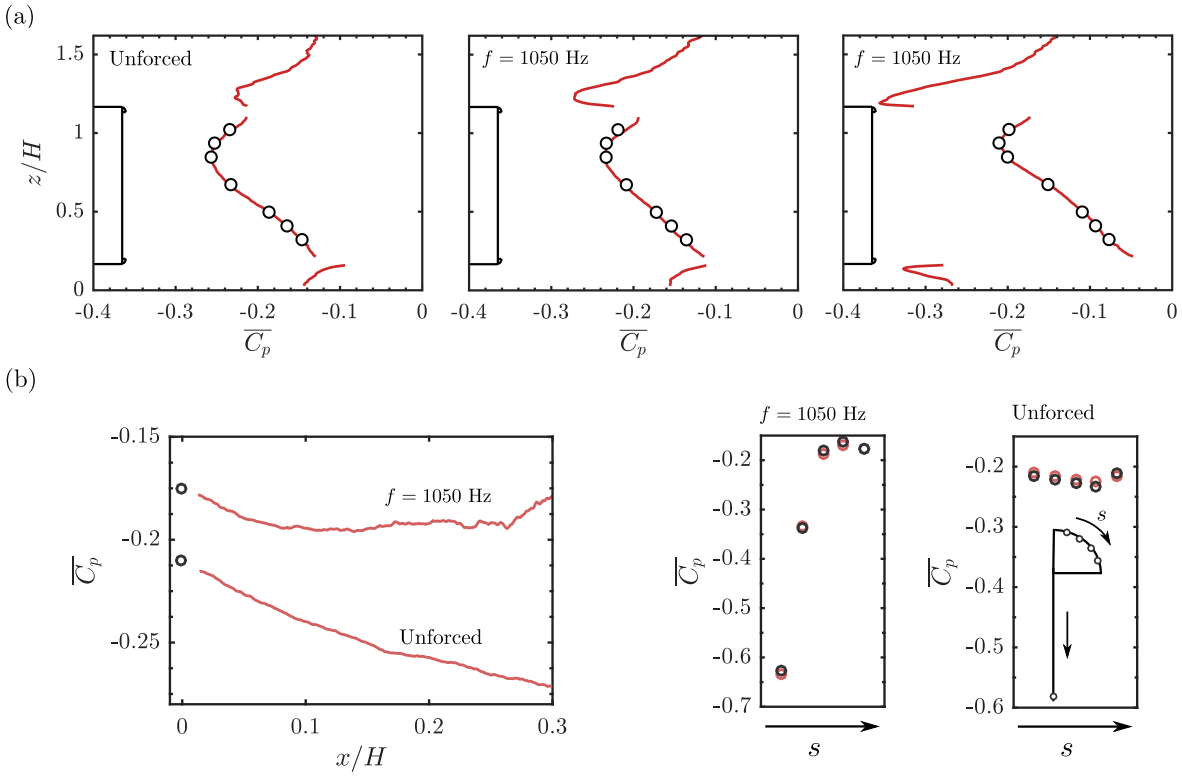

Figure 2.15: Validation of the pressure reconstruction technique in the different cases investigated. (a) Large vertical FOV. Full line is the pressure reconstruction at $x/H = 0.01$ and circles for all the pressure measurements located in the plane $y = 0$. (b) Small FOV. Red circles are the reconstructed pressure at the closest location from the actual pressure measurements in black circles. For each case both unforced and forced configurations are shown as examples.

Examples of comparison between pressure measurements on the base and reconstructed pressure field are presented in figure 2.15 for both unforced and forced conditions on both the large FOV and the small FOV in the vertical plane. The relative difference between the reconstructed pressure fields and the pressure measurements is less than 2% (resp. 5%) at maximum at a single location for taps at the base (resp. on the curved surface). The higher discrepancy over the curved surface is attributed to the difficulty to completely properly resolve the flow with PIV near the surface due to residual laser light reflections and to the absence of seeding in the pulsed jets. It is worth mentioning that despite the wake being highly three-dimensional, this pressure reconstruction leads to quite satisfying results on the large FOV in terms of base pressure. two main reasons account for this result : the statistical symmetry of the wake leads to no mean out-of-plane velocity in the symmetry plane, and the out-of-plane turbulent shear stresses $\overline{u'_x u'_y}$ and $\overline{u'_z u'_y}$ are expected

to be weak in the region near the base [6]. This remark would not hold anymore if the instantaneous pressure field was to be investigated or if the mean pressure field was investigated around the end of the recirculation region. For the small FOV however, the region of interest concerns the initial development of the shear layer where three-dimensional effects are still weak and as a consequence the 2D approximation in the pressure reconstruction looks quite pertinent. The method presented (and other equivalents in the literature as Liu & Katz (2006) or Wang *et al.* (2019)) has the main advantage of only requiring a single boundary condition compared to methods solving the Poisson equation for pressure (de Kat & van Oudheusden, 2012; van Oudheusden, 2013) where boundary conditions have to be known on all the boundaries of the domain.

[6] Evidence for this assertion is provided in Chapter 3 where these turbulent shear stresses are investigated in the whole wake.

Chapter 3

Natural flow

This chapter is a brief introduction to characterize the natural flow around the Ahmed body. The main features of the wake flow are presented as a seed for the forthcoming chapters. Notably, the focus is put on exhibiting the global peculiarities of the wake at the root of drag generation – which will be of major importance for our discussions on drag reduction mechanisms throughout the manuscript –, and characterizing the boundary conditions at separation – which is of major importance in the studies of wake forcing in chapter 5 and 6.

Contents

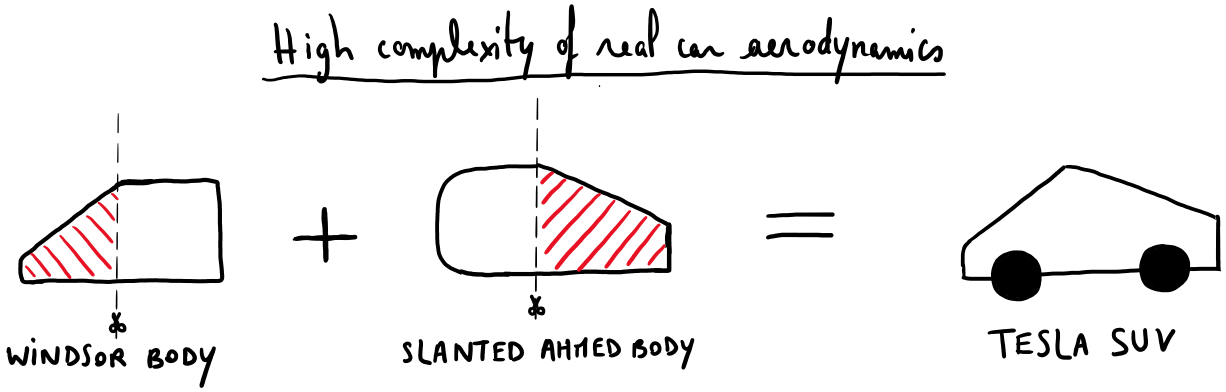

A global picture of the natural flow around the Ahmed body is given in this chapter. This study is based on specific indicators/notions introduced to capture the flow features which will be studied further in the forthcoming chapters. The turbulent wake flow is first extensively described for the canonical case with ground clearance $G/H = 0.167$ from the seminal study of Ahmed *et al.* (1984) using both a velocity and pressure characterization. The boundary conditions at rear separation are then commented to characterize the transition region between the model's boundary layers and the initial developing shear-layers surrounding the wake. Finally the flow at reduced ground clearance $G/H = 0.067$ is described, echoing important comments and parts of the studies in chapters 4 and 6.

3.1 Mean flow around the Ahmed body

The flow of the original configuration introduced by Ahmed *et al.* (1984) with $G/H = 0.167$ is first described. Mean streamwise velocity fields at $U_0 = 25$ m s^{-1} (corresponding to $Re_H = 5 \times 10^5$) are given in figure 3.1 in both vertical and horizontal planes of symmetry of the model focusing on the wake. The flow is characterized by a massive separation at the edges of the model's base resulting in a recirculation zone (with $\overline{u_x} < 0$) extending until $x/H = 1.58$. The wake presents an almost perfect statistical mirror symmetry in the horizontal plane linked to the only symmetry of the configuration, whereas there is a slight imbalance in the vertical direction most probably linked to the presence of the ground. The recirculation region is composed of two recirculating centers in each plane close to the mean separatrix. Important flow curvature is present at the closing of the recirculating region which denotes the presence of strong pressure gradients imposing a low pressure inside the recirculation region.

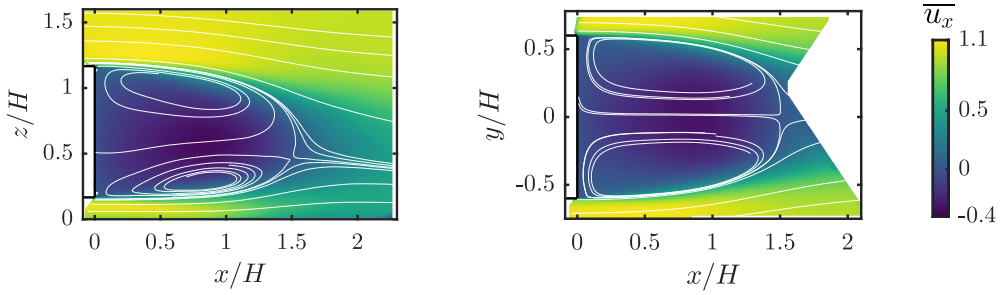

Figure 3.1: Mean streamwise velocity u_x superimposed with mean streamlines in the vertical symmetry plane $y/H = 0$ and in the horizontal plane $z/H = 0.67$ at $U_0 = 25$ m s^{-1}.

The mean separatrix delimiting the high-momentum free-stream region from the low-momentum recirculation region is characterized by a sharp drop in velocity at the location of the developing shear-layers. This region leads to the formation of local instabilities and thus an important mixing activity and high stresses statistically characterized by important Reynolds stresses. The main components resolved by the 2D-2C PIV in both planes are given in figure 3.2. Reynolds stresses are mainly located along the mean separatrix with increasing level from the separation because of the spatially developing shear-layers. The highest stresses are located at the closing of the recirculation region, highlighting the important role played by the Reynolds stresses in the formation of the recirculation region. Once again a slight vertical imbalance can be spotted from the asymmetry in the Reynolds stresses distribution. In particular the $\overline{u'_x u'_x}$ component presents levels quite more important in the lower shear-layer. The origin of these stresses and their global impact on the wake are studied in detail in chapter 4.

According to the flow momentum equations discussed in §2.4.4 for the estimation of pressure from PIV data, mean flow curvature and Reynolds stresses are the main contributors to pressure changes across the flow. Therefore, the mean pressure in the flow around the model is presented in figure 3.3. The mean pressure in the wake estimated from the PIV data in both planes is characterized by two local minima in each plane, localized near the separatrix at the position of the recirculating centers and in the vicinity of the location of highest Reynolds stresses. The contour $\overline{C_p} \sim -0.3$ is composed of two circular regions around these minima in each plane, which in

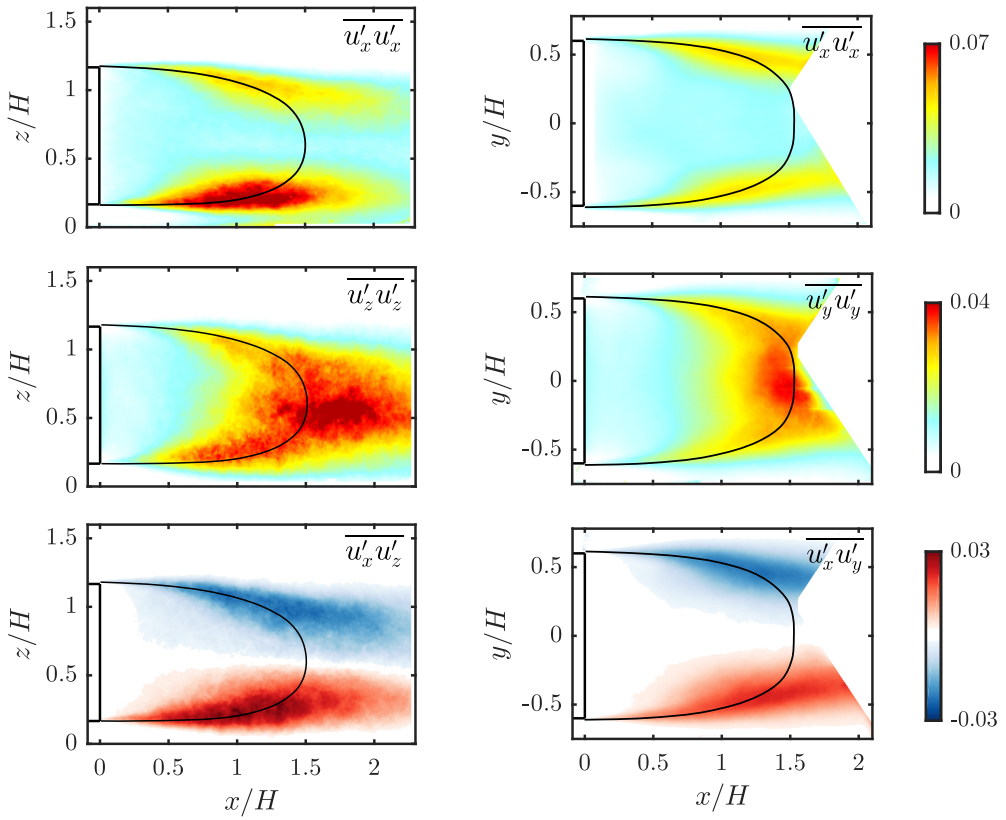

Figure 3.2: Mean Reynolds stresses in the vertical symmetry plane $y/H = 0$ and in the horizontal plane $z/H = 0.67$ at $U_0 = 25$ m s^{-1}. The black line indicates the mean separatrix.

3D is resulting in a toroidal low pressure structure as described qualitatively by Grandemange *et al.* (2013*a*) and more quantitatively by Lucas *et al.* (2017) and Dalla Longa *et al.* (2019). Important pressure gradient stemming from flow curvature are responsible for a strong flow recompression at the closing of the recirculation region after $x/H \sim 1.5$. As discussed in §2.4.4, it should be noted that in this region pressure estimation is more influenced by the omission of Reynolds stresses components not resolved by the PIV setup ($\overline{u'_y u'_y}$ in the plane $y/H = 0$ and $\overline{u'_z u'_z}$ in the plane $z/H = 0.67$) and which are not negligible anymore. The low pressure region keeping the slight vertical asymmetry noted on the mean flow leaves a low pressure imprint on the base of the model which accounts for most of the aerodynamic drag of the model. This base pressure distribution still keeps trace of the wake imbalance with a vertical stratification with slightly lower pressure in the top part. The global aerodynamic characteristics of the body, namely the base-averaged mean pressure $\overline{C_{pb}}$ and the drag and lift coefficients C_D and C_L, are summed up in table 3.1 for Re_H spanning the interval $[4; 8] \times 10^5$. No significant change out of the measurement uncertainty in $\overline{C_{pb}}$ can be seen over the range of Re_H of interest in this work and the body presents a characteristic value $\overline{C_{pb}} = -0.196$ which is consistent with the large amount of data available from the recent literature. The drag coefficient behaves quite similarly with only a slight increase of ~ 1.5 % at the lowest Re_H presented and a characteristic value of $C_D = 0.254$ at $U_0 = 25$ m s^{-1} also consistent with most of the recent literature. From the total drag, more than 80 % is due to pressure drag $\iint_{\text{body}} -p\underline{\underline{I}}\mathbf{n}dS$ among which ~ 77 % is resulting from the sole wake suction at the base. Only the lift coefficient showing a slight downforce has a decreasing trend with Re_H. This seems linked to changes in the confined flow in the underbody in relation to changes in boundary layer size on both sides of the underbody. The lateral force coefficient is not commented here as it is vanishing as a result of the statistical symmetry of the flow.

The pressure all around the model is given in figure 3.3(b). Important changes are seen on the front part where very low pressure regions appear on the rounded parts due to the curvature of the geometry. This creates an adverse pressure gradient just downstream the rounded part which is well known to provoke flow detachment and the local formation of a recirculation bubble (Spohn &

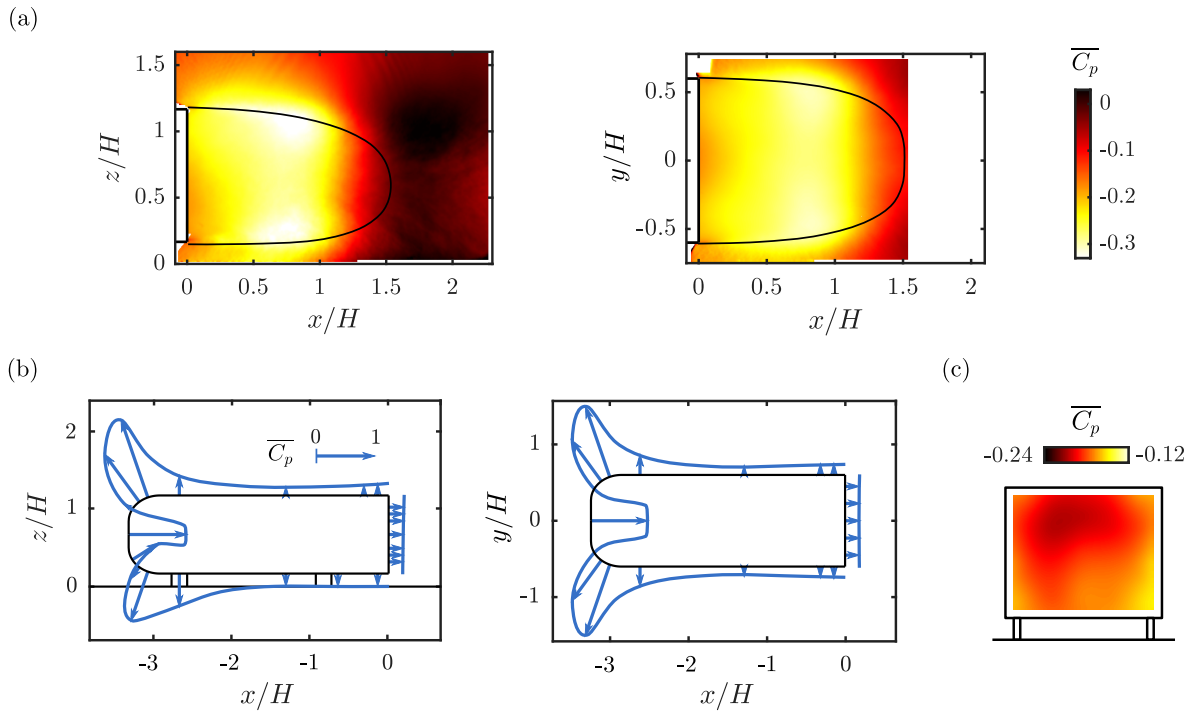

Figure 3.3: Mean pressure around the Ahmed body at $U_0 = 25$ m s^{-1}. (a) Mean pressure $\overline{C_p}$ in the vertical symmetry plane $y/H = 0$ and in the horizontal plane $z/H = 0.67$. The black line indicates the mean separatrix. (b) Pressure distribution around the body in the planes $y/H = 0$ and $z/H = 0.67$. Positive $\overline{C_p}$ is indicated with arrows pointing inwards. (c) Pressure distribution at the base.

Gilliéron, 2002). Similar measurements by Grandemange *et al.* (2013*a*) have shown a low pressure plateau at this location on the top and lateral facets of the Ahmed body which was characteristic of a recirculation bubble formed by the detachment and further reattachment of a turbulent boundary layer. Here the modified nose of the model prevents this flow detachment as can be spotted on the pressure measurements and as was monitored from surface oil flow visualizations. Only at a low velocity $U_0 = 15$ m s^{-1} (corresponding to $Re_H = 3 \times 10^5$) the seeds of a small recirculation bubble can be spotted. The absence of front detachment on the body explains the quasi constant values of base drag $\overline{C_{pb}}$ and drag $\overline{C_D}$ observed on the investigated range of Re_H. Moreover, as argued by Barros (2015), the front detachment had a significant impact on the boundary layers development and characteristics at rear separation which play an obvious role on the shear-layers features in the wake. The absence of front detachment in this work should thus also have an impact on the boundary condition at rear separation.

U_0 [m s^{-1}]	15	20	25	30	35	40
Re_H ($\times 10^5$)	3	4	5	6	7	8
$\overline{C_{pb}}$	-0.198	-0.196	-0.197	-0.197	-0.196	-0.196
$\overline{C_D}$	0.261	0.258	0.254	0.255	0.252	0.253
$\overline{C_L}$	-0.126	-0.122	-0.123	-0.119	-0.127	-0.120

Table 3.1: Evolution of the main aerodynamic characteristics of the flow with the free-stream velocity U_0 in m s^{-1}.

Finally, even if the wake exhibits statistical mirror symmetry in the horizontal direction, this is not the case instantaneously. The large-scale dynamics of the wake characterized by the instantaneous position (y_b, z_b) of the center of pressure (CoP) at the base are shown in figure 3.4. The

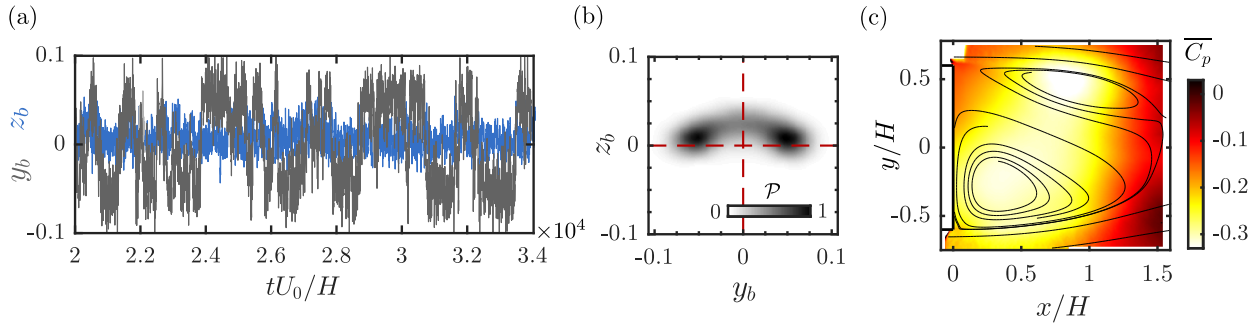

Figure 3.4: Large-scale pressure dynamics in the wake of the Ahmed body at $U_0 = 25$ m s^{-1}. (a) Time evolution of the lateral y_b and vertical z_b position of the center of pressure (CoP) on the base. (b) Joint probability density function $\mathcal{P}(y_b, z_b)$ of the CoP position. (c) Mean pressure field in the wake in the plane $z/H = 0.67$ conditionally-averaged on $y_b < 0$.

coordinates y_b and z_b are defined as

$$y_b = \frac{\sum_{i=1}^{N} y_i C_p(y_i, z_i, t)}{\sum_{i=1}^{N} C_p(y_i, z_i, t)}, \quad z_b = \frac{\sum_{i=1}^{N} z_i C_p(y_i, z_i, t)}{\sum_{i=1}^{N} C_p(y_i, z_i, t)} \tag{3.1}$$

over the N pressure taps at the base with an origin at the center of the base. From the time-series in figure 3.4(a), the lateral position y_b of the wake oscillates randomly between two equiprobable asymmetric position $y_b \sim \pm 0.055$ on long time-scales of order $O(10^3)$ convective time-scale H/U_0, while the vertical position z_b is fixed around an almost vanishing mean value. These lateral bi-modal dynamics are very similar to the ones described by Grandemange *et al.* (2013*b*) which were linked to the symmetry-breaking instability occurring in the laminar wake of the Ahmed body. The only small difference spotted from the joint probability density function $\mathcal{P}(y_b, z_b)$ is the transition between this two lateral asymmetric states which occurs through a vertical asymmetric state similarly to Varon *et al.* (2017) and contrary to Grandemange *et al.* (2013*b*) where it is almost perfectly symmetric. The mean pressure in the wake can be conditioned on the position of y_b to show the flow organization associated to these large-scale symmetry-breaking dynamics. In figure 3.4(c), the mean pressure for $y_b < 0$ shows a wake organization similar to the mean pressure with a low pressure toroidal structure but in this case it is tilted with the part close to the base on the side of the CoP. A slightly lower pressure is also noticed in the part of the structure tilted away from the base, which will discussed in detail in chapter 4.

3.2 Boundary conditions at rear separation

The boundary layers at Re_H ranging from 3 to 7×10^5 are characterized at separation from each of the edges of the base of the model using a combination of hot-wire anemometry and PIV measurements. The boundary layer profiles obtained are presented in outer variables (δ, U_e) scaling in figure 3.5(a) where δ is the boundary layer thickness and U_e the external velocity, and in inner variables $\delta_\nu = (\nu/u_\tau, u_\tau)$ scaling in figure 3.5(b) where u_τ is the friction velocity. u_τ is estimated using the Clauser chart method by looking for the value of u_τ leading to the best fit of the velocity profile in the log region to a characteristic log-linear law $\overline{u_x}/u_\tau = 1/\kappa \log(y/\delta_\nu) + B$ where κ and B are universal constants for zero pressure gradient boundary layers. However, here the boundary layer at separation is expected to deviate from this kind of boundary layers as it has been influenced in its development by a strong adverse pressure gradient on the front of the body and by a favourable pressure gradient just before the rear edges (which can be quantitatively assessed from the pressure field reconstruction from the small PIV FOV). For the constant κ, we thus refer the one used by Morris & Foss (2003) ($\kappa = 0.43$) in the study of the transition region between a turbulent boundary layer and a spatially developing shear-layer after inertial separation which is a flow locally qualitatively very similar to the one considered here. The associated constant B has

a value of 10 slightly higher than the one used by Morris & Foss (2003), suggesting the additional influence of the recirculating flow not present in their study. The estimations of characteristic boundary layer displacement and momentum thickness δ^* and θ, and of u_τ are provided in table 3.2 for the boundary layers at separation from each edge at various Re_H.

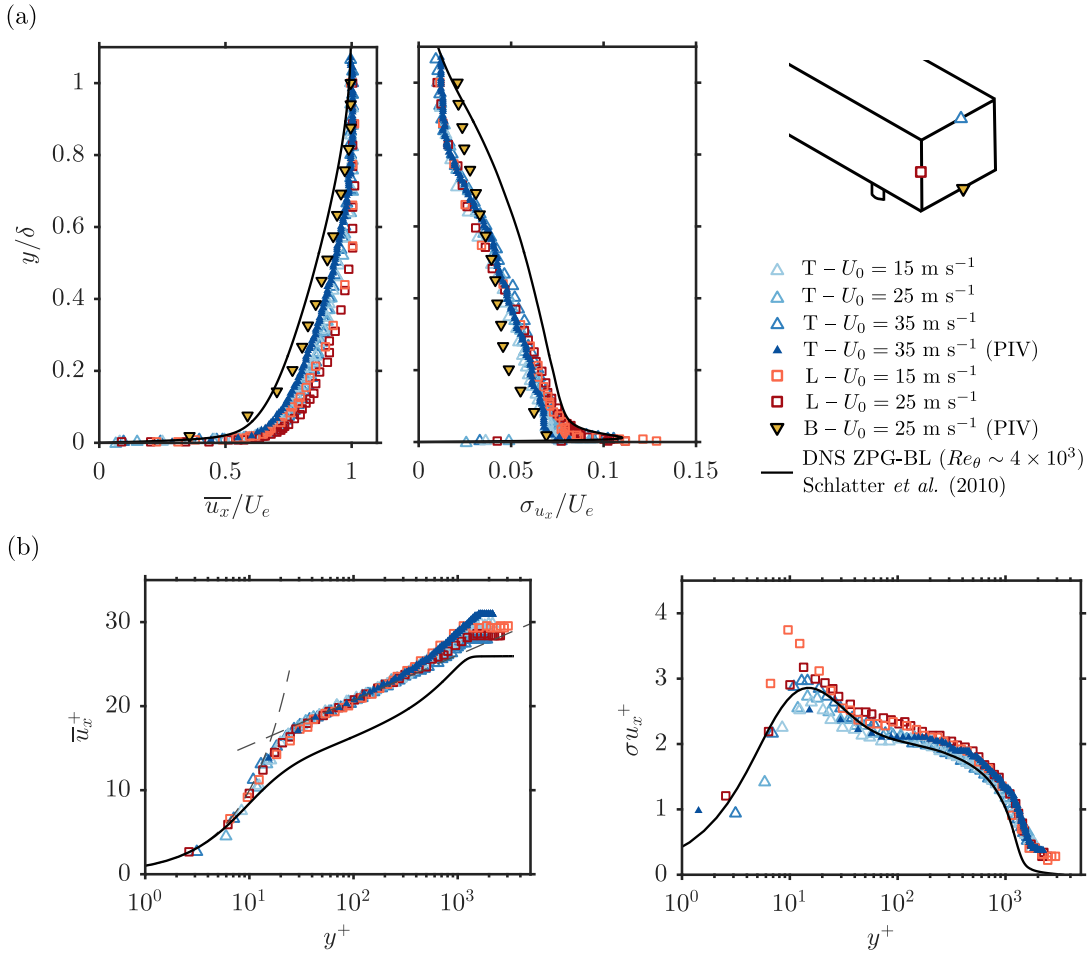

Figure 3.5: Mean $\overline{u_x}$ and fluctuating σ_{u_x} boundary layer velocity profiles at separation at each edge of the base of the body in (a) outer variables scaling and (b) inner variables scaling. By flow symmetry, only the left boundary layer is presented. Empty markers are hot-wire anemometry measurements taken 0.5 mm ($\sim \theta_0/4$) downstream separation. Filled markers are PIV data extracted at a similar location. DNS data of a turbulent boundary layer with zero pressure gradient at similar Re_θ of Schlatter & Örlü (2010) is given for comparison. $^+$ superscript denote an inner variable scaling.

Location	U_0 [m s^{-1}]	δ [mm]	δ^* [mm]	θ [mm]	H	u_τ [m s^{-1}]
T	15	45.2	4.28	3.10	1.38	0.58
T	25	33.3	3.31	2.19	1.51	0.88
T	35	27.7	2.72	1.88	1.45	1.15
L	15	69.5	4.06	3.15	1.29	0.56
L	25	35.5	2.46	1.87	1.32	0.89
B	25	25.3	3.14	2.08	1.51	0.84

Table 3.2: Main characteristics of the boundary layers at separation. T,B and L are respectively indicating top, bottom and lateral positions.

As a matter of comparison, a reference zero-pressure-gradient boundary layer is provided in figure 3.5 from the DNS results of Schlatter & Örlü (2010). All the mean profiles present less velocity deficit near the wall ($y/\delta < 1$) and an attenuation of the velocity fluctuations in the outer region of the boundary layer which is characteristic of the presence of a favourable pressure

gradient. In all the configurations, boundary layers present very similar scaled profiles, suggesting the Re_H-independence of the boundary layers and thus the almost vanishing influence of the front of the model on the boundary conditions at separation. The boundary layer profiles have a characteristic shape of fully turbulent boundary layers, which is confirmed by the shape factor values $H = \delta^*/\theta$ between 1.3 and 1.5. Characteristic thickness scales present a high degree of similarity between all the edges and all the thicknesses decrease with increasing Re_H. The values of θ and δ_ν are of peculiar importance in assessing the further dynamics of the spatially developing shear-layers as suggested by Ho & Huerre (1984) or Morris & Foss (2003). Both these length scales condition the initial shear-layer instability with a preferential frequency of $St_\theta = f\theta/U_0 = 0.022$ for turbulent boundary layers. As a matter of generalization, Morris & Foss (2003) proposed a universal scaling based on δ_ν to gather laminar and turbulent separating boundary layers which have two distinct values of St_θ. These aspects will be essential for the influence the shear-layers dynamics have on the recirculating region as shown in chapter 4 and for the interaction with the periodic forcing used in chapters 5 and 6.

3.3 Mean flow at reduced ground clearance

As a last part of this chapter, the flow at reduced ground clearance $G/H = 0.06$ is presented. This flow is rather prototypical of flows past lorries as shown by Szmigiel (2017) and Castelain *et al.* (2018) where the underbody flow momentum is quite impacted by the close proximity to the ground. For this value of the ground clearance, the wake is expected to be in a high base drag state according to Grandemange *et al.* (2013*c*) and Szmigiel (2017), which is confirmed by the $\overline{C_{pb}}$ value 5 % lower than for the canonical Ahmed body flow gathered in table 3.3. The wake is quite changed compared to the canonical Ahmed body flow as is described in figures 3.1 and 3.3. An important vertical asymmetry is introduced by high degree of interaction with the ground such that flow detachment from the ground occurs around $x/H \sim 1$ where the adverse pressure gradient is the strongest towards the end of the recirculation region. A strong low pressure imprint is left on the lower part of the base contributing to the increased base drag.

U_0 [m s^{-1}]	$\overline{C_{pb}}$	$\overline{C_D}$	$\overline{C_L}$
25	-0.207	0.257	-0.057

Table 3.3: Main aerodynamic characteristics of the flow for $G/H = 0.06$ at $U_0 = 25$ m s^{-1}.

Another key difference lies in the spatial distribution of the Reynolds stresses. Here again the vertical flow asymmetry is quite pronounced with high levels of Reynolds stresses in the top shear-layer somewhat 30 % higher than for the canonical Ahmed body flow. On the contrary, the lower shear-layer stemming from the underbody flow has very low levels of fluctuations suggesting a very stable flow. This aspect will be further commented and interpreted in chapter 4 to link the dynamics of the wake to the base drag and in chapter 6 when asymmetrically forcing the wake to manipulate the drag. Finally, the large-scale dynamics of the wake are completely different as no lateral bi-modal dynamics are present anymore. Instead, the wake presents an instantaneous lateral symmetry and mean vertical asymmetry linked to the close proximity of the ground. This is in line with the studies of Grandemange *et al.* (2013*a*) and Cadot *et al.* (2015) suggesting a stabilization of the symmetry-breaking by the close proximity of the ground.

3.4 Concluding remarks

The main features of the mean flow around the Ahmed body have been characterized. To summarize the results, three main features of the wake have been put forward which have a fundamental impact on the base drag of the body.

- The flow curvature along the wake separatrix results in large pressure gradients which separates the low pressure/momentum recirculating region from the high-pressure/momentum free-stream.

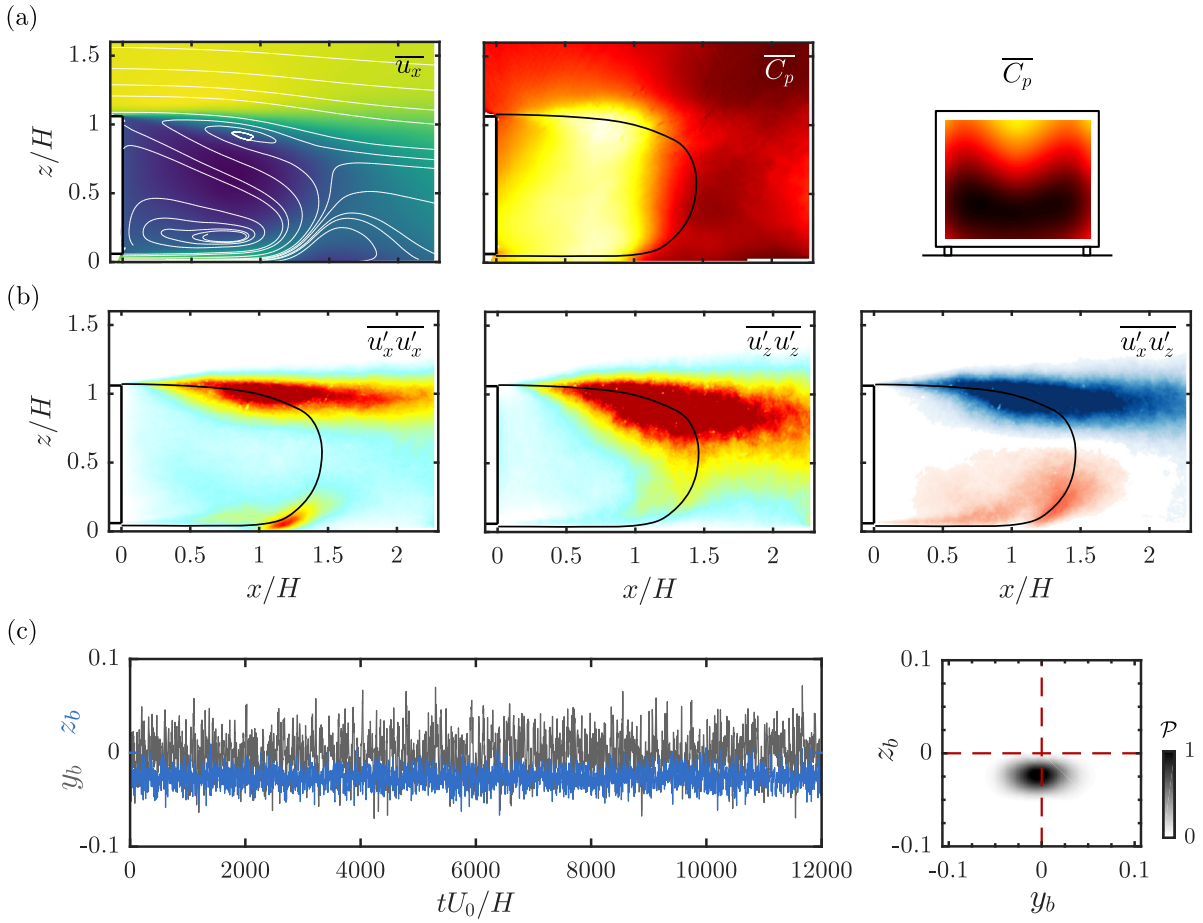

Figure 3.6: Mean flow for reduced ground clearance $G/H = 0.06$ at $U_0 = 25$ m s^{-1}. In a matter of comparison, color scales are the same than in figures 3.1, 3.3 and 3.2. (a) Mean flow, (b) Reynolds stresses and (c) large-scale dynamics of the CoP.

- The spatially developing shear-layers stemming from the inertial separation of the boundary layers which are sources of important Reynolds stresses and play a key role in the closing of the recirculation region.
- The recirculation flow inside the near-wake which further shapes the pressure structure of the wake with local pressure minima at the center of the recirculating flows.

These three key features will be at the center of the work in the coming chapters to analyse the base drag mechanisms, provide efficient drag-reducing flow control strategies, and study the drag changes in the flow manipulation experiments.

The asymmetries appearing in the mean flow and the peculiar link between the shear-layers and the recirculating flow are now to be studied in chapter 4 to provide a fine analysis of the base drag mechanisms introduced here.

Chapter 4

Wake asymmetries and reversals : equilibrium and drag

Most of these results are published in Haffner *et al.* (2020*a*) in the *Journal of Fluid Mechanics*. A combination of passive and active methods are used to manipulate the symmetry of the turbulent wake of the Ahmed body. Dedicated experiments to study the wake reversals occurring between symmetry-breaking states are performed. We show how transient symmetric states explored during the reversals differ from static symmetry-breaking states in the flow organization they induce. In asymmetric states, a strong interaction and coupling between the recirculating flow from one side and the shear-layer from opposite side triggers shear-layer instabilities and their amplification. The resulting large-scale flow engulfment in the recirculation region increases the recirculation intensity and thus increases base drag. By contrast, during the wake reversals the disorganization of the recirculating flow leads to a transient symmetric state with prevented shear-layer interaction and triggering mechanism with a concomitant drag reduction of $\sim 8\%$ compared to symmetry-breaking states. Recent experimental results for unbalanced wakes and methodologies addressing the control of wake asymmetries for drag reduction are finally discussed and interpreted based on the present findings. This leads us to provide new insights in control methods for wake asymmetries.

Contents

4.1 Large-scale wake asymmetries and drag

As discussed in the introductive chapter, an important feature of 3D blunt bodies flows is the strong sensitivity of the near-wake flow to different geometrical changes such as the aspect ratio H/W of the base (Grandemange *et al.*, 2013*c*), the ground clearance G (Cadot *et al.*, 2015), the ratio of the underbody velocity to the free-stream velocity (Castelain *et al.*, 2018) or small passive perturbations in the underbody (Barros *et al.*, 2017). All these parametrical changes lead to massive changes in the recirculating wake flow and also more importantly on the base drag.

One primary aspect of the dynamics of such wakes is the presence of large-scale asymmetries. Grandemange *et al.* (2012) showed that the laminar wake of an Ahmed body undergoes a symmetry-breaking bifurcation leading to high levels of asymmetry in the separated flow and which persist at higher turbulent Reynolds numbers Re_H. In this latter case, the work of Grandemange *et al.* (2013*b*) has investigated the bi-modal random switching on long time-scales between lateral asymmetric flow states. Grandemange *et al.* (2013*a*), Barros *et al.* (2017) and Bonnavion (2018) have recently experimentally observed a bifurcation scenario involving not only lateral asymmetric flow states but also wall-normal static asymmetric flow states. The existence of 4 different asymmetric modes aligned on the two symmetry planes of the geometry seems to be a specification of the general blunt axisymmetric case where the instantaneous wake presents asymmetry but with an instantaneous plane of symmetry whose azimuthal position is stochastically evolving (Rigas *et al.*, 2014, 2015). Grandemange *et al.* (2014*a*) provides a rough estimate between 4 and 9% of the contribution of the unsteady lateral asymmetry of the Ahmed body wake to the pressure drag. Nevertheless no clear mechanism has been identified to explain these asymmetry-related drag contributions.

Even if all these recent works give important insight in the behaviour of the symmetry-breaking instability in three-dimensional blunt body wakes, there still remains an important open question concerning the mechanism of symmetry-breaking and its relation to drag generation. The objective of this paper is thus to understand the mechanics of drag reduction observed during transient near wake reversals and concomitantly to explain the increase of drag in asymmetric states. In particular, we will show how transient symmetric states of the near wake explored during the reversals differ from the static symmetry-breaking states. This will be addressed by studying the coupling between lateral shear-layers showing very distinct unsteady structures in static or transient states. The chapter is organized as follows. The experiments are first described in §4.2. A global sensitivity study of the wake asymmetry and its relation to base drag is provided in §4.3. Then transient near-wake reversals are characterized using conditional and ensemble-averaged descriptions in §4.4. The peculiar coupled dynamics between the recirculating flow and

the shear-layers are characterized in §4.5 to provide a link between asymmetries and drag. This leads in §4.6 to the characterization of the flow dynamics during the transient wake reversals. Finally, based on the results a thorough discussion on asymmetric flow dynamics, their relation to the drag and their control is proposed in §6.4.

4.2 Experimental set-up

Details on peculiarities of the experiments performed for the investigations in this chapter are provided in figure 4.1. All the experiments carried out in this chapter are performed at $U_0 = 25$ m s^{-1} or $Re_H = 5 \times 10^5$. The symmetry of the Ahmed body flow is passively perturbed in different ways. The yaw angle β can be changed in order to influence the lateral symmetry of the flow (figure 4.1(a)). Independently, the vertical symmetry of the flow is perturbed using spanwise cylinders of different diameters d ranging from $0.01H$ to 0.066H [1] placed either on top or below the body as sketched in figure 4.1(c). Two different locations upstream from the base have been tested, namely $x/H = -1$ or -2, without noticeable influence on the effect they have on the wake. The results presented herein correspond to the case $x/H = -2$ for brevity without loss of generality.

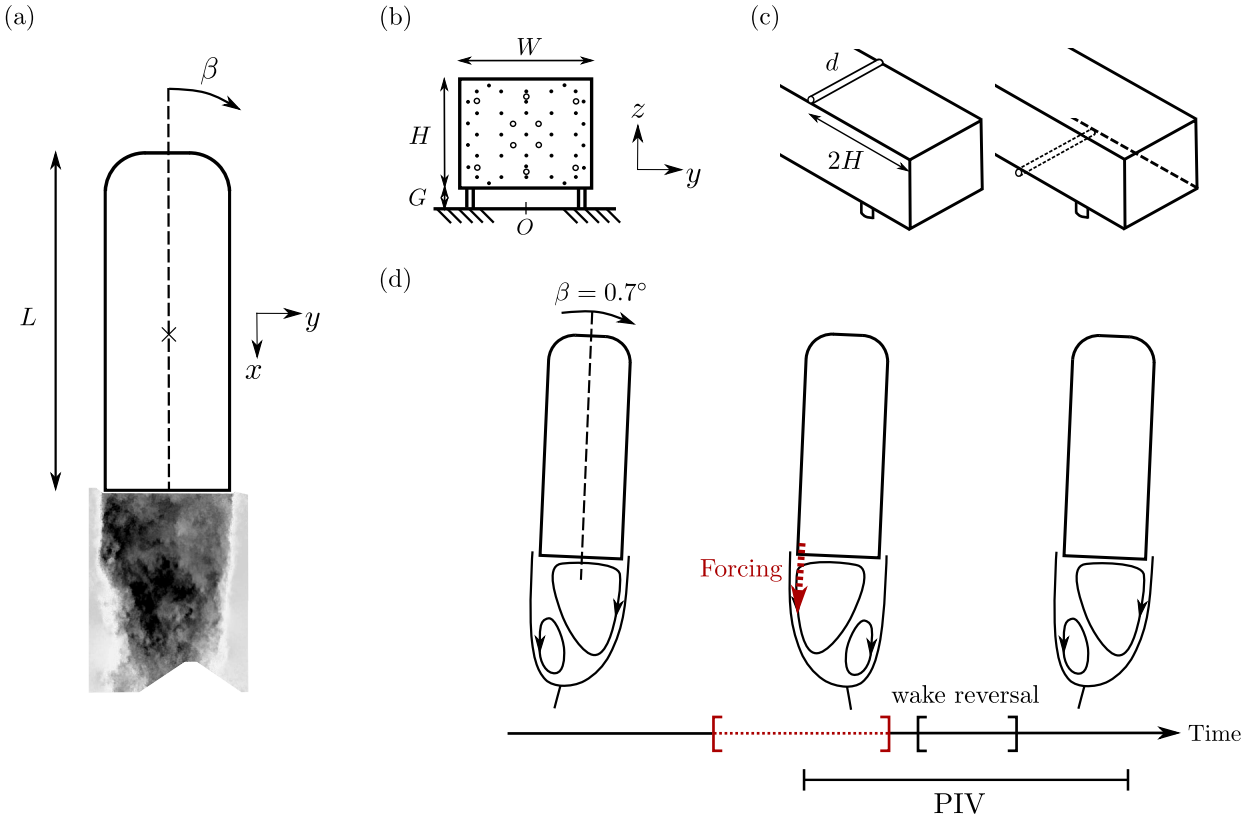

Figure 4.1: Peculiarities of the experimental setup. (a) Definition of the yaw angle β. (b) Pressure taps location around the model and on the base : points indicate mean pressure measurements location and circles time-resolved pressure measurements. Both measurements are used for different purposes (see text for details). (c) Disposition of the spanwise cylinders of diameter d used to passively perturb the natural equilibrium of the wake. (d) Method to trigger a lateral wake reversal. The model is yawed at an angle sufficient to completely lock one the lateral asymmetric states. Forcing at $St_W \sim 1$ on the windward side then maintains the wake in the opposite asymmetric state. When the forcing is stopped, the wake relaxes to the initial lateral asymmetric state producing a wake reversal. The whole process is captured by the time-resolved measurements.

Another important aspect of this chapter is the detailed investigation of the wake reversals occurring in lateral bi-modal wakes. Fine investigations of the reversal process are studied using coupled time-resolved PIV (TR-PIV) and base pressure measurements as sketched in figure

[1] This represents from around the boundary layer momentum thickness at rear separation θ_0 to 6 times its value.

Method	Number of realizations	Total duration [s]	Number of images
Natural	7	~ 3.5	~ 1700
Triggered	12	~ 6	~ 3000
Locked asymmetry	2	~ 11	~ 5000

Table 4.1: PIV characteristics of the wake reversal experiments. The total duration and number of images are only referring to the wake reversal period itself.

4.1(a,b). The wake reversal is a Poissonian random process (Grandemange *et al.*, 2013*a*). In order to only focus on the reversals and to acquire a sufficient number of them, two different strategies are adopted. As the TR-PIV can only record time segments of around 450 convective time units H/U_0 and as the mean duration between two wake reversals is of order $O(1000H/U_0)$, the capture of the wake reversal process is rather complex. The first method is to try to capture a wake reversal on the fly by hoping one occurs quite in the middle of the TR-PIV acquisition. This leads to important number of tries for only several wake reversals acquisitions. A second more efficient method is to trigger the reversals as sketched in figure 4.1(d). For this, the body is first yawed at an angle sufficient to lock permanently the wake in one of the lateral asymmetric states[2]. Then periodic forcing is applied on the windward side of the wake ($y < 0$ for $\beta > 0$) in order to lock the wake in the opposite asymmetric state following the results of Barros (2015) and Li *et al.* (2016). Periodic forcing is issued at small amplitude[3] at $St_W \sim 1$. This frequency will be shown to be related to peculiar dynamics of the shear layers in the wake. When forcing is stopped, the wake naturally relaxes to the initial lateral asymmetric state and the wake reversal is captured. With this method, wake reversals are more easily captured. In addition, as the wake is relaxed and not triggered by the forcing to realize the reversal, it results in a reversal with similar dynamics described in §4.6 and base drag evolution described in §4.4. PIV characteristics for the wake reversals captured by each method are summarized in table 4.1. The typical wake reversal experiment captures around 5 s of flow during which a reversal of ~ 0.5 s separates ~ 2 s of flow in both lateral asymmetric states. In addition the flow locked only in asymmetric states has also been captured with the body yawed at $\beta = 0.7$ deg as in the triggered wake reversal experiments. As discussed in Chapter 2, the PIV setup allows to resolve the flow at scales $\theta_0/2$ and $St_{\theta_0}/2$ where θ_0 and St_{θ_0} are respectively the spatial and time scales of the initial shear layer instability at separation.

4.3 Wake flow sensitivity : asymmetries and base drag

The focus is first put on the sensitivity of the wake asymmetries to perturbations to discuss their relation to the base drag of the Ahmed body. The asymmetry is characterized by the mean base pressure distributions in figure 4.2(a) and by the probability density function of the base center of pressure (CoP) position $\mathcal{P}(y_b, z_b)$ in figure 4.2(b). In this section, to investigate the asymmetry/drag relation in a statistical sense, all configurations are investigated over 15 minutes experiments using the pressure scanner and signals are low-pass filtered at 10 Hz to focus on the slow dynamics of wake reversals.

4.3.1 Vertical equilibrium

The vertical balance of the wake is studied by adding the passive perturbing cylinders. We present in figure 4.2 a bifurcation scenario from a wall-normal steady asymmetry of the wake ((i) named top state **T**) to a lateral bi-modal asymmetry ((ii), (iii) and (iv) between lateral asymmetric states named **L** and **R**) and to then a reversed vertical steady asymmetry ((v) named bottom state **B**) depending on the size and position of the perturbation used. Similar bifurcation scenario has been observed by Barros *et al.* (2017) with various kind of perturbations or by Bonnavion & Cadot (2018) with changes in pitch of a similar body. Interestingly, for configurations with small or

[2]Here this angle is chosen as $\beta = 0.7$ deg. which is slightly higher than the value needed to permanently lock the lateral asymmetry as shown in figure 4.4 without having an noticeable influence on the flow around the body itself.

[3]In terms of amplitude, $V_{j_{\max}} \sim 0.6U_0$ and $V_{j_{\text{eff}}} \sim 0.2U_0$.

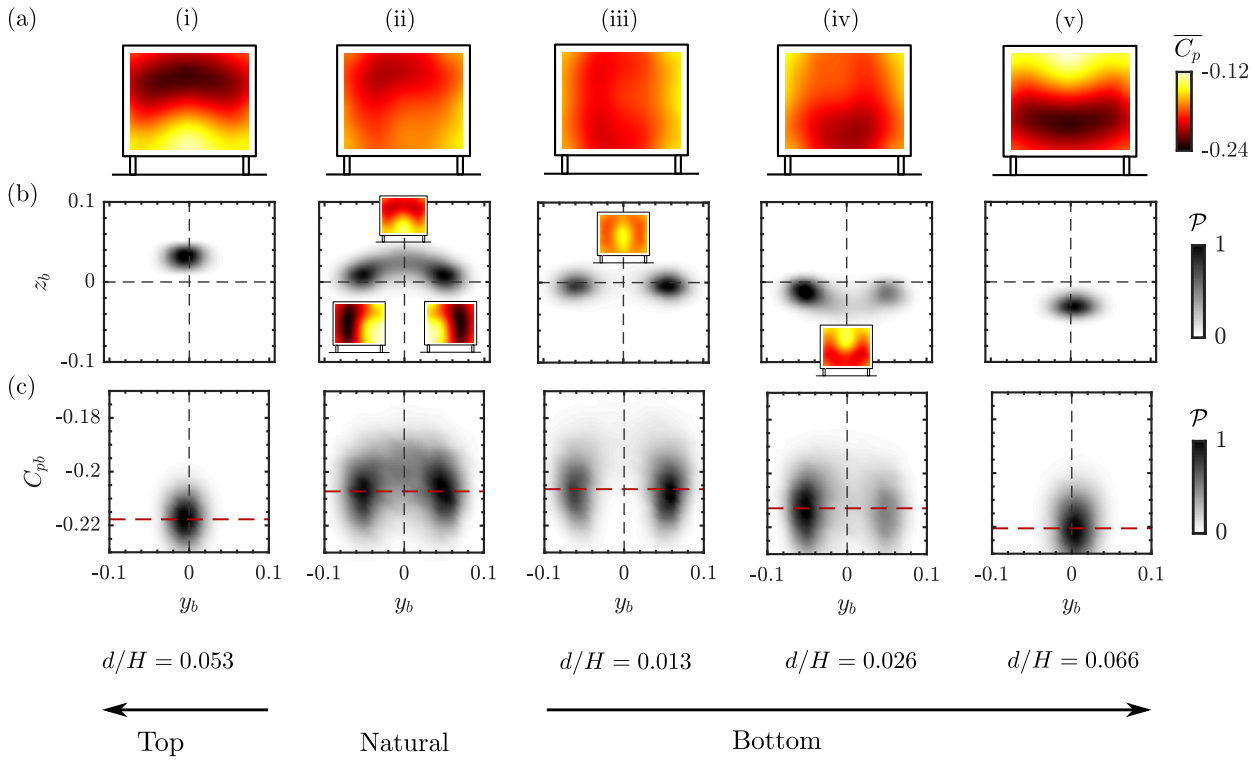

Figure 4.2: Sensitivity of the wake to different vertically-perturbed conditions. The arrows at bottom indicate where the perturbation is placed and points towards increasing diameter size d. Natural unperturbed case, $d/H = 0.053$ on top and $d/H = \{0.013, 0.026, 0.066\}$ on bottom. (a) Time-averaged base pressure coefficient distribution $\overline{C_p}$ on the base. (b) Probability density function (pdf) of the base pressure barycenter position $\mathcal{P}(y_b, z_b)$ normalized by its maximum value. Inserts represent the conditional average of the different wake states for non-static asymmetries. Thin black dashed lines denote the $y_b = 0$ and $z_b = 0$ axes. (c) Pdf of the lateral base CoP position and the space-averaged base pressure coefficient $\mathcal{P}(y_b, C_{pb})$ normalized by its maximum value. Red horizontal dashed lines indicate the time-averaged $\overline{C_{pb}}$ value in the different cases.

vanishing vertical asymmetry, the transition between the two preferred lateral asymmetric states does not occur through the same state. For vanishing vertical asymmetry, the transiting state is a perfectly symmetric state whereas as soon as vertical asymmetry is perturbed, the wake reversal occurs through a vertical asymmetric state (as shown on the conditional-averaged base pressure distribution inserts of (ii) and (iv)) which is close to the static vertical asymmetric state. The wake reversal dynamics depend on the degree of vertical asymmetry, not only because it selects a vertical asymmetric transient state, but also because the exploration of the transient state is changed. It has been checked that both the characteristic time-scale of the wake reversals and the frequency of exploration of vertically asymmetric transient states are greater than for the vertical symmetric state. This might be explained by these vertically asymmetric states being less unstable than the perfectly symmetric state as they are very close to the **T** and **B** states in terms of asymmetry.

In figure 4.2(c), we show the relation between the dynamics of the asymmetries and the base pressure coefficient C_{pb}. quantifying the base drag of the body by examining their joint probability density function $\mathcal{P}(y_b, C_{pb})$. The interesting aspect here is that in presence of wake reversals (flows (ii), (iii), (iv)), the transient wake state between the two lateral symmetry-breaking states is always characterized by less base drag no matter its vertical asymmetry. The vertical asymmetry still has an influence on the amount of base drag reduction relatively to the **L** or **R** state which varies from 5 to 9 % for the vertically asymmetric and symmetric transient states respectively.

The evolution of mean base drag $-\overline{C_{pb}}$ (and of mean total drag $\overline{C_D}$ for selected cases) depending on the mean vertical asymmetry is shown in figure 4.3 (a). It corroborates the fact that the wake vertically balanced and laterally bi-modal (iii) has the less base drag. As the vertical asymmetry is locked, base drag is increased and reaches its highest values. This aspect is consistent with what was suggested by Bonnavion & Cadot (2018) with pitch variations of the Ahmed body. It

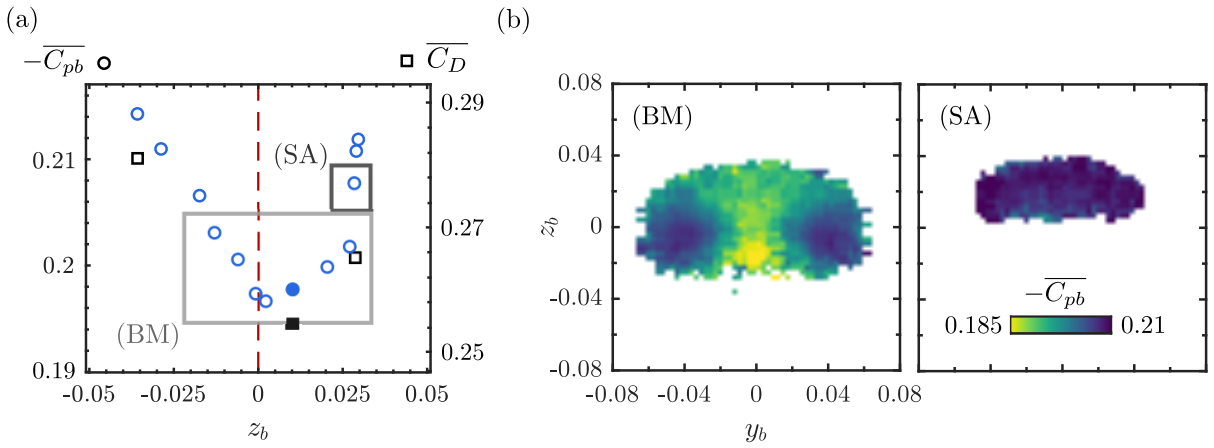

Figure 4.3: Sensitivity of the base drag $-C_{pb}$ of the model to vertically-perturbed conditions. (a) Evolution of the time-averaged base drag $-\overline{C_{pb}}$ with the mean vertical position of the base pressure barycenter $\overline{z_b}$. Total drag $\overline{C_D}$ is indicated by square symbols for selected configurations (see text for details about the correction method to subtract the contribution of the cylinder). Filled symbols represent the natural unperturbed wake. (b) Conditionally-averaged base drag $-C_{pb}$ as function of the instantaneous base pressure barycenter position (y_b, z_b). (BM) represents lateral bi-modal wakes highlighted by the light grey rectangle in (a). (SA) is the first vertical static symmetry-breaking wake obtained with a $d/H = 0.026$ perturbation placed on top.

should be noted that these results have been reproduced for different position of the perturbations ($x/H = -1$ in addition to the $x/H = -2$ case studied here) and that the conclusions are robust. In addition, base drag results are confirmed by the $\overline{C_D}$ evolution. As the cylinders are put directly on the body, the aerodynamic balance measures also the drag exerted on the cylinder itself. To correct for this and have a fair estimation of the drag of the body only, we follow the studies of Bearman & Zdravkovich (1978) and Zdravkovich (1985) to estimate the drag contribution of the perturbing cylinder on the wall. A C_D value of 0.5 for such flows leads to the body drag estimations provided on figure 4.3(a) which are corroborating the base drag evolution.

We further assess the peculiar low drag state of the transient states during wake reversals of all type in figure 4.3(b). Wake configurations are gathered in two groups. The first group denoted as (BM) gathers all lateral bi-modal configurations no matter their mean vertical asymmetry; the second one named (SA) is composed by the first configuration locked in the **T** asymmetric state only. The multi-conditional averaged base drag depending on the full CoP position (y_b, z_b) is given for each group. For (BM) two distinct zones are appearing : the two lateral symmetry-breaking states **L** and **R** with high base drag and all the transient states with low base drag and a minimum for the vertically balanced transient state. For equivalent degree of vertical asymmetry, the static asymmetry (SA) presents around 7 % more base drag than the transient vertically-asymmetric state. This implies that base drag is not only related to the degree of asymmetry, but also to the very transient nature of the asymmetric state suggesting the different flow organization for these two similar states. We show in the next section the difference in recirculating flow organization explaining these observations.

4.3.2 Lateral equilibrium

Similarly to vertical symmetry perturbations, we can assess the sensitivity of the wake to lateral symmetry perturbations by small changes in the yaw angle β of the model, as was also done by Cadot *et al.* (2015) or Bonnavion & Cadot (2018). The results of this sensitivity study are presented in figure 4.4 where both the evolution of the lateral position of the CoP and the base drag are investigated. To perform this sensitivity study, the wake with vanishing mean vertical asymmetry is selected, the one perturbed on bottom by a cylinder $d/H = 0.013$.

The wake is permanently locked in the lateral asymmetric state **R** for relatively small yaw perturbations of $\beta \sim 0.5$ deg after the wake started gradually to less explore the **L** state. This justifies the value $\beta = 0.7$ deg chosen to lock the wake in a lateral asymmetry for the wake reversal

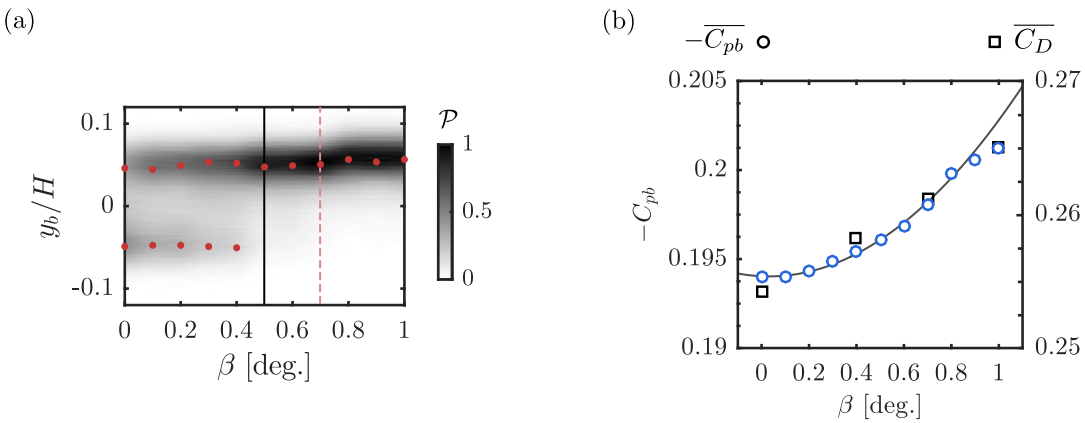

Figure 4.4: Sensitivity of the wake to small change in yaw angle β. (a) Evolution of the pdf of the lateral position of the base pressure barycenter $\mathcal{P}(y_b, \beta)$. Red dots highlight the most probable values, the vertical full line the threshold for static lateral symmetry-breaking and the dashed one the yaw angle used to statically lock the wake in the wake reversal experiments. (b) Evolution with yaw of the base drag and total drag for selected cases. The full gray line is a quadratic fit of $-\overline{C_{pb}}(\beta)$ for small yaw angles $\beta \leqslant 0.8$ deg.

experiments in the next section. Conversely, the base drag is gradually increased as the wake locks in the **R** state. A quadratic increase of the base drag is observed until $\beta = 0.8$ deg in agreement with the induced drag formalism linked to cross-flow forces introduced by Grandemange *et al.* (2014*b*). However, the total drag has a more linear evolution with β suggesting the different correlation values between base drag and drag found by Barros *et al.* (2016*b*) and Li *et al.* (2019) for the Ahmed body respectively aligned and yawed at $\beta = 5$ deg.

4.4 Conditional and phase-averaged description of near-wake reversals

Now that the global relation between drag and wake asymmetries has been characterized, the main mechanisms of asymmetries-related drag are distilled in this section. To this purpose, the lateral wake reversal experiments are analysed here. All wake reversal discussed in the remainder are those occurring on the wake with vanishing mean vertical asymmetry, the one perturbed on bottom by a cylinder $d/H = 0.013$.

First, conditional and phase-averaged description of the wake reversal events are presented. Based on the instantaneous lateral position of the base CoP y_b, three distinct states of the wake are objectively defined. Contrary to conventional conditional-averaging methods used to statistically characterize the asymmetries in the Ahmed body wake (Grandemange *et al.*, 2013*b*; Li *et al.*, 2016) which are only based on threshold values of the wake position, here we combine this approach with the use of the time-series of y_b to identify reversal events. The transient symmetric state $\mathbf{S}_{\mathrm{tr}}$ is defined as the transient period between the two lateral asymmetric states **L** and **R** and is identified both using the following criterion. The beginning of the $\mathbf{S}_{\mathrm{tr}}$ state occurs once the lateral position of the base CoP has crossed a threshold value of ± 0.025 (depending on the direction of the wake reversal) and remains in the threshold band $[-0.025; 0.025]$ for a sufficiently long time (typically 10 convective time units). This insures that only effective wake reversals are accounted for and not random explorations of a symmetric state due to high turbulent fluctuations. Then the whole period until y_b goes out of the threshold band for sufficiently long time to qualify it as permanent defines the whole $\mathbf{S}_{\mathrm{tr}}$ state. From this definition, lateral symmetry-breaking states are defined as all the rest of the time-series depending on the sign of y_b (< 0 for **L** and > 0 for **R**). It thus defines long time intervals associated to long-time dynamics of the wake rather than only looking at instantaneous lateral positions of the wake. The threshold value -0.025 is chosen based on the average absolute fluctuations of y_b around the most probable $y_b = \pm 0.04$ value. It should be noted that the conditionally-averaged results presented from then on are quite insensitive to small variations of this threshold value.

An example of this conditional decomposition of the different states is given in figure 4.5. In

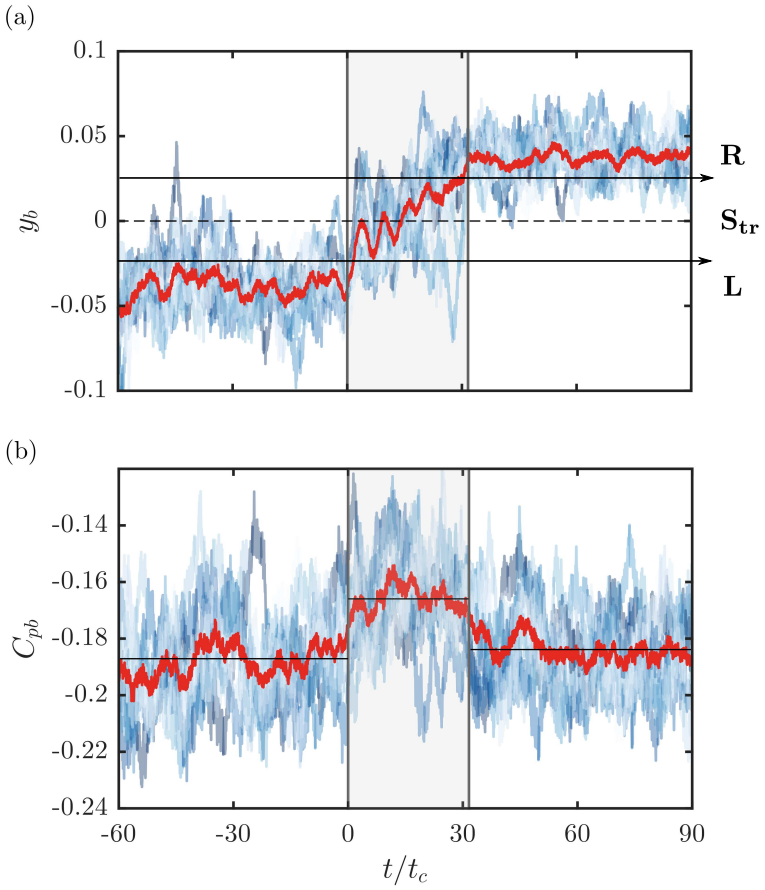

Figure 4.5: Ensemble-averaged evolution with time of (a) the lateral position of the base pressure barycenter y_b, and (b) the base drag C_{pb} for the 12 triggered wake reversals. Blue shades are all the different realizations and red lines indicate the ensemble-average. The lateral asymmetric wake states are defined as **R** for $y_b > 0$ and **L** for $y_b < 0$. The symmetric transient state $\mathbf{S}_{\text{tr}}$ is defined using threshold values indicated by the two horizontal full lines during the transient wake reversal indicated by the gray area.

order to give a statistical description of the wake reversal event, the ensemble- or phase-averaged wake reversal from all the triggered experiments is used in figure 4.5. By defining the middle of the wake reversal event as the time of vanishing lateral asymmetry, all the realizations can be ensemble- or phase-averaged to provide a statistical wake reversal. The wake reversal of typical duration ~ 30 convective time-units $t_c = W/U_0$ is characterized by a quite linear evolution of y_b between the two opposite lateral symmetry breaking states **R** and **L**. In terms of base drag C_{pb} whose evolution is given in figure 4.5(b), as discussed in the previous section, the wake reversal is characterized by lower base drag of around 9 % compared to states **R** and **L**. Interestingly, the base pressure recovery is quite pronounced during the whole transient and does not seem directly correlated to the degree of instantaneous lateral asymmetry of the wake. This aspect goes in the sense of an importance of the transient nature of the wake during the reversal on the base drag.

The mean flow of the conditional states is presented in figure 4.6. They are obtained using both the natural and triggered wake reversals. To allow for a fair comparison of the transient symmetric state $\mathbf{S}_{\text{tr}}$ and discuss the implications of the transient nature of the state, a static symmetric state **S** is defined as the average of lateral symmetry-breaking states **L** and **R**. The mean characteristics of these wakes like the recirculation length $L_r = \max_x(u_x < 0)$ are provided in table 4.2. The differences between the different wake states are not very pronounced except for the asymmetry of the lateral symmetry-breaking state (only **R** state is shown, **L** state is obtained by a mirror symmetry $y \to -y$). Small differences in recirculation length can be noticed, the length in the $\mathbf{S}_{\text{tr}}$ state being increased by around 2 % which is consistent with the base drag decrease observed

State	$\overline{C_{pb}}$	L_r/H
$\mathbf{S}_{\mathrm{tr}}$	-0.167	1.60
R	-0.184	1.58
S	-0.184	1.58

Table 4.2: Mean features of each wake state based on all the natural and triggered wake reversals. L_r is the mean recirculation length.

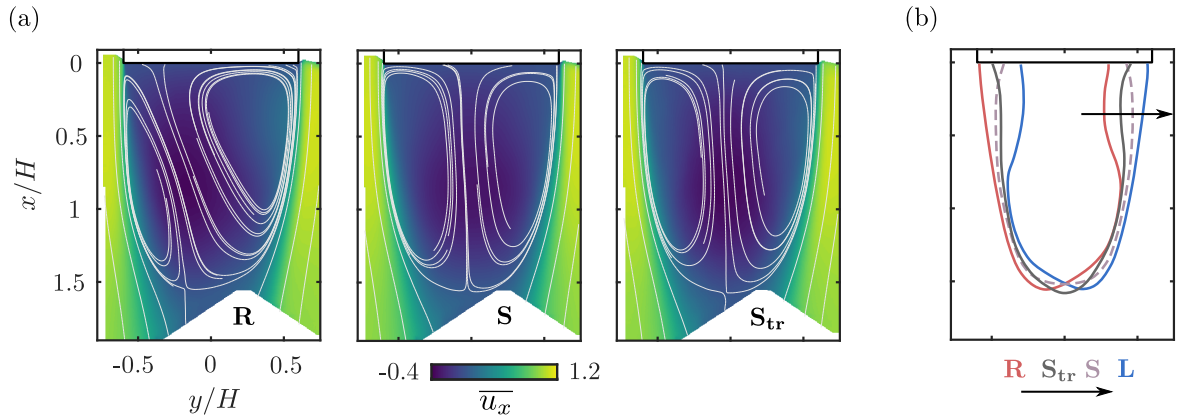

Figure 4.6: Conditionally-averaged mean wake. (a) Mean streamwise velocity $\overline{u_x}$ with mean streamlines superimposed in white. State **L** is not shown for brevity, it is obtained from state **R** by planar symmetry relative to the $y = 0$ plane. (b) Mean recirculation region defined as the iso-contour $\overline{u_x} = 0$ for each state. See the text for the definition of the symmetric state **S**.

(Bearman, 1967; Mariotti *et al.*, 2015; Grandemange *et al.*, 2013*a*; Lorite-Díez *et al.*, 2020).

More fundamental differences can be noticed when examining the Reynolds stresses in the wake as shown in figure 4.7. By definition for each state, the Reynolds stresses $\overline{u'_x u'_y}$ and $\overline{u'_y u'_y}$ are estimated by fluctuations around the mean velocity of this state. For the static symmetric state **S** it results in the average between the fluctuations around the **R** and **L** states. Comparison between the symmetric static and transient states **S** and $\mathbf{S}_{\mathrm{tr}}$ show a clear damping of the Reynolds stresses in each shear-layer along the separatrix, especially for the $\overline{u'_y u'_y}$ component. Only around the saddle point closing the separation bubble are the latter higher for the transient state. From the streamwise profiles of maximum Reynolds stresses along each side of the separatrix, in the $\mathbf{S}_{\mathrm{tr}}$ state the Reynolds stresses are damped along the whole separatrix without exception. The $\overline{u'_x u'_y}$ component is damped at maximum by ~ 15 % and the $\overline{u'_y u'_y}$ component by ~ 25 %. The $\overline{u'_x u'_x}$ component (not shown here for conciseness) is only more moderately damped. The streamwise increase rate of shear stresses along the separatrix starts to differ amongst all wake states and sides of the wake only after $x \sim 0.2$. This important point is further investigated in the next section. For 2D bluff body flows, the streamwise momentum balance on the contour delimited by the mean separatrix and the base of the body of Balachandar *et al.* (1997) reads

$$\overline{C_{pb}}W = 2\int_{\text{separatrix}} \overline{u'_x u'_x}(\mathbf{n}\cdot\mathbf{x})ds + 2\int_{\text{separatrix}} \overline{u'_x u'_y}(\mathbf{n}\cdot\mathbf{y})ds + \int_{\text{separatrix}} \overline{C_p}(\mathbf{n}\cdot\mathbf{x})ds \tag{4.1}$$

where n is a vector normal to the mean separatrix. In addition, the pressure term in the right-hand side of 4.1 can also be viewed through the normal momentum balance introduced by Bradshaw (1973)

$$\frac{\partial \overline{C_p}}{\partial n} = 2\kappa \overline{u_s}^2 - 2\frac{\partial \overline{u'_n u'_n}}{\partial n} \tag{4.2}$$

where u_s and v_n are the tangential and normal velocities and κ the local curvature of the separatrix. Along the developing shear layers composing the separatrix, $\overline{u'_y u'_y}$ is the dominant contribution to $\overline{u'_n u'_n}$. Following this analogy, the Reynolds stresses have a key role in the equilibrium of the recirculation region by acting on both the pressure gradients along its boundary and the fluctuating

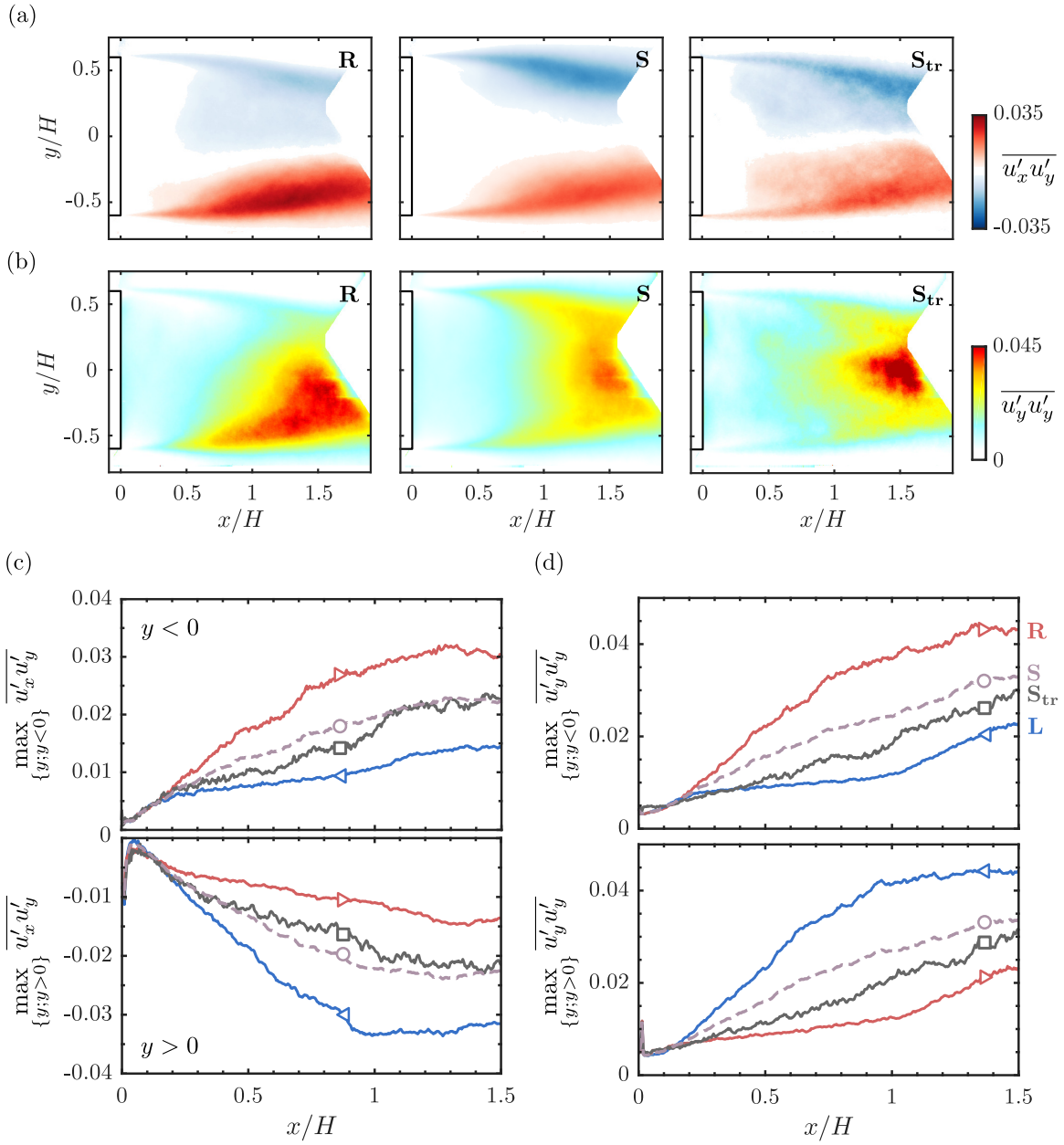

Figure 4.7: Conditionally-averaged mean Reynolds stresses for the different wake states. (a) Streamwise-lateral component $\overline{u'_x u'_y}$ and (b) lateral-lateral component $\overline{u'_y u'_y}$. (c,d) Streamwise profiles of maximum of Reynolds stresses $\overline{u'_x u'_y}$ and $\overline{u'_y u'_y}$ for each side of the wake ($y > 0$ or $y < 0$). See the details in the text for the exact definition of the velocity fluctuations for each state.

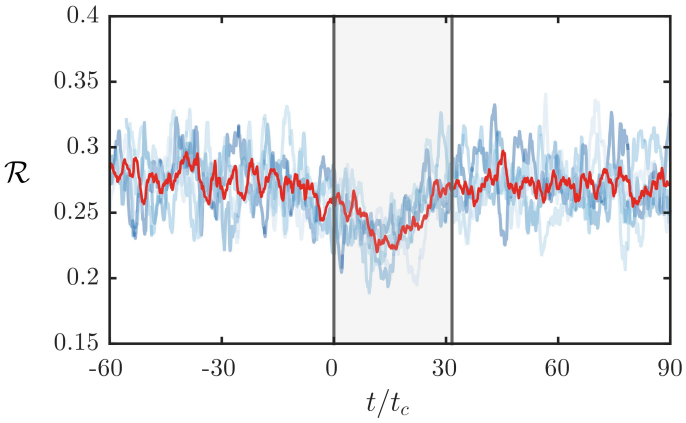

Figure 4.8: Ensemble-averaged evolution with time of the recirculation intensity $\mathcal{R}$ for the 12 triggered wake reversals. Blue shades are all the different realizations and red lines indicate the ensemble-average. The lateral asymmetric wake states are defined as $\mathbf{R}$ for $y_b > 0$ and $\mathbf{L}$ for $y_b < 0$. The transient wake reversal is indicated by the gray area.

momentum entrained inside. The strong damping of these shear stresses observed in figure 4.7 for the transient symmetric state $\mathbf{S}_{\text{tr}}$ is directly related to the reduced base drag observed during the wake reversals.

As the Reynolds stresses along the separatrix are greatly reduced during the wake reversal, it has also important consequences on the flow entrainment and engulfment inside the recirculation region. To quantify the intensity of the recirculating flow, the quantity $\mathcal{R}$ is introduced as

$$\mathcal{R} = \iint_{\{\mathbf{x};u_x<0\}} ||\mathbf{u}||dS. \tag{4.3}$$

The phase-averaged evolution of $\mathcal{R}$ from all the triggered wake reversals is shown in figure 4.8. An important drop of the recirculation region intensity occurs during the wake reversal period where $\mathcal{R}$ is reduced by ~ 15 %. Contrary to the change in base drag presented in figure 4.5(b), the drop in recirculation intensity is only important in the central part of the wake reversal period with a gradual decrease and increase respectively at the beginning and at the end of the wake reversal event. This drop in recirculation intensity can be associated with a transient disorganization of the recirculation region and thus a pressure recovery in the low pressure toroidal structure in the wake (Lucas *et al.*, 2017; Dalla Longa *et al.*, 2019). The transient disorganization of the wake is further investigated in the next section in order to unravel the flow mechanisms involved in asymmetry-related drag.

4.5 Near-wake coupled dynamics in asymmetric states

4.5.1 Coherent dynamics of the wake

To further discuss the origin of the reduced base drag during the wake reversals associated with damped shear-layers dynamics and weakened recirculation region, the wake dynamics for asymmetric states are investigated in detail.

First the dynamics of the recirculation region are investigated in figure 4.9. In (a), an example of the detection of the recirculation region $\{\mathbf{x}; u_x < 0\}$ is given in each of the three states $\mathbf{L}$, $\mathbf{S}_{\text{tr}}$ and $\mathbf{R}$ during a natural wake reversal realization. The supplementary movie 1 provides the velocity and lateral CoP dynamics for this natural wake reversal. To get insight about the dynamics of this recirculation region, premultiplied spectra of the recirculation intensity $\mathcal{R}$ and the recirculation region area

$$\mathcal{A} = \iint_{\{\mathbf{x};u_x<0\}} dS. \tag{4.4}$$

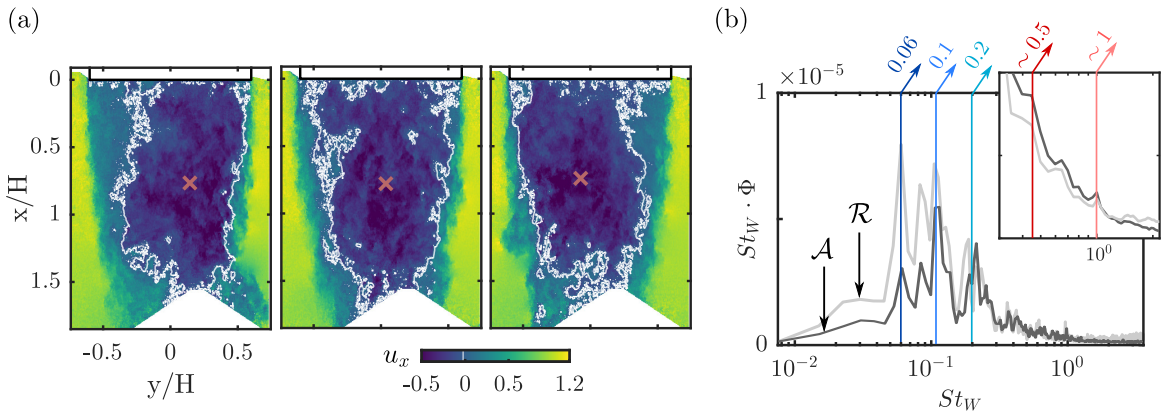

Figure 4.9: Dynamics of the recirculation region. (a) Instantaneous recirculation region in white contour and position of the wake momentum deficit barycenter indicated by the red cross. Snapshot are taken in the states **L**, $\mathbf{S}_{\text{tr}}$ and **R** from left to right respectively. (b) Premultiplied spectra of the recirculation intensity $\mathcal{R}$ and the recirculation area $\mathcal{A}$ when the wake is locked in the asymmetric state **R**. Vertical arrows indicate the dominant dynamics.

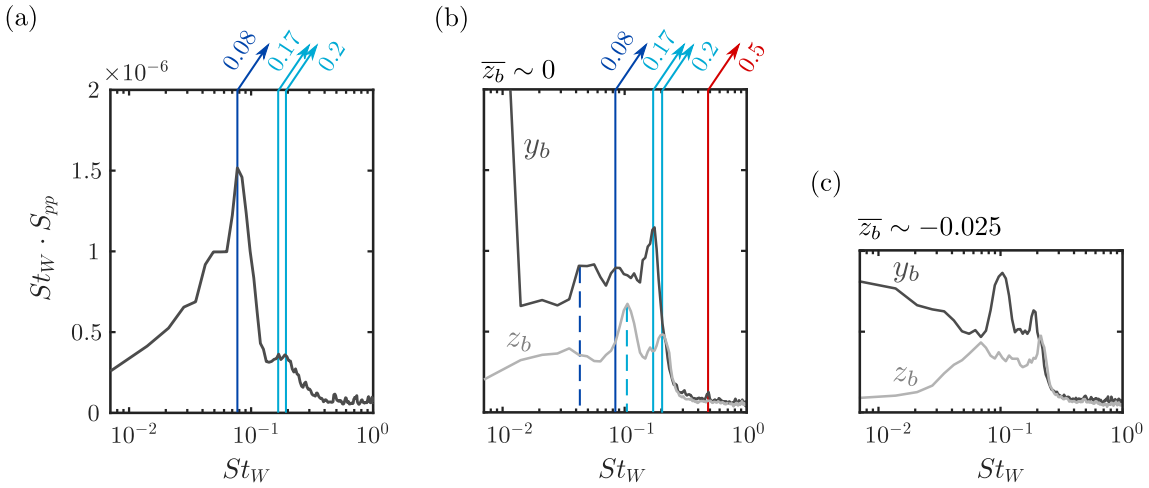

Figure 4.10: Dynamics of the base pressure from long-time experiments. Premultiplied spectra of (a) the base drag C_{pb} and (b) the lateral y_b and vertical z_b position of the base CoP. (c) Similar as (b) but for a wake locked in the vertical asymmetric state **B**. Vertical arrows indicate the dominant dynamics. Vertical dashed lines indicate subharmonic dynamics of the identified dominant dynamics. Attention is especially drawn on the changes in the dynamics of y_b and z_b at $St_W \sim 0.5$ between (b) and (c).

are shown on figure 4.9 for the wake locked in the **R** state. Both spectra highlight the presence of dominant coherent dynamics at several characteristic $St_W = fW/U_0$. Low frequency dynamics at $St_W = 0.06$ are particularly active on the recirculation intensity $\mathcal{R}$. These dynamics are usually associated with a pumping of the recirculation region leading to its shrinking and expansion as shown by Berger *et al.* (1990) in the wake of a normal disk and as discussed by Khalighi *et al.* (2001), Volpe *et al.* (2015) or Dalla Longa *et al.* (2019) in 3D blunt body wakes. Global vortex shedding dynamics studied in detail by Grandemange *et al.* (2013*b*) are also quite active at $St_W \sim 0.2$. More interestingly, the shrinking and expansion dynamics of the recirculation region, which are naturally linked with variations of $\mathcal{A}$ are rather dominated by the sub-harmonic of the lateral vortex shedding at $St_W \sim 0.1$. In general, these dynamics seem to be governed by quite complex non-linear interactions between the rather similar time-scales of the bubble-pumping and its first harmonic and vortex shedding and its subharmonic. At higher frequencies, peculiar coherent dynamics can also be seen at $St_W \sim 1$ and its subharmonic $St_W \sim 0.5$. These higher frequency dynamics are more likely related to the shear-layers surrounding the recirculation region and are thus of particular interest to explain the different Reynolds stresses statistics presented in the previous section.

Similar coherent dynamics are dominating the position of the base CoP as shown in figure

4.10(a,b). The only additional aspect is the high spectral energies in y_b at really low frequencies characteristic of the bi-modal dynamics. Spectra with longer time windows for the psd estimation reveal better these very low frequency dynamics (Grandemange *et al.*, 2013*a*), but here we focus on resolving and converging the higher frequency part of the spectra. Here a clear distinction can be made between lateral and vertical global vortex shedding dynamics at $St_W = 0.17$ and 0.2 appearing respectively on y_b and z_b. The ratio between these two frequencies corresponds to the ratio H/W. Flow dynamics at $St_W \sim 0.5$ are still appearing on the position of the CoP but not the higher one at $St_W \sim 1$, which is quite expected as the shear-layers have low direct imprint on the base pressure. Interestingly, the dynamics at $St_W \sim 0.5$ appear also on y_b but not on z_b. As this wake has vertical vanishing asymmetry and only lateral bi-modal dynamics, one can wonder what happens to this shear-layer signature at $St_W \sim 0.5$ when the direction of wake asymmetry is changed. To discuss this, figure 4.10(c) shows the spectra of the CoP position for the wake locked in the vertical asymmetric state **B**. The dynamics at $St_W \sim 0.5$ are quite mitigated on y_b compared to the lateral bi-modal wake, and conversely the one on z_b are relatively more pronounced. This change of direction in the dynamics is thus directly related to the change of wake asymmetry direction.

To gain further insight in these peculiar wake dynamics spectral proper orthogonal decomposition of the flow (SPOD) of the flow is performed as proposed by Lumley (1970) and Towne *et al.* (2018). This form of proper orthogonal decomposition allows to identify energy-ranked modes that each oscillate at a single frequency, are orthogonal to all other modes at the same frequency and, as a set, optimally represent the space-time flow statistics. To calculate the SPOD, first the flow state vector $\mathbf{q} = [u_x, u_y]^T(x, y, t)$ is arranged in n segments of n_f instantaneous snapshots $\mathbf{Q} = [\mathbf{q}^{(1)}\mathbf{q}^{(2)} \cdots \mathbf{q}^{(n)}]$ which are considered to be independent realizations of the flow. Then the discrete Fourier transform of $\mathbf{Q}$ is performed along the time dimension which yields the ensemble of Fourier flow realizations $\hat{\mathbf{Q}} = [\hat{\mathbf{q}}^{(1)}\hat{\mathbf{q}}^{(2)} \cdots \hat{\mathbf{q}}^{(n)}]$. For a given frequency f, the SPOD modes are finally obtained as for a direct space POD problem as a solution of the linear problem

$$\hat{\mathbf{S}}_\mathbf{f}\mathbf{\Psi}_\mathbf{f} = \mathbf{\Psi}_\mathbf{f}\mathbf{\Lambda}_\mathbf{f}. \tag{4.5}$$

Here $\hat{\mathbf{S}}_\mathbf{f}$ is the cross-spectral density matrix $\hat{\mathbf{S}}_\mathbf{f} = \hat{\mathbf{Q}}_\mathbf{f}\hat{\mathbf{Q}}_\mathbf{f}^*$ (where the superscript * denotes the Hermitian transpose) at a given frequency, $\mathbf{\Psi}_\mathbf{f} = [{\psi_\mathbf{f}}^{(1)}{\psi_\mathbf{f}}^{(2)} \cdots {\psi_\mathbf{f}}^{(n)}]$ are the eigenvectors of the problem or SPOD modes, and $\mathbf{\Lambda}_\mathbf{f} = \mathrm{diag}(\lambda_f^{(1)}, \lambda_f^{(2)}, \cdots, \lambda_f^{(n)})$ the associated eigenvalues in a decreasing value order. Here the SPOD is performed on two different realizations of the wake flow locked in the **R** state totalizing approximately 5000 snapshots. The time-series are divided in blocks of $n_f = 250$ or 500 snapshots (corresponding respectively to $\sim 30t_c$ and $\sim 70t_c$) with 50 % overlap to yield $\mathbf{Q}$, which results in respectively $n = 20$ and 40 SPOD modes. The choice of the segments length is motivated by a trade-off between the resolution of low frequencies (for which longer segments are used) and the good convergence of higher frequencies (for which more and shorter segments are used).

The results of the SPOD are provided in figure 4.11. As at all frequencies below $St_W \sim 1$ the first SPOD mode is rather dominant in terms of energy, we characterize globally this dominance by evaluating the energy ratio of all the i^{th} modes over all frequencies $\int_f \lambda_f^{(i)} df / \sum_i \int_f \lambda_f^{(i)} df$ in figure 4.11(a). In average, the first mode is around twice as energetic as the second one. When looking at the premultiplied spectrum[4] of the SPOD eigenvalues at each frequency for the first modes $St_W \cdot \lambda_{St_W}^{(1)}$, the same dominant flow dynamics are appearing as those spotted previously. The SPOD modes associated to these dominant eigenvalues are presented in figure 4.11, which gives valuable information about the spatial support of these specific time-dynamics. The vortex shedding mode appearing as vortex loops emanating from one side of the wake are quite in line with the conceptual description of this global mode in presence of lateral asymmetries which was proposed by Grandemange *et al.* (2013*b*). As expected from the literature, the low frequency bubble-pumping mode is involving the whole recirculating region. In particular, it underlines

[4]There is no real frequency spectrum of the SPOD eigenvalues as a proper orthogonal decomposition is performed separately at each frequency. However, when looking for a given mode number the energetic content at each frequency gives valuable qualitative information about the dominant dynamics of the flow.

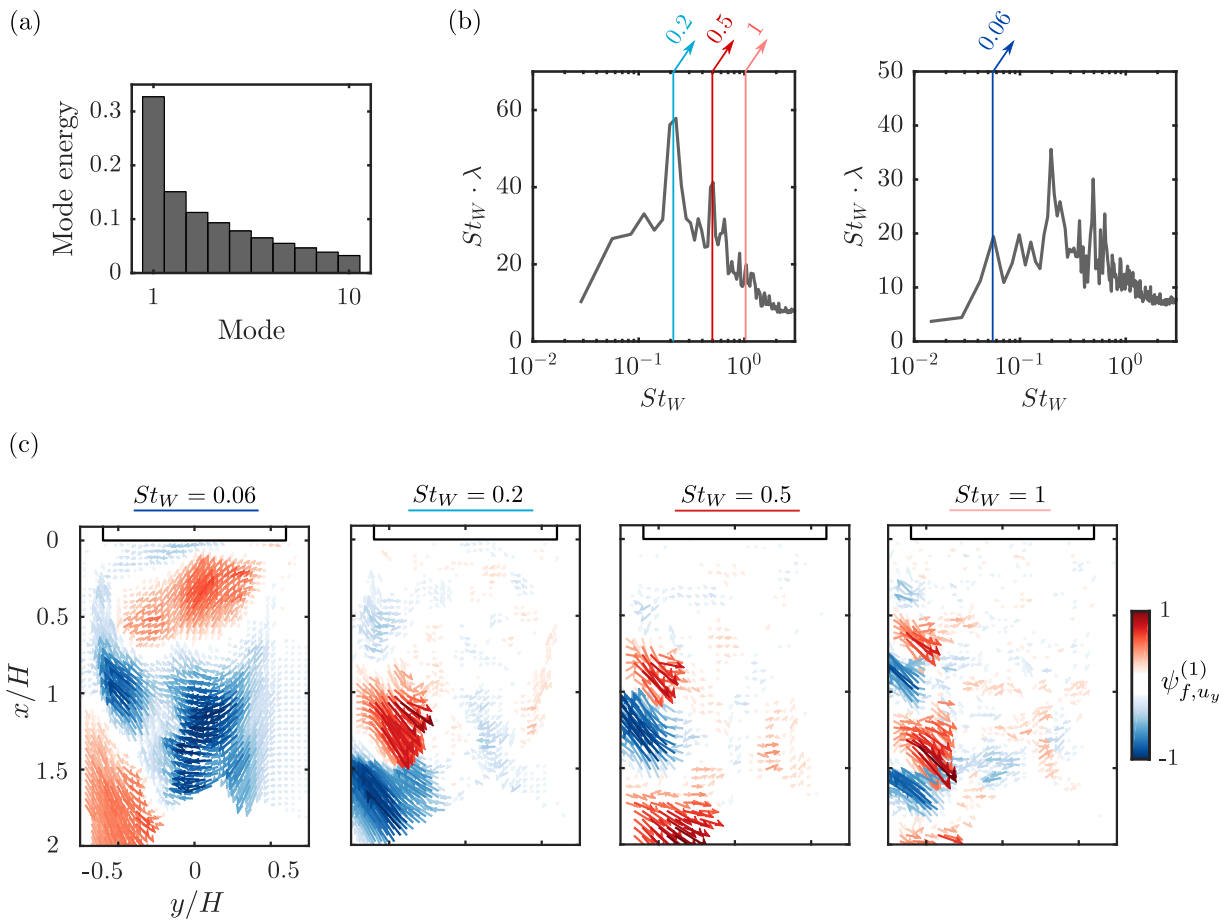

Figure 4.11: Spectral proper orthogonal decomposition (SPOD) of the velocity field for the wake locked in the lateral asymmetric state **R**. (a) Energy ratio of the 10 first modes spectra $\int_f \lambda_f^{(i)} df / \sum_i \int_f \lambda_f^{(i)} df$. (b) Premultiplied spectrum of the first SPOD modes eigenvalues $\lambda^{(1)}_{St_W}$. Different temporal window sizes are used for the Fourier transform estimation. A window of $\sim 30 t_c$ is used on left to converge the estimation at high St_W, and a window of $\sim 70 t_c$ is used on the right to resolve the dominant low St_W dynamics. Dominant dynamics are highlighted by colored vertical arrows in relation the ones of figures 4.9 and 4.10. (c) Spatial organization of the dominant dynamics. Vector field of the first mode at the given frequency $\psi^{(1)}_{St_W}$ colored by the lateral velocity component u_y. Only every tenth vector is shown in each direction for clarity.

the dominant recirculating flow coming from the right shear-layer ($y > 0$) and interacting with the opposite shear-layer ($y < 0$) when the wake is in the **R** state. The localization of the high frequency modes at $St_W \sim 0.5$ and 1 in the left shear-layer appears in relation to the interaction of the recirculating flow with this shear-layer. These two modes show up as large vortex loops dominating the shear-layer which are at the origin of the important Reynolds stresses from figure 4.7 found on the same side of the wake in the **R** state. These coherent structures are yielding a strong engulfment of fluid inside the recirculating region. The streamwise appearance of these two modes is also of particular interest. The SPOD mode at $St_W \sim 1$ originates around the location where the low-frequency mode interacts with this shear-layer and where the discrepancies in the streamwise growth rate of the lateral shear-layers are starting around $x/H \sim 0.25$ depending on the asymmetry of the wake as discussed previously. The $St_W \sim 0.5$ mode only develops at a farther streamwise extent which suggests this mode is resulting from a vortex merging process of the harmonic dynamics at $St_W \sim 1$.

A finer analysis of the interaction between the recirculating flow and the shear-layers is provided in figure 4.12. Representative snapshots of the vorticity ω_z in the left shear-layer ($y < 0$) along the velocity vector field in the recirculation region are shown in two different wake states : the wake in the symmetric transient state $\mathbf{S}_{\text{tr}}$ and the wake in the lateral symmetry-breaking **R** state. A

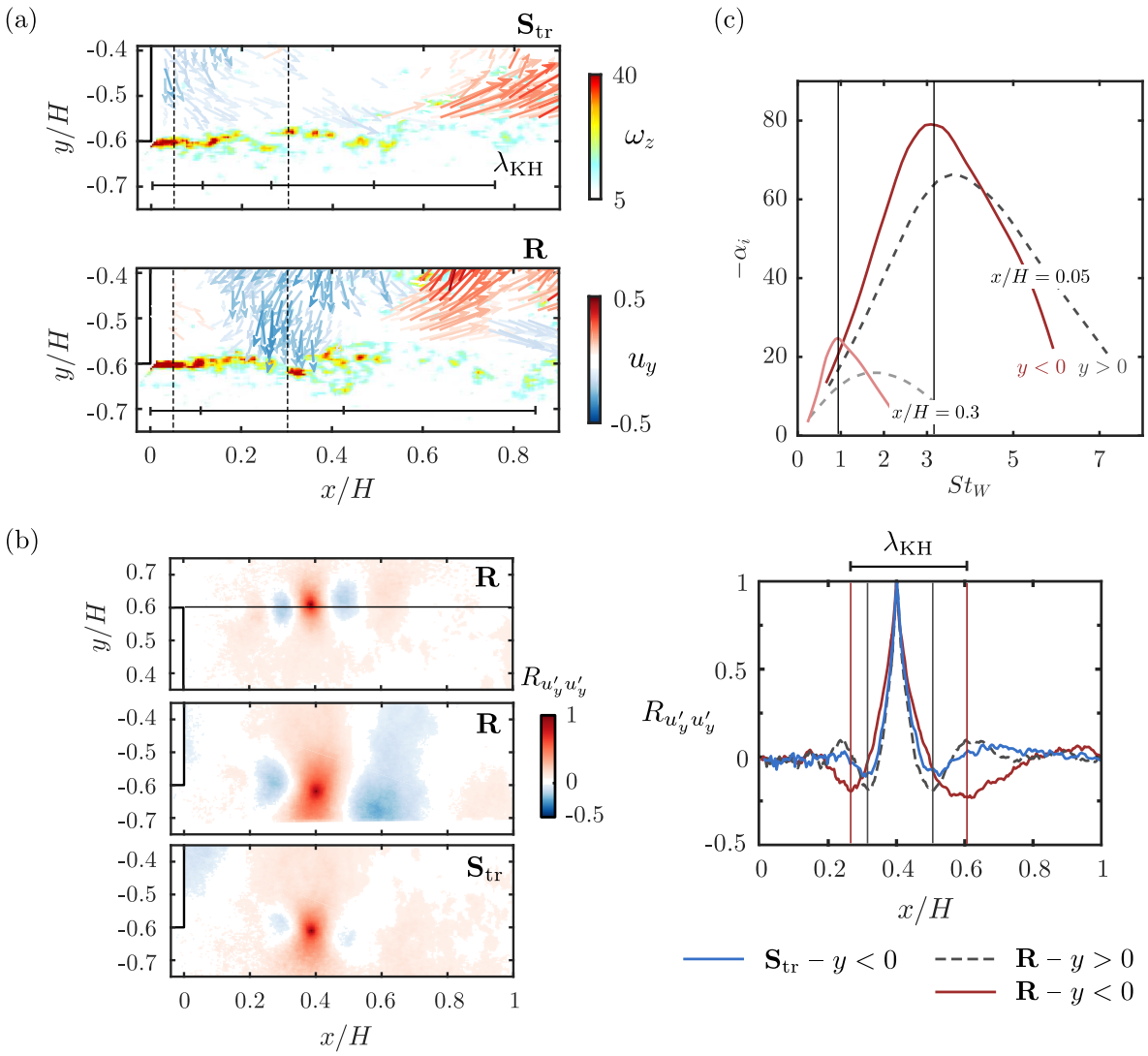

Figure 4.12: Characteristics of the shear-layer roll-up triggered by the interaction with the recirculating flow. (a) Representative snapshots of vertical vorticity ω_z in the shear-layer along the velocity field colored by lateral velocity u_y in the recirculation region : during the wake reversal in the symmetric state $\mathbf{S}_{tr}$ and in the locked lateral asymmetric state $\mathbf{R}$. (b) Spatial correlation of lateral velocity fluctuations $R_{u'_y u'_y}$ for both shear-layers of the asymmetric state $\mathbf{R}$ and for the left shear-layer of the symmetric state $\mathbf{S}_{tr}$. Streamwise profiles are extracted along the horizontal black line at $y/H = \pm 0.6$. (c) Growth rate curves of the most unstable mode obtained from a spatial local linear stability analysis of the mean velocity profiles $\overline{u_x(y)}$ in both shear layers in the locked lateral asymmetric state $\mathbf{R}$. Profiles are extracted right after separation at $x/H = 0.05$ and at the streamwise location of interaction with the recirculating region at $x/H = 0.3$.

clear roll-up of the shear-layer is seen in both cases arising from a Kelvin-Helmholtz-like instability of the shear-layer. However both cases do not exhibit similar length scales λ_{KH} for this roll-up process. The initial Kelvin-Helmholtz wavelength $\lambda_{KH,0} \sim 0.14$ is similar in both cases and, if taking the local shear velocity $0.45U_0$, the associated frequency is $St_W \sim 3.8$ or $St_{\theta_0} \sim 0.023$ which is quite close to the value $0.022 - 0.024$ proposed by Ho & Huerre (1984), Zaman & Hussain (1981) or Morris & Foss (2003) for turbulent free-shear layers originating from turbulent boundary layers. Nevertheless, if the initial instability presents similarities, the further evolution of the shear layer is completely different. In the lateral asymmetric $\mathbf{R}$ state the recirculating flow formed by the right shear layer impacts the left one around a preferred position $x/H \sim 0.3$ and triggers the shear-layer roll-up. The shear-layer behaves like being externally forced by the recirculating region. This leads to the formation of large-scale coherent structures visible in figure 4.12(a) with an apparent $\lambda_{KH} \sim 0.45$ corresponding to $St_W \sim 1.2$. This frequency coincides rather well with the dominant shear layer dynamics identified by the SPOD and in the global dynamics of the

recirculation region. Estimations of the roll-up length-scale λ_{KH} is performed by looking at the normalized spatial correlation of the lateral velocity fluctuations

$$R_{u'_y u'_y}(\mathbf{x}, \mathbf{dx}) = \frac{\overline{u'_y(\mathbf{x}, t) u'_y(\mathbf{x} + \mathbf{dx}, t)}}{\sigma_{u_y(\mathbf{x})} \sigma_{u_y(\mathbf{x}+\mathbf{dx})}} \tag{4.6}$$

where σ_{u_y} is the standard deviation of the vertical velocity. Evolution of $R_{u'_y u'_y}$ with a reference point at $(x/H, y/H) = (0.4, \pm 0.6)$ for both shear-layers in the asymmetric state $\mathbf{R}$ are provided in figure 4.12 and streamwise profiles are extracted in the continuity of the edges at $y/H = \pm 0.6$. A clear difference in the length-scales of the roll-up are observed which is linked to the triggering operated by the recirculating flow only on the left shear layer. $R_{u'_y u'_y}$ is also provided in the symmetric state $\mathbf{S}_{\mathrm{tr}}$ for the left shear-layer (by symmetry the opposite shear-layer has similar characteristics). The spatial correlations are estimated using all the available wake reversals. Strikingly, there is very low correlation in the shear-layers in this state. This suggests both the disorganization of the recirculating flow which does not interact with the shear-layers, and the decrease in coherent activity in the shear-layers linked to the smaller engulfed flow.

A spatial linear stability analysis is conducted on the experimental velocity profiles on both left ($y < 0$) and right ($y > 0$) shear layers of the wake in the $\mathbf{R}$ state. Velocity profiles $u_x(y)$ were extracted near the base at $x/H = 0.05$ and near the preferential streamwise location of recirculating flow interaction $x/H = 0.3$, between lateral locations $y/H = \pm 0.35$ and ± 0.75 depending on the shear-layer, and were prolonged on each side by a constant value to avoid too strong influence of end effects in the computations. As detailed by Bridges & Morris (1984), given a temporal periodic perturbation f the Orr-Sommerfeld equation is solved to get the complex streamwise wavenumber α using the Chebyshev collocation method, while the non-linearity of the spatial eigenvalue problem is handled using the companion matrix technique. Results of this spatial linear stability analysis are given in figure 4.12(c) in form of the evolution of the growth rate $-\alpha_i$ of the most unstable mode (the Kelvin-Helmholtz-like mode) with the St_W of the perturbation. At both streamwise locations on the left shear-layer, the most amplified St_W (3.2 at $x/H = 0.05$ and 1 at $x/H = 0.3$) is quite in agreement with the experimentally observed modes. This suggest how the dynamics in the left shear-layer are completely dominated by its roll-up at $x/H \sim 0.3$ forced by the recirculating flow and not by the initial Kelvin-Helmholtz instability of the shear-layer at separation. Interestingly, the left shear-layer appears also as more unstable than the right one, right after separation at $x/H = 0.05$ and especially at $x/H = 0.3$ where the difference in maximal growth rate is around 40 %. This difference is mainly due to the recirculating flow yielding in the mean velocity profiles a reverse flow on the inner side of the left shear-layer and a co-flow on the inner side of the right shear-layer, thus underlining the fundamental importance of the recirculating region in the destabilization of the wake. For a given asymmetry, the shear-layer with a more stable organisation of the vorticity sheet will naturally have a self-induced curving movement towards the recirculation region, while the more unstable shear-layer leading to the roll-up of the vortex sheet will remain more straight. Following the studies of Bradshaw (1969) and Castro & Bradshaw (1976), the mean curvature of the streamlines has a stabilizing effect on the shear-layer. This would explain why the right shear-layer can sustain an important degree of organization when it arrives as a recirculating flow in the vicinity of the preferential location of interaction with the left shear-layer.

4.5.2 A general feature of asymmetric wakes ?

Naturally, one might wonder if this strong interaction is a general feature of asymmetric 3D wakes and not only a peculiarity of the lateral bi-modal wake. To answer this question, the flow around an Ahmed body with a wake locked in the vertical asymmetric state $\mathbf{B}$ is investigated at lower $Re_H \sim 9000$. The body is a scaled-down version ($H = 0.1$ m) of the Ahmed body used in the rest of this work and is placed in a close-circuit water channel whose test section is 2.1 m (length) $\times$ 0.5 m (width) $\times$ 0.3 m (height). The free-stream flow is set at $U_0 = 0.12$ m s^{-1} and a slightly higher ground clearance $G/H = 0.23$ is used to account for the higher viscous blockage in the underbody. A detailed description of the setup is provided by Spohn & Gilliéron (2002). Hydrogen bubbles technique is used to visualize the flow (Smits & Lim, 2000).

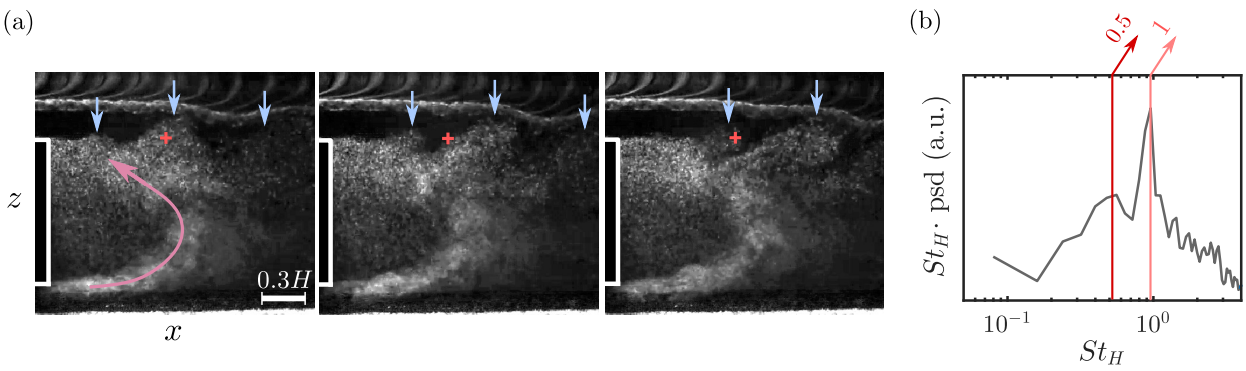

Figure 4.13: Ahmed body wake flow at low $Re_H \sim 9 \times 10^3$. For this configuration, the wake is locked in a static **B** asymmetric state (see the text for the details of the setup). (a) Hydrogen bubble visualization of the flow in the vertical mid-plane $y = 0$. Pink arrow denotes the recirculating flow fed by the bottom shear layer. Blue arrows indicate large scale roll-up vortices produced by the interaction of the recirculating flow with the top shear-layer and convected downstream. Images are separated by 0.4 convective time units H/U_0. (b) Premultiplied spectrum of the light intensity at the red cross location in (a).

Visualizations of the wake in the vertical plane of symmetry are provided in figure 4.13(a) at three consecutive time-instants separated by $0.4H/U_0$. The wake is locked in a vertical asymmetric **B** state and large-scale roll-up of the top shear-layer can be noticed in analogy with what has been described previously for the turbulent wake locked in a lateral asymmetric **R** state. It is quite clear from these flow visualizations that the bottom shear-layer forms a highly curved recirculating flow which interacts with the top shear-layer and triggers its roll-up and the formation of large-scale structures. The supplementary movie 2 provides an excerpt of the flow visualizations highlighting these dynamics. In figure 4.13(b), the premultiplied spectrum of the light intensity fluctuations at a location indicated by the red cross in the middle of the top shear-layer in the region of formation of the large-scale coherent structures is presented. Two dominant peaks are found in the dominant dynamics of the flow which are $St_H \sim 0.5$ and 1. The complete similarity with the turbulent lateral asymmetry can be further assessed by performing the SPOD of the flow visualizations in figure 4.14. In the same analogy, the two dominant modes at $St_H \sim 0.5$ and 1 are retrieved with a spatial structure quite identical to the dominant modes presented in figure 4.11. In addition, a similar low-frequency mode similar to the one obtained in the turbulent wake is present, characterizing the dynamics of the recirculation region and its interaction with the top shear-layer. In this sense, this interaction mechanism appears to be a universal feature of all these asymmetric wakes and the mechanism associated to asymmetry-related drag. From there on, one could wonder if this mechanism can even be traced back at the onset of symmetry-breaking in the laminar wake of the Ahmed body around $Re \sim 400$ as studied by Grandemange *et al.* (2012) and Evstafyeva *et al.* (2017).

At this point, it is of importance to point out the scaling of the dominant shear-layer modes obtained. From both flows with asymmetry in different directions (lateral or vertical) and with different flow regimes (low transitional at $Re_H = 9000$ or highly turbulent at $Re_H = 5 \times 10^5$), similar St_H or $St_W \sim 0.5$ and 1 have been obtained. At first sight, such values of St are quite consistent as these modes translate the interaction of both shear-layers through the recirculating flow. As such, the characteristic dimension of interest to scale the phenomenon is the distance between the two opposite shear layers of interest (left and right of top and bottom depending on the direction of the asymmetry), i.e. H or W. However, as this mode is linked to the roll-up of the shear-layer triggered by the recirculating flow, we could also expect a local scale such as the shear-layer thickness at the preferential location of interaction to be involved in the scaling of these dynamics. This is also further argued by the pertinence of the local stability analysis in the previous section to capture these peculiar dynamics. In this sense the important difference in the initial development of the shear-layer linked to the boundary layer characteristics at separation for both flows (laminar/transitional in one case and fully turbulent in the other) should have led to differences in the scaling of the dynamics if a local scale were to be involved. An additional argument is provided on this question in the final discussion.

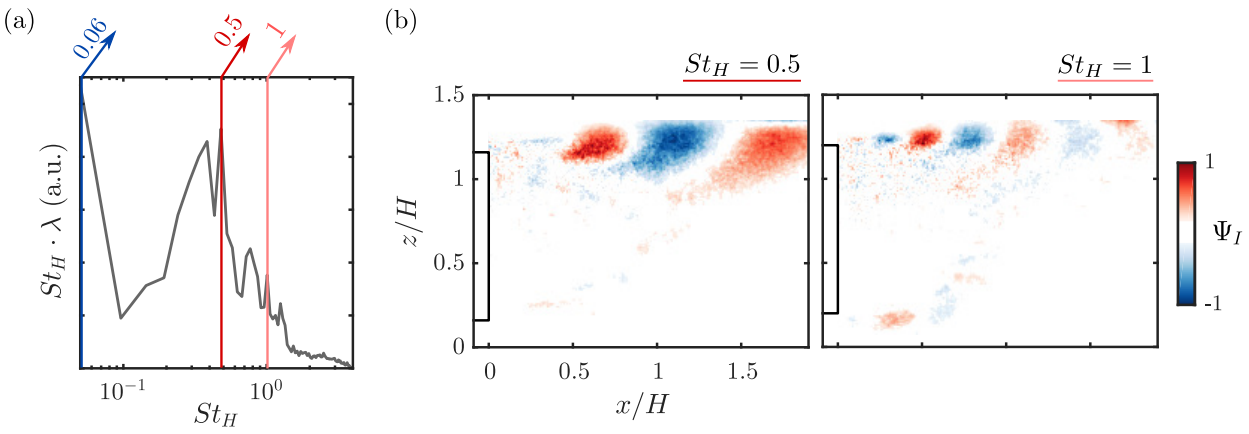

Figure 4.14: Spectral proper orthogonal decomposition (SPOD) of the light intensity field for the Ahmed body wake flow at low $Re_H \sim 9 \times 10^3$ locked in a vertical asymmetric state **B**. (a) Premultiplied spectrum of the first SPOD modes $\lambda^{(1)}_{St_H}$. Dominant dynamics are highlighted by colored vertical arrows. (b) Spatial organization of the dominant dynamics shown by first mode at the given frequency $\psi^{(1)}_{St_H}$.

4.6 Flow dynamics during near-wake reversals

Now that the peculiar state of the wake leading to additional asymmetry-related drag has been characterized, it can be extended to provide insight on the wake reversal event in the lateral bi-modal wake. To investigate the typical wake reversal and the precursory event triggering the reversal, the focus is put on a detailed description of the instantaneous dynamics of the wake. The relatively long time-scale of the typical wake reversal and the difficulty to gather a sufficient number of realizations makes it hard to successfully investigate these dynamics from a phase-averaged point of view as has recently been done by Schmidt & Schmid (2019) or Pineau & Bogey (2019) on rare acoustic bursts events in turbulent jets. However, the systematic investigation of each wake reversal, natural and triggered, captured in this experimental work, has shown that the dynamics remain qualitatively very similar between each realization. In this sense, the description of the wake reversal event provided in the remaining of this section does not lack of generality.

The dynamics of a natural wake reversal are elucidated in figure 4.15 through a time sequence of instantaneous velocity vector field colored by the lateral velocity u_y. These snapshots correspond to extracts from the time sequence acquired during a wake reversal between lateral asymmetric states **R** and **L** at particular instants of clear changes in y_b, depicted by the markers on the time evolution of y_b. The wake reversal can be separated in five phases denoted from (I) to (V) based on the peculiar flow dynamics during each phase. In the phase (I) launching the reversal, the wake is in the state **R** and the recirculating flow (a) resulting from the right shear-layer triggers quite strong roll-up of the left shear-layer through the interaction mechanism discussed in the previous section. Large-scale vortical structures (b) and (c) are formed in this shear-layer in the second and third snapshot of phase (I) associated to the coherent dynamics characterized in §4.5. These structures are quite similar to the hairpin vortices described by Dalla Longa *et al.* (2019) at the beginning of a wake reversal captured numerically. For sufficiently strong large-scale roll-up, the yielded flow engulfment (d) in the recirculation region forms a recirculating flow which interacts with the established recirculating flow from the opposite right shear-layer during phase (II). Both recirculating flows (a) and (d) originating from the two opposite shear-layers interact which pinches-off the original recirculating flow (a) characterizing the asymmetric state **R**. From then on, no coherent flow movement is established in the recirculation region and thus no triggering of the shear-layers roll-up takes place as discussed in previous section from figure 4.12. This leads to the highly unstable transient symmetric state $\mathbf{S}_{\mathrm{tr}}$ where the wake meanders around $y_b = 0$ with low drag due to the stabilization of the shear-layers and the absence of organized recirculating flow motion. As this wake is highly unstable in absence of coherent recirculating dynamics, small perturbation of the fluid engulfment (e) through the opposite shear-layers instantaneously breaks the equilibrium by triggering the roll-up of one of the shear-layers. It should be noted that rare examples of wake reversal with a wake returning to a similar asymmetric state have also been

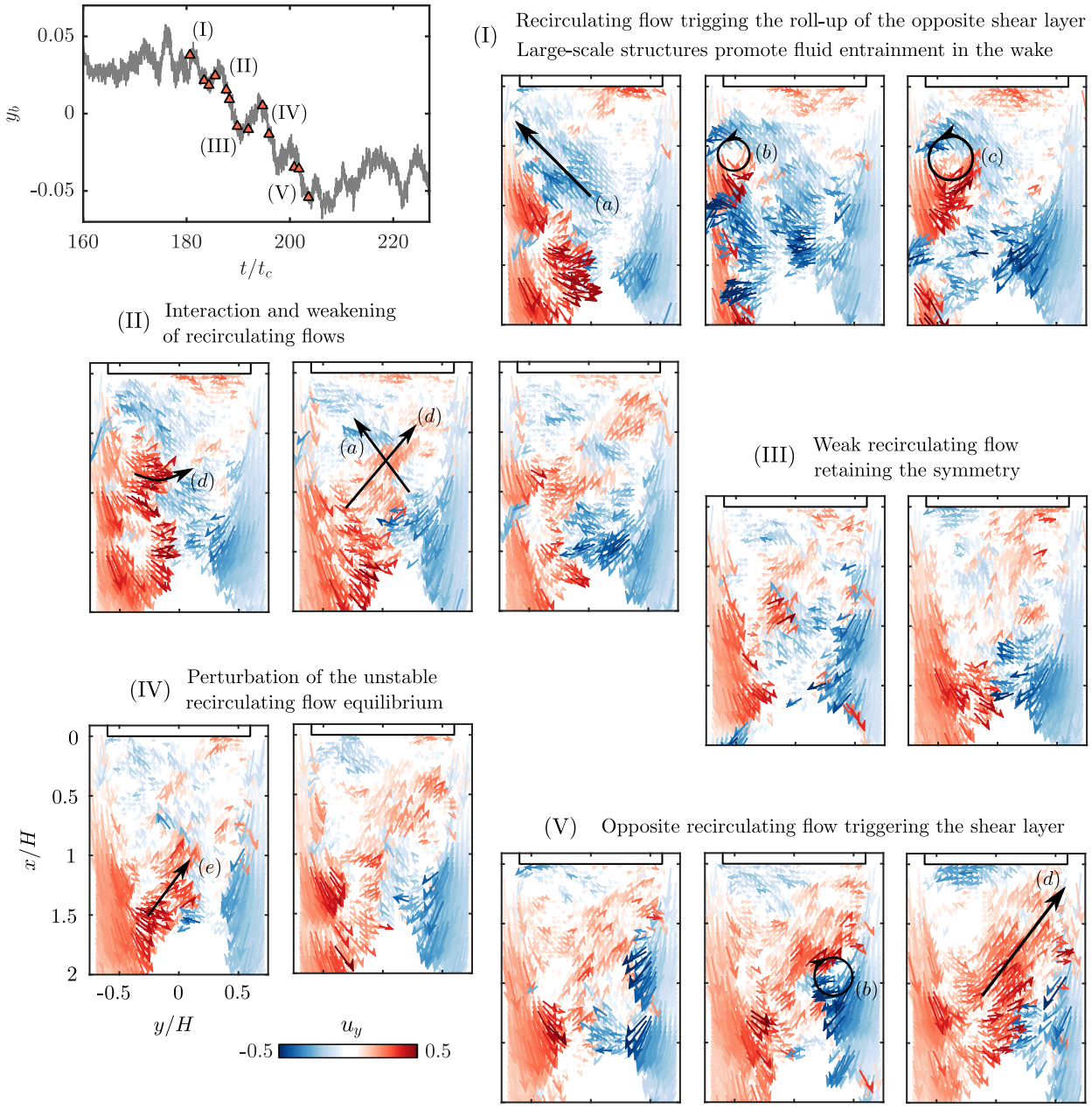

Figure 4.15: Characteristic wake reversal process exemplified on a natural wake reversal. The reversal is shown by the lateral base CoP position y_b. Selected snapshots are indicated by triangles and separated in 5 different phases. The wake snapshots show the velocity vector field colored by the lateral velocity u_y. Only one tenth vector is shown for clarity. Large black arrows indicate the main flows.

captured. This could suggest the role of inertia of the wake movement from the **R** state to the $\mathbf{S}_{\text{tr}}$ state in the sense it is highly more probable that the perturbation of the $\mathbf{S}_{\text{tr}}$ state will lead to a reversal to the opposite asymmetric **L** state. The small engulfment imbalance (e) leads to perturbation and triggering of roll-up in the opposite shear-layer (b). This roll-up finally interacts with left shear-layer to definitely form a strong recirculating flow (d) from left shear-layer which ends the wake reversal event in the asymmetric state **L**.

As seen from the wake reversal dynamics, the initial triggering of the reversal needs a strong enough recirculating flow to sufficiently trigger the shear-layer and create a fluid engulfment strong enough to disconnect the recirculating flow. In figure 4.16, we present the typical precursory event leading to the triggering of a wake reversal. To underline the generality of this precursory event, it is exemplified on a realization where 2 consecutive wake reversals are observed, from **L** to **R** and then from **R** to **L**. All the wake reversals captured present systematically the same precursory event triggering the reversal. In figure 4.16(a) different time-series of the lateral position of the CoP

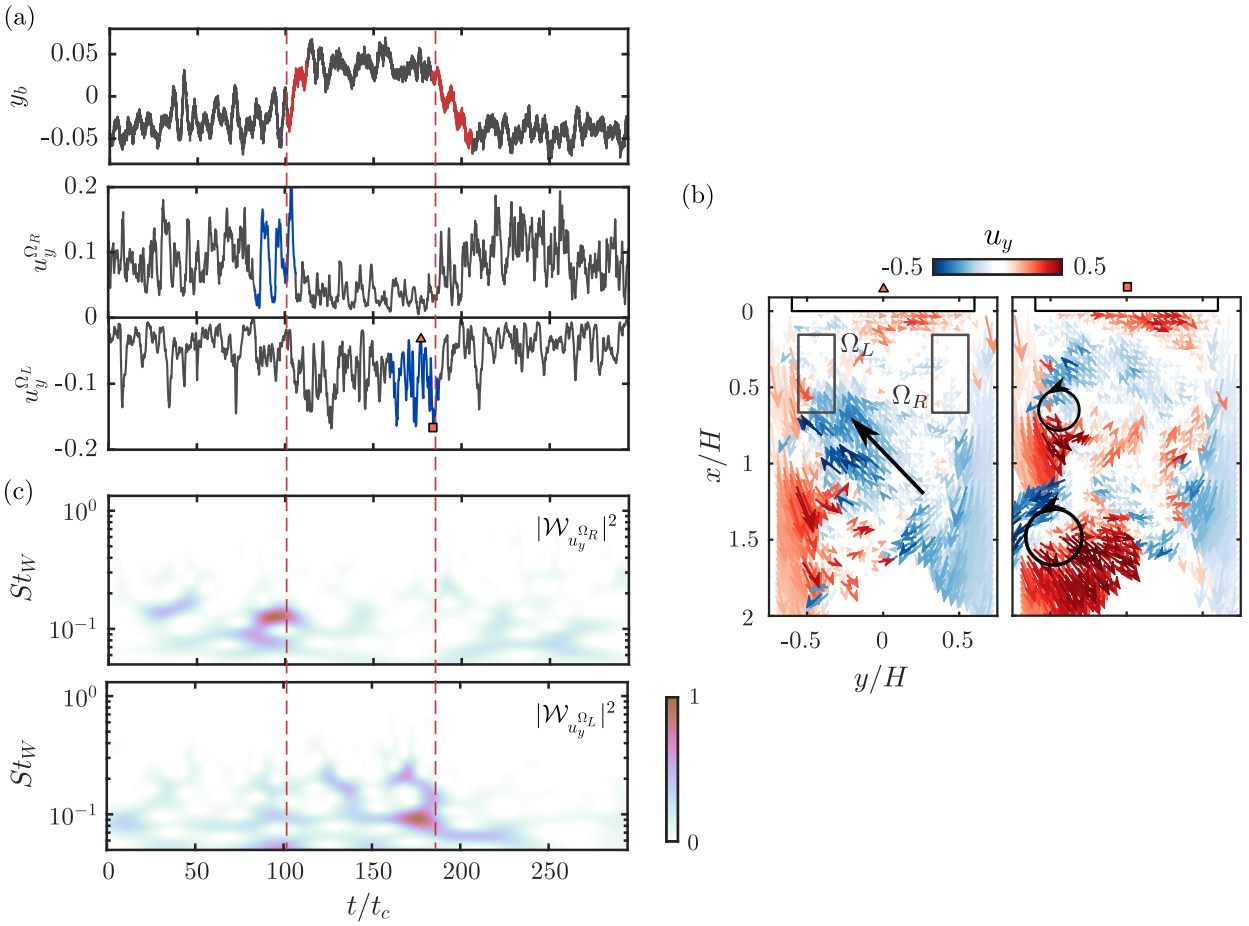

Figure 4.16: Precursory events of the wake reversal. (a) Natural wake reversal realization presenting a **L** to **R** followed by a **R** to **L** reversal. Beginning of each reversal is indicated by the vertical red dashed lines. The average lateral velocity $u_y^{\Omega_L}$ and $u_y^{\Omega_R}$ in the symmetric zones Ω_L and Ω_R where interaction between the recirculating flow and the opposite shear layer occurs in asymmetric states are monitored. Blue part of the velocity signal shows the precursory important oscillations of the interaction mechanism. Area $\mathcal{A}$ of the recirculation region shows important expansion and collapsing events indicated by blue arrows before the wake reversals. (b) Representative snapshots of velocity field colored by u_y for extremal $u_y^{\Omega_L}$ indicated in (a) by the triangles before a reversal. (c) Scalogram of $u_y^{\Omega_R}$ and $u_y^{\Omega_R}$ represented by the norm of their wavelet transform $|\mathcal{W}_{u_y^{\Omega_R}}|^2$ and $|\mathcal{W}_{u_y^{\Omega_L}}|^2$.

y_b, averaged lateral velocities over the preferential region of interaction $u_y^{\Omega_L}$ and $u_y^{\Omega_R}$ and the area of the recirculation region $\mathcal{A}$ are shown. Both wake reversals are preceded by strong fluctuations of the recirculating flow in the interaction region (either $u_y^{\Omega_L}$ in the **R** state or $u_y^{\Omega_R}$ in the **L** state). These fluctuations are quite similar to the ones monitored by Dalla Longa *et al.* (2019) but their interpretation is relatively different. These fluctuations exhibit a relative periodicity which can be elucidated using wavelet transform of the time-series. In figure 4.16(c), the time-resolved frequency content of the fluctuations $u_y^{\Omega_R}$ and $u_y^{\Omega_L}$ is provided through the norm of their continuous wavelet transform $|\mathcal{W}_{u_y^{\Omega_R}}|^2$ and $|\mathcal{W}_{u_y^{\Omega_L}}|^2$. The continuous wavelet transform is estimated by convolution of the fluctuations $u_y^{\Omega_R}$ with regular complex Morlet wavelets which allows for the best results. A peak around $St_W \sim 0.1$ is found just before the first wake reversal. Conversely, a similar peak in $|\mathcal{W}_{u_y^{\Omega_L}}|^2$ is also found just before the second wake reversal. This St_W is quite in agreement with the low frequency dynamics dominating the recirculating flow discussed from figure 4.9. In this sense, it suggests how the opposite shear-layer is strongly triggered by the recirculating flow just before the wake reversal. Conversely, the dynamics of the recirculation region $\mathcal{A}$, which is dominated by the low frequency dynamics, also exhibit these strong fluctuations just before the wake reversal. Maximal $\mathcal{A}$ is observed just before the wake reversal (marked by the blue arrows) and a strong collapse in the area occurs right at the beginning of the reversal. This means that

a strong recirculating flow is established just before the wake reversal which intensely triggers the roll-up of the opposite shear-layer and which consequently collapses the recirculation region by feeding the roll-up with the recirculating flow. This mechanism is pictured in figure 4.16(b) where two snapshots are shown corresponding to the local maximum and minimum of $u_y^{\Omega_L}$ indicated by the orange filled triangles in 4.16(a) just at the onset of wake reversal. In the process, the strong recirculating flow is established at minimal interaction (associated to minimal fluctuations $u_y^{\Omega_L}$). Once the shear-layer has been triggered by this flow at maximal interaction, all the recirculating flow is rolled-up with the shear-layer to form the large-scale structures which are triggering the wake reversal by flow engulfment to form the opposite recirculating flow. The knowledge of these precursory events could allow to predict the onset of wake reversal and favour their control by anticipating the event.

4.7 Discussions and concluding remarks

We summarize the main mechanisms of asymmetry-related drag and wake reversals. The aim is twofold : to interpret a broad range of important results from the literature through the new insights provided here, and to discuss potential efficient control methods for stabilizing a symmetric wake for drag reduction.

4.7.1 Flow dynamics in asymmetric and transient states

A conceptual scenario for the near-wake dynamics of asymmetric states is provided in figure 4.17 aiming at simplifying the complex process occurring in asymmetric wakes and during wake reversals. The scenario partly builds on the mechanism proposed by Gerrard (1966) for the formation of the recirculation region behind 2D bluff bodies through flow entrainment by the surrounding shear-layers. Although the present flow configuration is highly three-dimensional (**?**), which cannot be completely neglected, the interaction of opposite shear layers is an important feature of this flow configuration. Grandemange *et al.* (2013*b*) has shown the existence of global instabilities related to the interaction of opposite shear layers in the wake of the Ahmed body, similarly to the global instability in 2D wakes but with the notable difference that these interactions are less strong. Moreover, Lorite-Díez *et al.* (2020) has recently successfully applied the flow description of Gerrard (1966) concerning the momentum budget of the wake to the wake of an Ahmed body. Such a description can thus provide important insights about the main mechanisms involved. Four different sub-mechanisms are entangled with each another.

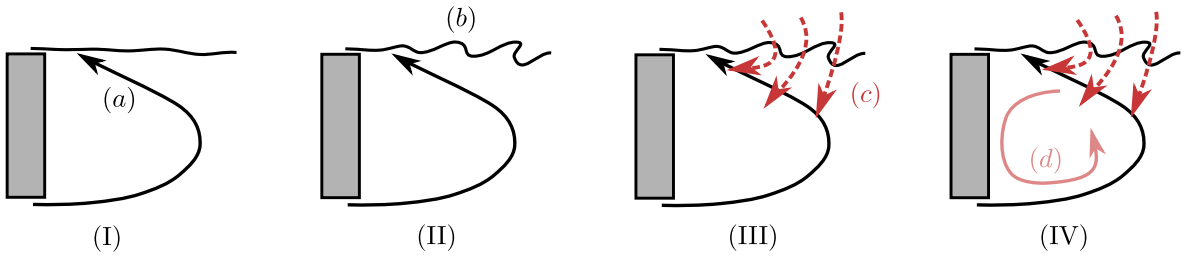

Figure 4.17: Conceptual scenario of the asymmetry-related drag mechanism. The recirculating flow (a) issued from the stable curved shear-layer interacts with the opposite shear-layer near the base. The interaction triggers the roll-up of the shear-layer (b) and the formation of large-scale vortical structures promoting the engulfment of fluid (c) inside the wake. The increased recirculating flow (d) fed by the fluid engulfment (c) leads to pressure decrease in the wake and on the base.

(I) The asymmetric wake, no matter its orientation, yields an imbalance between opposite shear-layers in the direction of the asymmetry. One shear-layer has small curvature whereas the opposite one high curvature leading to its stabilization and the formation of a coherent strong recirculating flow (a). This recirculation flow has fundamental importance in the mechanism as it allows feedback in the wake through its interaction with the opposite-shear layer.

(II) The interaction mechanism between the recirculating flow (a) formed by one shear-layer with the opposite one takes place near the initial development of the shear-layer with small cur-

vature. It triggers the shear-layer (b), which can be seen as an external forcing of the shear-layer. This leads to a strong increase in growth of this shear-layer, but also more importantly to its roll-up forming large-scale coherent structures with characteristic scale $St_C \sim 1$ where C is the characteristic cross-flow length scale in the direction of the wake asymmetry (ie the distance between the shear-layers of interest). At this point the difference between opposite shear-layers is quite great due to this feedback interaction.

(III) The strong roll-up of the shear-layer (b) results in its non-linear development and further subharmonic interaction which forms increasingly coherent and strong vortical structures. This yields an engulfment flow (c) which has complementary consequences. For one thing, the flow entrained in the wake by large-scale engulfment feeds the recirculating region. For another thing, the roll-up promotes the asymmetric recirculating flow (a) by induction. This promotes the asymmetry locking as long as the engulfment flow (c) is not too strong. Finally, as discussed by Gerrard (1966), the recirculation length L_r shrinks down by a relatively small amount, which is partially related to the increase of base drag in presence of large-scale asymmetries.

(IV) The increased flow inside the recirculating region (d) noticed in asymmetric states stems from the feeding by entrainment flow (c). This enhanced recirculating flow yields a lower pressure at the center in the toroidal low pressure structure described by Dalla Longa *et al.* (2019). In consequence the pressure imprint on the base is also lowered and the base drag is increased.

The same mechanism is at the origin of wake reversals in bi-modal wakes. The coupled dynamics of the recirculating flow triggering the shear-layer and the roll-up of the shear-layer leading to engulfed flow promoting and feeding the recirculating flow are the key process leading to wake reversal. When sufficient flow is engulfed, the feedback recirculating flow (a) can impose strong triggering on the opposite shear layer. Then the roll-up of the shear-layer (b) gets strong enough to form an opposite recirculating flow which pinches off the main recirculating flow (a) and its feedback necessary to maintain the asymmetry. As a consequence, the wake is brought in a symmetric transient unstable state where both opposing recirculating flows have cancelled each another. This leaves the transient symmetric recirculating wake in a state where no coherent recirculating motion are established. The consequences are twofold : shear-layers are not triggered by the recirculating flow which inhibits their growth, and the absence of coherent and organized recirculating motion leads to a higher static pressure in the near wake flow. This also accounts for the lower pressure drag observed even in asymmetric transient states during wake reversals as a similar disorganisation of the recirculating flow.

4.7.2 On drag changes of wakes influenced by ground clearance

Based on the mechanism described, results of the recent literature about vertical asymmetric wakes may also be interpreted. The changes in underbody flow and in interaction with the ground investigated especially by Grandemange *et al.* (2013*a*), Szmigiel (2017) and Castelain *et al.* (2018) have a strong impact on the vertical asymmetry of the wake and on the base drag generated by the body. These base drag changes may be interpreted using the same asymmetry-related drag mechanism described here. To do so, figure 4.18(a) reproduces an important result of Szmigiel (2017) which presents the evolution of mean base drag $\overline{C_{pb}}$ with underbody mass flow rate $q/(HU_0)$. The experiments of Szmigiel (2017) and Castelain *et al.* (2018) use a modified Ahmed body with aspect ratio $H/W > 1$, fixed ground clearance and side skirts closing the underbody where different perforated plates change the underbody mass flow rate. As a matter of generalization, it should be noted that Szmigiel (2017) assessed the qualitative similarity of these results with the ones of Grandemange *et al.* (2013*c*) obtained with a canonical Ahmed body with variable ground clearance. The main result of Castelain *et al.* (2018) is the identification of four very different flow classes depending on the underbody mass flow rate which have quite different base drag. If we focus on the three flow classes concerning the highest underbody mass flow rate[5], a basic sketch of the mean flow topology focusing on the direction of vertical asymmetry is provided in figure 4.18(b) based on the flow measurements in Castelain *et al.* (2018) and Grandemange *et al.* (2013*a*). The main

[5]The first class at low mass flow rates is actually more reminiscent of the flow around a 3D step on the ground whereas the three other flow classes allow for enough underbody mass flow rate to have a regular 3D bluff body flows with four shear layers surrounding the recirculation region.

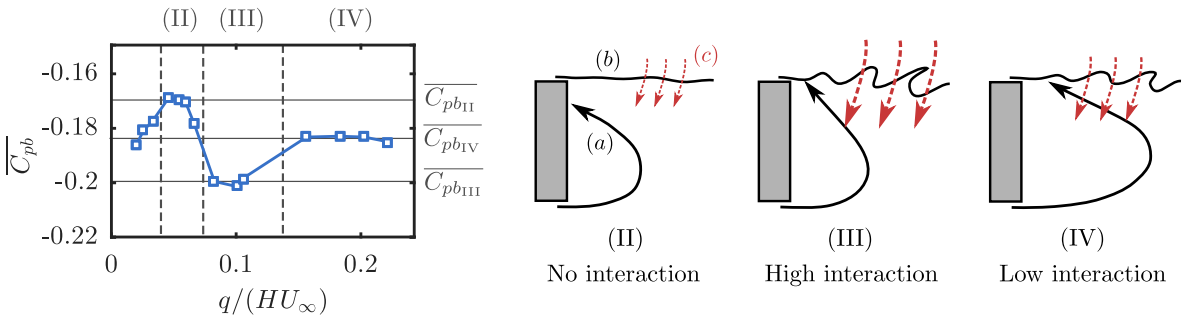

Figure 4.18: Interpretation of the changes in pressure drag $\overline{C_{pb}}$ for vertical asymmetric wakes. (a) Evolution of C_{pb} with the underbody mass flow rate q adapted from Szmigiel (2017). Data from Szmigiel (2017) and Castelain *et al.* (2018) correspond to a modified Ahmed body with aspect ratio $H/W = 1.12$, fixed ground clearance and pressure losses in the underbody to change q. Castelain *et al.* (2018) identified 4 different flow classes depending on the value of q, and qualitative similarity with the experiments of Grandemange *et al.* (2013*a*) on a canonical Ahmed body has been assessed by Szmigiel (2017). Flow classes (II), (III) and (IV) with important q can be ranked as having different degree of interaction between the recirculating flow (a) fed by the bottom shear-layer and the top shear-layer (b) as sketched in (b) following the PIV measurements of Grandemange *et al.* (2013*a*) and Castelain *et al.* (2018). The resulting changes in engulfment flow $(c_{\mathrm{II}}) < (c_{\mathrm{IV}}) < (c_{\mathrm{III}})$ can qualitatively explain the base drag changes for these flows $-\overline{C_{pb_{\mathrm{II}}}} < -\overline{C_{pb_{\mathrm{IV}}}} < -\overline{C_{pb_{\mathrm{III}}}}$.

criterion proposed by Castelain *et al.* (2018) to discriminate between these different flow classes is the mean curvature of the underbody flow (the flow noted (a) in figure 4.18). The interaction of the underbody flow with the top shear-layer is rather different between the three flow classes as suggested in the work of Szmigiel (2017). For class (II), almost no interaction occurs as the flow (a) is impinging on the base of the body and the top shear-layer develops quite linearly (b) with resulting low large-scale entrainment flow (c) inside the recirculating wake. On the contrary, for flow class (III), the flow (a) directly impinges quasi-normally the upper shear-layer with quite an important momentum. This flow (a) has the maximal mean curvature and as such it is strongly stabilized and keeps this important momentum. The high degree of interaction with the top-shear layer leads to a strong roll-up (b) and the highest engulfment flow (c). Finally, for the flow class (IV) which is equivalent to the vertical asymmetric state **B**, the degree of interaction is more moderate both because the recirculating flow (a) is not resulting from ground detachment and thus keeps lower momentum at the interaction location and because the interaction orientation is less normal. This degree of interaction is in agreement with the strength of the Reynolds stresses in the top shear-layer systematically measured by Szmigiel (2017). In consequence, the three flow classes can be ranked based on the degree of interaction, of top-shear layer destabilization, and of importance of the large-scale flow engulfment as $(c_{\mathrm{II}}) < (c_{\mathrm{IV}}) < (c_{\mathrm{III}})$. Following the asymmetry-related drag mechanism we introduced, the flow classes are ranked in terms of base drag $-\overline{C_{pb_{\mathrm{II}}}} < -\overline{C_{pb_{\mathrm{IV}}}} < -\overline{C_{pb_{\mathrm{III}}}}$, which is in qualitative agreement with the measured base drag values provided in figure 4.18. Legitimately, it can be argued that an important part of the generated base drag comes from the flow curvature of the near-wake at first order. However, the importance of the asymmetry-related drag mechanism and how it manifests at quite different degrees in these wakes seem fundamental to explain second-order base drag variations among these wakes which represent only 10 to 20 % of the total base drag.

4.7.3 Insights on control of wake asymmetries for drag reduction

Finally, the discussion is ended by the implications between wake asymmetries and their control for drag reduction. In the recent literature numerous studies have focused on trying to control and mitigate the asymmetries in the wake of the Ahmed body to reduced its base drag. However most of the control strategies developed had only mitigated results both in terms of stabilizing the symmetric low-drag state $\mathbf{S}_{\mathrm{tr}}$ and in terms of drag reduction. The efficacy of all the control strategies targeting the flow asymmetries of the Ahmed body may be interpreted through the asymmetry-related drag mechanism studied previously. A conceptual interpretation of all these

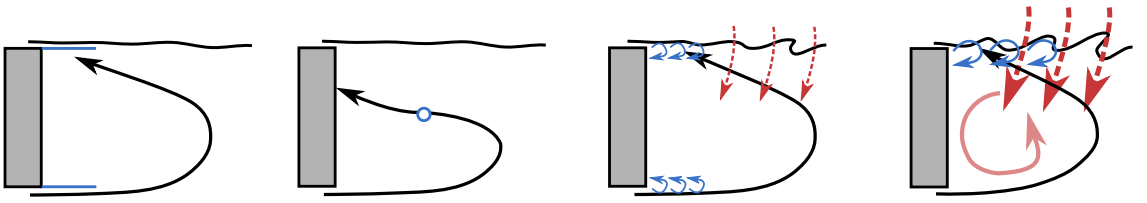

Figure 4.19: Interpretation of control methods efficacy to symmetrize the wake of the Ahmed body with concomitant drag reduction. Passive control methods as a sufficiently deep cavity at the base like in Evrard *et al.* (2016) and Lucas *et al.* (2017), or a spanwise control cylinder in the middle of the recirculation region like in Grandemange *et al.* (2014*b*) are able to satisfactorily suppress the lateral bi-stability by locking the unstable symmetric $\mathbf{S}_{\mathrm{tr}}$ mode and non-trivially decrease the base drag. This is achieved by preventing the interaction between the recirculating flow and the shear-layer. Active control methods involving steady and periodic blowing along the edges of the base (see details in the text for the references) can only act on the engulfment flow (*c*) without preventing the recirculation flow to interact with the shear-layers. This explains the lack of control authority of these methods for the symmetrization of the wake and the reduction of asymmetry-related drag.

control strategies is sketched in figure 4.19 on which the rest of discussion leans on.

Concerning the mitigation of the bi-modal dynamics and the stabilization of the transient symmetric state $\mathbf{S}_{\mathrm{tr}}$ which has received much of the attention lately, control strategies can be separated in three groups depending on the degree of stabilization and drag reduction they achieved. The efficacy of these control strategies to stabilize the wake is directly linked to the degree at which the interaction between the recirculating flow coming from one of the shear-layers and the opposite shear-layer is prevented.

- The passive cavity at the rear base is maybe the most enlightening case. The cavity was shown by Evrard *et al.* (2016) and Lucas *et al.* (2017) to completely stabilize the symmetric low-drag state of the wake under the condition the cavity was deep enough. The minimal cavity depth to achieve total stabilization of the symmetric low-drag state was found to be $0.25H$ which is in good quantitative agreement with the preferential location of the interaction of the recirculating flow with the opposite shear-layer identified in our present study. This means that the cavity is able to stabilize the low-drag symmetric state on the condition that it completely prevents the feedback from the recirculating flow in the asymmetry-related drag mechanism. The associated base drag decrease is quite important, around 9 %, but part of it is ascribed to the artificial elongation of the recirculation region due to the cavity depth.

- The small vertical control cylinder used by Grandemange *et al.* (2014*b*) on the bi-modal Ahmed body wake was only partially able to stabilize the wake in the unstable symmetric low-drag state when placed in the vicinity of the middle of the recirculation region. This position appears as the only one where the cylinder hinders the feedback of the asymmetric recirculating flow. Nevertheless, due to the small size of the cylinder, it only partially prevents the recirculation interaction. The wake still meanders around the most probable symmetric low drag state with almost similar amplitude as the bi-modal wake and the associated base drag decrease is only small, around 4 %, compared to the 8 to 10 % identified in the present study. A similar more efficient strategy to prevent the feedback recirculating flow may be to use a splitter-plate, as in the 2D bluff body study of Bearman (1965), with characteristic length of half of the wake length approximately.

- Active control strategies were used by Li *et al.* (2016) and Brackston *et al.* (2016) respectively with pulsed jets at the side edges of the base and flapping side flaps to stabilize the bi-modal wake of the Ahmed body. Both studies used closed loop control based on feedback of the lateral position of the wake y_b and showed how a pseudo-alternate left and right actuation could partially stabilize the symmetric state. However, Li *et al.* (2016) showed that the efficient forcing frequency to trigger the shear-layer on each side and have enough authority

to stabilize the symmetric state of the wake was around $St_W \sim 1$ which is the roll-up mode identified in the present study triggered by the recirculation flow feedback. In this sense, the control needed to force the wake reversal mechanism identified here by promoting the roll-up of the shear-layer. In consequence, the wake was just meandering around the symmetric state by alternatively forcing the wake reversal mechanism on each side. In addition, the symmetric state which was explored by the wake was a higher drag version of the $\mathbf{S}_{\text{tr}}$ state as the important flow engulfment promoted by the forcing lead to important organization of the recirculating flow. This is why these two studies only reported a mitigated 2 % of base drag decrease. Using these strategies, only the wake reversal mechanism is triggered, but nothing prevents the recirculating flow to develop and establish the feedback mechanism triggering one of the shear-layers. In this sense, the wake can only meander around the symmetric state but never be stabilized in it.

- Finally, homogeneous forcing around the whole base either with steady blowing or high-frequency blowing is not a fluidic equivalent of the base cavity. The studies of Barros (2015), Lorite-Díez *et al.* (2020) or the results presented in chapter 5 and 6 show that this type of forcing does not influence the lateral bi-modal dynamics of the Ahmed body wake. The jets exiting at the base only keep momentum for a small streamwise extent after being injected (typically 0.1H) before being dissipated by the surrounding flow. In this sense they do not act like a fluidic curtain equivalent to cavity hindering the feedback interaction of the recirculating flow. They only have a certain authority to slightly stabilize the shear-layers.

All these flow control results and their interpretation based on the asymmetry-related drag mechanism studied here show that the efficacy of a flow control strategy to stabilize the low-drag symmetric state is conditioned on the necessity of preventing the feedback mechanism between the recirculating flow issuing from one shear-layer and the opposite shear-layer. Control strategies should target the inner of the recirculation region to this purpose, because it appears as the region where the symmetry-breaking instability takes its root.

From the study of the unforced turbulent wake in chapters 3 and 4, several drag generation mechanisms have been evidenced and elements have been distilled on the means of tackling the drag reduction problem. It is now the focus of the chapters 5 and 6 to investigate in detail the forcing of the wake aiming at drag reduction.

Chapter 5

Unsteady Coanda effect for drag reduction

Most of these results are published in Haffner *et al.* (2020*b*) in the *Journal of Fluid Mechanics*. We study the unsteady forcing of the turbulent wake for drag reduction purposes. The influence of various parameters (forcing frequency and amplitude, curvature radius r of the additional surfaces, free-stream velocity U_0) on the base drag reduction is scrutinized. This provides key ingredients to identify proper scalings of the mechanisms involved and to model them. The flow reattachment and separation on the curved surfaces results in a boat-tailing of the wake leading to drag reductions up to 12% but is noticeably influenced by the time-scale of unsteadiness of the forcing. Indeed for high frequencies of order $O(U_0/r)$, strong vortical coherent structures produced by the interaction of the pulsed jets and the separating shear layer favours the interaction of the flow with the curved surfaces. Moreover, the local curvature and pressure gradients across the separating shear layer in the vicinity of flow separation are noticeably modified to result in a further pressure drag reduction for a given forcing amplitude. An inviscid-flow model allows us to confirm the peculiar induced effect of these coherent structures on the flow which explains both the curvature effects leading to additional drag decrease and the saturation in drag decrease for increasing forcing amplitude. Results point to the need of careful combination between forcing frequency and size of the curved surfaces to achieve all the potential of the unsteady Coanda effect in drag reduction.

Concise summary of this chapter

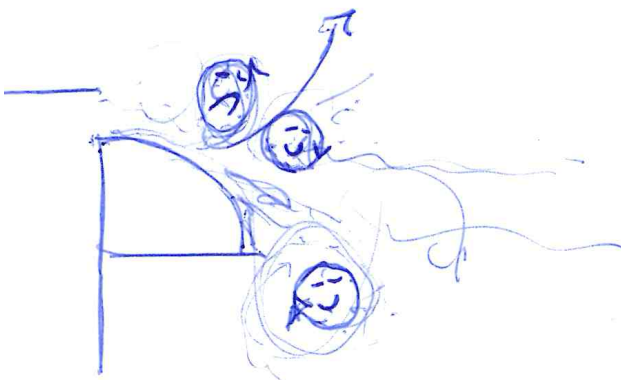

by an inspired advisor

Contents

As discussed in the introductory chapter 1, there is a significant body of work concerning the passive and active manipulation of blunt body wakes to reduce their pressure drag. The majority of the manipulation techniques build on a boat-tailing effect obtained passively with boat-tails or flaps or actively with a fluidic boat-tailing effect or with a combination of both.

The main difference between passive boat-tails or flaps and the combination of them with steady or pulsed jets is the ability for the jets to reattach the flow on the surface where it would be naturally detached. The jets dynamics are of primary importance in the interaction between the separated flow and the flap geometry. Greenblatt & Wygnanski (2000), Darabi & Wygnanski (2004*a*) and Darabi & Wygnanski (2004*b*) studied this reattachment and separation of the flow over a canonic flap geometry of length one order of magnitude higher than flaps used in the work of Szmigiel (2017) for instance. They showed how the optimal jet frequency for reattaching the flow over the flap was directly scaling with the free-stream velocity and the length of the flap. These aspects are or primary practical importance in large-scale applications such as the control of flow separation over an airfoil to prevent stall as shown by Glezer *et al.* (2005) for instance. Recently, several studies like Berk *et al.* (2017) and Stella *et al.* (2018) have started to focus on the fine-scale dynamic interaction between pulsed or synthetic jets and recirculating wake flows such as backward-facing steps in order to draw general scaling laws involving the formation of the pulsed jets and its influence on the recirculating wake. However, the particular mechanisms involved in the pressure drag reduction or any proper scaling laws of the phenomenon involving the main parameters like free-stream velocity, pulsed jets frequency and amplitude or size of the adjacent surfaces is lacking.

The present chapter aims at exhaustively describing what we will call in the remainder an unsteady Coanda effect which is shown to considerably differ from its 'steady' counterpart version which has been used in a broad range of applications in the fluid mechanics field. For that, we will focus on describing the peculiar effect of small-scale curved surfaces coupled to adjacent high-frequency pulsed jets. These jets are blowing at frequencies of order $O(U_0/r)$ (where U_0 is the free-stream velocity and r the radius of curvature of the surface). Compared with 'quasi-steady' blowing, they offer and additional advantage in reducing the pressure drag of an Ahmed-like body. The final focus is put on providing more general scaling laws of the described phenomena which will be of primary importance for further practical applications. A global view of the drag changes observed with extensive variation of the parameters of the problem is presented in §5.1. Based on these variations, a physical discussion on the time-scales of the unsteadiness of the separation from

the curved surface is introduced. From then on, a finer investigation in the vorticity dynamics at separation relates the observed drag changes to the way the flow is manipulated and we provide scaling laws describing the involved mechanisms through an inviscid-flow model in §5.2. A detailed picture of the peculiar flow mechanisms leading additional drag reduction at high-frequency is presented in §5.3 with particular attention to the flow curvature near the separation. The inviscid-flow model is additionally extended to further discuss the coupling between f and r and identify an optimal forcing frequency. Finally, in §5.4 we extend the discussions to provide more general implications of the present work before giving our concluding remarks.

5.1 Global effects of forcing : scalings and evidence of an unsteady effect

In this section, we first describe the global impact of forcing on the base pressure and aerodynamic drag of the model. To this end, we consider the evolution of three main global aerodynamic quantities of interest each characterized by a non-dimensional coefficient : the base pressure parameter γ_p, the pressure drag parameter γ_p^c and the drag parameter γ_D respectively defined as

$$\gamma_p = \frac{\overline{C_{pb}}}{\overline{C_{pb0}}}, \quad \gamma_p^c = \frac{\overline{C_{pb}^c}}{\overline{C_{pb0}^c}}, \quad \gamma_D = \frac{\overline{C_D}}{\overline{C_{D0}}}, \qquad (5.1a, b, c),$$

where the subscript 0 indicates the unforced case. $\overline{C_{pb}^c}$ is the time-averaged base pressure which accounts for the time-averaged pressure changes along the curved surfaces. With this definition, the pressure drag of the model becomes

$$S\overline{C_{pb}^c} = (S - S_{\rm cs})\overline{C_{pb}} + \frac{S_{\rm cs}}{N_{\rm cs}} \sum_{i=1}^{N_{\rm cs}} \overline{C_p(\theta_i)} \sin\theta_i \qquad (5.2)$$

with $N_{\rm cs}$ the number of pressure taps along the curved surface of total area $S_{\rm cs} \sim 2(H+W)\pi r/2$. θ_i indicates the local angular position of the pressure tap i along the curved surface starting from the slit. In equation 5.2, the curved surface is discretized in four facets centered at each pressure tap and tangent to the curved surface at each pressure tap location. As only 4 pressure taps are situated in the vertical plane of symmetry along the curved surface at the top edge of the base, we assume that the pressure distribution is homogeneous both along the span of the curved surface and between the curved surfaces on each edge of the base. The former assumption is justified by the fact that forcing conditions are close to spanwise homogeneity and that they impose the pressure over the curved surfaces. The latter assumption is justified by the unforced global equilibrium of the wake which leads to a nearly homogeneous mean pressure distribution on the base. All three parameters γ_p, γ_p^c and γ_D highlight a base pressure recovery (resp. pressure drag reduction, resp. aerodynamic drag reduction) when below unity (< 1), and conversely a base pressure decrease (resp. pressure drag increase, resp. aerodynamic drag increase) when above unity (> 1).

All the results will be discussed by referring to dimensional forcing frequencies and references to corresponding non-dimensional St numbers will only be made for physical discussion. Systematic reference to peculiar St numbers will be made when detailed mechanisms of the unsteady Coanda effect will be introduced. At this point, St_H and St_{θ_0} are the two dimensionless time-scales of interest to compare the forcing conditions used to the natural time-scales of the wake. Table 5.1 details the values of St_H and St_{θ_0} associated to the different forcing frequencies used in this chapter for different free-stream conditions. The global wake time-scale St_H is to be compared to the global instability at $St_H \sim 0.2$ corresponding to lateral and vertical vortex shedding, and to the instability at $St_H \sim 1$ involving the coupling between the recirculating flow and the shear-layers detailed in chapter 4. The local time-scale St_{θ_0} is related to the boundary layer momentum thickness at separation θ_0 as extensively characterized in chapter 3. This time-scale is to be compared to the initial Kelvin-Helmholtz instability of the shear-layers occurring at $St_{\theta_0} \sim 0.022$ (Zaman & Hussain, 1981; Morris & Foss, 2003). As all the shear-layers developing from all four edges are quite similar, all the estimations in table 5.1 are provided with the characteristics of the

Frequency [Hz]	St_H ($U_0 = 25/35\text{ms}^{-1}$)	St_{θ_0} ($U_0 = 25/35\text{ms}^{-1}$)
Steady	0	0
350	4.2/3	0.031/0.022
975	11.7/8.4	0.086/0.061
1050	12.6/9	0.092/0.066

Table 5.1: Characteristic dimensional f and non-dimensional St_H–St_θ frequencies used for forcing. $St_H = fH/U_0$ is the Strouhal number based on the height of the model and $St_{\theta_0} = f\theta_0/U_0$ the one based on the momentum thickness θ of the boundary layer at the trailing-edge of the model. Non-dimensional frequencies are given as indication at $U_0 = 25$ and 35ms^{-1}. For this flow, global absolute instability of the wake or vortex shedding is occurring at $St_H \sim 0.2$ (Grandemange *et al.*, 2013*b*), the instability studied in chapter 4 stemming from the interaction of the recirculating flow and the shear-layers at $St_H \sim 1$ and convective instability of the surrounding shear layers at $St_{\theta_0} \sim 0.021$ (Zaman & Hussain, 1981). The chosen forcing frequencies are thus mainly decoupled from the characteristic frequencies of the wake except for $f = 350$ Hz at $U_0 = 35$ m s^{-1}.

top shear-layer without loss of generality. It appears that all forcing conditions are completely decoupled from the global natural dynamics of the wake. If high forcing frequencies ($f = 975$ and 1050 Hz) are always also decoupled from the initial shear-layers dynamics, for $f = 350$ Hz, the forcing starts to interact with these dynamics at high free-stream velocities $U_0 = 35$ m s^{-1}. This decoupling is quite important as Barros *et al.* (2016*a*) showed the highly detrimental effect on the drag of forcing at frequencies close to $St_H \sim 0.2$ by promoting the vortex shedding dynamics which are quite weak in fully three-dimensional flows. Similarly, detrimental drag effects also occur when forcing around $St_H \sim 1$ following our discussions in chapter 4 and around $St_{\theta_0} \sim 0.022$ following the studies of Qubain (2009) and Oxlade *et al.* (2015) on the bullet-shaped body.

5.1.1 Aerodynamic drag variations of the forced wake : evidence of a peculiar unsteady Coanda effect

We analyse in figure 5.1(a,b) the base pressure changes when the order of magnitude of the forcing frequency is varied at a given free-stream velocity U_0. From the evolution of γ_p at both $U_0 = 25\text{ms}^{-1}$ and $U_0 = 35\text{ms}^{-1}$ (corresponding respectively to $Re_H = 5 \times 10^5$ and $Re_H = 7 \times 10^5$), there are two main effects of the change in forcing frequency over the chosen range of frequencies : (i) the magnitude of base pressure recovery is strongly dependent on the choice of the forcing frequency f, and (ii) the trends in the evolution of γ_p with forcing amplitude C_μ are fundamentally different depending on f.

The first aspect is clearly illustrated by the evolutions of γ_p in figure 5.1(b). Steady forcing is found to be inefficient to recover base pressure (γ_p remains between 0.98 and 1). This is surprising given the established efficiency of steady Coanda blowing for base drag reduction across the literature (Freund & Mungal (1994), Englar (2001) and Barros *et al.* (2016*b*)). Nevertheless, it should be pointed out that in the studies of Freund & Mungal (1994) and Englar (2001) r/h or r/H noticeably higher are used (r/h around 50). For unsteady forcing, a notable difference exists at given C_μ between forcing at $f = 350$ Hz and $f = 975 - 1050$ Hz. Indeed, forcing at $f = 1050$ Hz produces always a greater base pressure recovery in the range of investigated C_μ. For $U_0 = 35$ m s^{-1}, the difference culminates at 8% around $C_\mu \sim 1.6 \times 10^{-2}$. Nevertheless, as explicited in table 5.1, $f = 350$ Hz corresponds to St_θ of order 0.02 which is the most amplified frequency in a free-shear layer (Zaman & Hussain, 1981). This forcing frequency has been shown to induce base pressure decrease by Oxlade *et al.* (2015) on the bullet-shaped body. Even though, similar conclusions can be drawn from the results at $U_0 = 25\text{ms}^{-1}$ in figure 5.1(a). For this case, $f = 350$ Hz is above the most amplified frequency in the shear layers and thus decoupled from it. At this free-stream velocity, the difference in γ_p between both forcing frequencies culminates at 6% for $C_\mu \sim 3 \times 10^{-2}$.

Nevertheless for higher $C_\mu \sim 3.6 \times 10^{-2}$ there is the beginning of an inversion in terms of base pressure recovery efficiency between both forcings. This point leads to the second aspect introduced previously concerning the difference of trend observed in the evolution of γ_p. Indeed,

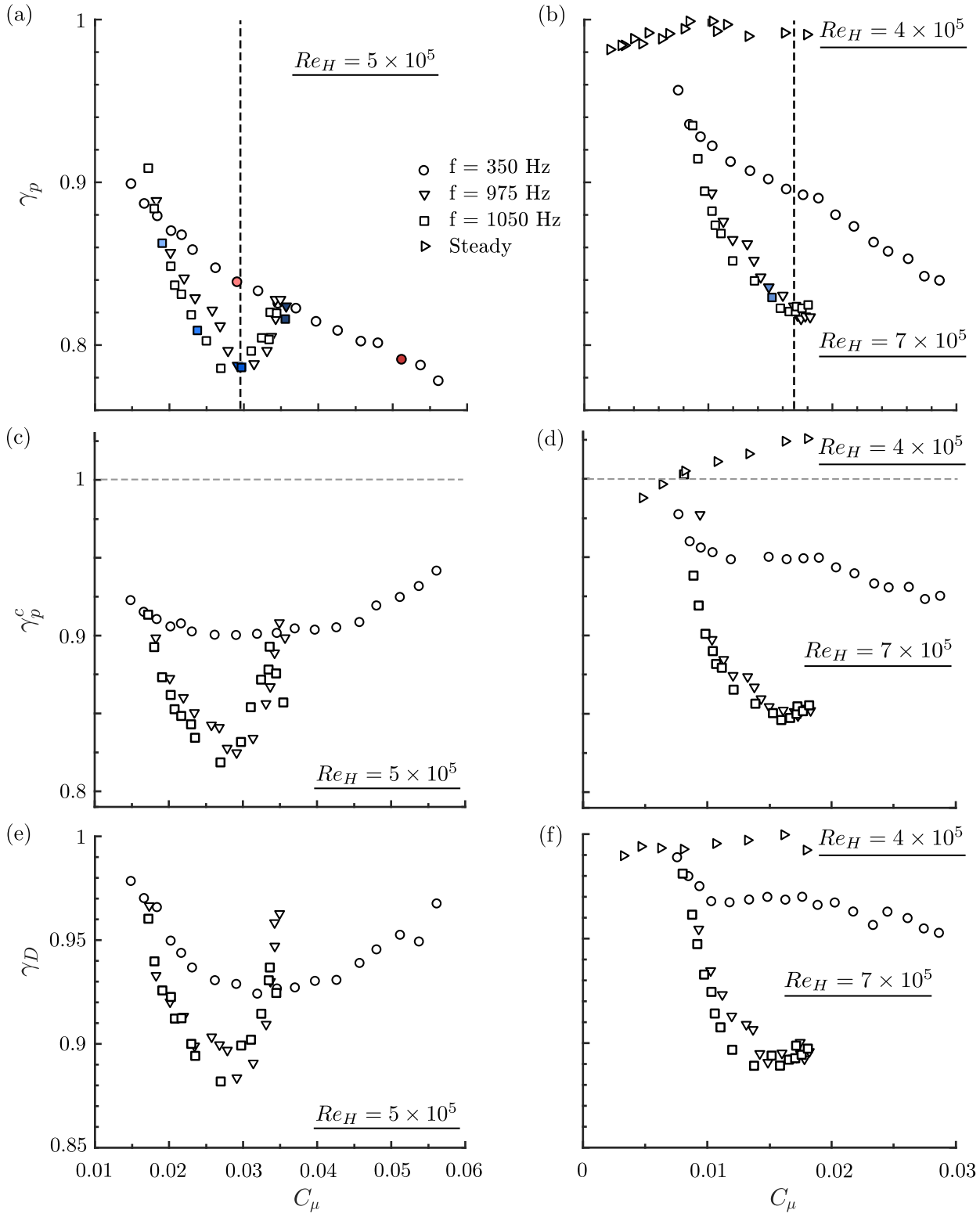

Figure 5.1: Evolution of (a,b) the base pressure parameter γ_p, (c,d) the corrected base pressure parameter γ_p^c and (e,f) the aerodynamic drag parameter γ_D with forcing amplitude C_μ for the curved surfaces of dimension $r = 9h$ at (a,c,e) $Re_H = 5 \times 10^5$ and (b,d,f) $Re_H = 7 \times 10^5$. Results for steady forcing in (b,d,f) were obtained for $Re_H = 4 \times 10^5$ in order to span a range of forcing amplitudes C_μ comparable with the ones of unsteady forcing. Filled markers are the cases further analysed in §5.3 for the detailed description of the drag reduction mechanisms and the unsteady Coanda effect. Vertical dashed lines indicate the C_μ at which saturation defined as a minimum in γ_p occurs.

Re_H ($\times 10^5$)	4	5	6	7	8
$f = 975$Hz	0.04	0.028	0.02	0.015	0.012
$f = 1050$Hz	0.039	0.028	0.021	0.017	–

Table 5.2: Evolution of the amplitude of saturation in base pressure recovery with the Reynolds number Re_H at high frequencies of forcing $f = 975$ and 1050Hz.

a clear saturation of the base pressure recovery takes place when forcing at $f = 975 - 1050$Hz starting at $C_\mu \sim 3 \times 10^{-2}$ at $U_0 = 25\text{ms}^{-1}$ (resp. $C_\mu \sim 1.6 \times 10^{-2}$ at $U_0 = 35\text{ms}^{-1}$). Above this threshold, the base pressure recovery is degraded. Such a saturation regime is not found at lower forcing frequency $f = 350$ Hz for which the decrease in γ_p with C_μ is monotonic. This aspect points to the peculiar mechanisms of the unsteady Coanda effect for the highest frequencies investigated which lead to a higher efficiency in base pressure recovery.

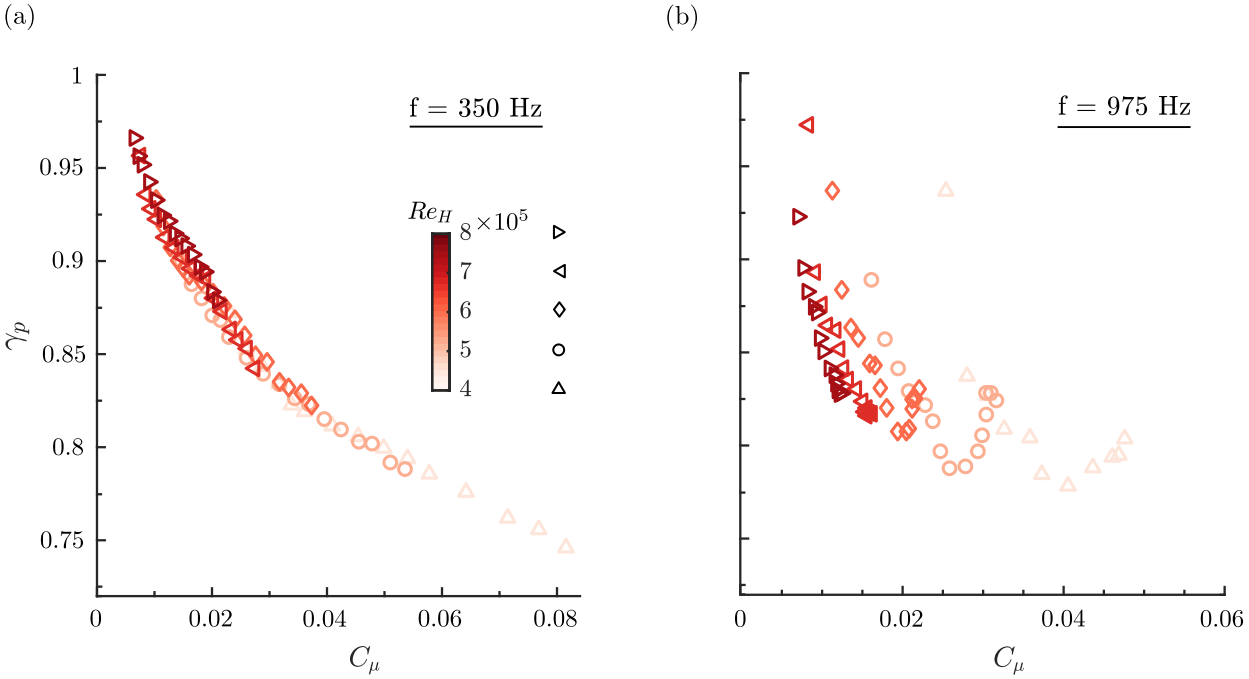

Figure 5.2: Scaling of the base pressure parameter γ_p variations with forcing amplitude C_μ and Reynolds number Re_H for the curved surfaces of dimension $r = 9h$ for forcing at (a) $f = 350$ Hz and (b) $f = 975$ Hz.

To further investigate this saturation regime at high forcing frequencies, a systematic variation of Re_H by changing the free-stream velocity U_0 is operated for forcing at $f = 350$Hz and $f = 975 - 1050$Hz in order to evidence scaling laws of the base pressure recovery. The evolution of γ_p presented in figure 5.2 for Re_H in the range $4 - 8 \times 10^5$ confirms that the amplitude coefficient C_μ defined by relation 2.3 is the right scaling parameter to explain the base pressure changes at $f = 350$Hz. Indeed, all the data gathered when forcing at $f = 350$Hz and varying Re_H collapse fairly well on a single curve on figure 5.2(a). However, the scaling based on the defined C_μ completely fails when forcing at higher frequencies ($f = 975$Hz in figure 5.2(b)) as the saturation threshold in γ_p occurs at different C_μ depending on Re_H and all the curves are horizontally offset. This complete lack of scaling using C_μ confirms the evidence of a peculiar mechanism of unsteady Coanda effect at high frequency, quite different from a classical Coanda effect as evidenced at $f = 350$Hz. In section §5.2, we will propose a scaling parameter to explain this peculiar effect. It is worth mentioning that the conclusions are equivalent when building a momentum coefficient C_μ not with the peak jet velocity $V_{j_{\max}}$ (as also done by Oxlade (2013)) but with the root-mean-square velocity as done by Barros *et al.* (2016*b*) for instance. Moreover, Oxlade *et al.* (2015) on an axisymmetric blunt body and Barros *et al.* (2016*b*) on an Ahmed body also evidenced such a saturation mechanism in base pressure recovery using simple high-frequency forcing without additional curved surfaces. This mechanism appeared to be governed by the pulsed jets dynamics.

As about 70% of the aerodynamic drag of such a body is originating from the low pressure region at the base (Grandemange *et al.* (2013*b*), Barros *et al.* (2016*b*)), monitoring the base pressure is a good indicator of the drag changes obtained. Nevertheless, as the curved surfaces are expected to be the place of a low pressure region due to the local acceleration of the flow and thus penalize the base pressure recovery obtained, we present in figure 5.1(c-f) the same evolutions as in figure 5.1(a,b) but for the base drag parameter γ_p^c (c,d) and for the aerodynamic drag parameter γ_D (e,f) defined in equations 5.1(b,c). Globally, tendencies in the evolution of γ_p^c and γ_D are confirming the observations made concerning the base pressure parameter γ_p. Maximal drag reduction of 12% (resp. 11%) at $U_0 = 25\text{ms}^{-1}$ (resp. $U_0 = 35\text{ms}^{-1}$) occurs at saturation for the high frequency forcing at $f = 975 - 1050$ Hz and is at least 5% more important than the drag decrease measured at $f = 350$Hz. The penalization resulting from the low pressure flow over the curved surfaces is clearly visible from the evolution of γ_p^c in figure 5.1(c,d). Indeed, on the one hand the saturation in base drag decrease is even more pronounced at high frequencies than observed on the γ_p curves with a higher penalization once the saturation threshold $C_\mu \sim 3 \times 10^{-2}$ has been exceeded. On the other hand, whereas forcing at $f = 350$ Hz led to a monotonic decrease in γ_p with C_μ, it here leads to a saturation in the decrease of γ_p^c above $C_\mu \sim 2.5 \times 10^{-2}$ at $U_0 = 25\text{ms}^{-1}$. Thus the penalization from the curved surfaces cannot be neglected and has to be carefully taken into account in our analysis.

As any active flow control strategy requires input energy in order to work, it is of important practical interest to know whether the developed control strategy is efficient. To assess the energetic performance of our control strategy, we follow energetic analyses discussed in a variety of previous studies (Freund & Mungal (1994), Choi *et al.* (2008), Barros *et al.* (2016*b*) or Li *et al.* (2019)). A forcing efficiency can be defined as the ratio between the energy saved by the drag reduction and the mechanical energy of the pulsed jets. For the best case investigated here at $f = 1050$ Hz around saturation at $U_0 = 35$ m s^{-1}, this efficiency ratio is around 11. Nevertheless, it should be noted that the forcing apparatus and strategy have not been optimized for energetic efficiency and this aspect remains a key research direction for practical applications which should be tackled by further studies. Further elements about energetic efficiency of the control are provided in Chapter 6.

5.1.2 Unsteady Coanda blowing along curved surfaces : coupling between forcing frequency and curvature radius

These first observations are here extended by varying the curvature radius r of the curved surface by almost halving and doubling the value of the radius ($r/h = 9$) previously analyzed.

Base pressure and drag reduction depend not only on the forcing amplitude C_μ but also on the combination of the forcing frequency and the curvature radius of the curved surfaces. Figure 5.3 illustrates the rather intriguing evolution of γ_p and γ_D for $Re = 5 \times 10^5$ (a,b) and $Re = 7 \times 10^5$ (c,d) as function of C_μ with r/h and f as parameters.

In order to highlight the trends, the tendency of each curve has been qualitatively sketched in thick lines. Tables 5.3 and 5.4 provide a summarized description of the two main results of figure 5.3 : 1) the qualitative description for a couple $(f, r/h)$ to succeed –or not– in reducing the pressure drag (table 5.3), and 2) the existence of a saturation of the base pressure recovery, maximal base pressure recovery and drag decrease at high forcing frequency (table 5.4).

The results gathered in figure 5.3 emphasize the strong coupling existing between forcing frequency and curvature radius of the add-ons. Clearly, combinations of r/h and f with a maximum of base pressure recovery and drag decrease exist. Over the range of C_μ investigated, higher reduction of γ_p requires higher forcing frequencies as the curvature radius decreases. While significant base pressure recovery and drag decrease are obtained at high forcing frequencies even for the smallest radius investigated $r/h = 5$ (respectively 8 and 6% of base pressure increase and drag decrease on figure 5.3(a) and (b)), it is not the case at the lower forcing frequency $f = 350$ Hz (figure 5.3(a,c) and table 5.3). Moreover, the steady blowing forcing requires greater radius of curvature to work and to have a clear impact on the drag as drag reduction is only obtained for $r/h = 16$. This is globally consistent with previous studies which mostly focused on steady or pulsed blowing coupled to curved surfaces of greater dimensions $r/h > 20$ (Freund & Mungal

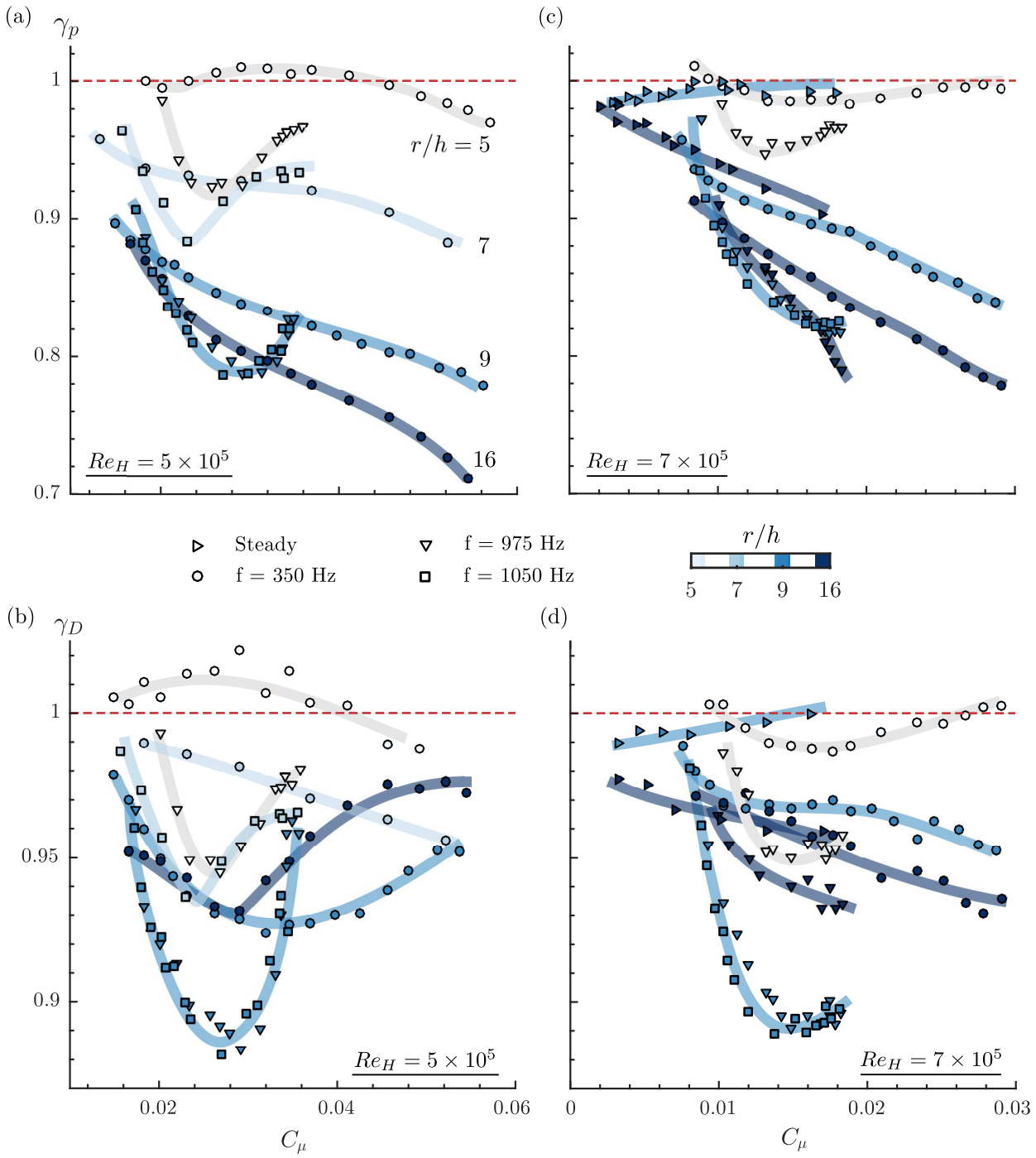

Figure 5.3: Evolution of (a) the base pressure parameter γ_p and (b) the aerodynamic drag parameter γ_D as function of the forcing amplitude C_μ with variable dimension and curvature radius $r/h = \{5, 7, 9, 16\}$ of the curved surfaces at $Re_H = 5 \times 10^5$ and $Re_H = 7 \times 10^5$. Markers are colored according to the curvature radius r/h. Similarly to figure 5.1, results for steady forcing are shown for $Re_H = 4 \times 10^5$ in order to keep forcing amplitudes C_μ comparable with the ones of unsteady forcing. Thick lines give the trend of each set of data in order to highlight the tendency of each curve. Main quantities and qualitative description of the recovery of γ_p and γ_D are gathered in tables 5.3 and 5.4.

	r/h			
f [Hz]	5	7	9	16
Steady	–	–	0.99	0.90
350	0.98	0.89	0.84	0.78
975-1050	0.92	0.88	0.82	0.79

Table 5.3: Qualitative efficiency of Coanda effect to reduce the pressure drag depending on the couple frequency–radius ($f - r/h$) based on results compiled in figure 5.3. Minimal values of γ_p measured for each couple colored in red (resp. blue) when failing (resp. succeeding) at reducing the pressure drag with a Coanda effect.

	r/h			
	5	7	9	16
$C_{\mu_{\text{sat}}}$	0.023	0.023	0.03	–
$\min \gamma_p$	0.92	0.88	0.82	0.79
$\min \gamma_D$	0.94	0.93	0.88	0.93

Table 5.4: Evolution of the saturation threshold $C_{\mu_{\text{sat}}}$, the maximal base pressure recovery $\min \gamma_p$ and the maximal aerodynamic drag decrease $\min \gamma_D$ at high forcing frequencies $f = 975$ and 1050Hz for various curved surface radius $r = \{5, 7, 9, 16\}h$. No saturation was observed for $r = 16h$ over the range of C_μ investigated.

(1994), Englar (2001), Abramson *et al.* (2011), Lambert *et al.* (2019)).

For every curved surface radius the high frequency forcing always surpasses at a given C_μ the lower frequency $f = 350$ Hz forcing both in γ_p and γ_D even if for the biggest radius $r/h = 16$ the difference in base pressure recovery at a given C_μ is reduced (see figure 5.3(a) at $Re_H = 7 \times 10^5$). Nevertheless, a clear difference of about 2% in γ_D still subsists, accounting for a difference in drag penalties from the curved surfaces between the two forcing frequencies.

These differences in pressure drag penalties due to the curved surface underline a difference in the base pressure recovery mechanisms involved. Even if the base pressure recovery is approximately the same for $r = 9h$ and $r = 16h$ (respectively 22 and 25% recovery at maximum), the penalization induced by the low pressure region extending along the curved surface is noticeably higher resulting in a lower aerodynamic drag decrease (respectively 12 and 7% decrease). As the curved surface radius is decreased the penalization is reduced according to the maximal base pressure recovery and drag decrease gathered in table 5.4. For all radii $r/h < 16$, the saturation effect persists and occurs at smaller C_μ as r/h is decreased (see table 5.4). Only for $r/h = 16$, the saturation in γ_p disappears over the investigated range of C_μ.

5.1.3 Time-scales of the unsteady separation over the curved surface

Role of the jet acceleration time-scale

Guided by Van Dyke (1969) and Bradshaw (1973), we can derive the equation for the tangential momentum balance along a mean streamline of the separating wall jet. In order to retain the effects of coherent time-fluctuations introduced by the forcing, we perform a phase-averaged decomposition of the flow so that the phase-averaged tangential momentum balance reads :

$$\frac{1}{\rho}\frac{\partial \langle p \rangle}{\partial s} = -\frac{\partial \langle U_s \rangle}{\partial t} - \langle U_s \rangle \frac{\partial \langle U_s \rangle}{\partial s} - \frac{\partial \langle u_s' u_s' \rangle}{\partial s} - \frac{\partial \langle u_s' v_n' \rangle}{\partial n} + \text{viscous term}. \tag{5.3}$$

Here, the phase-averaged decomposition of a quantity χ respective to phase t/T of the forcing cycle is defined as

$$\langle \chi(\mathbf{x}, t/T) \rangle = \frac{1}{N} \sum_{n=0}^{N} \chi(\mathbf{x}, t/T + n). \tag{5.4}$$

Frequency [Hz]	$r = 5h$	$r = 9h$	$r = 16h$
350	4.02	2.23	1.26
975	1.61	0.90	0.51
1050	1.38	0.76	0.43

Table 5.5: Evolution of the ratio t_a/t_{cr} between the pulsed jet acceleration time-scale t_a and the local convective time-scale $t_{cr} = r/U_0$ for the different frequencies and radii of curvature investigated at $U_0 = 25\text{ms}^{-1}$. A ratio < 1 indicates a pulsed jet time-scale faster than the local curved surface convective time-scale. The occurrence of jet attachment over the curved surface is possible if the ratio is around 1 or smaller, in line with the qualitative description of the base pressure recovery and drag decrease in table 5.3.

The viscous terms are not explicited for the sake of simplicity but are kept in the equation in order to perform a time-scale analysis which emphasizes the importance of unsteady effects along the curved surfaces. Two main aspects appear :

- If evaluating the viscous diffusion effects in equation 5.3, $\delta = \sqrt{\nu/f}$ allows to estimate which thickness from the surface is impacted by the viscosity during the forcing cycle. For the typical high frequency forcing time-scales used in our study, $f = 1050$ Hz, $\delta \sim 10^{-4}$ m which is one order of magnitude smaller than h and two orders of magnitude smaller than r. It thus means that viscous diffusion only has time to affect a small thickness of the flow near the curved surface during a forcing period. As a consequence the flow momentum near the curved surface is higher preventing the jet from separating from the curved surface under the influence of an adverse pressure gradient imposed by the curvature. Such effect partly arguments the inefficiency of steady blowing to work when decreasing the curved surface radius ($\delta \sim h/2$ for a Poiseuille flow in this case).
- On the other side, in equation 5.3, the time-derivative of the tangential velocity partly balances the tangential pressure gradient along the curved surface. Given the sign of each quantity, one would expect this term to allow the pulsed wall jet to sustain a stronger adverse pressure gradient along the curved surface during the peaking phase of the forcing cycle. For a positive time-derivative of the tangential velocity corresponding to the acceleration phase of the pulsed jet, the adverse pressure gradient along the curved surface diminishes and thus the flow can remain attached farther on the surface. As a consequence, a strong positive tangential acceleration $\frac{\partial \widetilde{U_s}}{\partial t}$ would allow the unsteady Coanda blowing to still work with smaller curvature radius, which goes in line with our results gathered in figure 5.3 and table 5.3.

To further underline this last point, we compare in table 5.5 for different couples $(f, r/h)$ the acceleration time-scale t_a to the characteristic convective time-scale related to the curved surface $t_{cr} = r/U_0$. This scaling appears to physically explain why the lower frequency forcing $f = 350$Hz is not able to reduce the pressure drag when coupled to the smaller curved surface $r = 5h$ whereas the higher frequency forcing is. Indeed, for both $r/h = 5$ and 9, t_a for high frequency forcing is of order the local convective time-scale. Nevertheless, when forcing at $f = 350$Hz, t_a eventually becomes around 4 times greater than the convective time-scale when r is decreased to $5h$. In this last case, the unsteady term may no longer be sufficient for the pulsed jet to sustain the stronger adverse pressure gradient along the curved surface, and thus the Coanda effect is unable to occur to reduce the pressure drag of the body. This comparison of the local convective time-scale t_{cr} with the pulsed jet acceleration time-scale t_a allows to qualitatively predict the occurrence of the Coanda effect indicated in table 5.3.

Adaptation of the forcing frequency to the curved surface

To characterize the unsteadiness of the dynamics of flow separation and reattachment over the curved surfaces, we consider now a Strouhal number St_r based on the convection time-scale over the curved surface t_{cr} :

$$St_r = f t_{cr} = f \frac{r}{U_0}. \tag{5.5}$$

This leads to values of $St_r \sim 0.13$ for $f = 350$Hz and 0.39 for $f = 1050$Hz. For $St_r \sim 1$, the forcing time-scale is similar to the characteristic convection time-scale over the curved surface. Thus when a new forcing period begins and produces a new pulsed jet, the previous one is still interacting with the curved surface. In this sense the interaction between the curved surface and the pulsed jet is called adapted. When St_r is much smaller than one, here for $f = 350$Hz $St_r = 0.13$, the forcing is unadapted because the flow perturbation from the forcing has the time to be completely convected away from the curved surface before a new forcing period occurs. As a result, the dynamics of the flow over the curved surface become more unsteady with a detrimental impact on the base pressure recovery.

The dynamics of flow reattachment and separation over the curved surface (Waldon *et al.*, 2008) are investigated in more detail for the two different forcing frequencies of interest with the curved surface $r/h = 9$. To this purpose, we focus on the spanwise vorticity defined as

$$\omega_y = \frac{\partial u_x}{\partial z} - \frac{\partial u_z}{\partial x}. \tag{5.6}$$

To characterize the evolution of the flow state over the curved surface during one forcing period, we introduce a criterion based on the phase-averaged vorticity $\langle\omega_y\rangle$ to estimate the flow separation location on the curved surface. It is defined as the minimal angular position near the curved surface (with an origin taken at the slit as indicated on figure 5.4(a)) where positive phase-averaged vorticity is found (opposite sign of the vorticity present in the separated shear-layer)

$$\theta_S = \min_{\theta}(\langle\omega_y\rangle \geqslant 0), \tag{5.7}$$

Moreover, to confirm the pertinence of this local criterion, we define a global indicator Γ_S characterizing the strength of the flow separation along the curved surface. It is defined as the total positive circulation in a contour surrounding the detached region over the curved surface (see figure 5.4(a))

$$\Gamma_S = \iint\limits_{C\cap\{\langle\omega_y\rangle\geqslant 0\}} \langle\omega_y\rangle dxdz. \tag{5.8}$$

The region C is chosen so as to capture only the positive vorticity induced by the recirculating flow over the downstream part of the curved surface. Indeed, all the positive vorticity originating from the pulsed jets and their interaction with the shear layer is always out of the chosen contour. The separation dynamics presented in figure 5.4 show that the mean separation angle θ_S is higher and the mean separation strength Γ_S lower for the high frequency case $f = 1050$Hz than for the lower frequency case $f = 350$Hz at $C_\mu \sim 3 \times 10^{-2}$ around saturation. Moreover, the lower frequency forcing at $f = 350$Hz exhibits stronger fluctuations of both quantities, which accounts for a strong unsteadiness in the reattachment and separation dynamics. This leads to high values of both tangential-normal $\overline{u_s' v_n'}$ and normal-normal $\overline{v_n' v_n'}$ Reynolds stresses near the curved surface, especially in the vicinity of the mean flow separation from the curved surface, as explicited in figure 5.4(b-d). A further penalization of the base pressure recovery is thus due to the highly unsteady dynamics of the separation and reattachment process when forcing at $f = 350$Hz.

5.1.4 Effect of the unsteady reattachment and separation on the surface pressure

The dynamics of the base pressure C_{pb} (figure 5.5(a)) and the pressure over the curved surface (figure 5.5(c)) for forcing at $f = 1050$Hz for amplitudes $C_\mu = \{1.9, 2.5, 3, 3.6\}$ spanning the whole investigated range are in complete phase opposition and dictated by the dynamics imposed by the pulsed jets. The evolution of C_{pb} indicates that the base pressure recovery is directly related to the importance of the flow reattachment over the curved surface which dictates the boat-tailing imposed to the wake. A large depression is created over the curved surface during the peaking phase of the pulsed jet velocity followed by an important recompression in the following phase. The amplitude of this recompression can be seen to evolve monotonically with C_μ until the saturation

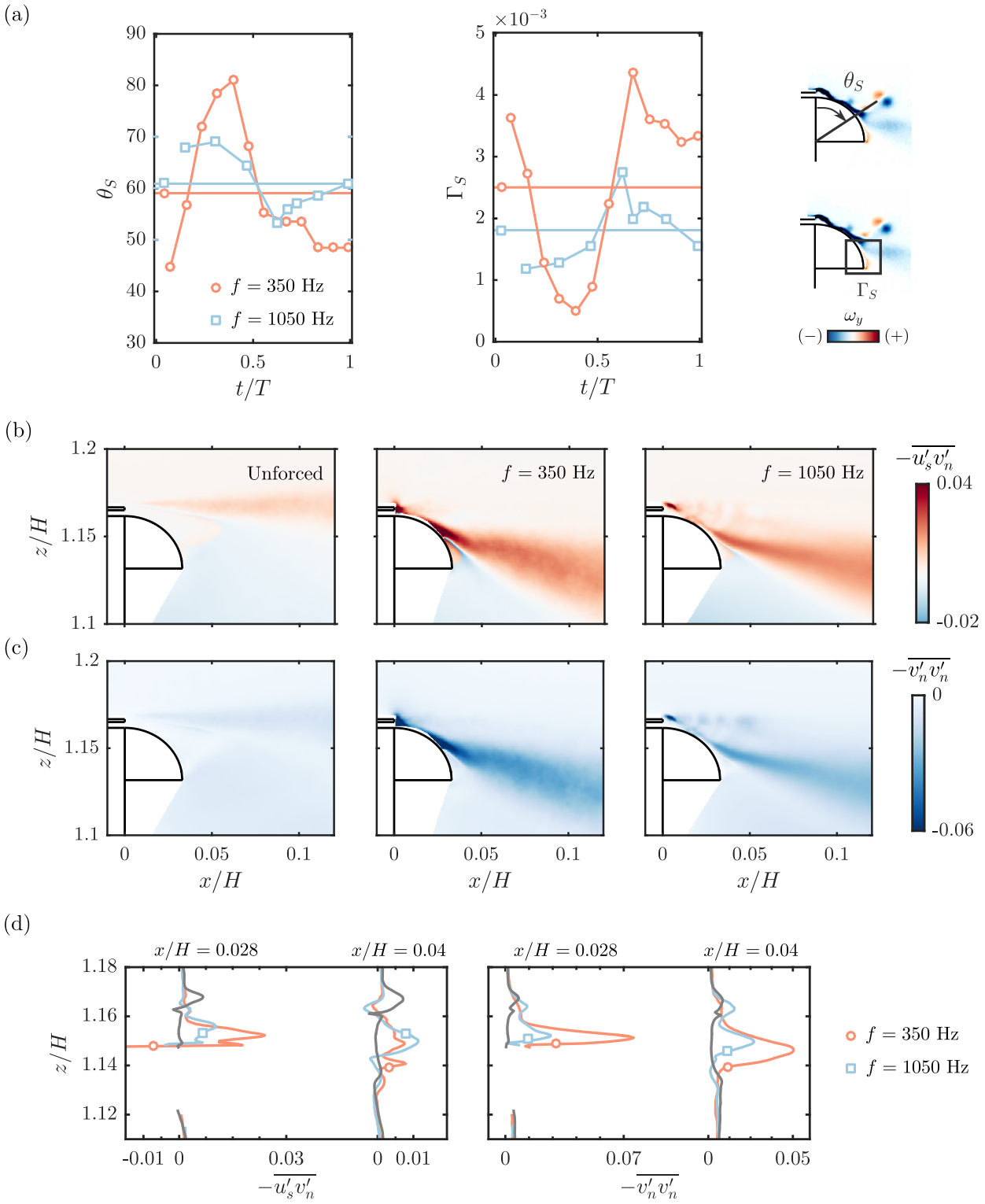

Figure 5.4: Phase-averaged description of the dynamics of the unsteady reattachment and separation over the curved surface for forcing at $f = 350$ Hz and $f = 1050$ Hz at similar forcing amplitude $C_\mu \sim 3 \times 10^{-2}$ with the $r/h = 9$ curved surfaces. (a) Phase-averaged evolution of the separation angle θ_S and the positive circulation Γ_S in the separated region over the curved surface. Horizontal lines denote the time-averaged quantities. (b) Tangential-normal Reynolds stresses $-\overline{u_s' v_n'}$ and (c) normal-normal Reynolds stresses $-\overline{v_n' v_n'}$. (d) Vertical profiles of Reynolds stresses shown in (b,c) at selected streamwise locations $x/H = 0.028$ (just after the mean location of flow separation from the curved surface) and $x/H = 0.04$ (just after the end of the curved surface).

with a following decrease at higher C_μ. These pressure dynamics are completely in line with the flow separation dynamics previously presented in figure 5.4. Moreover, it should be noted that the pressure dynamics over the curved surface and at the base for forcing at $f = 350$ Hz (not shown here for brevity) follow similar behaviour as Γ_S and θ_S with variations of quite larger amplitude over a forcing cycle compared to $f = 1050$ Hz (for instance, at the optimum $C_\mu \sim 3 \times 10^{-2}$, the base pressure C_{pb} undergoes fluctuations of amplitude 60% higher at $f = 350$ Hz), confirming the difference in adaptation of the pulsed jet/curved surface interaction.

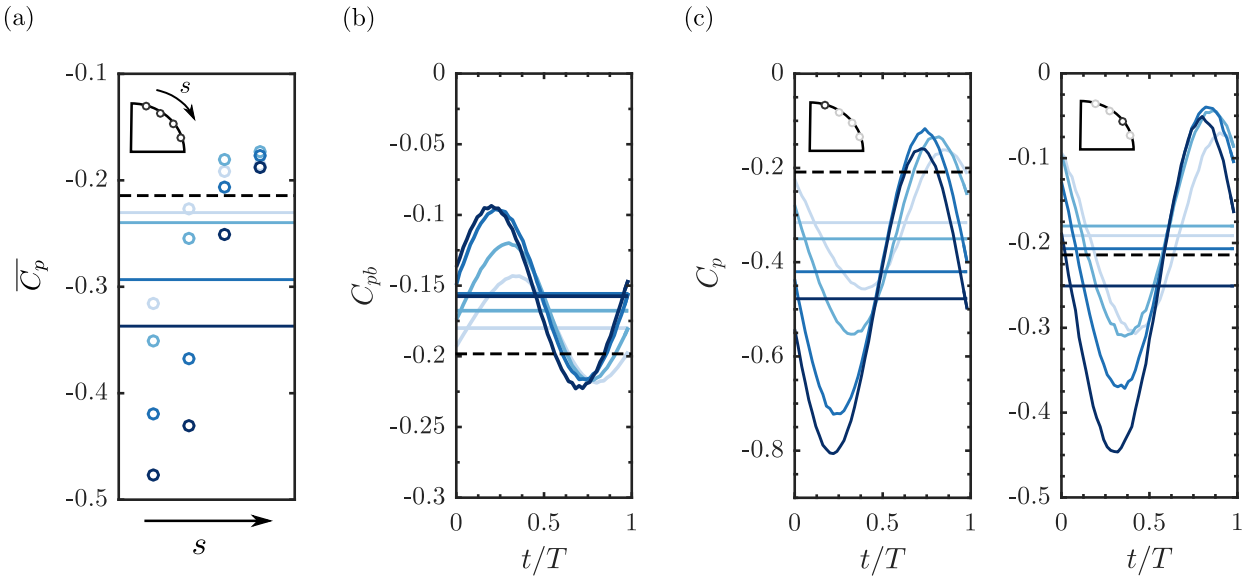

Figure 5.5: Evolution of the wall pressure coefficient C_p for forcing at $f = 1050$ Hz with various amplitudes $C_\mu = \{1.9, 2.5, 3, 3.6\}$. Darker shades of blue indicate increasing forcing amplitude C_μ. (a) Phase-averaged base pressure coefficient C_{pb}. (b) Evolution of the time-averaged pressure coefficient $\overline{C_p}$ along the curved surface. Horizontal lines indicate the corresponding mean pressure coefficient averaged along the curved surface $\overline{C_{pc}}$. (c) Phase-averaged pressure coefficient along the curved surface. Horizontal lines indicate the corresponding time-averaged pressure coefficient $\overline{C_p}$. In (c) the inserted schemes indicate the position of the considered pressure measurement. Horizontal dashed black lines correspond to the unforced flow.

The flow acceleration over the curved surface results in a low pressure region as expected in the common Coanda effect which is penalizing the base pressure recovery. This penalization was observed to further increase after the saturation in base pressure recovery at high frequencies of forcing (see figure 5.1). The average pressure distribution over the curved surface given in figure 5.5(b) shows the important depression created on the curved surface in the vicinity of the slit. This depression grows with C_μ and is attenuated when progressing towards the end of the curved surface. It thereby highlights the creation of a low pressure region whose extent is time-dependent. The first pressure tap considered in figure 5.5(c) is located upstream of $\overline{\theta_S}$ and therefore the local pressure value is below the value of the naturally detached unforced flow. The second pressure tap is located in the vicinity of $\overline{\theta_S}$ where the flow detaches. When comparing the $\overline{C_p}$ at each location with the average pressure distribution over the curved surface in the unforced case, we can see how the flow detaches farther downstream as C_μ is increased. This appears very clearly from the $\overline{C_p}$ being below the unforced average value at the third pressure tap location only for the highest C_μ (see figure 5.5(b)). This observation accounts for the overly increased penalization induced by the curved surface after the saturation in base pressure recovery.

Now that the main effects of forcing on the pressure drag of the body have been characterized and interpretations of the main time-scales governing the unsteady Coanda effect have been introduced, the remainder of the paper focuses on analysing in detail the mechanisms of base drag decrease and trying to build a pertinent model incorporating all the mechanisms behind the unsteady Coanda effect.

5.2 Scaling the base drag changes : unsteady vorticity dynamics

In this section, an extensive analysis of the unsteady vorticity dynamics driven by the forcing is performed. The aim is to derive a scaling for the base pressure and drag changes observed at high frequency in §5.1, able to physically explain the saturation effect.

5.2.1 Local vorticity-flux dynamics at separation

We focus on a fine-scale analysis of the flow interaction with the forcing near the separating edge both from a dynamical point of view. This is motivated by the unsteady separation analysis in the previous section having shown the important differences in separation dynamics and their relation to drag changes.

First, it should be noted from the time-averaged spanwise vorticity field depicted on figure 5.6(a) that the unforced flow is completely detached from the curved surface. This is expected because of the boundary condition imposed at the salient edge over the curved surface. A strong negative vorticity sheet is formed in the continuity of the detachment of the boundary layer at the edge of the base. A weaker positive vorticity sheet is formed from the recirculating flow in the wake interacting with the lower edge of the curved surface (zone denoted (D)), which was previously used to describe the flow separation dynamics.

As the pulsed jets are responsible for the modulation of the vorticity flux in the vicinity of separation, the wake dynamics are investigated through a phase-averaged description over the forcing cycle starting at the beginning of the blowing phase. The vorticity dynamics are described in figure 5.6(b,c) for the two basic forced cases at $C_\mu \sim 3\times10^{-2}$ at both $f = 350$Hz and $f = 1050$Hz, the latter corresponding to the highest base drag reduction case.

At $f = 1050$ Hz (figure 5.6(b)), the strong negative vortex sheet is partially attached on the curved surface over a length which can be seen to fluctuate throughout the forcing cycle. The vorticity dynamics during the forcing cycle exhibit the formation of two main coherent structures of opposite vorticity denoted respectively (I) and (II). These are convected downstream while interacting with the curved surface and the outer potential flow. The structure with negative vorticity denoted (I) appears to be formed during the first instants of the forcing cycle (until $t/T \sim 0.15$, corresponding to the peaking time of the pulsed jet velocity) by the pinch-off of the separating boundary layer. The vorticity sheet formed at the separation of the boundary-layer at the edge of the base is brutally perturbed by the begin of the blowing phase of the pulsed jets and thus pinches off because of the sudden change in the orientation of separation. It then rolls up to form a structure of apparent size h. The positive coherent structure (II) is formed just after (I) around $t/T \sim 0.3$. This positive vorticity coherent structure is likely to originate from the flux of vorticity from the pulsed jet as there is no other source of positive vorticity in the flow (Gharib *et al.*, 1998). It is then convected away in a pair with (I) and they pass over the curved surface where they play a key role in the flow reattachment process over the curved surface. At the end of the forcing cycle the two counter-rotating structures have reached approximately $x \sim 2r$ and still remain coherent enough to be detected. Thus, this leads to the formation of a train of coherent structures over a couple of forcing cycles which is materialized by the structure denoted (I_{-1}) which is the structure (I) persisting from the previous forcing cycle. This train of coherent structures seems characteristic of this type of high-frequency forcing as it was already observed through similar measurement techniques by Oxlade *et al.* (2015).

The formation of the negative coherent structure (I) at the lower frequency of $f = 350$ Hz in figure 5.6(c) does not appear clearly and is more likely absent. Nevertheless, the positive coherent structure (II) is still formed in a similar fashion. As the forcing cycle is 3 times longer at this forcing frequency, most of the forcing cycle is marked by the absence of coherent structures in the vicinity of the curved surface. This appears as one of the most striking difference with the high-frequency forcing and should consequently affect the interaction with the flow reattachment process over the curved surface.

To further characterize the formation, evolution and convection of these coherent structures (I) and (II), and to analyze their role in the unsteady Coanda effect, we describe their strength by their total circulation Γ_I and Γ_II. The circulation of a coherent structure is estimated with the

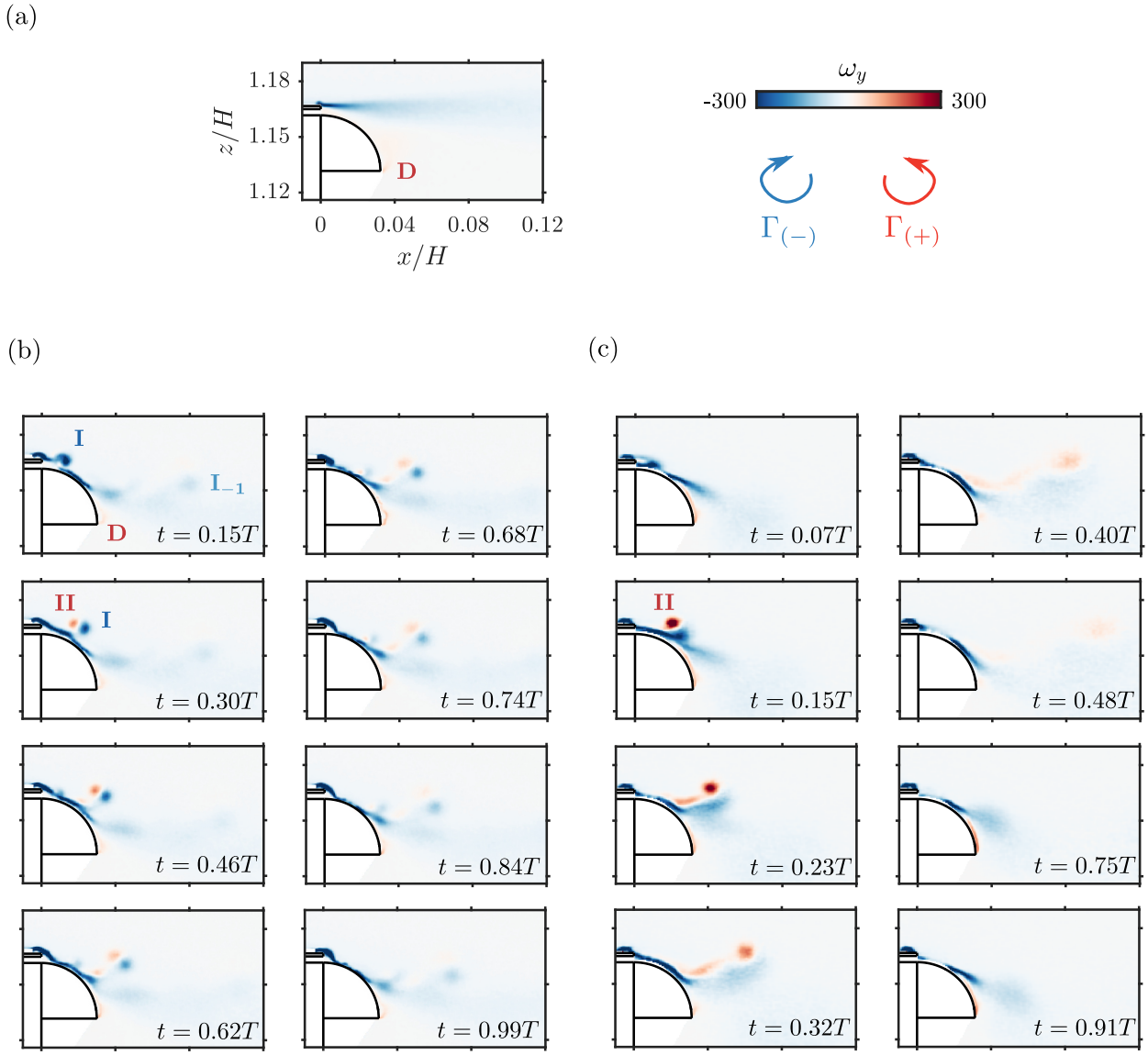

Figure 5.6: Phase-averaged description of the spanwise vorticity ω_y dynamics under forcing for the curved surfaces of dimension $r = 9h$ at $Re_H = 5 \times 10^5$. (a) Time-averaged vorticity $\overline{\omega_y}$ of the unforced flow. Phase-averaged vorticity for flow forced (b) at $f = 1050$ Hz and $C_\mu = 3 \times 10^{-2}$ at times t = {0.15, 0.3, 0.46, 0.62, 0.68, 0.74, 0.84, 0.99}, and (c) at $f = 350$ Hz and $C_\mu = 3 \times 10^{-2}$ at times t = {0.07, 0.15, 0.23, 0.32, 0.4, 0.48, 0.75, 0.91}. Annotations on the figures correspond respectively to the negative coherent structure forming during the pulsed jet acceleration phase (I), the same coherent structure persisting from previous forcing period (I_{-1}), the positive coherent structure forming from the pulsed jet (II), and the region where the flow is detached from the curved surface (D).

following procedure. The structure is identified using a 2D swirling strength criterion (Zhou *et al.*, 1999), the threshold of which is chosen high enough to isolate it from the background noise and make the identification unambiguous. Then a rectangular contour C is manually drawn around the identified structure to have a supporting contour containing the whole structure where the circulation will be evaluated[1]. The circulation Γ_{I} (resp. Γ_{II}) is computed as the summation over only negative (resp. positive) phase-averaged vorticity $\langle\omega_y\rangle$:

$$\Gamma_{\mathrm{I}} = \iint\limits_{C\cap\{(x,z);\langle\omega_y\rangle<0\}} \langle\omega_y\rangle dxdz, \quad \Gamma_{\mathrm{II}} = \iint\limits_{C\cap\{(x,z);\langle\omega_y\rangle>0\}} \langle\omega_y\rangle dxdz. \tag{5.9a, b}$$

The position $\mathbf{x}_{\mathrm{I}} = [x_{\mathrm{I}}, z_{\mathrm{I}}]$ of the structure (I) (and analogously for the structure (II)) is finally evaluated as the barycenter of the identified coherent vorticity :

$$\mathbf{x}_{\mathrm{I}} = \frac{\displaystyle\iint\limits_{C\cap\{(x,z);\langle\omega_y\rangle<0\}} \mathbf{x}\langle\omega_y\rangle dxdz}{\displaystyle\iint\limits_{C\cap\{(x,z);\langle\omega_y\rangle<0\}} \langle\omega_y\rangle dxdz}. \tag{5.10}$$

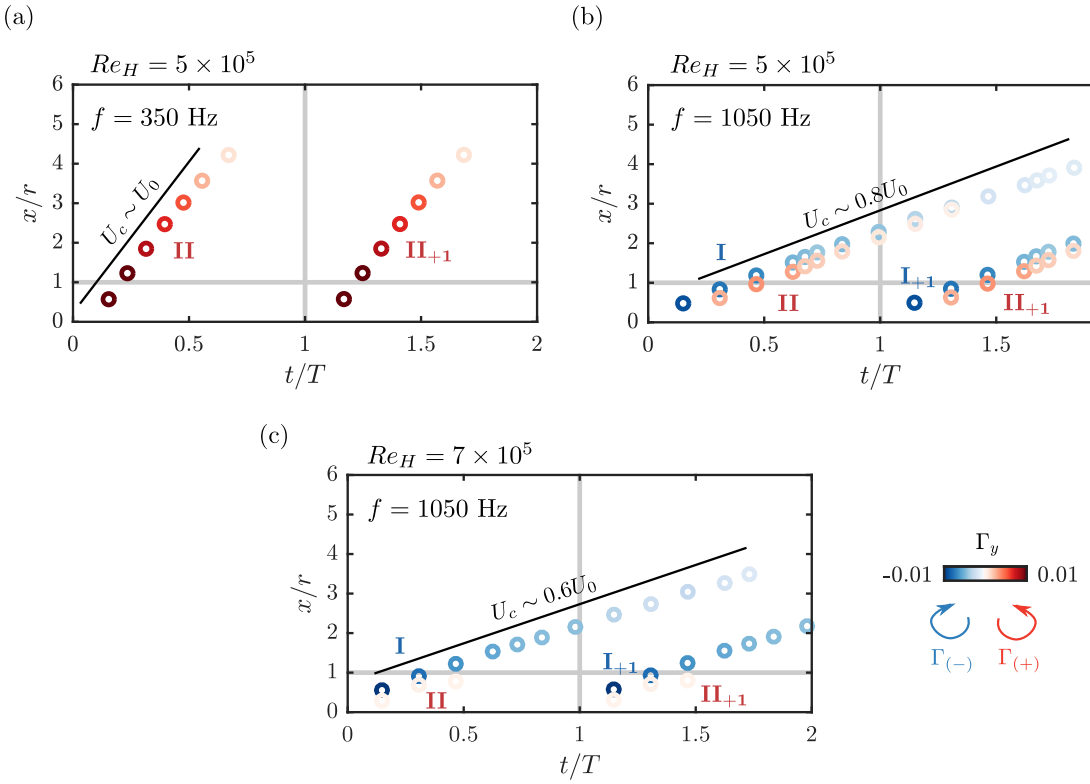

Figure 5.7: Streamwise convection and evolution of the circulation Γ of the two counter-rotating coherent structures (I) and (II) identified in figure 5.6 when forcing at $C_\mu = 3\times10^{-2}$ at (a) f = 350 Hz and (b) f = 1050 Hz at $Re_H = 5\times10^5$ and at (c) f = 1050 Hz at $Re_H = 7\times10^5$ for $r/h = 9$. Each marker is colored according to the circulation Γ of the coherent structure. Black lines indicate an estimation of the mean convection velocity of coherent structure (I).

The strength Γ and the streamwise position of the coherent structures (I) and (II) thus tracked are shown in figure 5.7 for both the forced cases investigated so far in this section at $C_\mu \sim 3\times10^{-2}$ around the saturation in base pressure recovery. The tracking highlights the formation of a train of vortices at high frequency f = 1050Hz which increases the presence density of coherent structures

[1]There is only very weak sensitivity of the estimated circulations to the choice of this contour as the vorticity decays fast to zero when going away from the center of the identified region (see figure 5.16 for instance).

in the vicinity of the curved surface during the whole forcing period. There is hence an important interaction between these structures and the flow near the curved surfaces which is absent when forcing at $f = 350$Hz where structures are only present in the vicinity of the curved surface for a reduced amount of time (around a quarter of a forcing period). This confirms the strong coupling between forcing frequency and radius of curvature discussed in §5.1. The convection velocity of the coherent structures can also be evaluated based on their tracking. Interestingly, when comparing similar pulsed jets velocity forcing conditions at $f = 1050$Hz at different Reynolds numbers $Re_H = 5$ and 7×10^5 in figure 5.7(b,c), the convection velocity U_c can be seen to remain globally constant during the forcing period but with quite different values depending on Re_H varying from $0.8U_0$ to $0.6U_0$ at increasing Re_H. As the convection velocity is globally set by the mean velocity around the structure, this informs us that coherent structures are not positioned in the same way relatively to the mean separatrix of the wake depending on C_μ. Indeed, as will be discussed in the next section from figure 5.12(b), the wake gets narrower with increasing C_μ as the mean separatrix is deflected inwards by the interaction with the curved surfaces. As a consequence, the coherent structures which are formed at a constant vertical position are evolving in a surrounding flow of higher velocity close to or exceeding U_0 for high C_μ and important narrowing of the wake, and of lower velocity close to the shear layer velocity $U_0/2$ for low C_μ and less important narrowing. This convection velocity U_c could be used as a further refinement in the definition of the local Strouhal number introduced in relation 5.5 as it represents the actual velocity governing the interaction of the coherent structures with the flow above the curved surface.

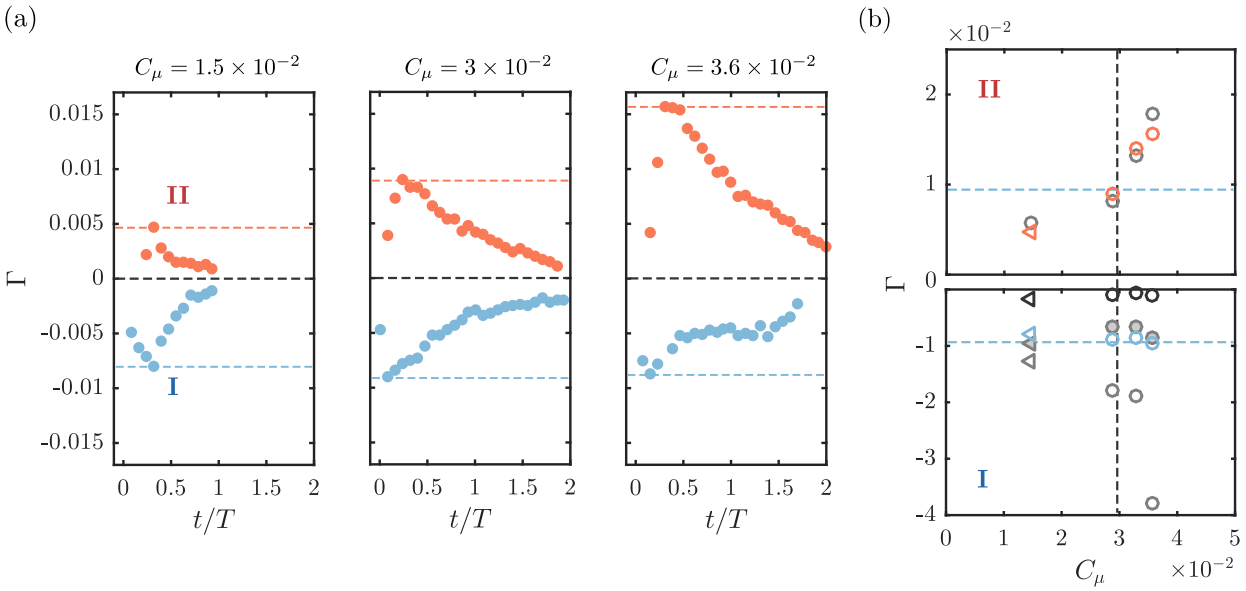

Figure 5.8: Evolution and scaling of the circulation Γ of the two counter-rotating structures (I) and (II). (a) Formation and evolution in time for different forcing amplitudes C_μ. The colored horizontal dashed lines indicate the approximate maximal circulation reached by each structure. (b) Evolution of the peak values of Γ with C_μ : experimentally measured Γ in red and blue, theoretical model of circulation in gray. (II) : pulsed jet-based circulation from equation 5.13 in light gray empty symbols. (I) : boundary-layer-based circulation from equation 5.14 in gray filled symbols, pulsed jet-based circulation from equation 5.15 in empty light and dark gray symbols (see text for further description). As in figure 5.2, circles for $Re_H = 5 \times 10^5$ and left-pointing triangles for $Re_H = 7 \times 10^5$. The horizontal blue dashed lines indicate approximately $\pm$ the maximal circulation reached by (I) and the vertical dashed line the C_μ at which saturation occurs.

The evolution of the strength of the coherent structures is more finely analyzed in figure 5.8 in order to further describe their origin and formation. Time evolution of Γ_I and Γ_II are described for forcing at $f = 975$Hz and varying C_μ spanning both below and over saturation regimes ($f = 975$Hz is chosen to take advantage of the more important phases available in our measurements, but evolution are qualitatively and quantitatively similar at $f = 1050$Hz). For both structures, in all the cases, clear distinction can be made between the formation period and the convection and dissipation period. The formation period occurs with a fast time-scale for both structures, until maximal absolute circulation has been reached, compared to the dissipation time-scale of the

structure which is one order of magnitude longer. Circulation quasi-linearly increases during the formation period before exponential decay occurs during the dissipation of the structure. Careful examination of the formation times of each structure (I) and (II) leads to the following estimations :

- Formation of structure (I) starts at $t/T = 0$ and lasts a time roughly equivalent to the peaking time t_p of the pulsed-jet velocity V_j.
- Formation of structure (II) starts when V_j begins to exceed the surrounding flow velocity at the location of formation (of order U_0) which allows the vorticity to positively roll up, against the vorticity of the shear layer. Similarly, it stops when V_j ceases to exceed the surrounding velocity at the location of formation of order U_0.

These time-scales are further exemplified in figure 5.16(a) on a particular example to highlight their accordance with the measured circulation dynamics.

5.2.2 Scaling the saturation in base pressure recovery

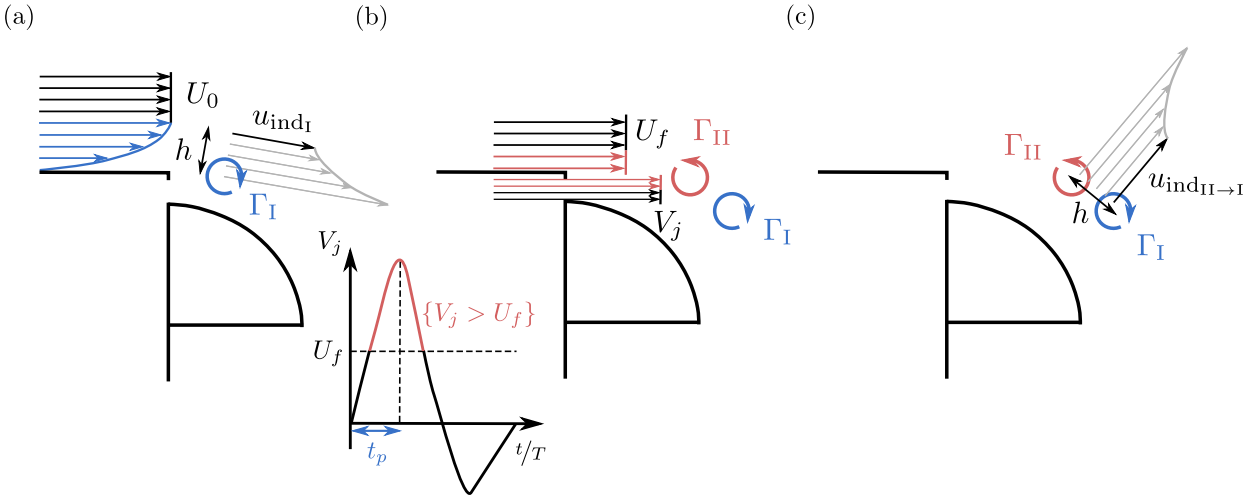

Figure 5.9: Theoretical inviscid-flow model for the interaction between the pulsed jet and the shear layers surrounding the recirculating wake. (a) Pinch-off of the separating boundary layer by the pulsed jet during the peaking time t_p leading by rolling-up of the boundary-layer vorticity to the formation of structure (I) inducing velocity $u_{\mathrm{ind_I}}$ on the potential region of the wake flow. (b) Formation of the counter-rotating structure (II) during the phase where jet velocity V_j exceeds the local surrounding flow velocity U_f. (c) Saturation in base pressure recovery mechanism where the upward velocity induced by (II) $u_{\mathrm{ind_{II\to I}}}$ prevents the Coanda effect.

We propose to describe the vorticity dynamics in the vicinity of the separating edge by an inviscid-flow model. The aim is to explain the increased drag reduction observed when forcing at high frequencies of order $O(U_0/r)$ and the concomitant saturation effect at high forcing amplitude C_μ.

Following Shariff & Leonard (1992) and Berk *et al.* (2017), under local two-dimensional flow assumption, the vorticity flux per unit width can be expressed as

$$\frac{d\Gamma}{dt} = \int \langle \omega_y \rangle \langle u_x \rangle dz = \int \frac{\partial \langle u_x \rangle}{\partial z} \langle u_x \rangle dz = \frac{1}{2} \langle u_x \rangle^2 (t) \tag{5.11}$$

with the notations referring to the case of the top shear layer. When further integrating over a period t, it comes the total amount of circulation Γ created over a given time period

$$\Gamma = \frac{1}{2} \int_0^t \langle u_x \rangle^2 dt. \tag{5.12}$$

As from the vorticity dynamics described in previous section we identified two main coherent structures forming during the forcing cycle, we want to link their formation to the dynamics of the shear layer and the pulsed jets. To do so, figure 5.9(a,b) conceptualizes the formation process of the identified counter-rotating structures (I) and (II).

The formation of the structure (II) is determined by the vorticity flux occuring from the pulsed jet and its interaction with the surrounding flow. It is thus dictated by the difference between the pulsed jet velocity V_j and a local surrounding flow velocity U_f at the location where the structure is formed, in the vicinity of the separating edge. This velocity depends on the relative position between the structure (II) and the wake separatrix which is highly influenced by the flow reattachment over the curved surface and the flow deviation dictated by the curved surface (similarly as discussed previously for U_c). As such, it is highly unlikely that this local flow velocity is directly the reference free-stream velocity U_0. Rather, U_f will more depend on a combination of both U_0 fixing the velocity farther from the separating edge and the ratio $V_{j_{\max}}/U_0$ dictating the flow deviation over the curved surface and the flow acceleration when circumventing the salient edge. Therefore, a pertinent, albeit gross, approximation of this complex formation process is to set the velocity U_f involved in the formation process of structure (II) as a constant. To partially support this approximation, we can turn back to the convection velocity U_c of the coherent structures analyzed in figure 5.7 which is also a local mean flow velocity over the curved surface where the structures are transported. The convection velocity U_c of these structures was found to vary from $0.8U_0$ at $Re_H = 5\times10^5$ to $0.6U_0$ at $Re_H = 7\times10^5$ for the same forcing conditions at high frequency. Nevertheless, these two convection velocities represent approximately the same dimensional velocity. The local formation velocity is thus set at a value of $U_f \sim 30$ m s^{-1} in the remainder of our analysis based on a fit of the theoretical circulation Γ_{II} to the measured circulation in figure 5.8(b).

Besides, this formation process can only occur if the jet velocity V_j exceeds U_f, sine qua non condition for positive circulation to be generated. The time horizon corresponding to this condition is highlighted in red in figure 5.9(b). Finally, as the pulsed jet flow near the curved surface can remain attached to the surface, only velocity from the upper half of the slit is contributing to the circulation of the structure (II). It thus leads for the theoretical circulation Γ_{II}

$$\Gamma_{\mathrm{II}} = \frac{1}{2} \int\limits_{t\in\{t;V_j(t)>U_f\}} (V_j(t) - U_f)^2 dt. \tag{5.13}$$

This theoretical circulation estimation is quite satisfyingly in line with the experimentally measured circulation Γ_{II} as shown in figure 5.8(b).

Structure (I) forms from the rolling-up of the vorticity of the model's boundary layer. As such, the total circulation Γ_{I} contained in (I) is derived from equation 5.12 and reads as

$$\Gamma_{\mathrm{I}} = -\frac{1}{2}\int_0^{t_p} U_0^2 dt = -t_p\frac{U_0^2}{2} \tag{5.14}$$

where t_p is the peaking time of the pulsed jets (the time to reach the maximal jet velocity $V_{j_{\max}}$ as defined in figure 5.9(b)) and U_0 the free-stream velocity as the formation process of (I) involves the vorticity contained in the model's boundary layer at separation. The choice of t_p as time horizon for the formation of structure (I) is physically based on the accelerating nature of the peaking phase followed by a decelerating phase which ends the disruption and roll-up process of the vorticity contained in the boundary layer. It is confirmed by the circulation dynamics analyzed in figures 5.6 and 5.8 and exemplified on a particular example in figure 5.16. The physical origin of structure (I) is validated by the comparison of relation 5.14 with measured circulations in figure 5.8(b). The other possible origin of (I) would be circulation produced directly by the pulsed jet similarly to the creation of (II), but this hypothesis is rejected by the pulsed-jet-based estimation of circulation on figure 5.8(b). Analogously to relation 5.13, a pulsed-jet origin of the circulation

contained in (I) would be captured by a relation

$$\Gamma = -\frac{1}{2}\int_0^{T_f} V_j(t)^2 dt. \tag{5.15}$$

where T_f could either be the time horizon for which V_j reaches U_f (on similar grounds as the ones given for (II)) or t_p. Both estimations are inadequate to capture neither the order of magnitude nor the trend in the evolution of Γ_{I} with C_μ on figure 5.8(b).

Two important aspects of these circulation models for Γ_{I} and Γ_{II} are :

1. The high sensitivity of Γ_{II} to the amplitude of the forcing C_μ contrary to Γ_{I} which remains fairly constant across the investigated configurations.

2. The optimality of the pressure drag decrease obtained for values of Γ_{I} and Γ_{II} of similar order of magnitude ($|\Gamma_{\mathrm{I}}| \sim |\Gamma_{\mathrm{II}}|$) which appears on figure 5.8.

As such, the interplay between structures (I) and (II) points naturally out to a possible mechanism explaining the saturation in pressure drag which we will further detail.

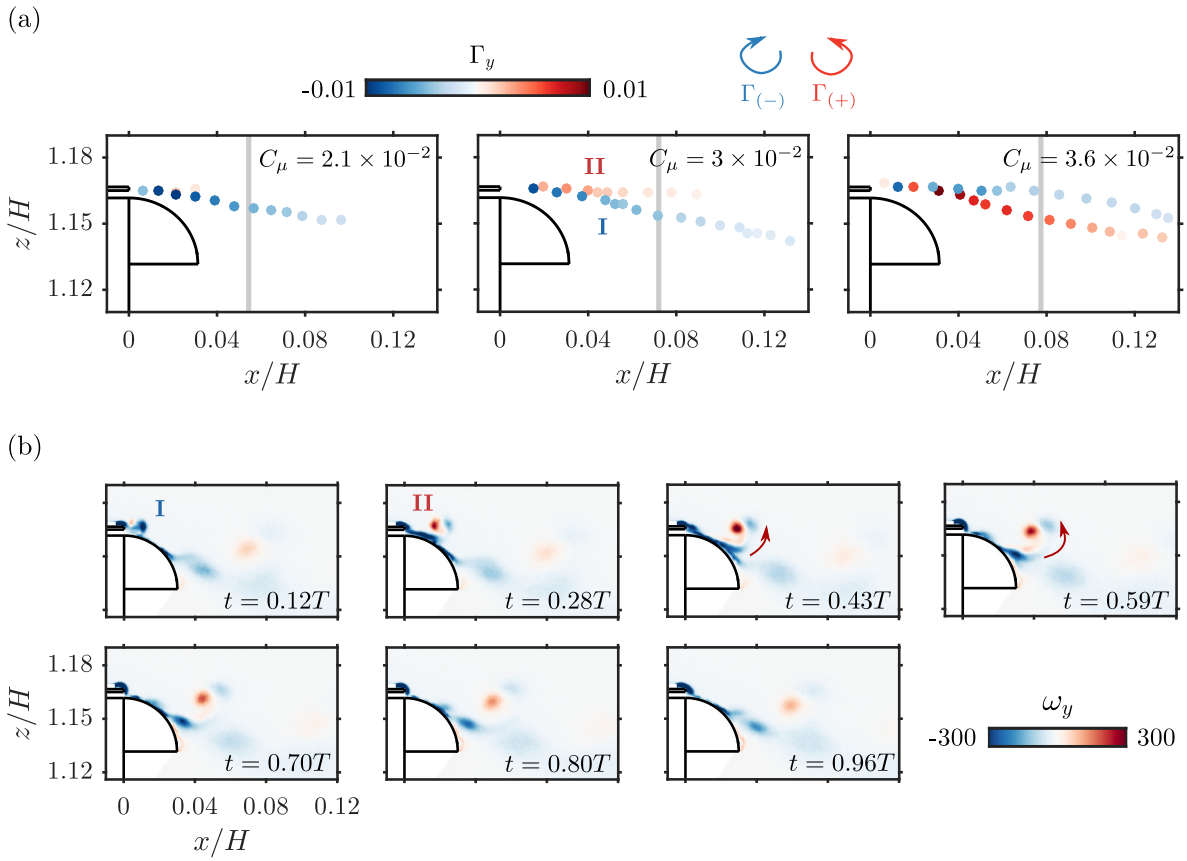

Figure 5.10: Circulation dynamics in the base pressure recovery saturation mechanism for forcing at f = 1050 Hz. (a) Tracking of the circulation Γ of the two counter-rotating coherent structures (I) and (II) identified in figure 5.6 when forcing at $C_\mu = \{2.1, 3, 3.6\} \times 10^{-2}$ at $Re_H = 5 \times 10^5$ for $r/h = 9$. Each marker is colored according to the circulation Γ of the coherent structure. The vertical grey line indicates the position of (I) after one period T of forcing. (b) Phase-averaged sequence of the spanwise vorticity ω_y dynamics for $C_\mu = 3.6 \times 10^{-2}$ after saturation of the base pressure recovery. The red arrows qualitatively illustrate the induced velocity from (II) entraining (I) away from the curved surface.

The presence of the unsteady pulsed jet over the curved surface allows for two main positive factors which explain the base drag reduction observed. For one thing the pulsed jet leads to the unsteady attachment and separation of the flow over the curved surfaces and the boat-tailing in the wake. For another thing, the structure of negative vorticity (I) plays an important role on

the curvature of the wake separatrix in the vicinity of separation from the curved surface. This aspect will be further analysed and detailed in section 5.3. On the other hand, if the pulsed jet becomes too strong, then the circulation Γ_{II} importantly increases and dominates the dynamics around separation. As described in figure 5.9(c), the circulation Γ_{II} of the coherent structure (II) induces an upward velocity on both the structure (I) and the flow attached to the curved surface which tends to mitigate the positive effect of the structure (I) and to prevent the flow from further reattaching to the curved surface. These detrimental effects are directly linked to the observed saturation in base pressure recovery. Indeed, the circulation dynamics at high frequency detailed in figure 5.10 show the dominant influence of the structure (II) when increasing C_μ above the base pressure saturation threshold. Whereas the dynamics of (I) remain only moderately influenced by (II) below $C_\mu \sim 3 \times 10^{-2}$ – which can be seen from the undisturbed trajectory of (I) curving inwards tangentially to the curved surface –, its formation and trajectory are strongly disturbed by the presence of structure (II) above the saturation threshold at $C_\mu \sim 3.6 \times 10^{-2}$. As a consequence, (I) is entrained by (II) and has an upwards trajectory towards the end of the curved surface. This lift-off movement is clearly seen from the phase-averaged dynamics detailed in figure 5.10(b). The global upwards trajectory and rolling-up movement of (I) induced by (II) at the end of its formation highlight the dominance of (II) in the dynamics after saturation.

Using the Biot-Savart law, the velocity induced by structure (II) on structure (I) is given by

$$\mathbf{u}_{\mathrm{ind}_{\mathrm{II}\to\mathrm{I}}} = \frac{\Gamma_{\mathrm{II}}}{2\pi}\frac{\mathbf{e_y}\times\mathbf{d_{II\to I}}}{|\mathbf{d_{II\to I}}|^2} \sim \frac{\Gamma_{\mathrm{II}}}{2\pi}\frac{\mathbf{e_y}\times\mathbf{d_{II\to I}}}{h^2} \tag{5.16}$$

where $\mathbf{d_{II\to I}}$ is the distance between structures (II) and (I) whose norm is of order h. Equation 5.16 holds under the assumption of infinitely long structure (II) in the spanwise direction, which is relevant according to the very high aspect ratio of the slits from which emanate the pulsed jets.

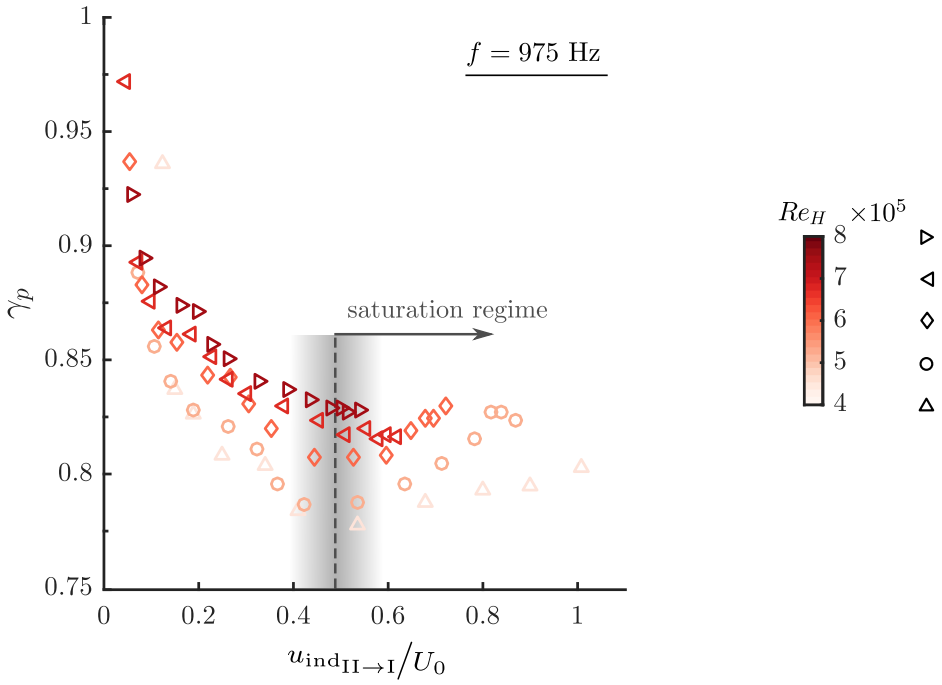

Figure 5.11: Scaling of the base pressure parameter γ_p variations with the dimensionless induced velocity by structure (II) on structure (I) $u_{\mathrm{ind}_{\mathrm{II}\to\mathrm{I}}}/U_0$ for the various Reynolds number $Re_H = \{4, 5, 6, 7, 8\} \times 10^5$ studied for forcing at $f = 975$ Hz with the curved surface $r/h = 9$. The vertical gray shading indicates the approximate constant saturation velocity ratio observed for all Re_H.

In figure 5.11 we scale the evolution of the base pressure parameter γ_p with the velocity ratio $u_{\mathrm{ind}_{\mathrm{II}\to\mathrm{I}}}/U_0$. All the γ_p curves for the investigated range of Re_H have a saturation collapsing on a single value of the induced velocity ratio around $u_{\mathrm{ind}_{\mathrm{II}\to\mathrm{I}}}/U_0 \sim 0.5$. This confirms that the interaction between the boundary layer and the pulsed jet coherent structures is responsible for the saturation and the pertinence of the model and scaling proposed. The good scaling obtained

for the complex interaction between the forcing and the wake flow near separation also justifies a posteriori the approximations made in order to model a local formation velocity U_f discussed in equation 5.13. Moreover, from the obtained scaling, the flow mechanisms involved in the base drag reduction are operating rather differently from what was observed by Barros *et al.* (2016*b*) without curved surfaces where a saturation in base pressure increase was observed at a constant root-mean-square jet velocity at all U_0, therefore purely dictated by the dynamics of the pulsed jet.

5.3 Mechanisms of pressure drag decrease : a matter of flow curvature near separation

The peculiar flow mechanism resulting in additional pressure recovery for high-frequency forcing is now scrutinized. As briefly evoked in the previous section, the focus is put on a fine-scale analysis of the curvature of the separatrix which is highly influenced by the identified negative vorticity structure (I) in the reattachment process.

5.3.1 Global picture of the wake

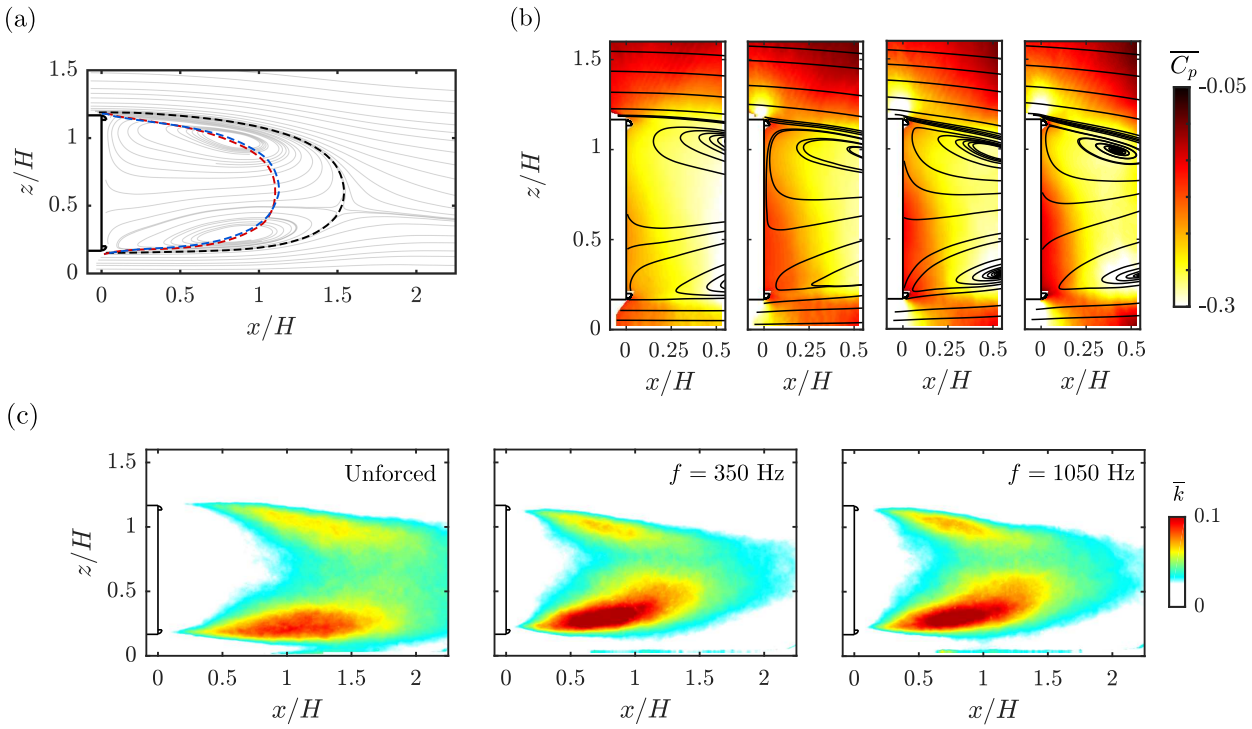

Figure 5.12: Global view of the wake. (a) Wake separatrix for the unforced (black) and for the forced wake at $f = 350$ Hz (red) and $f = 1050$ Hz (blue) at $C_\mu \sim 3 \times 10^{-2}$. Grey lines represent the projected streamlines in the vertical mid-plane of the unforced wake. (b) Pressure field obtained by direct integration of the momentum equations (see Appendix **??**) with superimposed streamlines for the unforced wake and the wake forced at $f = 1050$ Hz and increasing $C_\mu = \{2.1, 3, 3.6\} \times 10^{-2}$ (respectively from left to right) at $Re_H = 5 \times 10^5$ for $r/h = 9$. (c) Mean turbulent kinetic energy $\overline{k}$ for the unforced and for the forced wake at $f = 350$ Hz and $f = 1050$ Hz at $C_\mu \sim 3 \times 10^{-2}$.

The effects of forcing on the wake are first presented from a global viewpoint in figure 5.12. In figure 5.12(a) the focus is directed on a comparison between unforced and forced wakes at both $f = 350$ and 1050Hz at $Re_H = 5{\times}10^5$ at similar $C_\mu \sim 3{\times}10^{-2}$, around saturation in high-frequency forcing (see figure 5.1(a)). Despite a notable difference of 6% in base pressure recovery between the two forced cases, both wakes remain very similar : the wake separatrix presents similar shape for both forcings. It is thinner and shorter than the unforced wake which is qualitatively similar to the observations of Oxlade *et al.* (2015) for instance on the axisymmetric blunt body. Such a

thinner wake is in accordance with the theories of Roshko (1993) and Sychev *et al.* (1998) resulting in a lower momentum deficit and thus increased base pressure as measured. The fact that this shorter wake is associated with base pressure recovery is rather opposite to the the conventional relation between increased recirculation length and base pressure recovery found throughout the literature for square-back geometries (Grandemange *et al.*, 2013*a*; Mariotti *et al.*, 2015; Lorite-Díez *et al.*, 2020). In this case, there exists a relatively simple relation between the base pressure and the recirculation length L_r since the flow curvature can be estimated by the ratio L_r/H. On the contrary, in the present case, the important local changes in flow curvature around the separation due to the flow reattachment noticeably alter and complexify this relation. Nevertheless, no clear distinction between the different forcing frequencies can be made on the basis of a global observation of the wake topology. Furthermore the turbulent fluctuations visualized in figure 5.12(c) by the turbulent kinetic energy $\overline{k} = 0.5 \cdot (\overline{u'_x u'_x} + \overline{u'_z u'_z})$ are globally similar in both forced wake, suggesting a similar activity in the shear layers and flow entrainment in the recirculating wake at a large scale. The pressure field reconstructed from PIV measurements presented in figure 5.12(b) are consistent with the changes in wake topology as a recompression throughout the whole wake is observed resulting in the measured base pressure recovery. It is also worth mentioning that the equilibrium of the wake is fundamentally not affected by the global forcing applied at the base and that the unforced lateral bi-modal dynamics persist with qualitatively similar features, as will be detailed in Chapter 6. Thus differences in base pressure are not due to wake asymmetries in the present chapter.

As no fundamental differences between both forced wakes emanate from a global point of view of the recirculating wake, our investigation further focuses on the flow differences in the vicinity of separation from the curved surfaces.

5.3.2 Flow curvature in the vicinity of separation

We build on the theory of Sychev *et al.* (1998) which shows the peculiar importance of the curvature of the separatrix around separation to the problem of base pressure generation in the wake of a bluff blunt body ((Trip & Fransson, 2017) recently experimentally showed the importance of flow curvature around separation on the base pressure of the two-dimensional blunt body). Following Van Dyke (1969) and Bradshaw (1973), the normal momentum balance along a mean streamline with tangential coordinate s can be written :

$$\frac{1}{\rho}\frac{\partial \overline{p}}{\partial n} = \kappa \overline{U_s}^2 - \frac{\partial \overline{u'_s v'_n}}{\partial s} - \frac{\partial \overline{v'_n v'_n}}{\partial n}, \tag{5.17}$$

where n is the coordinate along an axis locally normal to the streamline and $\kappa = \det(\mathbf{x}', \mathbf{x}'')/||\mathbf{x}'||^3$ the local streamline curvature with $\boldsymbol{x}(s) = (x(s), z(s))$. Equation 5.17 is of fundamental interest in analysing the normal pressure gradient across the wake separatrix which allows to interpret the pressure changes in the recirculating wake and near the base. The normal gradient of normal velocity fluctuations $\partial \overline{v'_n v'_n}/\partial n$ in equation 5.17 can be neglected in our first-order analysis : it is one order of magnitude smaller than the curvature term for forced cases and it acts only by locally generating a low pressure region inside the shear layer without contributing notably to the pressure gradient across the separatrix on large scales. Moreover, the tangential gradient of normal-tangential velocity fluctuations $\partial \overline{u'_s v'_n}/\partial s$ appears also as one order of magnitude smaller than the curvature term after careful investigation (not detailed here for brevity). We therefore first focus on the curvature term $\kappa \overline{U_s}^2$ which is preponderant in establishing the pressure gradient, and analyse the simplified balance of equation 5.17 on the separatrix near the curved surface in figure 5.13. To this purpose, a series of 5 adjacent mean streamlines are chosen as exemplified in figure 5.13(a) to scrutinize the curvature effects. Streamlines are originating around a location $z \sim G + H + \theta$, thus one momentum thickness above the trailing-edge. The local curvature of each streamline is estimated from the PIV measurements and results are averaged across all streamlines to reduce the influence of measurement noise in the second order spatial derivatives required by the curvature estimation. The sepatrices of the analysed cases are depicted in figure 5.13(b). For all the forcing cases the separatrix is importantly deviated inwards compared to the unforced separatrix. This results in a lowered momentum deficit in the wake, and therefore a wake

recompression and base pressure recovery as a regular boat-tailing effect would do. Nevertheless, the separatrices with the higher deflection angles at the end of the considered region, for forcing at $f = 350$Hz and $C_\mu \sim 3 \times 10^{-2}$ and for forcing at $f = 1050$Hz and $C_\mu \sim 3.6 \times 10^{-2}$, are not those resulting in the highest base pressure recovery or equivalently lowest base drag. Indeed, for forcing conditions around the saturation ($f = 1050$Hz and $C_\mu \sim 3 \times 10^{-2}$, even if the deflection angle is less important at the end of the region of interest, the separatrix exhibits greater curvature in the vicinity of the curved surface. This is further assessed through the tangential evolution of the curvature term of the normal pressure gradient $\kappa\overline{U_s}^2$ in figure 5.13(c).

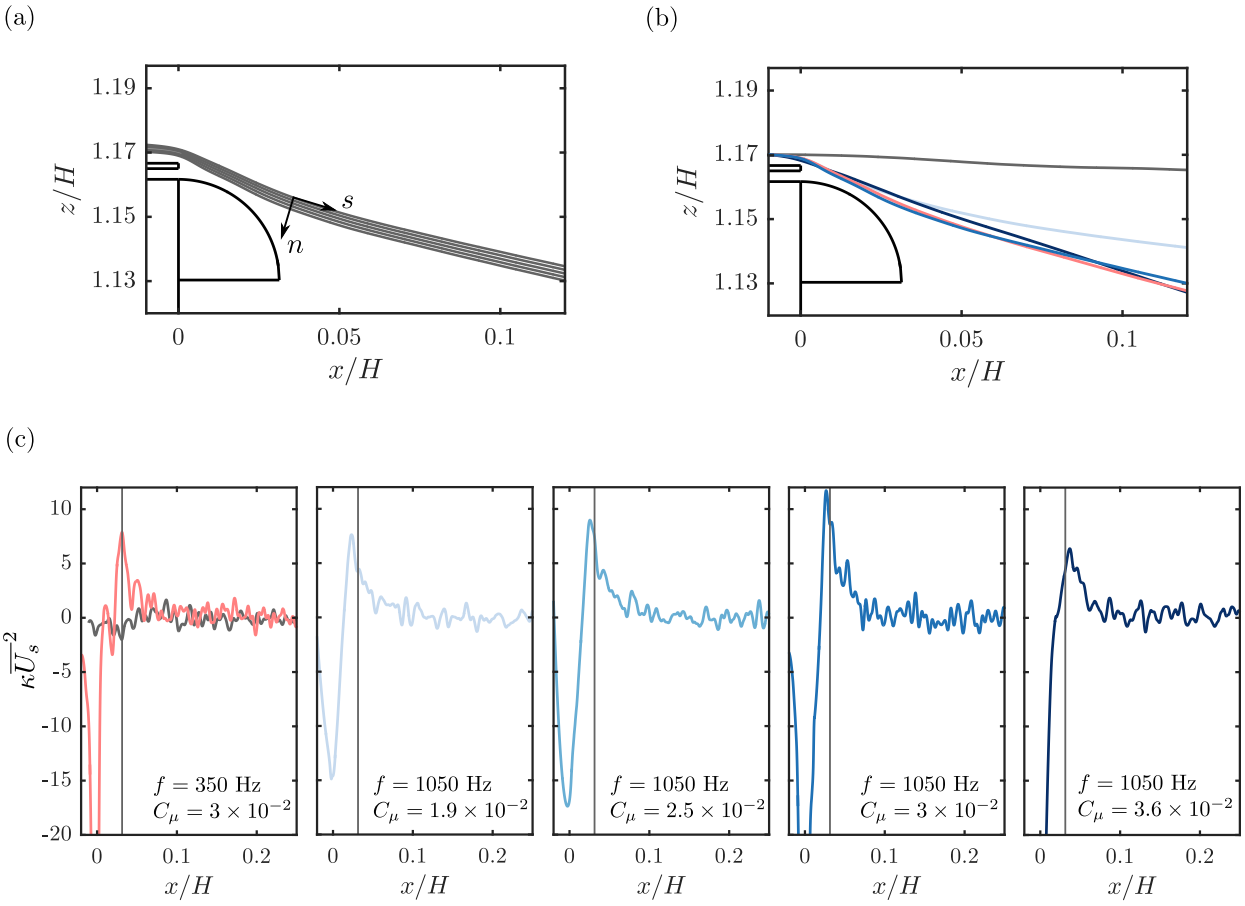

Figure 5.13: Streamwise evolution along the separating streamline of the normal pressure gradient $\frac{\partial p}{\partial n}$ related to curvature obtained from equation 5.17. (a) Example of an ensemble of 5 streamlines originating around $z \sim G + H + \theta$ used for averaging the curvature κ and the normal pressure gradient $\frac{\partial p}{\partial n}$ estimation. (b) Separating streamlines originating from the same point for unforced and various forced cases. The colours are defined the same as in (c). (c) Streamwise evolution of the normal pressure gradient estimated from the curvature part of equation 5.17 for forcing at $f = 350$ Hz and $C_\mu = 3 \times 10^{-2}$, and at $f = 1050$ Hz and $C_\mu = \{1.9, 2.5, 3, 3.6\}$. The unforced case is additionally shown in grey in the first graph. Thin vertical grey lines indicate the streamwise extent of the curved surface.

When forcing is applied, an important peak in the term can be seen around the end of the curved surface at $x/H \sim 0.04$, corresponding to a local curvature inversion due to the presence of an inflexion point in the separatrix. Such a curvature inversion is interpreted through equation 5.17 as a local inversion of the normal pressure gradient across the separatrix and thus as leading to a recompression inside the recirculating wake region and base pressure recovery. Around the saturation in base pressure recovery at $C_\mu \sim 3 \times 10^{-2}$ the peak in curvature is notably higher at $f = 1050$Hz than at $f = 350$Hz, about 30% more, which explains the observed difference in base pressure recovery. Conversely at $f = 1050$Hz, the peak of curvature is seen to monotonically increase with C_μ until the saturation in base pressure is reached before this amplitude collapses, being thus inline with the measured base pressure changes. The maxima of the curvature term $\max_s(\kappa\overline{U_s}^2)$ and the averaged curvature over the region where curvature is reversed $\left\langle \kappa\overline{U_s}^2 \right\rangle_{\{s;\kappa\overline{U_s}^2>0\}}$

Frequency [Hz]	C_μ	$\max_s(\kappa\overline{U_s}^2)$	$\left\langle \kappa\overline{U_s}^2 \right\rangle_{\{s;\kappa\overline{U_s}^2>0\}}$
Unforced	–	–	–
350	0.019	5.85	2.10
350	0.03	7.89	2.45
350	0.05	7.25	2.34
1050	0.019	7.62	2.40
1050	0.025	9.11	2.81
1050	0.03	11.71	3.79
1050	0.036	6.38	2.29

Table 5.6: Quantitative characteristics of the curvature inversion. Extreme values of $\kappa\overline{U_s}^2$ and spatial average value $\left\langle \kappa\overline{U_s}^2 \right\rangle_{\{s;\kappa\overline{U_s}^2>0\}}$ where the sign of the quantity is reversed corresponding to the curvature inversion region.

for the different forcing conditions are gathered in table 5.6 to confirm our reasoning. These curvature changes implied by the induced velocity effects discussed previously are therefore the supplemental mechanism behind the unsteady Coanda effect allowing for further base pressure recovery. These peculiar curvature inversion changes complement the other known effect of wake thinning seen from the inwards deviation of the separatrix in the base pressure recovery mechanism.

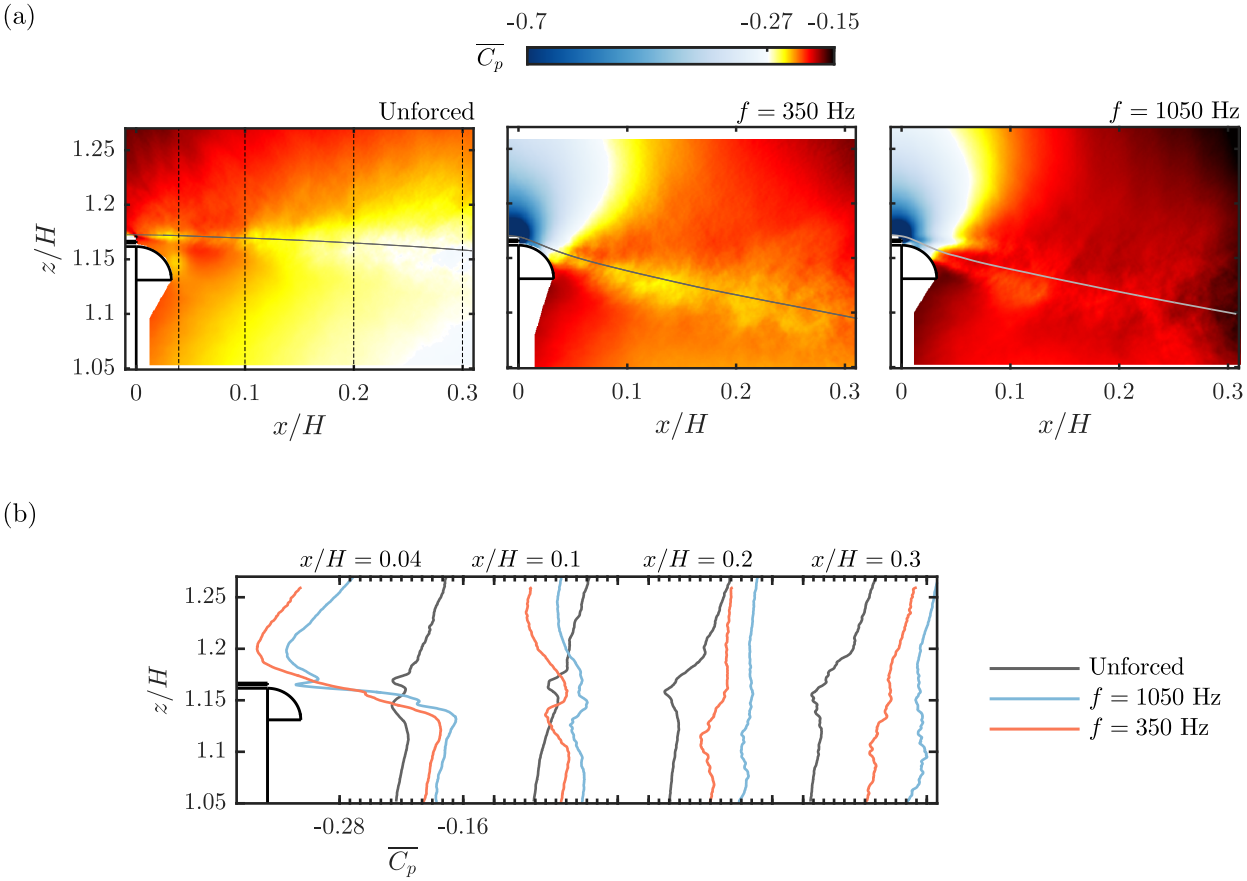

Figure 5.14: Mean pressure coefficient $\overline{C_p}$ obtained by integration of the momentum equations in the (x, z)-plane. (a) $\overline{C_p}$ fields for unforced, and $f = 350$ and 1050 Hz at similar forcing amplitude $C_\mu = 3 \times 10^{-2}$ around the saturation in base pressure recovery at $Re_H = 5 \times 10^5$ with the $r/h = 9$ curved surfaces. The blue shades colormap allows for scrutinizing the very low pressure region near the separating edge when forcing. (b) Corresponding $\overline{C_p}$ vertical profiles at different streamwise locations $x/H = \{0.04, 0.1, 0.2, 0.3\}$. The mean separating streamlines are given in grey and black vertical dashed lines in the first field give the streamwise position of the profiles plotted in (b).

To further argument and confirm our curvature analysis from use of equation 5.17, we show in

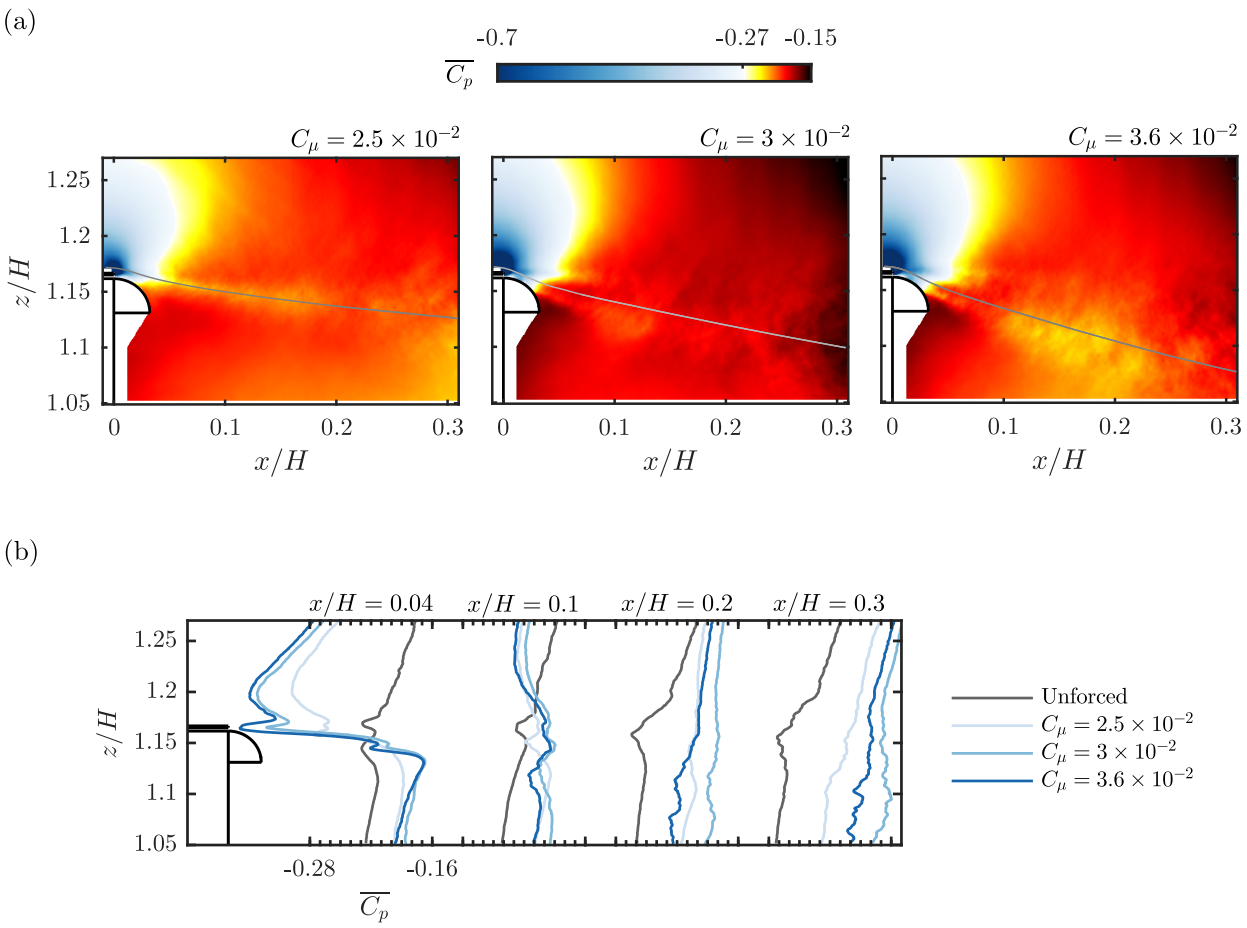

Figure 5.15: Effect of forcing amplitude on the mean pressure coefficient $\overline{C_p}$ obtained by integration of the momentum equations in the (x, z)-plane. (a) $\overline{C_p}$ fields for $f = 1050$ Hz at $C_\mu = \{2.5, 3, 3.6\} \times 10^{-2}$ around the saturation in base pressure recovery at $Re_H = 5 \times 10^5$ with the $r/h = 9$ curved surfaces. The blue shades colormap allows for scrutinizing the very low pressure region near the separating edge when forcing. (b) Corresponding $\overline{C_p}$ vertical profiles at different streamwise locations $x/H = \{0.04, 0.1, 0.2, 0.3\}$. The mean separating streamlines are given in grey.

figures 5.14 and 5.15 the pressure fields obtained by direct integration of the momentum equations from the PIV velocity fields. The method is briefly described and carefully validated in Appendix **??**. The effect of forcing frequency at $C_\mu \sim 3 \times 10^{-2}$ around saturation is first exposed in figure 5.14. Two main observations can be made for both forcings based on these $\overline{C_p}$ fields :

- A region of strong depression is formed around the trailing-edge due to the local acceleration of the flow which extends over the curved surface, thus penalizing the aerodynamic drag reduction as confirmed by the pressure measurements on the curved surface.

- A global recompression takes place in the wake which extends by continuity to the pressure at the base of the model.

The region of strong depression can be seen to extend farther at $f = 350$Hz, which is clearly quantified by the vertical pressure profiles at $x/H = 0.04$. This explains the further penalization at these unadapted frequencies for this choice of r/h and the advantage given by the unsteady Coanda effect. A low pressure trace at $f = 1050$Hz in the flow can be identified, coinciding with the trajectory of the coherent structures (I) and (II) formed by the forcing at high frequency, as was also observed by Oxlade *et al.* (2015). On the wake side of the separatrix, locally around the end of the curved surface, the recompression in the flow is more important at $f = 1050$Hz. This is in particular visible from the vertical profile at $x/H = 0.04$ at the end of the curved surface in figure 5.14(b) where very locally below the separatrix the pressure is further increased to its highest value and by continuity spreading in the wake then. This location coincides with the location of

the peak in curvature presented in figure 5.13 which confirms the peculiar effect of flow curvature in the unsteady Coanda effect for obtaining further drag decrease. Finally, when looking at high forcing frequency $f = 1050$Hz for increasing C_μ in figure 5.15, the depression around the trailing-edge can be seen to increase monotonically with C_μ whereas the recompression on the wake side saturates for $C_\mu \sim 3 \times 10^{-2}$ to weaken when further increasing the forcing amplitude. This further highlights the advantage of flow curvature resulting from the unsteady Coanda effect in producing a recompression of the wake without important penalties on the contrary of a common inwards flow deviation which induced strong penalization from the low pressure region extending over the curved surface.

5.3.3 An inviscid-flow model to evaluate frequency-radius coupling effects

As was stated in the previous section, the flow curvature just after separation is the key mechanism explaining the differences in base drag changes. We thus seek to relate these additional curvature changes to the coherent circulation dynamics previously described. This is done by further developing the inviscid-flow model previously introduced with the aim of taking into account the frequency-radius coupling in the unsteady Coanda effect.

Inspired by the study of Berk & Ganapathisubramani (2019) about the induced velocity effects of a pulsed jet in a cross-flow using an inviscid-flow model, the model from section 5.2 is further refined to describe the influence of the coherent circulation dynamics on the wake separatrix. To this purpose, the inviscid-flow model from equations 5.14, 5.13 and 5.16 is extended to characterize the flow induced by the peculiar coherent structures at high-St_r forcing. Figure 5.16(a-b) explicits the ingredients of this extended model on one peculiar case which is chosen to be the forcing at $f = 1050$Hz ($St_r \sim 0.39$) around the saturation where the base drag decrease is maximal. The measured time-evolutions of the circulation of structures (I) and (II) are fitted with a physical model building on the approach of equations 5.14 and 5.13 (full lines in figure 5.16(a)) :

$$\Gamma_\mathrm{I}(t) = \begin{cases} \frac{t}{t_p}\Gamma_{\mathrm{I}_0} \exp\left(-\frac{t_p}{\tau_\mathrm{I}}\right), & t < t_p \\ \Gamma_{\mathrm{I}_0} \exp\left(-\frac{t}{\tau_\mathrm{I}}\right), & t > t_p. \end{cases} \tag{5.18}$$

$$\Gamma_\mathrm{II}(t) = \begin{cases} 0, & t < t_{\min_\mathrm{II}} \\ \frac{t - t_{\min_\mathrm{II}}}{t_{\max_\mathrm{II}} - t_{\min_\mathrm{II}}}\Gamma_{\mathrm{II}_0} \exp\left(-\frac{t_{\max_\mathrm{II}}}{\tau_\mathrm{II}}\right), & t_{\min_\mathrm{II}} < t < t_{\max_\mathrm{II}} \\ \Gamma_{\mathrm{II}_0} \exp\left(-\frac{t}{\tau_\mathrm{II}}\right), & t > t_{\max_\mathrm{II}}. \end{cases} \tag{5.19}$$

where $t_{\min_\mathrm{II}} = \min_t\{t; V_j(t) > U_f\}$, $t_{\max_\mathrm{II}} = \max_t\{t; V_j(t) > U_f\}$, and Γ_{I_0} (< 0), τ_I, Γ_{II_0} (> 0) and τ_II are the fitting parameters of the model. Each time-evolution of the circulation is based on a linear increase of Γ during the formation period, followed by an exponential decay primarily dictated by the dissipation of the coherent structures. If assuming a constant t_p/T in concordance with our HWA measurements on the pulsed jets, $t_{\min_\mathrm{II}}/T$ and $t_{\max_\mathrm{II}}/T$ are also constant and it allows for a forcing frequency parametrization of the model with a circulation Γ scaling as T. In a similar way, the evolution of the position of the centre of the coherent structures $\mathbf{x}_\mathrm{I}$ and $\mathbf{x}_\mathrm{II}$ is fitted with linear time-evolutions as appeared from the constant convection velocities estimated in figure 5.7. Using the modelled circulation, the associated spatial distribution of vorticity is accurately approximated by that of a gaussian or Lamb-Oseen vortex, which gives for structure (I) for instance :

$$\omega_{y_\mathrm{I}}(\mathbf{x}, t) = \frac{\Gamma_\mathrm{I}(t)}{\pi|\mathbf{x} - \mathbf{x}_\mathrm{I}|^2} \exp\left(-\frac{|\mathbf{x} - \mathbf{x}_\mathrm{I}|^2}{r_\mathrm{I}(t)^2}\right). \tag{5.20}$$

Here r_I is the radius of structure (I) given as a fitting parameter from the measurements whose evolution during time can be approximated as constant and of order $\sim h$ (thereby justifying the exponential decay of circulation completely dominated by dissipation over diffusion). An example of the experimentally measured vorticity compared to the model of equation 5.20 for one time-instant is given in 5.16(c) confirming the pertinence of the model. The total vorticity field $\omega_y(\mathbf{x}, t)$ of the train of coherent structures identified is then the sum of the vorticity distribution from all

structures (I) and (II) and their equivalent from previous forcing periods. In order to satisfy the no-penetration condition on the curved surface, for each external vorticity source at a location $\mathbf{x_S}$, an image vortex of equal but opposite circulation is located at the inverse square point $\mathbf{x'_S}$ defined as $(\mathbf{x_S} - \mathbf{x_C}) \cdot (\mathbf{x'_S} - \mathbf{x_C}) = r^2$, where $\mathbf{x_C}$ is the center of the circle defining the curved surface. Finally, a vortex of equal circulation to each of the external vorticity source is located at $\mathbf{x_C}$ to cancel the total circulation of the internal vorticity sources of the images (Saffman, 1992; Ford & Babinsky, 2013). An example of the total vorticity field obtained at a given time instant is provided in figure 5.16(c). As discussed by Berk & Ganapathisubramani (2019), the associated induced velocity field is then obtained by application of the Biot-Savart law

$$\mathbf{u}^{\mathrm{ind}}(\mathbf{x}, t) = \iint \frac{\omega_y(x', z', t)}{2\pi \max(|\mathbf{x}' - \mathbf{x}|, r_R)} \frac{\mathbf{e_y} \times (\mathbf{x}' - \mathbf{x})}{|\mathbf{x}' - \mathbf{x}|} dx' dz', \tag{5.21}$$

where the summation is performed over the vorticity contributions from each location (dx', dz') of the field. r_R is an equivalent Rankine vortex radius used to keep a finite velocity everywhere in the field and which is empirically chosen as $\sqrt{(0.5dx')^2 + (0.5dz')^2}$ related to the field pitch. An example of the induced velocity field $\mathbf{u}^{\mathrm{ind}}(\mathbf{x}, t)$ thus computed is given in figure 5.16(c).

It should be noted here, that the proposed model is also implicitly parametrized in forcing frequency through the time dependence in relations 5.18 and 5.19. Indeed, the peak in circulations $|\Gamma_{\mathrm{I}}|$ and $|\Gamma_{\mathrm{II}}|$ will by definition theoretically scale with $1/f$ (Shariff & Leonard (1992), Berk & Ganapathisubramani (2019)). In addition, as all the formation time parameters in relations 5.18 and 5.19 are expressed relatively to the forcing period duration T, the assumption is then that time-evolution of circulation is homothetic when frequency is varied in the model. This is in line with the properties of our pulsed jets discussed in §2.3. Indeed, the time evolution of the pulsed jets velocity is close to homothetic at the investigated forcing frequencies, with constant duty-cycle used, and near-constant non-dimensional peaking time t_p/T. As a consequence, the inviscid-flow model discussed herein and built on the experimental results of the optimal base drag decrease ($f = 1050$Hz and $C_\mu \sim 3 \times 10^{-2}$) can be reasonably used to at least qualitatively investigate the forcing frequency effects on the velocity induced by the coherent structures.

To analyse the influence of these coherent structures on the mean flow in the vicinity of the curved surface we examine the mean vertical induced velocity $\overline{u_z^{\mathrm{ind}}}$ in figure 5.17. The $\overline{u_z^{\mathrm{ind}}}$ field at $f = 1050$Hz ($St_r = 0.39$) is exhibiting two distinct zones with opposite velocities : a region near the slit and the curved surface with positive $\overline{u_z^{\mathrm{ind}}}$, followed by a region with negative $\overline{u_z^{\mathrm{ind}}}$. The latter region is contributing to the flow deviation and to the curvature of the wake separatrix that lead to an additional base pressure recovery. To quantify the importance of this influence, the induced vertical velocity is around one-fifth of the vertical velocity measured by the PIV in the same region. This mean negative vertical induced velocity only appears farther downstream ($x/r > 2$) when forcing at $f = 350$Hz ($St_r = 0.13$) and the vicinity of the curved surface is characterized by the presence of positive vertical induced velocity. The effect of forcing frequency variation is further scrutinized in the profiles of $\overline{u_z^{\mathrm{ind}}}$ on a line following the mean direction of convection of the coherent structures in figure 5.17(b). These forcing frequency variations show that $St_r \sim 0.5$ appears as an optimum to maximise the negative induced vertical velocity just at the end of the curved surface for the peculiar $r = 9h$ dimension. Indeed, forcing frequencies one order of magnitude below lead to the vanishing of the induced velocity effects. Similarly, forcing frequencies one order of magnitude above lead to a reduced peak of negative induced velocity displaced towards the trailing-edge and a progressive vanishing of the velocity towards the end of the curved surface. To quantify this optimality, the evolution with St_r of the mean induced vertical velocity $\langle \overline{u_z^{\mathrm{ind}}} \rangle$ averaged over the zone $(x, z) \in [0.03, 0.1] \times [1.14, 1.175]$ is shown in 5.17(c). This zone corresponds to the location of the peak in flow curvature and its vicinity where flow curvature is inverted as shown in figure 5.13. The induced velocity effect is only downwards for sufficiently high St_r and an optimum in the downwards induced velocity occurs around $St_r \sim 0.5$. The present model shows unambiguously the strong coupling effect existing between the size of the curved surface used and the forcing frequency in the additional induced velocity effect in base pressure recovery, and provides a scaling of this coupling through St_r.

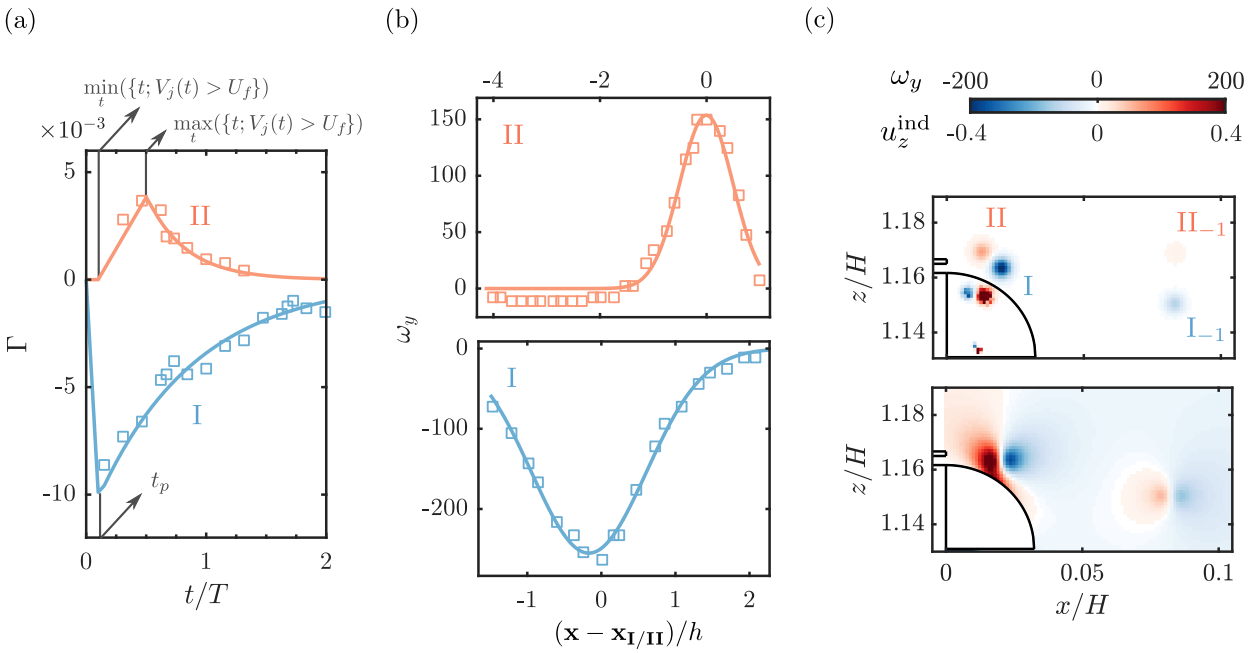

Figure 5.16: Inviscid model for the velocity induced by the identified coherent structures. (a) Fitting of the temporal evolution of the circulation Γ of counter-rotating coherent structures (I) and (II) for the case of optimal base pressure recovery at $f = 1050$ Hz ($St_r \sim 0.39$) and $C_\mu \sim 3 \times 10^{-2}$. Squares are experimental results, and full lines the fit to these points from equations 5.18 and 5.19. (b) Fitting of the spatial evolution of the spanwise vorticity ω_y of counter-rotating coherent structures (I) and (II). Squares are experimental results, and full lines the fit to these points from equations 5.20 describing a Lamb-Oseen vortex. (c) Example of spanwise vorticity ω_y (top) and induced vertical velocity u_z^{ind} (bottom) fields at a given time instant of the forcing cycle obtained from the inviscid model. The vorticity field includes the vorticity images inside the curved surface.

5.4 Concluding remarks and further discussions

The impact of periodic forcing coupled to small-scale surfaces on the wake and aerodynamic drag of a canonical blunt body is investigated. Pulsed jets with variable frequency f and amplitude C_μ are blown at the edges of the base over flush-mounted curved surfaces with characteristic radius of curvature one order of magnitude greater than the pulsed-jet size h. Complementary drag and pressure measurements as well as highly spatially resolved particle image velocimetry help to reveal the main mechanisms and draw fundamental scaling models of the unsteady Coanda effect allowing for up to 12% reduction of the pressure drag of the body.

Our study highlights the relatively different base pressure recovery mechanisms involved in the forcing depending on the relation between the time-scale of the periodic forcing and the convective time-scale over the curved surface r/U_0. For any forcing time-scale above the natural wake time-scales investigated, the flow reattachment over the curved surfaces results in a deviation of the separatrix associated with a thinning of the wake leading to drag reductions of order 10%. Experimental results show that when the time-scale of the forcing is of the same order as the convective time-scale r/U_0, additional 6% in base pressure recovery and 5% in drag decrease is observed compared to a forcing with a time-scale one order of magnitude greater than the convective time-scale for the same forcing amplitude C_μ. Although the two forced wakes present similar qualitative features (length, width, form) at a global scale, differences at the local scale in the vicinity of the curved surface explain the drag difference. Local pressure gradients across the separatrix are found to behave radically differently, highlighting two different mechanisms for base pressure recovery. A conventional inwards flow deviation and wake thinning is observed for all forcing time-scales, very similar to the effect of a boat-tail. Nevertheless, at the forcing time-scale of r/U_0 additional flow curvature effects take place and the flow curvature inversion in the vicinity of the end of the curved surface leads to pressure gradient inversion and local recompression on the wake side of the separatrix explaining the additional drag decrease. This curvature mechanism

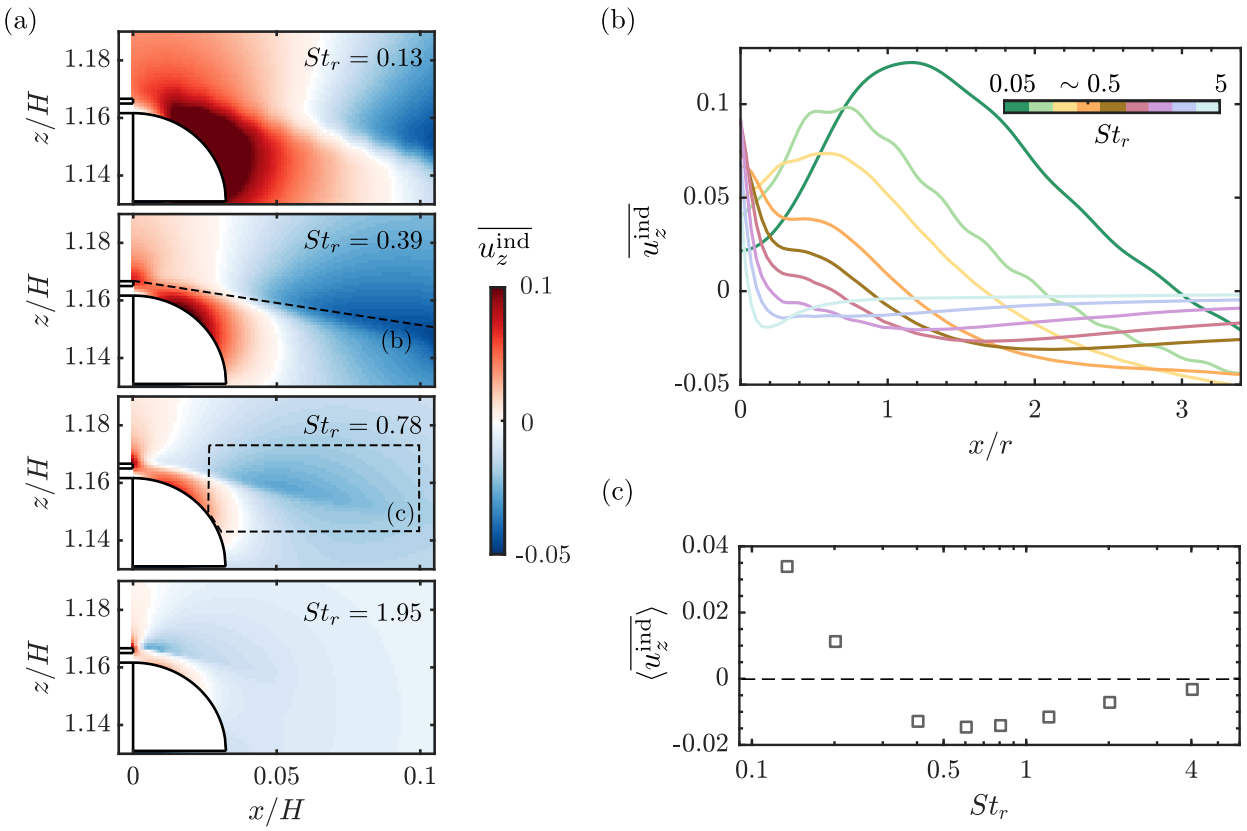

Figure 5.17: Inviscid model for the velocity induced by the identified coherent structures. (a) Time-averaged vertical induced velocity $\overline{u_z^{\mathrm{ind}}}$ for the nominal case $St_r = 0.39$ and for lower ($St_r = 0.13$) and higher ($St_r = 0.78$ and $St_r = 1.17$) frequencies. (b) Time-averaged induced vertical velocity $\overline{u_z^{\mathrm{ind}}}$ on a line originating at the trailing-edge and following the mean direction of convection of the coherent structures (depicted in (a)) for various forcing frequencies $St_r = \{0.04, 0.13, 0.26, 0.39, 0.78, 1.17, 1.95, 3.9\}$. Colormap appears in logarithmic scale. (c) Evolution with St_r of the time-averaged induced vertical velocity $\langle \overline{u_z^{\mathrm{ind}}} \rangle$ averaged over the zone $(x, z) \in [0.03, 0.1] \times [1.14, 1.175]$ (depicted in (a)) around the peak in flow curvature and where flow curvature is inverted in figure 5.13.

is not only observed to provide additional drag decrease, but it prevents the drag penalization from the low pressure region extending over the curved surfaces when the base pressure recovery is mainly achieved by flow deviation. Furthermore, it allows for important drag reduction with only very small geometric additions of order r/H at high free-stream velocities. This is rather important as the performance of simple high-frequency forcing (Oxlade *et al.* (2015), Barros *et al.* (2016*b*)) was found to deteriorate significantly with increasing free-stream velocity.

The fundamentally different evolution in the drag changes with C_μ and U_0 between the two different periodic forcing time-scales account for the difference in mechanisms governing the base pressure recovery. Whereas the base pressure recovery satisfactorily scales with the injected momentum by the pulsed jets at the lower forcing frequency, this scaling fails for the forcing frequency of order U_0/r. In addition, for the latter, a saturation in the base pressure recovery occurs (with a recovery of 22% and an associated drag decrease of 12%) for a C_μ depending on the free-stream velocity U_0 with a subsequent degradation in the drag decrease at higher amplitudes. A theoretical inviscid-flow model is developed in order to scale the drag changes and the saturation mechanism based on the tracking and characterization of the peculiar pair of counter-rotating coherent structures resulting from the forcing. The first coherent structure with circulation of the same sign as the surrounding shear layer is formed by the pinch-off and subsequent roll-up of the vorticity sheet originating from the boundary layer of the body during the peaking phase of the pulsed jet. The second structure of opposite sign circulation is formed by the interaction roll-up of the pulsed jet when its velocity exceeds the velocity of the surrounding flow. The model is able to satisfactorily scale the saturation in base pressure recovery with the ratio between the velocity induced by the second structure on the first one and the free-stream velocity. This highlights the mechanism of

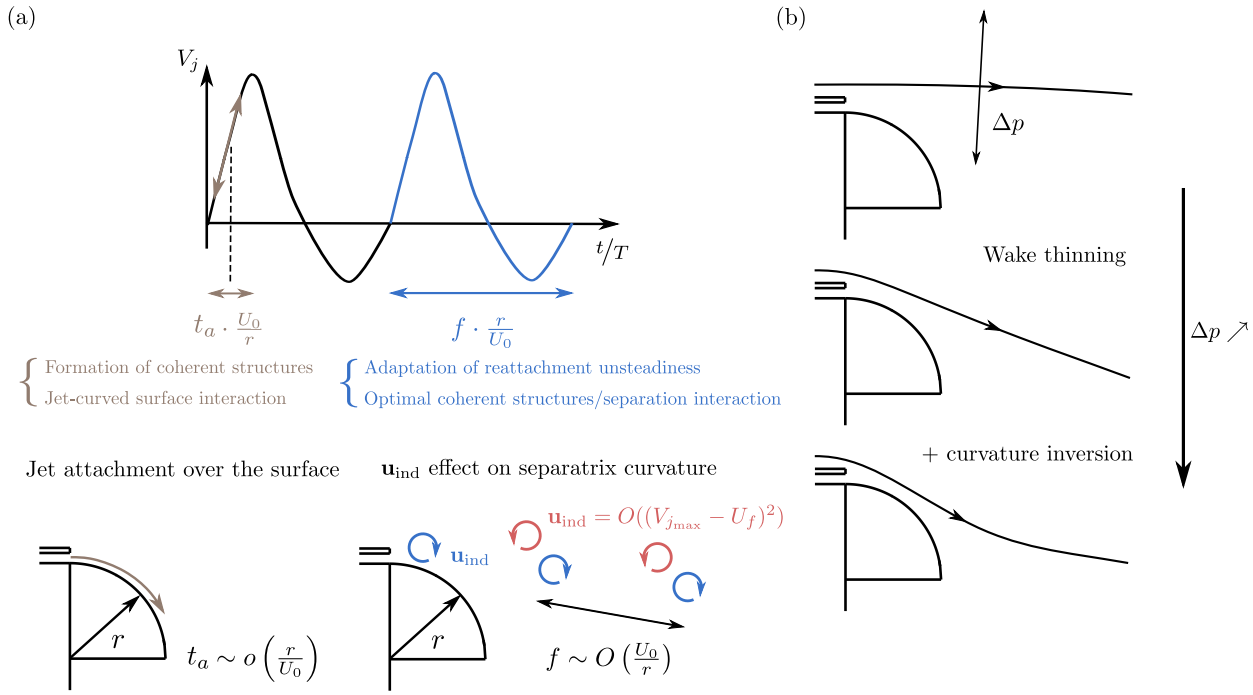

Figure 5.18: Simplified description of the unsteady Coanda effect. (a) Time-scales involved in the unsteady Coanda effect. A fast time-scale (in brown) corresponding to the pulsed-jet peaking time governs the attachment of the pulsed-jet over the curved surface (and the possibility of having or not an efficient base pressure recovery) and the formation of coherent structures involved in the unsteady Coanda effect. The corresponding non-dimensional scaling is $t_a \frac{U_0}{r}$. A slower time-scale (in blue) corresponding to the pulsed-jet period governs the interaction between the coherent structures created by the pulsed-jet and the curved surface for appearance or not of the induced velocity effect on the curvature of the separatrix, and pilots the unsteadiness of the separation from the curved surface. The corresponding non-dimensional scaling is $f \frac{r}{U_0}$. The negative structure formed by the roll-up of the separating boundary layer induces flow curvature effects leading to further drag reduction. The positive structure scales with the pulsed jet velocity excess from the local flow velocity and pilots the saturation of the unsteady Coanda effect. (b) Base pressure recovery/pressure drag decrease mechanism. Regular wake thinning consequence of the flow deviation by a conventional Coanda effect, and additional induced curvature effects stemming from the unsteady Coanda effect.

outwards flow entrainment operated by the second structure after saturation. Finally, an extension of the model parametrized with the forcing frequency allows for the identification of the velocity induced by these transient coherent structures as the mechanism leading to additional flow curvature effects for drag reduction. The model also shows the optimality of the forcing time-scale of order $O(r/U_0)$ in the induced flow curvature effect. Further variations of the curved surface radius r confirm the strong coupling between r and the forcing time-scale in the efficiency of the unsteady Coanda effect in drag reduction, pointing to the need for careful combination between forcing frequency and size of the curved surfaces to achieve all the potential of the unsteady Coanda effect in drag reduction.

A simplified description of the observed unsteady Coanda effect is given in figure 5.18. Two fundamental time-scales are at the origin of the unsteady Coanda effect mechanisms :

1. A time-scale $1/f$ associated to the periodicity of the forcing which accounts for :
   - The unsteady interaction between the coherent structures formed by the periodic forcing, the curved surface and the outer potential flow. Providing the time-scale is of order r/U_0, this results in an optimality of the interaction between coherent structures and flow separation to produce flow curvature leading to further drag decrease.
   - An adaptation of the unsteadiness of the flow separation from the curved surface when the time-scale is of order r/U_0 resulting in a reduced unsteadiness of the separation and reattachment dynamics.

2. Another time-scale associated to the peaking time t_p of the forcing, which grants importance to the velocity profile of the forcing. This time-scale quantifies the acceleration effects of the forcing and allows for :

   - Attachment or not of the pulsed jet to the curved surface to promote or not a base pressure recovery through a Coanda effect. This results in a conventional thinning of the wake resulting in lower flow momentum deficit in the wake and thus to a recompression in the near-wake.
   - The possible formation of the negative coherent structure (I) from the roll-up of the separating boundary layer leading to additional flow curvature effects and drag reduction.

5.4.1 Asymptotic behaviour in the absence of curved surface

A brief conceptual discussion is presented here about the asymptotic behaviour of the unsteady Coanda effect in the limit $r/h \to 0$ corresponding to the absence of additional curved surfaces. The aim is to provide a link between the mechanics of the unsteady Coanda effect presented in this chapter and of the *fluidic boat-tailing* occurring with high-frequency forcing in absence of additional curved surfaces as studied by Oxlade *et al.* (2015) and Barros *et al.* (2016*b*).

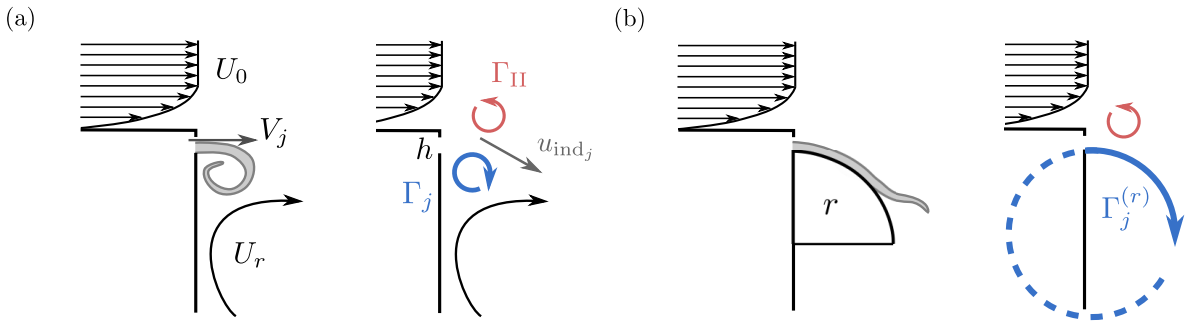

Figure 5.19: Conceptual model of the unsteady Coanda effect in the limit $r/h \to 0$. (a) High-frequency forcing (a) without curved surfaces, and (b) with curved surfaces. The sketch on the left shows the behaviour of the flow momentum injected by the pulsed jets, and the one on the left the equivalent flow model. The slug of vorticity emanating from the jet is sketched in gray. In (b) only the part of the equivalent vortex Γ_j where vorticity flux from the jet is actually present is in full line.

For this, we follow the conceptual model of Barros *et al.* (2016*b*) on the flow deviation at the base by the high-frequency forcing. Fluidic boat-tailing is the main mechanism by which base drag is reduced. The conceptual model is given in figure 5.19(a). The key aspect is the formation of a starting jet vortex of total circulation Γ_j at the base of the slit which induces an inwards velocity u_{ind_j} deviating the main flow at separation. The order of magnitude of the induced velocity u_{ind_j} is given by $\Gamma_j/(U_0 h)$, still following the potential flow models used previously. Following Gharib *et al.* (1998) as discussed by Barros *et al.* (2016*b*), the circulation of the starting vortex fed entirely by the vorticity flux from the jet can be expressed as $\Gamma_j = 0.5 T_F V_{j_{\mathrm{eff}}}^2$ (which seems to be supported by the circulation measurements of Oxlade *et al.* (2015)). According to Gharib *et al.* (1998), T_F is the formation time of the starting vortex. Maximal value of T_f is limited by a ratio between the theoretical length of the slug of vorticity from the jet $\int_0^{T_F} V_j(t)dt \sim T_F \overline{V_j}$ and the characteristic length scale of the slit, h here, of ~ 4. For simplification of the analysis, we can assume at first order $\overline{V_j} \sim V_{j_{\mathrm{eff}}}$, which results in $T_F \sim 4h/V_{j_{\mathrm{eff}}}$ and then $\Gamma_j \sim 2hV_{j_{\mathrm{eff}}}$ quantifying the maximal circulation borne by the starting jet vortex.

When a curved surface of radius r/h is present, the slug of vorticity does not roll-up to form a vortex but stays attached to the curved surface to form a wall-jet. The inwards induced velocity comes at first order from this wall-jet as discussed in 5.1 and at second order from the additional structure (I) coming from the boundary-layer pinch-off seen in 5.2. The wall-jet along the curved surface can be seen as a stationary starting vortex of equivalent radius $\sim r + h$. In this sense,

the total circulation borne by the vortex $\Gamma_j^{(r)} \sim 2\pi\alpha(r+h)V_{j_{\text{eff}}}$, where α is the portion of the equivalent vortex where the wall-jet is attached to the surface and feds the vortex with actual vorticity. According to the dynamics of attachment and separation presented in figure 5.4, in first approximation $\alpha \sim 1/4$ to account for a flow attachment over the major length of the curved surface. This leads to a rough approximation of $\Gamma_j^{(r)} \sim 2(r+h)V_{j_{\text{eff}}}$ which in the limit $r \to 0$ is in line with Γ_j obtained without curved surfaces.

Based on this conceptual model, a couple of interpretations on the drag reduction obtained can be made.

- As the radius of the curved surface is increased, the circulation $\Gamma_j^{(r)}$ increases and so does the induced velocity. Conversely, the amount of base drag decrease is increased with r, which is in line with the results obtained here and the results obtained by Barros *et al.* (2016*b*) for $r = 0$.

- The sensitivity of the base drag decrease to the free-stream flow U_0 is importantly increased for $r = 0$. As long as the curved surface is present, the equivalent vortex $\Gamma_j^{(r)}$ can be assumed as stationary in first approximation as the vorticity is attached to the wall. On the contrary, when $r = 0$, the vortex Γ_j is free to move, and as stated by Barros *et al.* (2016*b*) it will be convected away downstream with a velocity which is function of U_0, V_j, U_r and the boundary layer characteristics (which both depend on U_0). The actual circulation that stays in the vicinity of the edge is thus a strong function of U_0 and decreases importantly with increasing U_0 resulting in quite importantly decreasing in base drag decrease with U_0. As this dependence of $\Gamma_j^{(r)}$ on U_0 is quite weak, the base drag reduction sensitivity on U_0 for $r > 0$ is also expected to be weak. This is in agreement with what is observed in this study where the minimal γ_p drops only from 0.78 to 0.82 in the case $r/h = 9$ between $U_0 = 20$ and 40 m s^{-1}. In the same time, in the study of Barros *et al.* (2016*b*), for $r = 0$, the minimal γ_p drops from 0.74 to 0.93 between $U_0 = 10$ and 20 m s^{-1}. This aspect is quite important for high-Re_H applications as it highlights the need of adjacent curved surfaces to reduce the sensitivity of drag reduction to U_0 in order to be efficient at high U_0.

- As there is a strong dependence of the actual Γ_j and the base drag reduction on U_0 in the case $r = 0$ the saturation mechanism in base drag reduction is also likely to be more complex than the $r > 0$ case and more dependent on U_0. For $r > 0$, the saturation mechanism was piloted by the ratio between the velocity induced by the opposite jet structure (II) and U_0. As this induced velocity has been shown to also depend on U_0, the saturation mechanism has a weaker dependence on U_0. On the contrary, for $r = 0$ the saturation mechanism (evidenced on γ_p by Barros *et al.* (2016*b*) and Oxlade *et al.* (2015)) is not only dependent on the jet structure (II) as suggested by the measurements of Oxlade (2013). It has also a strong dependence directly on V_j as the circulation Γ_j is convected away from the edge with a velocity depending directly on the jet velocity when this quantity becomes important. This may explain why in this case the saturation occurs at an almost constant value of $V_{j_{\text{eff}}}$ with U_0 in Barros *et al.* (2016*b*) where the convection imposed by V_j has a role at least as important as the structure (II) in the saturation mechanism. In consequence, the strong sensitivity of the saturation mechanism to $V_{j_{\text{eff}}}$ implies important reductions in base drag reduction at high U_0 which cannot be prevented by increasing importantly $V_{j_{\text{eff}}}$ to keep similar C_μ without occurrence of the saturation as in the $r > 0$ case.

5.4.2 Final remarks

Even if in the current study we performed all the analyses on a given form of curved surface with constant curvature, an interesting aspect would be to extend and confront the mechanisms and scalings involved in the unsteady Coanda effect derived in this study to straight surfaces as flaps which have been widely used for the flow control of blunt bodies (Chaligné (2013), Schmidt *et al.* (2015)). Additionally, the acceleration effects related to t_p are highly forcing-apparatus dependent. Here we tried to investigate a quite canonical forcing velocity profile with a triangular shape in order to introduce the t_p time-scale. Undoubtedly, the formation process of the coherent

structures and pulsed jet attachment over the curved surface will depend on the velocity profile. An interesting aspect would thus to extend the present results to other canonic forcing profiles such as a step function with finite acceleration.

The peculiar unsteady Coanda effect analyzed in this study and its scaling laws and models identified provide both an efficient drag reduction mechanism for blunt bodies and a framework for adapting the strategy at real-world scales or on fundamentally different fluid mechanics problems involving flow separation. In particular, the unsteady dynamics involved in the unsteady Coanda effect discussed here are very reminiscent of the optimal dynamics of separation and reattachment over a forced flap at a higher spatial scale studied by Darabi & Wygnanski (2004*a*), Darabi & Wygnanski (2004*b*) or Amitay & Glezer (2002) for the control of stalled airfoils.

The peculiarity of the phenomenon involving small-scale pulsed jets and curved surface makes it a promising strategy to be applied on road vehicles and heavy-truck where strong geometric constraints are imposed in the design and only minor geometric modifications are allowed. In this regard, the concluding chapter will introduce an opening towards application of this drag reduction strategy on more realistic car geometries. The unsteady Coanda effect used in this chapter as a global forcing strategy on the wake has a strong authority on the flow orientation at separation. In this sense, the natural question that arises concerns the authority it can have on the large-scale flow asymmetries of the wake discussed in chapter 4 if adopting a forcing strategy localized only along certain edges of the base. The chapter 6 will now show this localized forcing strategy may be used as an active fluidic flap to manipulate the wake asymmetries and the drag related to them.

Chapter 6

Manipulation of wake asymmetries

Most of these results are submitted to the *Journal of Fluid Mechanics* (Haffner *et al.*, 2020*c*). Combination of passive and active flow control are used to force the turbulent wake. The aim is to manipulate the wake asymmetries with an objective of drag reduction. By using passive perturbations around the model, the large-scale asymmetry of the unforced recirculation region is modified. Depending on the unforced wake equilibrium, additional high-frequency pulsed blowing coupled to small curved surfaces along all or selected edges of the base produces a very different impact on the drag. Besides a global fluidic boat-tailing effect, the reorganization of the recirculation region equilibrium plays a key role in the observed drag changes. In particular, the symmetrisation of the wake through control appears to be one of the main mechanisms involved in drag reduction. Even if asymmetric forcing strategies targeting the symmetrisation of the wake provide more modest drag reduction up to 7%, they are shown to be more efficient from an energetic point of view. These strategies allow to combine to different extents the benefit on the drag of a wake symmetrization and of a boat-tailing. This study provides key ingredients to adapt forcing strategies for drag reduction in presence of various wake asymmetries typical of the flow around such body. Massive wake equilibrium changes being essentially caused by minor geometric and flow conditions changes, flow control strategies targeting the mitigation of asymmetries are essential for industrial automotive applications.

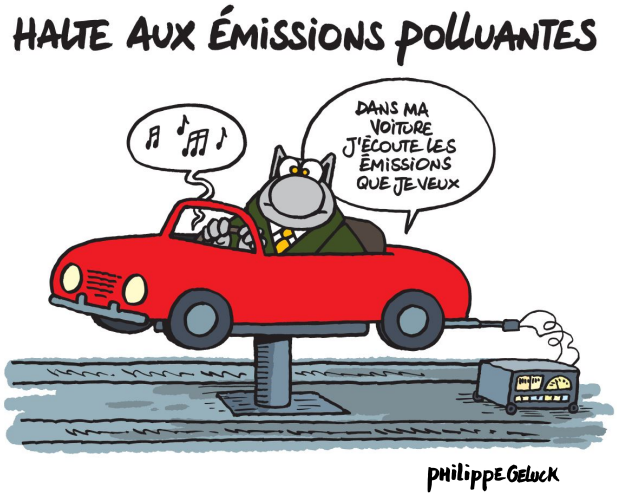

Contents

As discussed in the introductory chapter, large-scale asymmetries are an important feature of 3D blunt body wakes. They represent one of the main drag source in these wakes as studied in chapter 4 and in this sense their manipulation is a key point in the aim of drag reduction. Following the drag reduction results obtained by a global unsteady Coanda forcing of the wake in chapter 5, there is a legitimate question arising about the interaction between an asymmetric forcing strategy at the base and the large-scale asymmetries of the wake. To answer this question, we capitalize on the unsteady Coanda effect evidenced in the previous chapter to build various asymmetric forcing strategies localized only along certain edges of the base with the aim of interacting with different large-scale asymmetries.

6.1 Experimental set-up

Details on specificities of the experiments performed for the investigations in this chapter are provided in this section. First the different wakes with various large-scale asymmetries used for this study are described briefly. Then the forcing conditions adopted to interact with the asymmetries are described in detail. All the experiments presented in this chapter are performed at $U_0 = 25$ m s^{-1} or equivalently $Re_H = 5 \times 10^5$.

6.1.1 Unforced flows

In order to investigate from a general point-of-view the interaction of forcing with large-scale asymmetries of the wake, baseline flows with different kind of asymmetries are selected. To this end, three wakes presenting different orientations of the symmetry-breaking mode are considered : the natural unperturbed wake presenting lateral bi-modality, the wake locked in the **T** (resp. **B**) symmetry-breaking state obtained by perturbing the model on top with a $d/H = 0.053$ spanwise cylinder (resp. at bottom with a $d/H = 0.066$ spanwise cylinder).

The wake flow in the vertical symmetry plane of these three wakes is provided in figure 6.1 and the corresponding mean aerodynamic coefficients are gathered in table 6.1. The mean streamlines show how the wake flow locks in a vertical asymmetric configuration for perturbations placed on top of and under the model, with a characteristic large recirculation zone on the side where the base pressure is the lowest. Important fluctuations characterized by the mean turbulent kinetic energy $\overline{k} = (\overline{u'_x u'_x} + \overline{u'_z u'_z})/2$ in the measurement plane (which can also be considered as the averaged normal stress in the measurement plane) are observed in the top (resp. bottom) shear-layer when the wake is locked in the **B** (resp. **T**) symmetry-breaking state due to the interaction mechanism between the recirculating flow from the top (resp. bottom) edge and the opposite shear-layer as

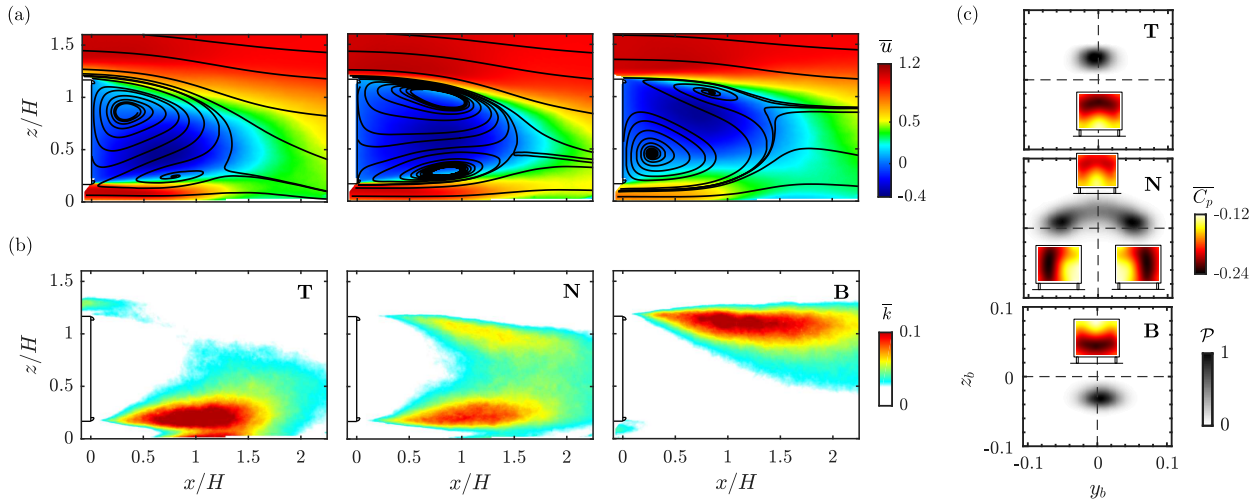

Figure 6.1: Unforced baseline flows considered using passive perturbations. (a) Mean streamwise velocity $\overline{u}$ and (b) mean turbulent kinetic energy $\overline{k} = (\overline{u'u'} + \overline{v'v'})/2$ in the vertical plane of symmetry $y = 0$ for the top perturbed **T**, natural **N** and bottom perturbed **B** wakes. (c) Joint probability density function (p.d.f) of the base center of pressure (CoP) position. Base pressure distributions are given for each wake state.

Case	G/H	d/H	$\overline{C_{pb}}$	$\overline{C_D}$	$\overline{C_L}$	$\overline{z_b}$
N	0.167	–	−0.197	0.254	−0.123	0.010
T	0.167	0.053	−0.210	0.265	−0.077	0.030
B	0.167	0.066	−0.214	0.282	−0.126	−0.035
Low ground clearance	0.067	–	−0.207	0.257	−0.057	−0.026

Table 6.1: Characteristic mean aerodynamic coefficients for the three baseline configurations which are further used for investigations with forcing in sections 6.2 and 6.3. **N** refers to the unperturbed configuration and **T** (resp. **B**) to the configuration with the perturbation placed on top of (resp. under) the model. For the top and bottom perturbed configurations, $\overline{C_D}$ refers to the mean drag coefficient corrected for the presence of the cylinder using the methodology introduced in chapter 4. The low ground clearance case is used in the further discussions of section 6.4.

explained in chapter 4. The natural unperturbed configuration exhibits a characteristic vanishing vertical asymmetry with almost balanced vertical distribution of low mean turbulent kinetic energy resulting from a weakened interaction mechanism. In this case, the asymmetry has been re-oriented in the horizontal direction in a bi-modal form. The characteristics of the large-scale dynamics of these wakes are given in figure 6.1(c) by the joint probability density function (p.d.f.) of the base CoP position.

To complete the type of wakes investigated, a fourth case with reduced ground clearance $G/H = 0.067$ is investigated as presented in chapter 3. This configuration inhibits the symmetry-breaking instability as shown by Cadot *et al.* (2015) and introduces a vertical asymmetry linked to the proximity of the ground. The reader is referred to chapter 3 for a more detailed description of this flow. This flow is quite close to the high base drag flow class identified by Castelain *et al.* (2018) and Grandemange *et al.* (2013*c*).

6.1.2 Forcing

To interact with the various large-scale asymmetries exhibited by these wakes, forcing is issued through only selected edges of the base in asymmetric distributions. All the different forcing distributions used are summed up in figure 6.2 and are denoted F_{X} where X refers to the edges of the base where forcing is issued (T for top, B for bottom, L for left, R for right and combination of them). Spatial homogeneity of the forcing conditions presented in chapter 2 are expected to be satisfactory enough so that at first order only the forcing distribution on the edges has an effect on the equilibrium of the wake.

In order to capitalize on the unsteady Coanda effect evidenced in chapter 5, the couple

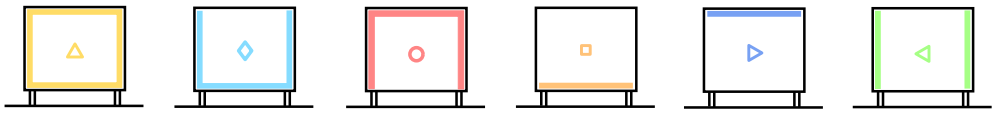

Figure 6.2: Sketch of the different forcing distributions used to manipulate the wakes. Edges of the base where forcing is active are highlighted in color. The color and symbol codes used throughout the whole chapter are defined from there.

$(r/h, f) = (9, 1050\ \mathrm{Hz})$ of curved surface radius and forcing frequency of the pulsed jets is chosen as a near-optimal one in term of drag reduction in the global F_{TBLR} forcing distribution. The forced flow reattachment on the curved surfaces is expected to have a good authority on the asymmetry of the wake in asymmetric forcing distributions as a flap would (de la Cruz *et al.*, 2017*a*).

In order to capitalize on the unsteady Coanda effect evidenced in chapter 5, the couple $(r, f) = (9h, 1050\ \mathrm{Hz})$ used here corresponds to an optimum for the unsteady Coanda effect and the drag reduction achieved when forcing along all the edges of the base F_{TBLR}, as seen in chapter 5. It results in an optimized cross-flow momentum near the edges of the base to both shape and re-orient the wake. The forced flow reattachment on the curved surfaces is expected to have a good authority on the asymmetry of the wake in asymmetric forcing distributions as a flap would (de la Cruz *et al.*, 2017*a*).

6.2 Overview of the effects of forcing

In this section, we describe the impact of forcing on the base pressure and the aerodynamic drag of the model for the three different wake orientations of symmetry-breaking mode. Figure 6.3 and 6.4 gather the evolutions of γ_p and γ_d with forcing amplitude C_μ for various types of global and asymmetric forcing.

We first examine drag changes with a global forcing F_{TBLR} which respects the symmetry of the body and may only have a weak effect on wake asymmetries. Global forcing in figure 6.3 leads to very similar evolution of γ_p and γ_D independently of the initial configuration of the unforced flow. All curves related to F_{TBLR} can be unambiguously split in two distinct regions as studied in detail in chapter 5. First, γ_p decreases with C_μ before the base pressure recovery saturates above $C_\mu \sim 0.025$. The saturation mechanism is mostly governed by the local interaction between the pulsed jets, the curved surface and the local flow conditions near the slits. In this sense the global orientation of the symmetry-breaking mode has only a weak influence on the unsteady Coanda effect governing the base pressure recovery. Only small differences in the saturating C_μ and the base pressure trend after saturation are observed between the three configurations which might be ascribed to the local flow differences where the pulsed jets are issued due to the reorientation of the asymmetry. As discussed in section 6.3 and explained by Barros *et al.* (2016*b*) or Haffner *et al.* (2020*b*), this forcing enables to reduce importantly the drag by an action on the flow curvature around separation leading to wake shaping, as a geometric boat-tail would do (Wong & Mair (1983); Bonnavion & Cadot (2019)).

One might wonder how the drag changes evolve when the symmetry of the forcing is modified so that it might have authority on the wake asymmetry. To answer this, drag changes when either the top or bottom edge is left unforced are also presented in figure 6.3. In this sense, the wake shaping mechanism is expected to be mostly kept while the vertical asymmetry of the forcing is expected to affect wake development by inducing a change in the vertical asymmetry of the wake. For these asymmetric forcing distributions F_{TLR} and F_{BLR}, the evolution of base drag is very sensitive to the combination of the forcing distribution and the initial orientation of the symmetry-breaking mode. Two main behaviours can be observed depending on the unforced configuration :

- When the unforced wake is locked in a vertical steady asymmetric state (**T** or **B** configurations), forcing removed along the edge on the CoP side (F_{BLR} for the **T** configuration, and F_{TLR} for **B**) leads to an important base pressure recovery, with a trend similar to global forcing F_{TBLR}. Conversely, forcing removed along the edge on the side opposite to the CoP

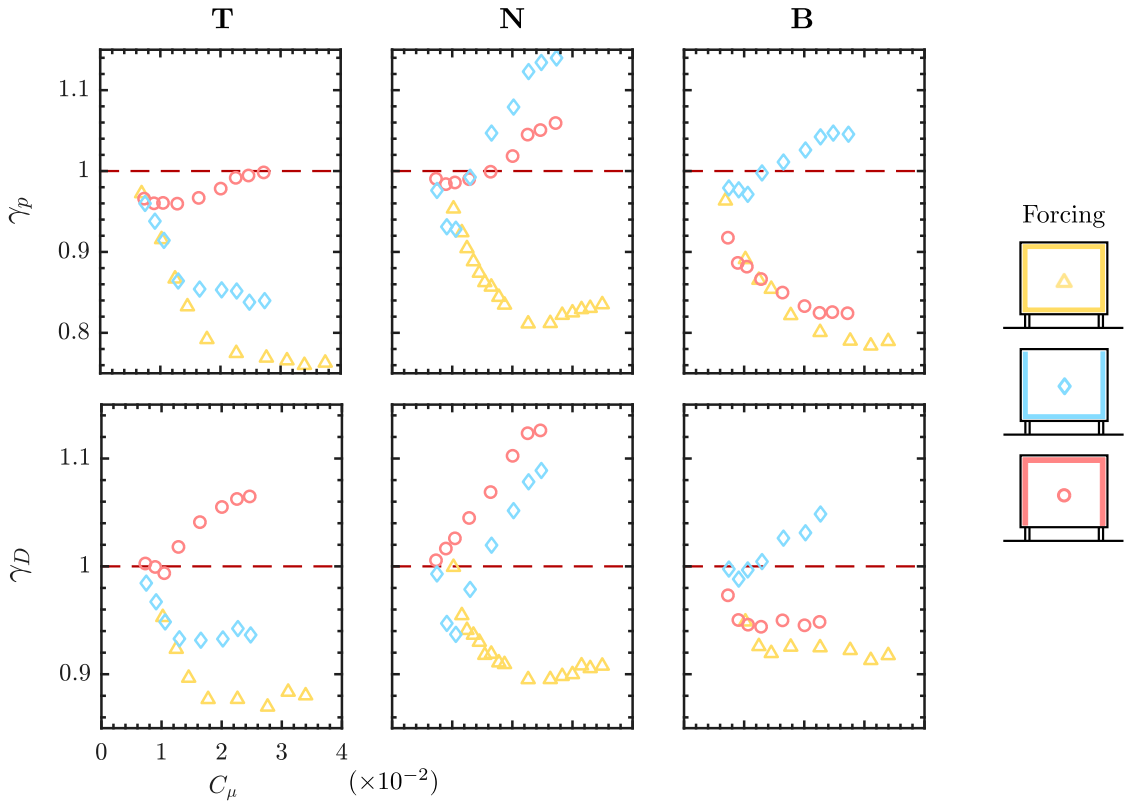

Figure 6.3: Evolution of the base pressure parameter γ_p and the drag parameter γ_D of the top perturbed **T**, natural **N** and bottom perturbed **B** wakes with forcing amplitude C_μ for forcing distributions involving all edges or three of the edges of the base.

(F_{TLR} for the top perturbed configuration, and F_{BLR} for the bottom perturbed one) leads to at most very moderate base pressure recovery (less than 4%) and in most cases to an increase in base drag for increasing C_μ.

- For the natural lateral bi-modal configuration, the evolution of γ_p and γ_D under asymmetric forcing is rather specific. Indeed, for the F_{BLR} forcing distribution a clear minimum of $\gamma_p = 0.92$ is observed at $C_\mu \sim 0.01$. Interestingly, after the minimum, γ_p increases with C_μ with quite a strong rate. For F_{BLR} forcing, this results in a base pressure decrease of 14% at the maximum C_μ studied here. This is much more important than for the top and bottom perturbed configurations which were forced on the less advantageous side (respectively F_{TLR} and F_{BLR}) which resulted in a maximal 5% base pressure increase.

Naturally, the question of how the drag changes evolve when the wake is subjected to the simplest asymmetric forcing arises. In this case where forcing is only issued along the top F_{T} or bottom edge F_{B}, the forcing is expected to affect essentially the symmetry of the wake. To answer this, drag changes are shown in figure 6.4 for the three baseline configurations subjected to single-sided forcings F_{T} or F_{B}. Reflecting the observations made for F_{TLR} and F_{BLR} forcings, the evolution of base drag is even more sensitive to the location of the forcing and the initial orientation of the symmetry-breaking mode. In this single-sided forcing case, for both mean asymmetric baseline configurations **T** and **B**, the base drag is either monotonically decreasing (for forcing on the side opposite to the CoP) or increasing (for forcing on the CoP side) with values between -12 and $+10$%. It should also be noted that drag variations for both baseline configurations are quite far from a mirror symmetry, as the base drag variations for the **B** configuration are more pronounced than the **T** configuration. This aspect highlights the influence of ground proximity in the results obtained. For the bi-modal configuration **N**, in any case the base drag is importantly increased up to 16%. This behaviour is far from the one observed with F_{BLR} exhibiting an optimal drag decrease for a given amplitude C_μ. The only common feature for single-sided forcing of the **N** wake configuration is the high sensitivity of drag to C_μ variations.

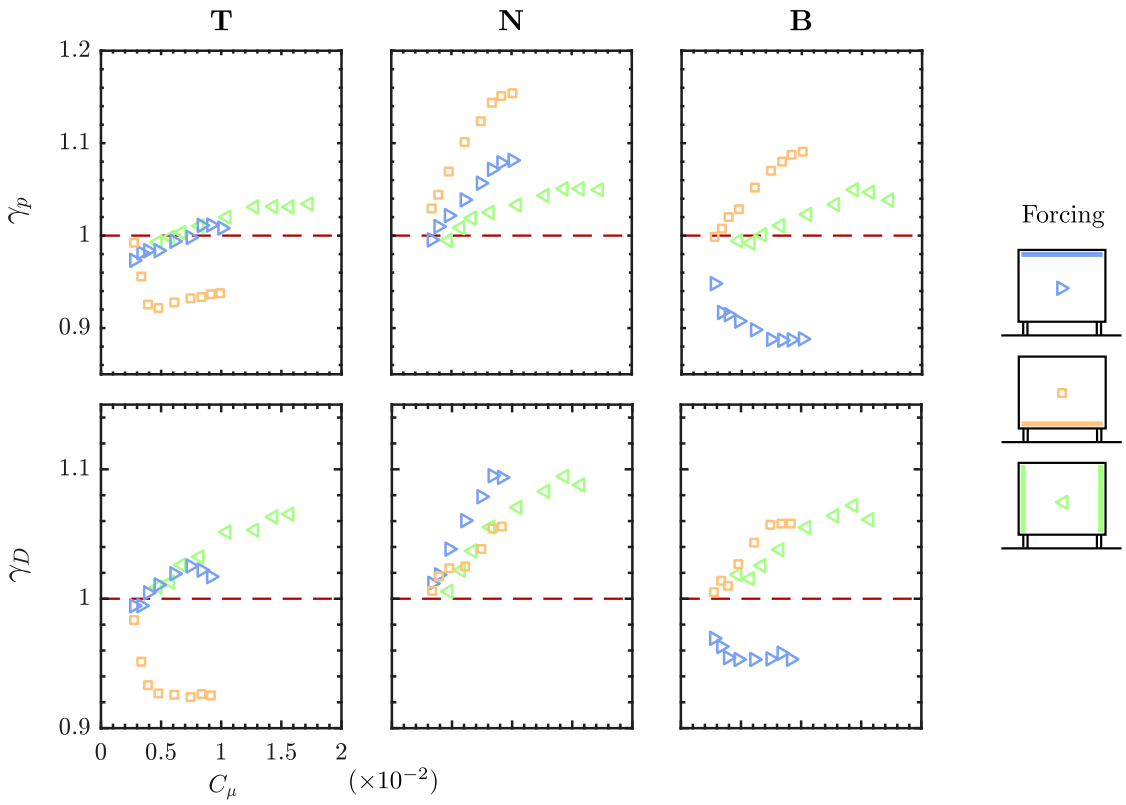

Figure 6.4: Evolution of the base pressure parameter γ_p and the drag parameter γ_D of the top perturbed **T**, natural **N** and bottom perturbed **B** wakes with forcing amplitude C_μ for forcing distributions involving only one edge or both lateral edges of the base.

Finally, one may wonder what happens to drag variations if only lateral edges are kept in the forcing. This case F_{LR} may be expected to give intermediate drag variations between forcing distributions where one edge is removed (F_{TLR} and F_{BLR}) and the single-sided forcing (F_{T} and F_{B}). Surprisingly, the drag changes only show monotonic increase with C_μ for all baseline configurations. Interestingly, in the **T** configuration, the rate of increase of γ_p and γ_D is very similar to the one of the single-sided forcing F_{T} located on the CoP side. This behaviour suggests that drag changes do not evolve as a linear superposition of the contributions of each forcing, but rather emerge from more complex interactions. It should be pointed out that Sujar-Garrido *et al.* (2019) found opposite drag variations with lateral forcing F_{LR} on a similar configuration with inverted aspect ratio of the base ($H/W > 1$) and underbody flow blockage (and with the use of straight flaps rather than curved surfaces) with up to 8% pressure drag decrease instead of increase. Both studies indicate that the base aspect ratio H/W and the underbody flow impact dramatically the evolution of drag with increasing c_μ. Conversely, the effect of F_{TB} would be of interest to further investigate the role of H/W, but it was out of the scope of the present study as the focus is on vertical wake asymmetry.

As would be expected for a three-dimensional blunt body, figure 6.3 and 6.4 show a qualitatively similar evolution of the drag parameter γ_D and the base pressure parameter γ_p with increasing C_μ. Depending on number of edges involved in forcing, the pressure drag penalization linked to the low pressure region forming over the curved surfaces due to flow reattachment (Haffner *et al.*, 2020*b*) varies significantly. As a consequence, the correlation between γ_p and γ_D slightly evolves between single-edge forcing and global forcing. Small differences appear also among cases with single-edge forcing, for which the correlation between the base pressure and the aerodynamic drag is changed depending on the initial wake equilibrium. For T and B configurations under single-edge forcing leading to drag reduction (F_{B} and F_{T} respectively) for instance, the correlation coefficient between γ_p and γ_D evolves between 0.9 for the former and 0.5 for the latter. We attribute these differences to the influence of ground proximity for which forcing can alter both the interaction between the recirculation region of the wake with the ground and the penalization induced over the curved

surfaces.

One important consequence of playing on the forcing distribution along the edges of the base is the implication for energetic efficiency of the control. Indeed, as the number of edges involved in the forcing is decreased, even if the drag decrease might be less, the energetic efficiency might be considerably increased, meaning that the energy spent in forcing leads to relative higher energy savings due to drag decrease. To quantify this interesting aspect, the energetic efficiency and the aerodynamic parameters variations of the best performing asymmetric forcing strategies are provided in table 6.2. For the sake of providing an objective point of comparison, energetic efficiency is provided for the global forcing case F_{TBLR} at the best performing C_μ as well as at a C_μ giving similar drag reduction with asymmetric forcing. To assess the energetic efficiency of the different forcings, we follow energetic analyses discussed in a variety of previous studies (Freund & Mungal (1994), Choi *et al.* (2008), Pfeiffer & King (2012), Barros *et al.* (2016*b*) or Li *et al.* (2019)). The power to overcome aerodynamic drag power P_D and the power saving ΔP_D due to a drag decrease associated to γ_D may be defined as

$$P_{D0} = \frac{1}{2} C_{D0} \rho S U_0^3. \tag{6.1}$$

and

$$\Delta P_D = \frac{1}{2} (1 - \gamma_D) C_{D0} \rho S U_0^3. \tag{6.2}$$

On the other hand, the amount of power spent in the control P_j by the pulsed jets can be estimated by

$$P_j = \frac{1}{2} \rho N_j S_j \overline{\langle V_j \rangle^3}, \tag{6.3}$$

where $\langle V_j \rangle$ is the pulsed exit velocity averaged over the section of one slit. As our pulsed jets system is composed of a regular diffuser exiting in the wake through a slit, we may approximate $\langle V_j \rangle$ from V_j (which was defined as the exit velocity at the center of the slit and to which we have access by our hot-wire anemometry measurements) by

$$\langle V_j \rangle = \alpha V_j. \tag{6.4}$$

Under the assumption of a Poiseuille flow in-between parallel walls (as we have $l >> h$ for this slit geometry) $\alpha = 2/3$. If a completely flat velocity profile was to occur across the slit ($\alpha = 1$), the power spent in the control would be increased by a factor $(3/2)^3$. This underlines the high dependence of the control energetic efficiency on the slit geometry, and in this sense further studies focusing on parametric variations of h should be undertaken to focus on this aspect. Finally, we define the energetic gain η of the control and the relative power saved π_s by

$$\eta = \frac{\Delta P_D}{P_j}, \qquad \pi_s = \frac{\Delta P_D - P_j}{P_{D0}}. \tag{6.5}$$

Note that the ratio $P_j / P_{D0} = \pi_s / (\eta - 1)$ characterizes the relative aeraulic power of the pulsed jets. It is also worth mentioning that the energy balance used here does take into account neither the power needed to compress the air fed into the solenoid valves nor the electrical power consumed by the solenoid valves themselves. The control apparatus was not designed with in mind to optimize these two energy contributions which are technology-dependent, and thus we are mainly concerned with the aeraulic energy of the pulsed jets in the present approach.

The energy balance of the main control strategies leading to drag reduction are gathered in figure 6.5 in the plane $(\eta, 1 - \gamma_D)$ and in table 6.2. As a first remark, all the control cases leading to substantial drag reductions exhibit an efficiency $\eta > 1$ which means that in any case there is a net power saving. The $(\eta, 1 - \gamma_D)$ plane can qualitatively be separated in two regions gathering global forcing strategy with high drag reductions and lower efficiency on one side, and asymmetric forcing strategies with lower drag reduction and higher efficiency on the other side. A notable specificity is the low ground clearance case where asymmetric forcing is even able to outperform global forcing in terms of drag reduction due to the particular wake asymmetry introduced by the interaction with the ground. It appears that asymmetric forcing strategies, when well in line with

Case	Forcing	$C_\mu(\times 10^{-2})$	$\overline{C_{pb}}$	γ_p	$\overline{C_D}$	γ_D	η	π_s [%]
N	–	–	-0.197	–	0.254	–	–	–
N	F_{TBLR}	1.5	-0.169	0.86	0.236	0.93	10	6.3
N	F_{TBLR}	2.3	-0.159	0.81	0.226	0.89	5.4	8.9
N	F_{BLR}	1.0	-0.181	0.92	0.236	0.93	17.2	6.6
T	F_{TBLR}	1.2	-0.183	0.87	0.246	0.93	9.6	6.2
T	F_{TBLR}	1.9	-0.166	0.79	0.231	0.87	6.7	11
T	F_{BLR}	1.3	-0.181	0.86	0.246	0.93	13.9	6.5
T	F_{B}	0.5	-0.193	0.92	0.246	0.93	32.1	6.8
B	F_{TBLR}	1.4	-0.182	0.85	0.259	0.92	9.2	7.1
B	F_{TLR}	1.0	-0.186	0.87	0.265	0.94	16.1	5.6
B	F_{T}	0.4	-0.193	0.9	0.268	0.95	25.9	4.8

Table 6.2: Characteristic mean aerodynamic coefficients and energetic gain for the three baseline configurations under different forcing conditions leading to the best drag reductions. For the top and bottom perturbed configurations, $\overline{C_D}$ refers to the mean drag coefficient corrected for the presence of the cylinder using the methodology used in Haffner *et al.* (2020*a*).

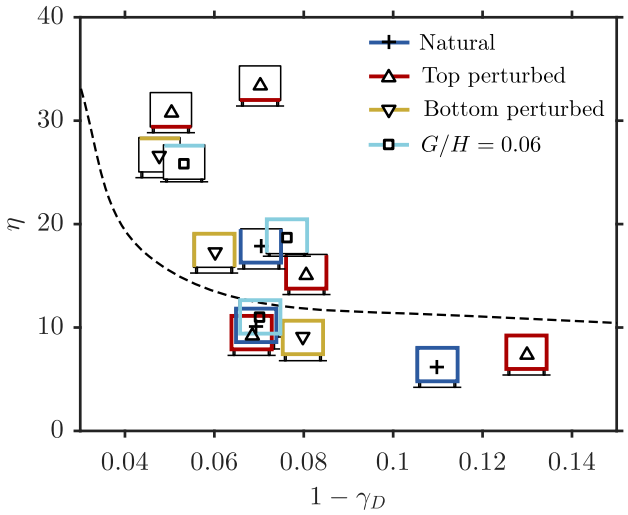

Figure 6.5: Correlation map between drag reduction $1-\gamma_D$ and energetic efficiency of the forcing η for various forcing strategies. Each value is associated with a marker depicting the forcing distribution at the base with thick colored lines. A qualitative separation between asymmetric and global forcings is provided by the dashed line.

the initial wake asymmetry orientation, give considerably higher energetic gains even if maximal drag reductions are reduced. When energetic gain η is looked at rather similar drag reductions, single-sided forcing appears up to 3 times more efficient than global forcing, suggesting the high interest in this kind of control strategies.

6.3 Mechanisms of drag changes under asymmetric forcing

In this section, we focus on the physical mechanisms behind the various drag changes observed in section 6.2 resulting from localized forcing on the three wakes with different asymmetries studied. In particular, we investigate the relation between modifications of the wake equilibrium and the corresponding drag variations depending on the type of asymmetric forcing.

6.3.1 Conceptual picture of the main drag reduction mechanisms

To introduce the flow analysis of the observed drag changes under asymmetric forcing, 6.6 presents a qualitative illustration of the wake flow mechanisms which can be triggered by the forcing for drag reduction. A clear distinction can be made between two different drag reduction mechanisms

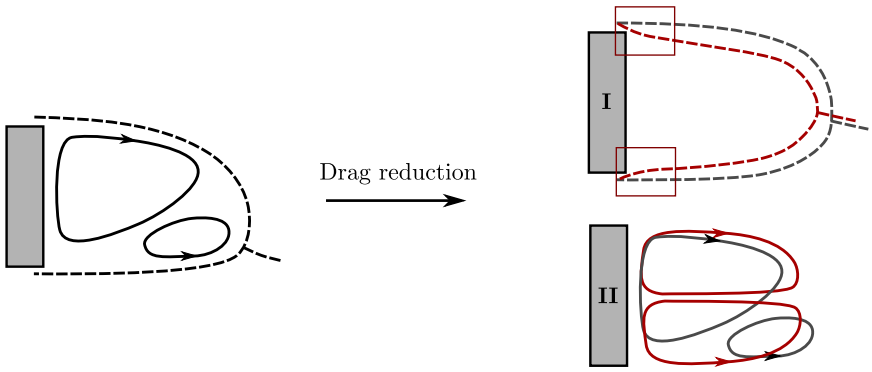

Figure 6.6: Quatitative illustations of different flow mechanisms leading to the reduction of pressure drag. **I** Wake shaping and change of flow curvature near the base (red rectangles denote the near separation region where flow curvature effects are preponderent according to Haffner *et al.* (2020*b*)). **II** Symmetrisation of the wake. In practice both mechanims can be superimposed.

: wake symmetrization as observed by Grandemange *et al.* (2014*b*); de la Cruz *et al.* (2017*b*); Li *et al.* (2019); Haffner *et al.* (2020*a*) (among others) and wake shaping as described by Oxlade *et al.* (2015); Barros *et al.* (2016*b*); Haffner *et al.* (2020*b*) and detailed in chapter 5. On the one hand, the wake shaping mechanism globally increases the pressure through the whole wake by reducing its transversal section with minimal reorganization of the recirculating flow. In this sense, it acts by raising the pressure C_p through the whole near-wake with small influence on the pressure gradients inside the recirculating region. The shaping of the wake directly acts on the pressure gradients across the separatrix in the vicinity of separation. As shown in chapter 5, the flow curvature in the vicinity of separation and its inversion have a strong influence on the drag decrease. On the other hand, the mean symmetrization of the wake acts by strongly reorganizing the mean recirculating wake and the pressure gradients inside governing the low pressure imprint on the base. The symmetrization of the recirculation region allows to reduce the imprint of the low pressure region located farther downstream of the base. In the same time, it prevents the development of the interaction mechanism in asymmetric wake leading to additional base drag as shown in chapter 4. In the remainder of this section, we will show how the drag changes observed in section 6.2 under asymmetric forcing can be explained by these two complementary mechanisms. Also, it will be shown how the combination of the baseline wake asymmetry and the forcing distribution strongly influences the drag changes.

6.3.2 Influence of global forcing on the symmetry of the wake

The effect of global forcing F_{TBLR} on the symmetry of the three wakes is first briefly described. Due to the symmetry of global forcing, it is expected to impose only minor changes on wake symmetry. However, this forcing type represents a baseline for the exclusive action of the wake shaping mechanism. As shown in figure 6.7, the initial type of asymmetry remains unchanged under global forcing : permanent vertical symmetry-breaking states and lateral bi-modal dynamics are kept for the configurations **T**, **B** and **N**. For the bi-modal wake **N**, even if the forcing distribution presents a fair degree of homogeneity, the bi-modal dynamics are still very sensitive to small deviation from a perfectly homogeneous distribution. This leads to a wake exploring quantitatively more one of the lateral symmetry-breaking states for certain C_μ. The influence on the pressure drag is only weak as $\overline{C_{pb}}$ differs only by less than 2% between a perfectly bi-modal wake and a wake locked in a lateral symmetry-breaking state (Haffner *et al.*, 2020*a*). The main difference is the increase of the mean asymmetry strength $\overline{R_b}$ with forcing amplitude C_μ which is defined as $R_b = \sqrt{y_b^2 + z_b^2}$. There is a linear increase of the asymmetry strength with C_μ for all baseline configurations in the direction of the initial asymmetry. A similar trend was found by Oxlade (2013) on an axisymmetric bullet-shaped body with high-frequency forcing at the base. This increase of asymmetry strength R_b suggests that wake shaping leads to more pressure recovery on the high pressure side of the wake than on the low pressure side. It will be shown in further discussions in section 6.4 how it is

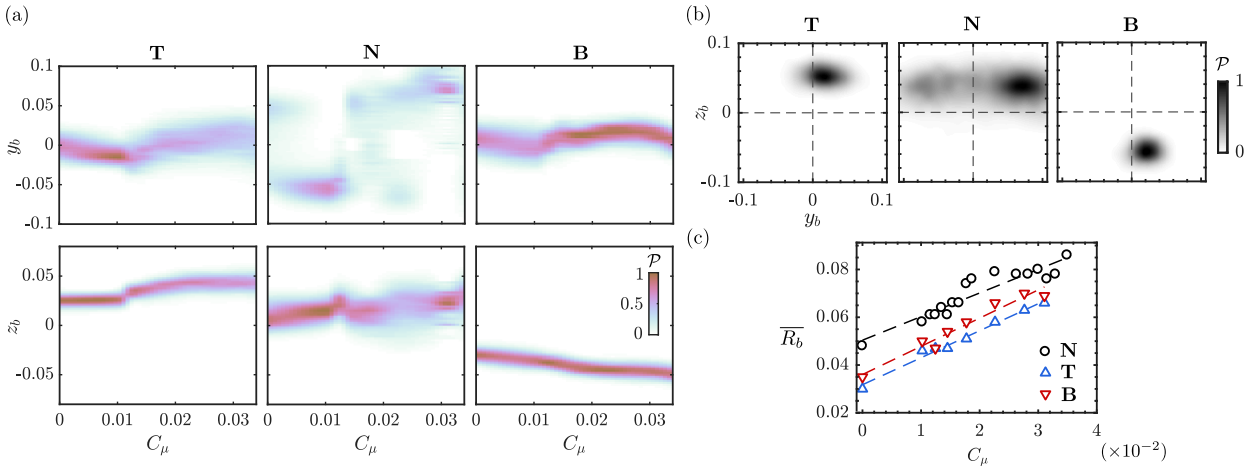

Figure 6.7: Effect of global forcing F_{TBLR} on the base pressure for **T**, **N** and **B** configurations. (a) Sensitivity maps of the CoP position y_b and z_b to forcing amplitude C_μ. (b) P.d.f. $\mathcal{P}(y_b, z_b)$ of the CoP at maximal base pressure recovery ($C_\mu = 0.024$ for **N**, $C_\mu = 0.034$ for **T** and $C_\mu = 0.031$ for **B**). (c) Evolution of the mean wake asymmetry $\overline{R_b} = \sqrt{y_b^2 + z_b^2}$ with C_μ. Dashed lines indicate linear fits to the evolution.

linked to asymmetries in the wake.

In figure 6.8, we present the mean base pressure coefficient $\overline{C_{pb}}$ evolution with amplitude of F_{TBLR} forcing for the three different wakes. Note that the evolution of $\overline{C_{pb}}$ relative to the unforced value was presented in figure 6.3. Here the idea is to look at the absolute base pressure recovery obtained under global forcing conditions. This might give insightful indications about control strategies targeting the maximal drag reduction achievable for such a blunt body. Surprisingly, the maximal achieved base pressure coefficient C_{pb} is of similar value between the **N** and **T** configurations, although it is reached for a slightly smaller amplitude C_μ for the former. This means that the absolute maximal base pressure recovery achieved for global F_{TBLR} forcing is around 7% greater for the **T** configuration. In other words, the same base pressure coefficient is obtained with wake asymmetries of different nature and not contributing to the same extent to the drag of the blunt body as seen in chapter 4. While keeping a given wake asymmetry, the wake shaping mechanism evidenced in chapter 5 is more efficient for the **T** configuration than on the **N** configuration. It somehow suggests a trade-off existing between both drag generating mechanisms, the global flow curvature and the asymmetry of the wake, when looking for the lowest drag flow. For the **B** configuration, the maximal mean base pressure coefficient $\overline{C_{pb}}$ obtained is smaller, suggesting an additional influence of the ground proximity.

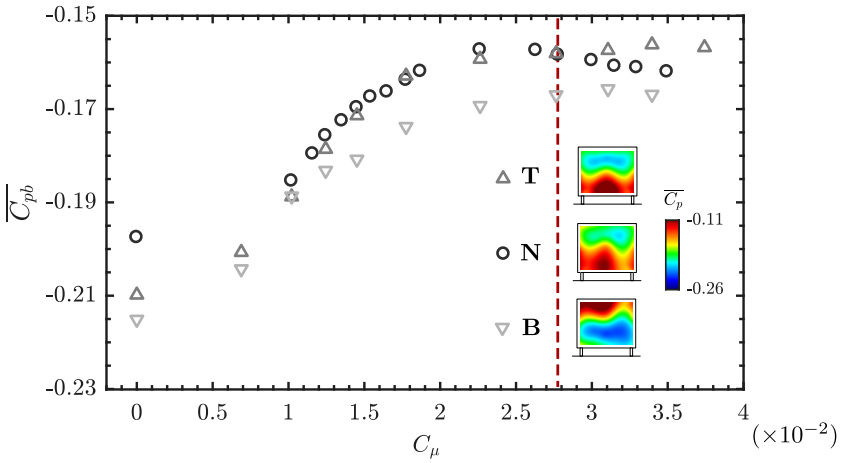

Figure 6.8: Evolution of the mean base pressure coefficient $\overline{C_{pb}}$ as function of forcing amplitude C_μ for the global forcing of the three unforced configurations **N**, **T** and **B**. Inserts show the mean base pressure distribution around saturation of the base pressure recovery (at the C_μ value shown by the vertical red dashed line).

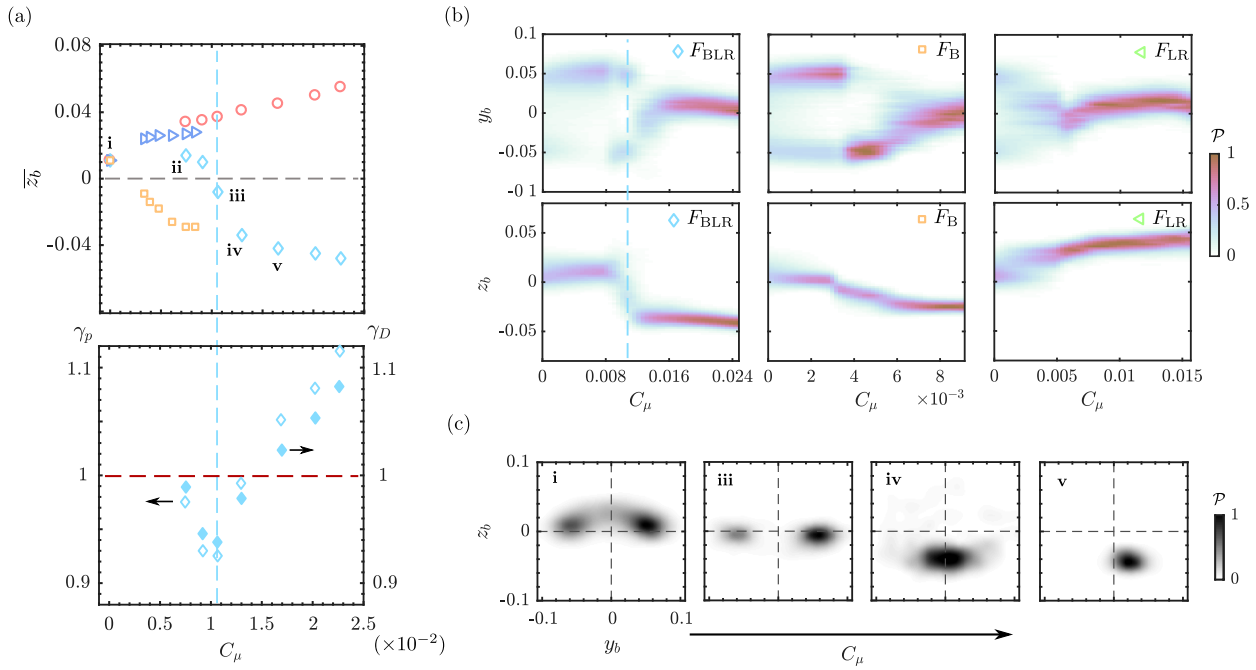

Figure 6.9: Effect of localized forcing on the base pressure of the unperturbed configuration. (a) Top : mean vertical position $\overline{z_b}$ of the CoP for all different asymmetric forcings (color and symbol scheme is defined in figure 2.4(b)). Bottom : Evolution of base pressure γ_p and drag γ_D parameters with forcing amplitude C_μ for F_{BLR} forcing. Vertical dashed line shows the optimal drag reduction for F_{BLR}. (b) Sensitivity maps of the CoP position y_b and z_b to forcing amplitude C_μ for F_{BLR}, F_{B} and F_{LR}. Vertical dashed line shows the optimal drag reduction for F_{BLR}. (c) Evolution of the base CoP under F_{BLR} forcing for peculiar forcing amplitudes indicated by the roman numbers in (a).

6.3.3 Asymmetric forcing of a bi-modal wake

In this section, we focus on asymmetric forcing of the natural unperturbed wake presenting lateral bi-modality with a slight mean vertical asymmetry.

Figure 6.9 shows the base pressure dynamics when the wake is subjected to asymmetric forcing distributions at various forcing amplitudes C_μ. In figure 6.9(a), the evolution of the mean vertical position of the base CoP $\overline{z_b}$ with C_μ is shown for all types of asymmetric forcings considered together with the corresponding trends of γ_p and γ_D for F_{BLR} forcing. In this configuration, at minimal γ_p and γ_D, we find the smallest vertical asymmetry (i.e. the smallest value of $|z_b|$). Moreover, from the evolution of $\overline{z_b}$ with the forcing amplitude, at C_μ values above 0.013, a plateau around $\overline{z_b} \sim -0.04$ can be observed, which stands for the locking of the wake in a vertical asymmetric state similar to the unforced wake **B**. Intriguingly, the transition from the perfectly vertical symmetric wake to a vertically asymmetric wake occurs very abruptly around $C_\mu = 0.01$, which means that finding the right amount of forcing momentum in order to optimally balance the wake depending on the initial degree of asymmetry is an intricate task. Interestingly, when keeping only the bottom edge for forcing F_{B}, the wake reverses its vertical asymmetry even more quickly, so that a minimum in drag or base pressure is not observed over the range of C_μ studied. We can speculate that one-side forcing F_{B} has greater authority on the wake orientation and even lower forcing momentum would be needed to reorient the wake asymmetry. This was not possible with the present setup since a minimal pressure is needed to completely close the solenoid valves and obtain the pulsed jet presented in figure 2.4(c) but it remains an interesting question. One could thence expect that an optimal drag reduction depending on C_μ similar to F_{BLR} forcing could be obtained with only F_{B} forcing at smaller forcing amplitudes. On the contrary, when forcing is applied on the opposite side, either as F_{TLR} or F_{T}, the slight vertical asymmetry already present in the unforced wake is directly enhanced. As a consequence, drag is only increased since the vertical asymmetry is only increased. Surprisingly, a lateral forcing F_{LR} leads to a reorientation of the asymmetry in the vertical direction explaining the increase of drag evidenced in this case in previous section. Although the lateral mirror symmetry of this configuration is respected by the forcing, the initial slight vertical mean

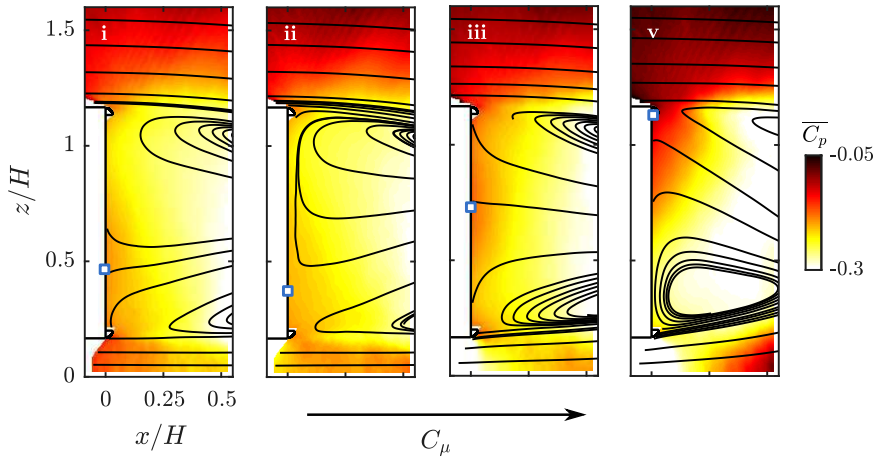

Figure 6.10: Mean pressure field $\overline{C_p}$ in the near-wake superimposed with mean velocity streamlines under F_{BLR} forcing for forcing amplitudes indicated by the roman numbers in figure 6.9(a). Blue square symbols indicate the position of the mean reattachment point on the base.

asymmetry of the wake or the ground proximity could be reasons for such a behaviour. This kind of reorientation was not witnessed by Lorite-Díez *et al.* (2020) using continuous blowing on an Ahmed body with higher ground clearance and presenting lateral bi-modal wake dynamics with vanishing vertical asymmetry.

The mean pressure fields $\overline{C_p}$ associated to F_{BLR} forcing at given C_μ are compared in figure 6.10. In particular, it can be seen how at the minimum of drag (case **iii**) the wake presents an increased floor-normal symmetry compared to the unforced case (case **i**). When the forcing amplitude becomes too strong, the initial vertical asymmetry is reversed and the wake qualitatively resembles the unforced bottom perturbed wake. Moreover, the pressure in the mean low pressure structure in the wake is clearly lowered leaving a stronger imprint on the base. The transition is also apparent from the evolution of the position of the flow reattachment point on the base which is the most vertically balanced at the minimum of drag and evolves to the upper edge as drag is increased. As will be discussed in section 6.4, the position of this point is informative on the degree of interaction of the recirculating flow with the opposite shear-layer and leads to increased drag generation due to the asymmetry. As previously said, after the minimum, γ_p and γ_D increase rapidly with the forcing amplitude not only because of apparition of a strong vertical asymmetry, but also because we are now in a configuration analogous to the bottom perturbed wake with F_{BLR} forcing which has been shown to increase the drag of the model. This point is of particular interest as it shows that the importance of the asymmetric state of the wake is twofold. On the one hand, the degree and kind of asymmetry in the wake contributes to the generation of a fair amount of drag as shown in previous sections. On the other hand, it also dictates the sensitivity of the control as a means of raising the pressure in the wake and providing or not drag reduction.

6.3.4 Asymmetric forcing of a mean asymmetric wake

We focus in this section on the effect of asymmetric forcing on the two wake configurations **T** and **B**, which are both locked in a static vertical asymmetry. We aim here at generalizing on a wake with stronger initial vertical asymmetry the relation between drag changes and wake symmetry changes observed previously on the bi-modal wake.

Figure 6.11 illustrates the evolution with forcing amplitude C_μ of the base pressure under asymmetric forcing. For conciseness, the figure only displays results for the **T** configuration since the results for the **B** configuration are very similar taking into account the top/bottom symmetry.

Forcing along the CoP side of the base (F_{TLR} and F_{T}) results in a monotonic increase of the vertical asymmetry $|z_b|$ with C_μ. For F_{T} forcing, this is consistent with the monotonic base pressure and drag increase observed based on the contribution of asymmetries to the drag. In contrast, for F_{TLR}, the relation between vertical wake asymmetry strength, base pressure and drag is not monotonic anymore. Indeed, the evolution of base pressure and drag with C_μ exhibits a minimum

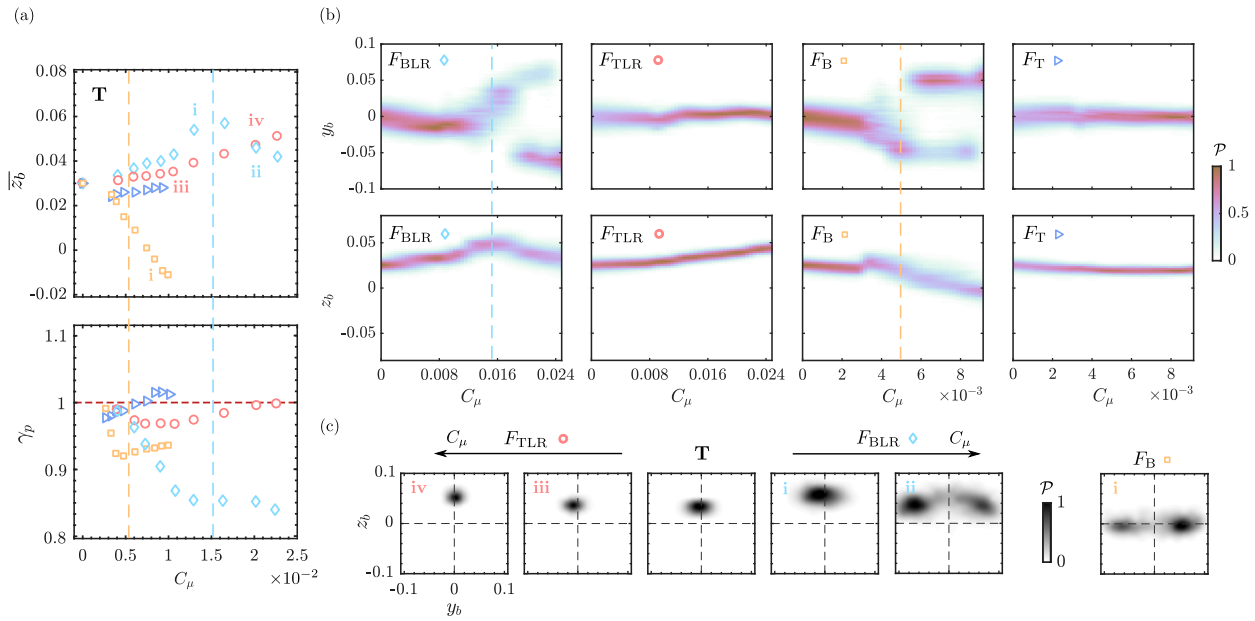

Figure 6.11: Effect of asymmetric forcing on the base pressure of the top perturbed configuration **T** (**B** configurations has qualitatively similar mirror trends and are not shown for conciseness). (a) Evolution of the mean vertical CoP position $\overline{z_b}$ with C_μ under asymmetric forcing. The associated evolutions of γ_p are recalled below. Colored roman numbers indicate the cases presented in (c). Yellow (resp. blue) vertical dashed line indicates the maximal base pressure recovery for F_{B} (resp. F_{BLR}). (b) Sensitivity maps of the CoP position y_b and z_b to forcing amplitude C_μ for F_{BLR}, F_{TLR}, F_{B} and F_{T}. Vertical dashed lines show the maximal base pressure recovery for F_{BLR} and F_{B}.(c) P.d.f. of the CoP position $\mathcal{P}(y_b, z_b)$ for specific C_μ of asymmetric forcings F_{TLR} and F_{BLR} and F_{B}. Horizontal arrows point towards increasing forcing amplitude C_μ.

at low $C_\mu \sim 0.01$ even though the drag reduction is very moderate. This is interpreted as the result of two competing effects : the reinforcement of the wake asymmetry and a global pressure recovery in the wake issued from a wake-shaping occurring when forcing along three of the four base edges similarly to what was discussed in section 6.3.2.

On the contrary, when forcing along the edge opposite to the CoP (F_{BLR} and F_{B}), the drag of the model decreases notably. Single-edge forcing F_{B} results in a manifest vertical symmetrisation of the wake with increasing forcing amplitude C_μ. For the top perturbed configuration **T**, the sign of $\overline{z_b}$ even changes for the highest forcing amplitudes. For even higher forcing amplitudes a wake reversal is expected leading to further drag increase. In all the cases it suggests that asymmetric forcing seems to lead to the existence of an optimal forcing amplitude for which the wake is symmetrized and the drag minimal. Figure 6.11(b,c) shows the clear change of large-scale base pressure dynamics, where the p.d.f. of the base CoP under single-edge forcing at the highest studied C_μ exhibits a vanishing vertical asymmetry and a restored lateral bi-modality. For the **T** configuration, the transition between the two lateral symmetry-breaking modes is operated through a perfectly symmetric state whereas for the **B** configuration, the forcing amplitude only enables to transit through a bottom asymmetric state, which is consistent with the mean values of z_b observed.

Concerning F_{BLR} forcing (corresponding to the side opposite to the CoP), the evolution of the vertical asymmetry is not monotonic anymore with C_μ. In both configurations **T** and **B**, $|z_b|$ is first increasing with the forcing amplitude for values of $C_\mu < 0.015$ and only then a reduction in $|z_b|$ is observed with increasing C_μ as in the single-edge forcing configuration. This is shown on the base CoP p.d.f. and sensitivity maps in figure 6.11(b,c) where forcing on the side leading to the highest drag reduction leads gradually to the restoration of lateral bi-modal wake dynamics with first an unlocking of the vertical static mode. This initial asymmetry increase is qualitatively similar to what was observed for a global forcing F_{TBLR} of the wake and is linked to the wake shaping mechanism existing which is preponderant for three-sides forcing but less when forcing along a single edge. Interestingly, the maximal base drag reduction occurs around the transition

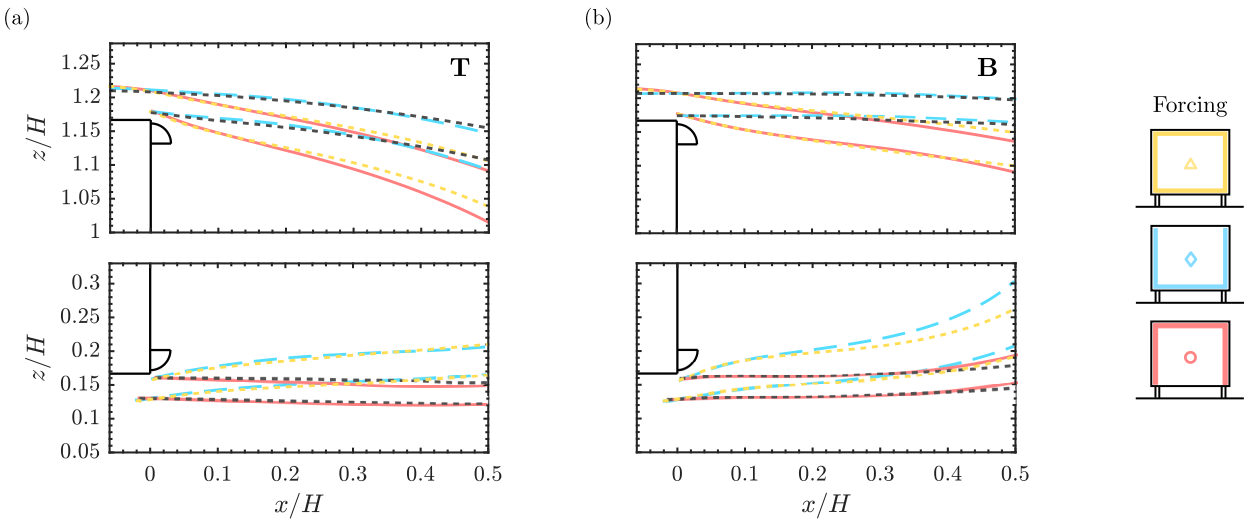

Figure 6.12: Influence of forcing conditions on separating streamlines on top and bottom edges of the model. **B** (a) and **T** (b) configurations. Colors are defined in figure 2.4(b). Unforced separating streamlines are given in black. Forcing amplitudes are $C_\mu = 0.02$ for asymmetric forcings F_{TLR} and F_{BLR} and 0.028 for global forcing F_{TBLR}.

between the vertical static asymmetric wake and the lateral bi-modal wake suggesting once again the importance of the symmetrization in drag reduction. On the contrary, the opposite forcing case for each configuration leads to an increase of the vertical asymmetry and, even more interestingly, to a further stabilization of the base CoP position which appears through a narrowing of the support of the p.d.f. A drag reduction hence does not directly relate to a reduction of the fluctuations of the base pressure. This is completely opposite to the studies of Dahan *et al.* (2012); Dalla Longa *et al.* (2017); Evstafyeva *et al.* (2017) where closed-loop control was targeting the attenuation of the base pressure fluctuations in order to reduce drag. Here the drag reduction is linked to a reorientation of the asymmetry in the direction of the larger side of the base which leads to increased fluctuations as the bi-modal dynamics appear.

Under global forcing, Haffner *et al.* (2020*b*) observed that the main mechanism leading to drag reduction is the inwards flow deviation at the edges and the changes in flow curvature along the dividing streamline. We observe indeed a narrowing of the wake resulting from inwards flow deviation under global forcing F_{TBLR} for both configurations in figure 6.12 where the separating streamlines in the median plane are compared. Nevertheless, we can also point out that there is a similar flow deviation and curvature for both F_{TLR} and F_{BLR} of both the top and bottom perturbed configurations but with fundamentally different effects on the drag and base pressure. This underlines the importance of the inner structure of the recirculating region and fundamental differences brought by the asymmetry to the flow on the different sides of the wake. We thereby aim at showing how the reorganization of the mean inner recirculation in terms of symmetry can explain these different drag variations.

Figure 6.13 shows the reconstructed mean pressure fields in the vertical plane of symmetry with superimposed streamlines for the same unforced and forced cases as in figure 6.12. It has to be acknowledged that the turbulent wake past this Ahmed body is of three-dimensional nature. Nevertheless, our rather two-dimensional reasoning for those previous aspects remains consistent as the wake presents a mean pressure distribution on the base which can be stratified in the vertical direction – for the vertical asymmetric configurations – or vertically homogeneous for the lateral bi-modal configuration but, in any case, with a rather homogeneous horizontal distribution except near the very side edges of the model. This is further assessed by the deviation from the unforced case of the base pressure distribution for the forced cases presented in figure 6.14 for the **T** configuration, where horizontal inhomogeneities in the changes of base pressure are rather mild. Moreover, the 2D approach in the symmetry plane to reconstruct the pressure field gives results very close to the base pressure measurements, further accounting for the consistency of our analysis. In a general manner, where forcing is applied a local zone of intense depression is created

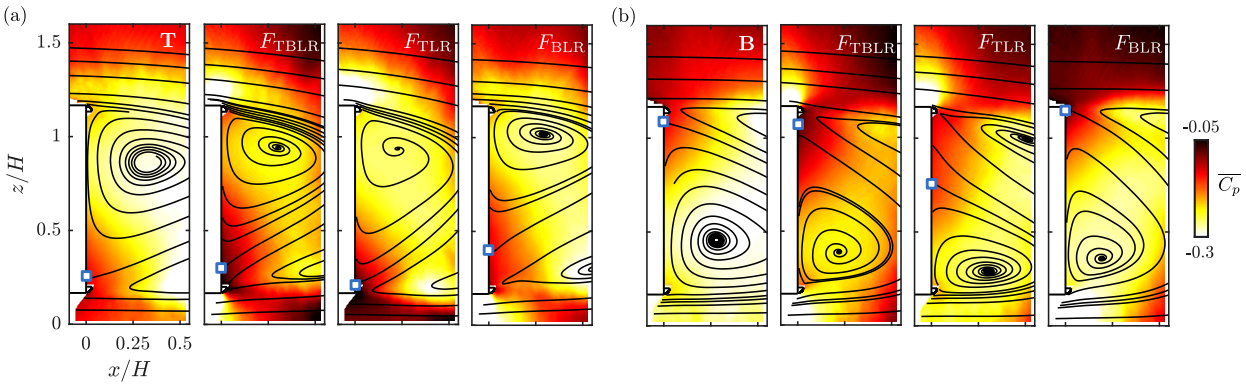

Figure 6.13: Effect of asymmetric forcing on the mean pressure $\overline{C_p}$ field and the velocity streamlines in the wake of the perturbed steady vertical asymmetric configurations. (a) **T** and (b) **B** configurations. Global forcing F_{TBLR} at $C_\mu = 0.028$. F_{TLR} and F_{BLR} asymmetric forcing at $C_\mu = 0.02$. Reattachment point on the base is indicated by blue square symbol.

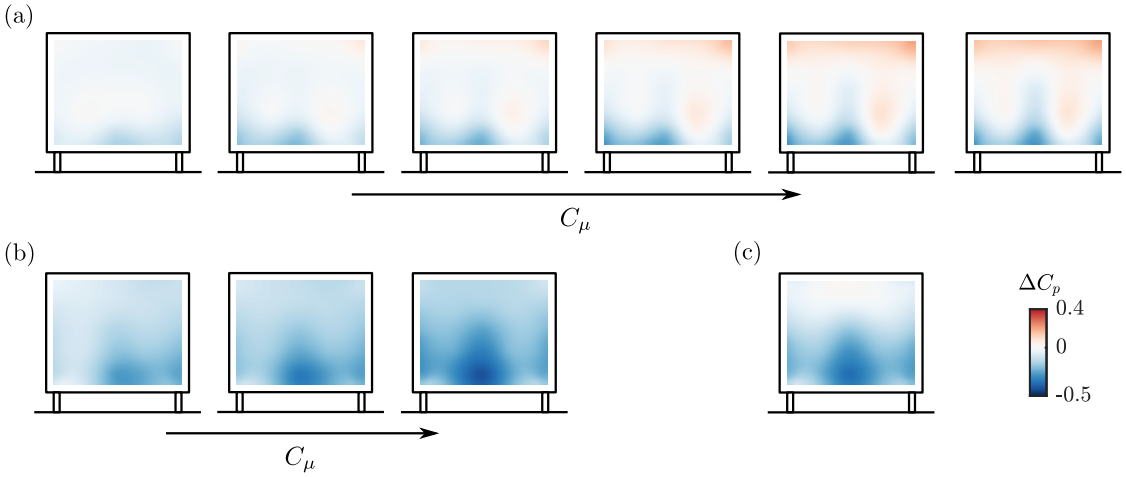

Figure 6.14: Distribution of base pressure coefficient difference relative to the unforced flow $\Delta C_p = C_p - C_{p0}$ at different forcing conditions for the flow with perturbation localized on top. (a) Forcing localized at top in increasing order of forcing amplitude : $C_\mu = 0.0095$, 0.013, 0.0165, 0.02, 0.0225 and 0.025. (b) All-edges forcing in increasing order of forcing amplitude : $C_\mu = 0.0125$, 0.015 and 0.018. (c) Forcing localized at bottom for $C_\mu = 0.0013$. Positive (resp. negative) ΔC_p indicates base pressure decrease (resp. increase).

around the edge of the model, witnessing the acceleration of the flow around the corner which leads to a narrowing of the wake. Also generally, when forcing is applied, regardless of its localization, the strength of the pressure minima in the near-wake is reduced compared to the unforced case. Nevertheless, this wake pressure recovery is not translated in the same way on the base. The main changes are operated inside the recirculating wake where the pressure field is reorganized in different ways depending on the forcing localization. When global F_{TBLR} forcing is used, there is a global pressure recovery through the whole wake which is stronger than when only asymmetric F_{TLR} or F_{BLR} forcings are used. Here the base pressure recovery is related to the narrowing of the wake as a global recovery through the whole recirculating wake. On the contrary, asymmetric forcings F_{TLR} and F_{BLR} are responsible for important reorganization of the pressure field in the wake, consistent with the observed changes of base pressure dynamics and asymmetry detailed previously. This suggests the combination of wake-shaping and symmetrization mechanisms to reduce the base drag. Forcing on the CoP side (F_{TLR} for the **T** configuration and F_{BLR} for the **B** configuration) induces a global pressure recovery through the wake but reorganizes the inner recirculating region and its asymmetry. This contributes to give to the low pressure region in the wake a stronger imprint on the base.

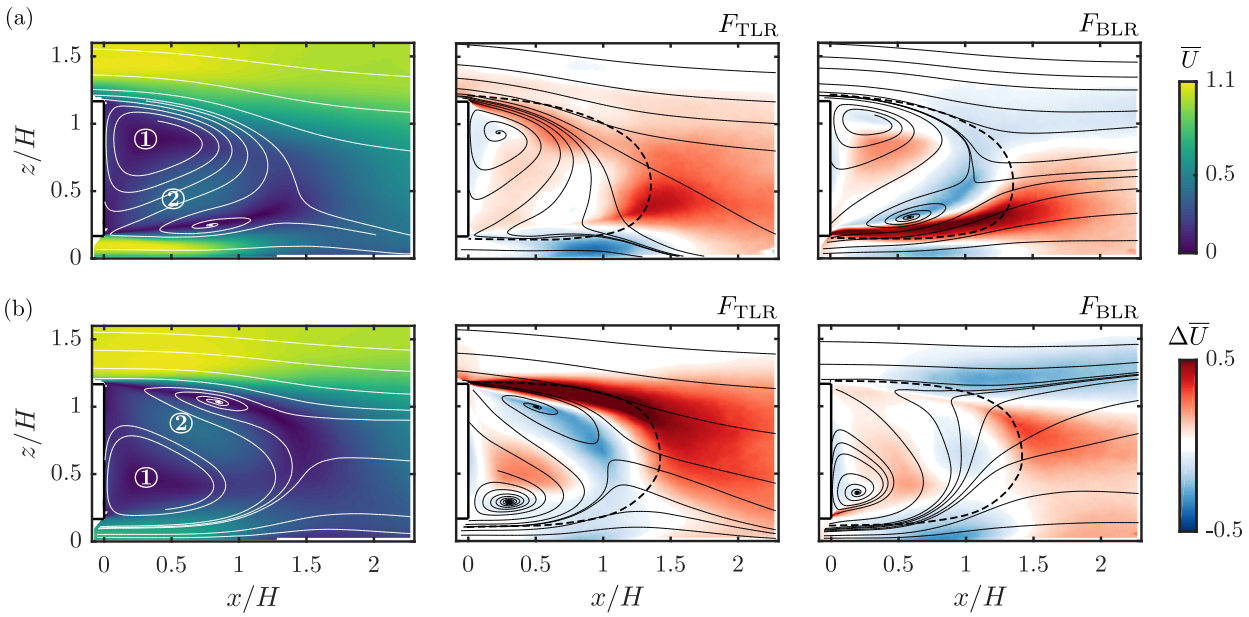

Figure 6.15: Effect of asymmetric forcing on the mean momentum difference $\Delta\overline{U}$ between forced and unforced flows in the wake of the perturbed steady vertical asymmetric configurations. **T** (a) and **B** (b) configurations. From left to right : the mean momentum $\overline{U}$ in the unforced flow superimposed with mean streamlines, the momentum difference $\Delta\overline{U}$ to the unforced flow for F_{TLR} and F_{BLR} asymmetric forcing at $C_\mu = 0.02$ superimposed with mean streamlines of the forced case. Dashed lines indicate the separatrix of the unforced flows. ① and ② indicate respectively the lower and higher flow momentum parts of the recirculation region, as discussed in the main text.

6.4 Further discussions and concluding remarks

In this last section, we aim at discussing the main results of this experimental study in a more global frame about drag generation and control strategies for drag reduction of squareback bluff bodies. We also capitalize on the qualitative wake model of Haffner *et al.* (2020*a*) to account for the different base drag changes observed and discuss the outcomes.

6.4.1 Mechanisms of drag changes

All the different drag changes observed under asymmetric forcing can be explained by extending the conceptual wake model drawn by Haffner *et al.* (2020*a*) which is recalled in figure 6.16. The main aspects of this asymmetric wake model is the recirculating flow (a) issued from one shear-layer feeding the recirculation region flow (d) and interacting with the opposite shear-layer (b)

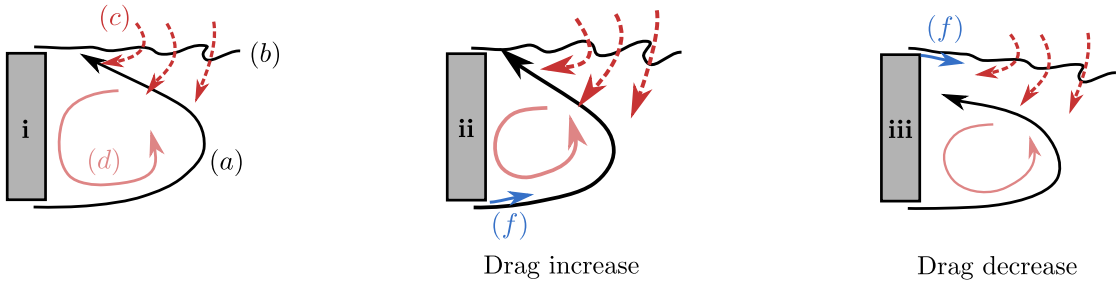

Figure 6.16: Conceptual model of the drag changes based on the model proposed by Haffner *et al.* (2020*a*). The different flow sketched are : (a) the recirculating flow formed by one shear-layer in the asymmetry direction, (b) the opposite highly fluctuating shear-layer triggered by (a), (c) the engulfment flow across this shear-layer, and (d) the recirculating flow in the separated region. Drag increase **ii** (resp. decrease **iii**) occurring when asymmetric forcing is issued on the side of the CoP (resp. on the opposite side of the CoP) is explained through the different redistribution of the momentum injected (f) and deviated by the forcing.

to trigger its roll-up and the large-scale engulfment (c) of fluid of high momentum. To feed this conceptual model, we lean on the main wake changes under forcing highlighted by the momentum difference $\Delta\overline{U} = |\overline{\mathbf{u}}| - |\overline{\mathbf{u_0}}|$ between the forced and unforced wakes given in figure 6.15 for the two baseline configurations **T** and **B**. Depending on the asymmetric forcing distribution and the initial wake orientation, the momentum is redistributed in quite different ways. The drag changes of the asymmetric wake are very sensitive to the asymmetric forcing distribution for the main reason that forcing is issued in flow regions of rather different nature.

When the forcing flow (f) is issued on the base CoP side of the wake (case **ii** in figure 6.16(b)), leading to important drag increase, the recirculating flow (a) from the shear-layer on the CoP side is fed directly by the high momentum flow of the deviated flow from the outer region as is evidenced in figure 6.15. The enhancement of the recirculating feedback flow (a) leads to an enhancement of both the recirculating region (d) and the interaction mechanism with the opposite shear-layer (b). The enhanced interacting mechanism leads to a greater flow engulfment (c) and thus both to an increased wake asymmetry and base drag. Moreover, the forcing is issued along the lower momentum large-scale recirculation region (as highlighted in figure 6.15 by the region ①). As a consequence, little wake shaping occurs as the high momentum outer flow deviated by the forcing cannot be balanced by the lower momentum side of the recirculation region.

Conversely, when the forcing (f) is issued on the side opposite to the base CoP (case **iii** in figure 6.16(b)), leading to important drag decrease, the injection and deviation of high momentum flow counteracts the interaction mechanism between the recirculating flow (a) of opposite momentum and the shear-layer (b). This results in the weakening of this flow mechanism which controls the asymmetry of the wake as shown in figure 6.15, and the asymmetry of the wake is thus balanced. The recirculation region is characterized by a momentum exchange between the lower momentum region ① close to the base on the side of the CoP and the higher momentum region ② far from the base on the opposite side witnessed in figure 6.15 (F_{BLR} in (a) and F_{TLR} in (b)) which evidences the symmetrisation of the wake. In this sense, the weakened interaction mechanism leads to base drag reduction related also to the symmetrisation of the wake. As the wake is symmetrized in the vertical direction, bi-modality in the lateral direction appears. Nevertheless, given the aspect ratio of the base $H/W < 1$, the interaction mechanism is less intense as the distance between opposite shear layers considered is increased. As a consequence, the drag of the bi-modal wake is less than the wake with an asymmetry in the vertical direction as was observed by Bonnavion & Cadot (2018) and Haffner *et al.* (2020*a*). Complementarily, when the wake evolves from a vertical static asymmetry to a lateral bi-modality, the wake explores a transient symmetric state with reduced base drag (Grandemange *et al.*, 2014*b*; Li *et al.*, 2016; Haffner *et al.*, 2020*a*) which further contributes to decrease the drag. Moreover, the forcing is issued next to the higher momentum region of the wake (as highlighted in figure 6.15 by the region ②). The high momentum injected by the forcing (f) has thus the ability to efficiently shape the wake as the deviated free-stream flow is balanced by both the high momentum zone of the recirculation region and the cross-flow momentum of the recirculating flow (a).

These two mechanisms (wake shaping and wake symmetrization) provide thus complementary means of reducing the drag of such bluff bodies but to different extents. Drag reduction obtained through wake shaping will be significantly more important but will also require more energy input, whereas symmetrization, albeit leading to smaller drag reductions, can be obtained with a large efficiency by a minimal single-edge forcing. One last aspect of the forcing concerns the global forcing which is a combination of both situations illustrated in figure 6.16. As explained the momentum injected by the forcing is redistributed in different ways depending on the side considered compared to the initial wake asymmetry direction. In global forcing conditions, the behaviour is similar. On the opposite side of the CoP, the forcing will be almost exclusively involved in wake shaping whereas on the CoP side it will lead to a lesser extent to shaping and to feeding of the the recirculating flow (a). This might explain why the wake asymmetry is observed to increase even under global forcing as both the opposite of the CoP side is more recompressed by the shaping and the recirculating flow is partially fed by the forcing. This aspect might explain the trade-off existing between the two drag reducing mechanisms of wake shaping and symmetrization. In this sense it could give hints about the potential lowest base drag achievable for this kind of body. A consequence of this is that we observed an initially lateral bi-modal wake and an initially vertical asymmetric

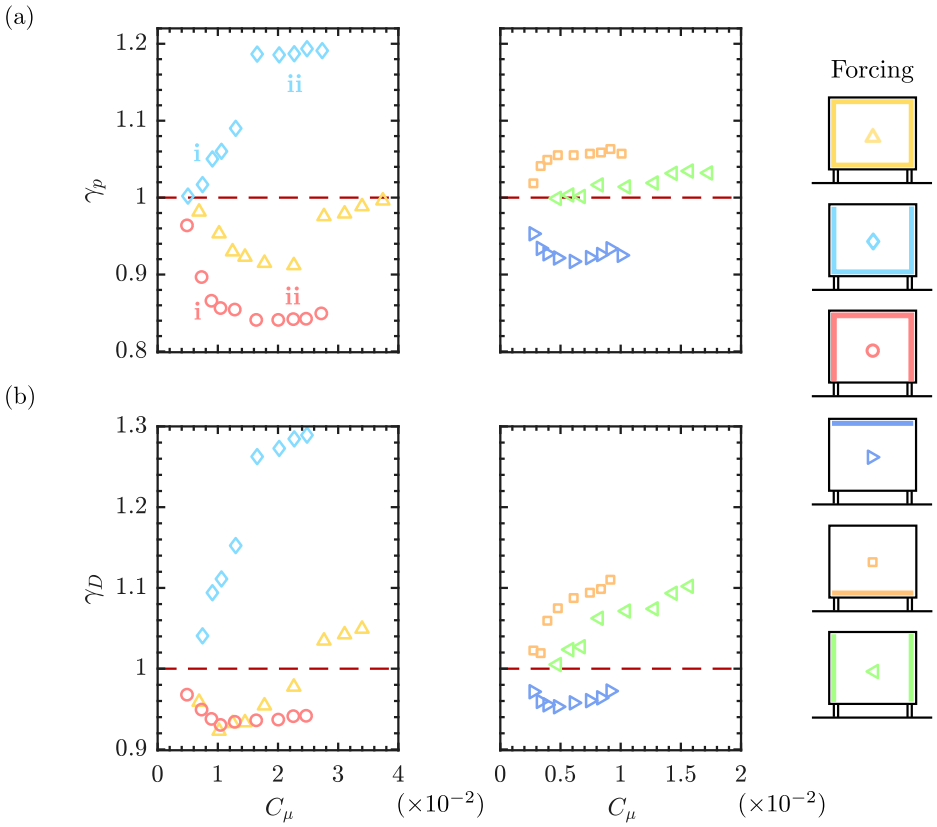

Figure 6.17: Evolution of the base pressure parameter γ_p (a) and the drag parameter γ_D (b) with the forcing amplitude C_μ for the configuration with reduced ground clearance $G/H = 0.06$ under various forcing distributions. Roman numbers refer to the cases presented in figure 6.18.

wake reaching the same optimal base drag under global forcing while keeping similar asymmetry characteristics.

6.4.2 Extension to different asymmetries : ground effect

To complete the type of wakes investigated, a fourth case with reduced ground clearance $G/H = 0.067$ is investigated. This configuration inhibits the symmetry-breaking instability as shown by Cadot *et al.* (2015) and introduces a vertical asymmetry linked to the close presence of the ground. This flow is quite close to the high base drag flow class identified by Castelain *et al.* (2018) and Grandemange *et al.* (2013*c*). The aim is to provide more generality on the drag changes mechanisms described previously by accounting for the effects of ground proximity which are of high relevance in this type of flow. A brief picture of the flow is given in figure 6.18(a) and the main aerodynamic characteristics were provided in table 6.1. The flow presents a vertical permanent asymmetry with a wake deviated towards the top as in the **B** configuration, the main difference being that the asymmetry is not related to an instability but to the ground proximity causing a flow momentum imbalance between the top of the model and the underbody. In this case, strong turbulent activity is found in the top shear layer due to the interaction mechanism which appears the strongest in all the different types of wakes encountered in ground proximity.

The effect of global and asymmetric forcing strategies is studied. The evolution of the base pressure parameter and the drag parameter are presented in figure 6.17. The trends observed in the γ_p and γ_D curves are qualitatively similar to those obtained with the bottom perturbed wake locked in a vertical static asymmetry (figure 6.3 and 6.4, configuration **B**). Forcing on the CoP side of the base leads to large drag increase up to 30%, whereas forcing on the opposite side leads to drag decrease up to 7%. Interestingly, in such configuration the asymmetric forcing F_{TLR} or F_{T} proves to be at least as efficient for base pressure reduction as global forcing, which was not the case for the asymmetries related to the symmetry-breaking mode. Another peculiarity of the drag changes concerns the sudden drag increase observed for forcings involving the bottom edge.

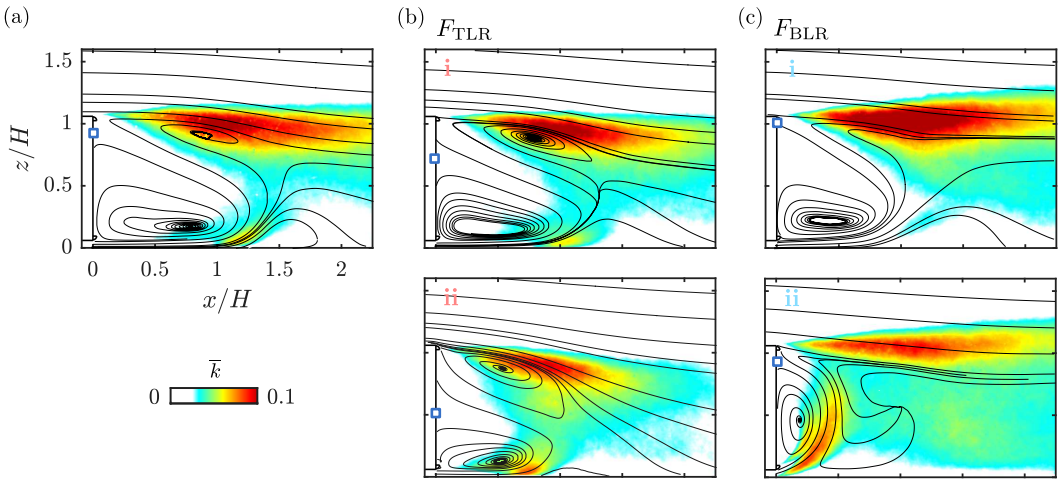

Figure 6.18: Effect of asymmetric forcing on the mean turbulent kinetic energy $\overline{k}$ field and the velocity streamlines in the wake of the reduced ground clearance configuration $G/H = 0.06$. (a) Unforced flow. Forced flow for cases identified in figure 6.17 for asymmetric forcings F_{TLR} (b) and F_{BLR} (c). Blue square symbols indicate the flow reattachment point on the base.

Globally, similar flow mechanisms are at play to explain the drag changes observed as the ones evidenced in the previous section with a wake governed by the symmetry-breaking instability. One peculiarity of this flow is the strong interaction of the underbody recirculating flow with the top shear-layer leading to increased base drag. In figure 6.18 mean turbulent kinetic energy $\overline{k}$ is depicted for selected forced cases with asymmetric forcings F_{TLR} and F_{BLR} to further focus on this mechanism under forcing. Once again, forcing on the side opposite to the base CoP (F_{TLR}, figure 6.18(b)) leads to a vertical symmetrisation of the wake which reduces the degree of interaction of the recirculating flow and reduced level of fluctuations in the top shear-layer. On the contrary, when forcing F_{BLR} (figure 6.18(c)), the momentum of the recirculating flow is enhanced and further interaction is promoted with a concomitant high level of fluctuations in the top shear-layer contributing to the drag increase observed. Nevertheless, the ground proximity leads to a different evolution when the forcing amplitude C_μ is increased. Above a C_μ threshold flow detachment from the ground is promoted and the flow transitions to a wake dominated by a recirculating flow issued from the underbody and attached to the whole base (figure 6.18(c), case **ii**). This prevents considerably the interaction mechanism. However, all the momentum injected by the forcing and issued from the underbody now feeds the attached recirculation region leading to a strong recirculating motion with low pressure explaining the sudden increase in drag only observed when the bottom edge is forced.

6.4.3 Outcomes for drag reduction of blunt bodies

From an energetic efficiency of the control, asymmetric control provides a highly efficient drag reducing mechanism by acting on the symmetry of the wake. This is the result of both localizing the control and the high sensitivity of the symmetry-breaking modes to small amounts of momentum injected by the forcing. Nevertheless, the outcomes in terms of drag changes are very sensitive to blowing location and initial wake asymmetry direction. The initial asymmetric state of the wake has been shown to be strongly sensitive to small geometric or flow conditions changes; in real conditions, it can impair the drag reduction targeted by asymmetric forcing. From a dynamical point of view, in real conditions, asymmetries can constantly vary as flow conditions do. For instance, for small cross-flow changes, the wake asymmetry can oscillate between lateral bi-modal dynamics and a static symmetry-breaking in either horizontal directions. This remark points to very interesting research paths involving any form of closed-loop control which would adapt the asymmetric location to the measured wake asymmetry in order to achieve all the drag reduction potential of asymmetric forcing strategies as proposed in **?** and Mariette (2020). There is here an important potential to provide a rather simple adaptive active flow control strategy which would succeed in efficient drag reduction in dynamical flow conditions.

Of course, the focus of this study was put on vertical asymmetries stemming from the lock-in of a symmetry-breaking mode in a static position and on lateral bi-modality when the vertical asymmetry vanishes. Nevertheless, it is expected that these results on control and the associated discussions on drag-change mechanisms are of general matter concerning asymmetries in the wake of such blunt bodies. The lock-in of the symmetry-breaking mode in static asymmetric positions can also occur in the horizontal direction of the base when for the model is put in small yaw for instance (Cadot *et al.* (2015), Bonnavion & Cadot (2018), Li *et al.* (2019)). Our conclusions should be generalizable to such horizontal asymmetries as it is only moves the asymmetry in the horizontal direction and turns the problem explored in this work in the orthogonal plane. It should provide control research paths to mitigate these asymmetries as well, as de la Cruz *et al.* (2017*a*), Li *et al.* (2019) and Lorite-Díez *et al.* (2020) explored for the Ahmed body in small yawing conditions.

Chapter 7

General synthesis and perspectives

This chapter proposes a general synthesis of the work presented in this manuscript. Main results about the natural and manipulated flows are exposed and discussed to a broader extent. On this basis, some perspectives are provided for future work with an emphasis on wake manipulation for drag reduction.

Contents

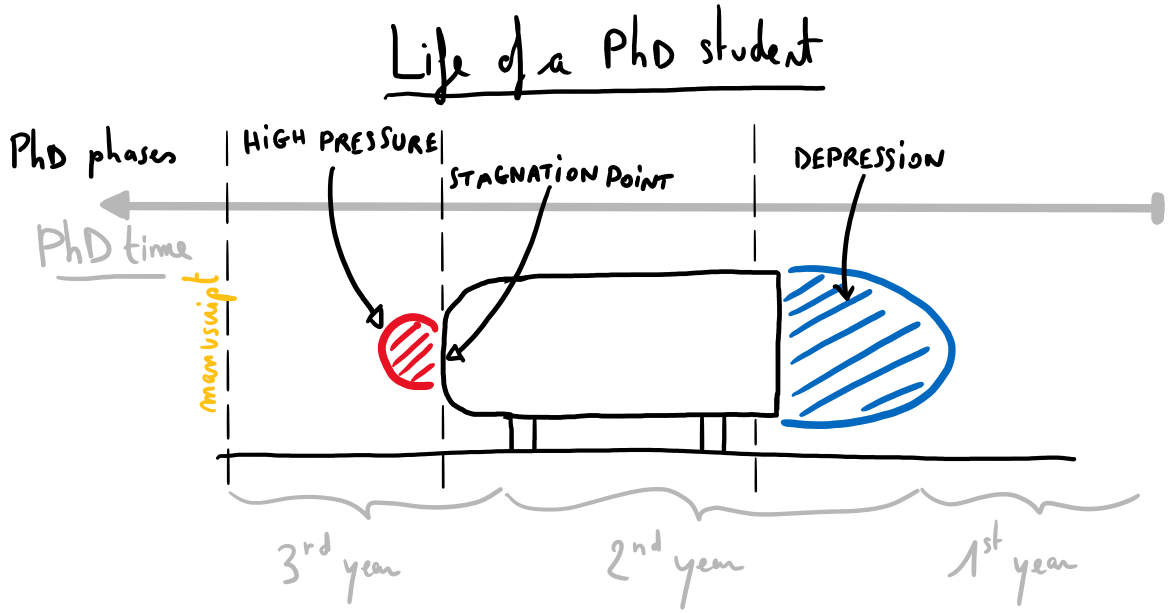

7.1 General synthesis

7.1.1 Blunt bodies drag generation mechanisms

The turbulent wake of a three-dimensional blunt body in ground proximity has been thoroughly investigated and manipulated with the aim of reducing its pressure drag. This flow exhibits a very wide variety of different length and time scales which are involved in the complex generation of pressure drag and need to be finely understood to develop efficient drag reduction strategies.

At the scale of the body, the symmetry-breaking instability leads the instantaneous loss of symmetry properties of the wake which manifest by a variety of large-scale wake dynamics. For the geometry investigated, these dynamics exhibit bi-modality between two lateral asymmetric states which statistically restores the reflectional symmetry of the setup (Grandemange *et al.*, 2013*a*). These dynamics and the orientation of the wake asymmetry are very sensitive to small flow changes such as perturbing bodies around the model, small yaw variations or ground clearance changes and contribute to pressure drag changes at a second order compared to mean curvature effects of the near-wake. At the scale of the separating boundary-layer, one to two orders of magnitude below, the unstable dynamics of the shear-layers are involved in the formation process of the recirculation region they surround through flow entrainment. When bi-modal dynamics are present, the random wake reversal is operated through transient symmetric states exhibiting reduced pressure drag. We showed how transient symmetric states explored during the reversals differ from static symmetry-breaking states in the flow organization they induce. In asymmetric states, a strong interaction and coupling mechanism between the two main length scales of the wake lead to drag generation. The recirculating flow from one side triggers shear-layer instabilities of the shear-layer from opposite side and their amplification. The resulting large-scale flow engulfment in the recirculation region increases the recirculation intensity and thus increases base drag. By contrast, during the wake reversals the disorganization of the recirculating flow leads to a transient symmetric state with prevented shear-layer interaction and triggering mechanism with a concomitant drag reduction of $\sim 8\%$ compared to symmetry-breaking states. As a consequence, drag is increased depending of the strength of the interaction mechanism. In particular, the interaction strength is likely to be stronger between opposite shear-layers which are closer. It thus means that stronger interaction and higher drag is obtained when the asymmetry is oriented in the direction of the small side of the base. This is why bi-modal wakes, which are only exhibited in the direction of the large dimension of the base (Grandemange *et al.*, 2013*c*; Bonnavion & Cadot, 2018), result in less drag than static symmetry-breaking wakes aligned on the small side of the base. This interaction mechanism appears as a generality of three-dimensional turbulent wakes where symmetry-breaking occurs and contributes to pressure drag generation as shown from the example of the sphere (Pier, 2008) and as a consequence its role in the problem of drag reduction looks major. Moreover the mechanism identified allows for a coherent interpretation of various recent experiments of flow control of the symmetry-breaking instability and opens new path for its stabilization which are discussed in §7.3.

7.1.2 Wake manipulation for drag reduction

Targeting the different main drag sources identified in the turbulent wakes, active manipulation of the flow through various active flow control strategies has aimed at drag reduction of the blunt body. Unsteady periodic forcing of the wake with pulsed jets coupled to small-scale adjacent surfaces along the edges of the base has been used to force the wake. Different drag mechanisms have been targeted by playing on the spatial distribution of forcing around the base.

For a global forcing along all edges of the base –which is not interacting with the large-scale wake asymmetries–, the local interaction dynamics between the jets, the curved surfaces and the flow reattachment over them have a key role on the drag reduction obtained by an unsteady Coanda effect shaping the wake. This aerodynamic wake shaping targets the high pressure gradients localized around the wake separatrix to recompress the wake. The influence of various parameters (forcing frequency f and amplitude C_μ, curvature radius r of the additional curved surfaces, free-stream velocity U_0) on the base drag reduction has been scrutinized to identify proper scalings of the mechanisms involved and to model them. The flow reattachment and separation on the curved surfaces results in a boat-tailing of the wake leading to drag reductions up to 12% but is

noticeably influenced by the time-scale of unsteadiness of the forcing. For high forcing frequencies of order $O(U_0/r)$, strong vortical counter-rotating coherent structures produced by the interaction of the pulsed jets and the separating shear-layer favours the interaction of the flow with the curved surfaces. The coherent structure of vorticity with same sign as the surrounding shear-layer notably influences local flow curvature and pressure gradients across the separating shear-layer in the vicinity of flow separation to result in a further pressure drag reduction for a given forcing amplitude. For high forcing amplitudes, the drag reduction saturates due to the detrimental effect of the coherent structure of opposite vorticity resulting from the starting jet. An inviscid-flow model allows to confirm the peculiar induced effect of these coherent structures on the flow which explains both the curvature effects leading to additional drag decrease and the saturation in drag decrease for increasing forcing amplitude. The model finally allowed to identify an optimum for the unsteady Coanda effect at forcing frequencies of order $O(U_0/r)$. These results point to the need of careful combination between forcing frequency and size of the curved surfaces to achieve all the potential of the unsteady Coanda effect in drag reduction.

As the dynamics of forced flow reattachment over the curved surfaces are quite reminiscent of an active flap, asymmetric distribution of forcing along only selected edges of the wake has been used to target the large-scale wake asymmetries and their associated drag contribution. By using passive perturbations around the model, the large-scale asymmetry of the unforced recirculation region is modified and wakes with different asymmetry orientation are selected to be manipulated with asymmetric forcing. Depending on the unforced wake equilibrium, additional high-frequency pulsed blowing coupled to small curved surfaces along all or selected edges of the base produces a very different impact on the drag. Besides a global fluidic boat-tailing effect, the reorganization of the recirculation region equilibrium plays a key role in the observed drag changes. In particular, the symmetrisation of the wake through control appears to be one of the main mechanisms involved in drag reduction. These drag changes are explained by an extension of the wake model proposed in Chapter 4 to interpret the drag generation in presence of wake asymmetry. Depending on the forcing distribution relative to the initial asymmetry orientation, the momentum issued by the pulsed-jets coupled to the curved surfaces is either promoting a local wake-shaping and the symmetrisation of the wake resulting in drag reduction, or promoting the recirculating flow with only little local wake-shaping and with concomitant increased interaction strength, asymmetry and drag. Even if asymmetric forcing strategies targeting the symmetrisation of the wake provide more modest drag reduction up to 7%, they are shown to be more efficient from an energetic point of view. These strategies allow to combine to different extents the benefit on the drag of a wake symmetrization and of wake-shaping. This study provides key ingredients to adapt forcing strategies for drag reduction in presence of various wake asymmetries typical of the flow around such body.

7.2 Extensions and related works

In the same frame of the ANR project *Activ_ROAD* as the work presented in this manuscript, various studies orbiting around the same problem are complementing and extending the present work and exploring some perspectives given throughout the manuscript. Some aspects of these complementary studies are commented here for the sake of generalization.

Wake manipulation on the lorry model Extension and generalization of the results of asymmetric manipulation of the Ahmed body wake in Chapter 6 have been provided by the work on the lorry model exposed in Sujar-Garrido *et al.* (2019). The lorry model, which was briefly presented in figure 1.6 in Chapter 1, is representative of the flow found around lorries with an aspect ratio of the base $H/W > 1$. These type of flows are close to the Ahmed body flow with reduced ground clearance and stabilized symmetry-breaking instability used in Chapter 3 and 6. The asymmetry of the wake still persists but is now related to the ground proximity or equivalently to the underbody flow conditions and has quantifiable effect on the base drag as discussed in Chapter 4. General results about the asymmetric forcing of these kind of wakes is provided by the base drag changes with various forcing distributions in figure 7.1(a) from Sujar-Garrido *et al.* (2019). Qualitatively,

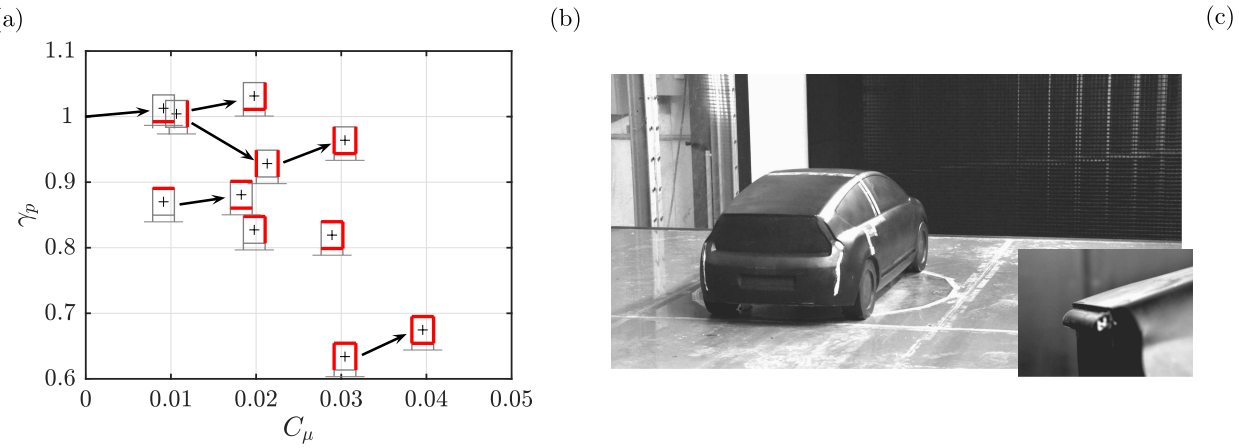

Figure 7.1: Various works related to the work presented in this manuscript. (a) Base pressure changes for asymmetric forcing of the wake of the lorry model described in figure 1.6, adapted from Sujar-Garrido *et al.* (2019). The natural wake has a vertical asymmetry imposed by the ground proximity. Forcing is similar to the one used in the present work with straight flaps instead of curved surfaces. Forcing distribution is highlighted in red on each marker. The arrows indicate the evolution when forcing is added along one of the edges. (b) Picture of the experimental setup for a real car model (Citroën C4 Coupé) with detail of the slits and curved surfaces used for forcing.

drag changes are very similar to the ones obtained with the Ahmed body at reduced ground clearance in Chapter 6. Here again asymmetric forcing ignoring the bottom edge outperforms global forcing of the wake and bottom edge forcing only contributes to increase the base drag in any case. This result generalizes the flow mechanisms exposed in Chapter 4 and 6 explaining the base drag changes in forced asymmetric wakes and base drag generation in presence of asymmetries. This confirmation along the detailed discussion on base drag generation in asymmetric wakes might help the building of a generalized wake model for flows around three-dimensional bluff bodies in ground proximity or not.

Feedback closed-loop control As discussed in Chapter 6, asymmetric forcing strategies have the advantage of leading to relatively important drag reduction with increased energetic efficiency provided the asymmetric forcing distribution is well positioned regarding the initial orientation of the wake asymmetry. If not well positioned, an asymmetric forcing can lead to important base drag increase. Nevertheless, the large-scale asymmetry orientation and its dynamics has been shown to be very sensitive to small geometric perturbations. For these reasons, these asymmetric forcing strategies are only viable if the asymmetry orientation can be known to adapt the forcing distribution in order to always keep it well positioned regarding the asymmetry orientation. This remark is the starting point of the feedback closed-loop control experiments which have been conjointly undertaken with Laboratoire Ampère to increase the robustness of this flow control strategy towards small flow changes. The experiments some of the results of are gathered in Mariette (2020) and Haffner *et al.* (2020*d*) mainly try to mitigate the lateral bi-stable dynamics of the Ahmed body wake and to adapt asymmetric forcing in yawed flow conditions. The closed-loop control method builds on Sliding-Mode Control and gets feedback for the position of the base CoP to adapt the forcing on needed edges of the base with success in yawed conditions where the wake asymmetry locks in the lateral direction. These results make it a promising robust control strategy targeting one of the main feature of blunt bodies wake

Real blunt car geometry Results of Chapter 5 and 6 about global and asymmetric wake manipulation using the unsteady Coanda effect have been confronted to the wake of more realistic car geometries through manipulation experiments on a common blunt passenger car Citroën C4 Coupé. From an industrial point-of-view, as shown by Bonnavion *et al.* (2019) the symmetry-breaking instability also governs the large-scale structure of the wake of real blunt vehicles. Here the geometry is one small step more complex than the vehicles from the study of Bonnavion & Cadot (2019), mainly because of the natural boat-tail imposed by the roof and side angles, which

increases further the gap with the simple Ahmed body. Nevertheless, in these experiments, results qualitatively rather similar to the Ahmed body have been obtained concerning asymmetric forcing related to the initial symmetry of the wake in various experiments where the wake is perturbed or not by small yaw. In this sense, there is hope for the wake manipulation results presented in this manuscript to be generalizable at the industrial scale provided the vehicle shapes remain simple and close enough to a squareback which is the case for lorries, commercial vehicles or other SUVs.

7.3 Perspectives

Through the work presented in this manuscript, a broad field of new academic and industrial perspectives has been opened concerning bluff body wakes, their drag sources and their manipulation for drag reduction. From there, some guidelines are provided to tackle challenging research paths in the future.

The study of near wake reversals and wakes subjected to the symmetry-breaking instability has provided the main flow mechanisms causing the apparition of large-scale asymmetries with their role as drag sources and triggering the wake reversals in bi-modal wakes. For one thing, these findings open interesting paths for the manipulation of wake asymmetries and the challenging stabilization of the symmetry-breaking instability and their consequences on aerodynamic drag. As explained, the flow mechanism causing apparition of asymmetries in the wake and triggering wake reversals takes its roots in the recirculating flow and the interaction between opposite shear-layers. As a consequence, it appears now clearly that targeting a stabilization of the symmetry-breaking instability would require to act on the flow where this flow mechanism takes place. Contrarily to all recent attempts only partially successful to mitigate these asymmetries and provide drag reduction (Grandemange *et al.*, 2014*b*; Li *et al.*, 2015; Brackston *et al.*, 2016; Evstafyeva *et al.*, 2017; Varon *et al.*, 2019; Plumejeau *et al.*, 2019; Haffner *et al.*, 2020*d*) which have focused on manipulating directly the shear-layers at the edges of the base, flow control strategies should focus on preventing the interaction mechanism directly inside the recirculation region. This strategy appears as the only one who could provide a real stabilization of the symmetric wake with the concomitant drag reduction expected as has done the cavity (Evrard *et al.*, 2016; Lucas *et al.*, 2017). Nevertheless building an active flow control strategy able to interact directly with this mechanism in the recirculating region farther from the base and without the flow amplifier properties of the shear-layers seems quite intricate and one has to come up with quite disruptive ideas to tackle successfully the problem.

As the interaction mechanism is occurring from the recirculating region it also raises the fundamental question about the appearance of the symmetry-breaking instability. By analogy with vortex shedding dominating wakes of 2D bluff bodies (Huerre & Monkewitz, 1990), it could suggest that this symmetry-breaking takes the form of a global instability of the wake. This aspect could certainly motivate theoretical and numerical studies on 3D bluff bodies in general to model and discuss the apparition of this instability and draw its sensitivity maps (Marquet *et al.*, 2008) as has been undertaken experimentally by Grandemange *et al.* (2014*b*). Such piece of research would be of great interest to help tackling the problem of wake manipulation for the stabilization of the symmetry-breaking. Moreover, the origin of the instability localized in the near-wake suggests that boundary layer conditions at separation from the base edges might not have a preponderant role in its apparition. In this sense, the problem could be numerically tackled by less complex numerical simulations not requiring resolving the boundary layers around the body. This remains a problem of broader extent than only the one of vehicles in ground proximity as the phenomenon is a general feature of all 3D bluff body wakes. It could be also of great interest for the prediction and manipulation of unsteady cross-flow loads in fluid-structure interaction problems involving bluff bodies in the fields of civil engineering or energy harvesting. In any case, extensively investigating the turbulent wake flow of a 3D blunt body remain a hard challenge because of both the three-dimensionality of the flow and the important separation in time and length scales quite peculiar to this type of flow[1]. Experimentally it requires complex and heavy flow diagnostic techniques

[1]For instance, for the flow forced at high frequencies, there are more than two order of magnitude separating the smallest scale of interest (the size of the coherent structures from the forcing and the boundary-layer momentum

to resolve most of the various time and length scales of interest in the wake only on a 2D slice, and in the coming years investigating the wake in a volumetric sense using tomographic PIV for instance (Pavia *et al.*, 2019) will remain constrained to the mean flow at a rather poor spatial resolution. For these reasons, a key aspect will be the complementary between experiments and high-resolution flow simulation like the one of Dalla Longa *et al.* (2019) to further elucidate these wakes even if the longest wake time-scales are hard to catch.

Massive wake equilibrium changes being essentially caused by minor geometric and flow conditions changes even on real blunt vehicles (Bonnavion *et al.*, 2019), flow control strategies targeting the mitigation of asymmetries are essential for industrial automotive applications. To this extent, the insight provided on the drag mechanisms in symmetry-breaking states could be of great value in designing real-scale flow control strategies targeting the suppression of the symmetry-breaking with a concomitant favourable effect on cross-flow loads and drag. The elements on flow manipulation in presence of large-scale asymmetries in Chapter 6 suggest the strong potential of active flow control to efficiently reduce the drag of blunt bodies with the control authority given on the large-scale asymmetries. The generality of these results for various asymmetries which have also been confirmed for yaw asymmetries by de la Cruz *et al.* (2017*a*) and Li *et al.* (2019) places the real-time adaptation of active flow control strategies to the instantaneous asymmetry of the wake at the center of the problem of efficiently reducing the drag of vehicles (Haffner *et al.*, 2020*d*). This feedback regarding the asymmetry of the wake is of fundamental importance to ensure the robustness of this flow control strategy in varying flow conditions which are representative of real vehicles flow and are a key feature to account for in experiments.

From the viewpoint of active flow control, the work on the unsteady Coanda effect opens also interesting path in fields of a broader extent than just application to drag reduction of blunt bodies. The scaling laws evidenced for this phenomenon make this kind of actuator adaptable to various experiments involving flow separation. One of the most interesting application could concern high lift devices used on airfoils or jet and thrust vectoring in aircraft and rockets applications (Lambert *et al.*, 2019). Furthermore, canonical studies about the forced unsteady separation and reattachment process could be of great interest to deepen the comprehension of the unsteady Coanda effect and complete the scaling laws of the phenomenon. Investigation about the geometry influence from curved surface to straight flaps could bring more generality to the present work and allow for a general shared vision with the reattachment process over straight flaps or airfoils at a larger scale (Darabi & Wygnanski, 2004*a*). For the application of interest in this study, the drag reduction of blunt bodies, the unsteady Coanda effect occurring on the designed flow control device has the main advantage of having authority on all the main drag sources of the wake, namely the pressure gradients across the separatrix and the large-scale asymmetries of the wake. This active flow control device is thus quite versatile as it can combine the advantages of a passive boat-tail with only minimal geometric adaptation and of adaptive flaps depending on the forcing distribution. For these reasons, we believe it could be a valuable active flow control device to further control the wake of 3D blunt bodies in various dynamic flow conditions where strong authority on the symmetry of the wake is sought.

thickness at separation) and the largest scale which is the cross-flow characteristic dimension of the blunt body. Similarly, there are around 4 orders of magnitude between the smallest time-scales of interest (the initial shear-layer instability at separation or the forcing time-scale used in the Coanda effect) and the largest time-scale related to the persisting time in asymmetric states in bi-modal wakes.

References

Abramson, P., Vukasinovic, B. & Glezer, A. 2011 Direct measurements of controlled aerodynamic forces on a wire-suspended axisymmetric body. *Exp. fluids* **50**, 1711–1725.

Ahmed, S. R., Ramn, G. & Faltin, G. 1984 Some salient features of the time averaged ground vehicle wake. *SAE Tech. Report. No. 840300, Society of Automotive Engineers, Inc., Warrendale, PA* .

Amitay, M. & Glezer, A. 2002 Role of actuation frequency in controlled flow reattachment over a stalled airfoil. *AIAA Journal* **40** (2).

Apelt, G.S. West C.J. 1982 The effects of tunnel blockage and aspect ratio on the mean flow past a circular cylinder with reynolds numbers between 10^4 and 10^5. *J. Fluid Mech.* **114**, 361–377.

Balachandar, S., Mittal, R. & Najjar, F. M. 1997 Properties of the mean recirculation region in the wakes of two-dimensional bluff bodies. *J. Fluid Mech.* **351**, 167–199.

Barros, D. 2015 Wake and drag manipulation of a bluff body using periodic fluidic forcing. PhD thesis, Ecole Nationale Supérieure de Mécanique et d'Aérotechnique (ENSMA).

Barros, D., Borée, J., Cadot, O., Spohn, A. & Noack, B. R. 2017 Forcing symmetry exchanges and flow reversals in turbulent wakes. *J. Fluid Mech.* **829**, R1.

Barros, D., Borée, J., Noack, B. R. & Spohn, A. 2016*a* Resonances in the forced turbulent wake past a 3d blunt body. *Phys. Fluids* **28** (065104).

Barros, D., Borée, J., Noack, B. R., Spohn, A. & Ruiz, T. 2016*b* Bluff body drag manipulation using pulsed jets and coanda effect. *J. Fluid Mech.* **805**, 422–459.

Barros, D., Ruiz, T., Borée, J. & Noack, B. R. 2014 Control of a three-dimensional blunt body wake using low and high frequency pulsed jets. *International Journal of Flow Control* **6**, 61–74.

Batchelor, G. K. 1956 A proposal concerning laminar wakes behind bluff bodies at large reynolds number. *J. Fluid Mech.* **1**, 388–398.

Bearman, P. W. 1965 Investigation of the flow behind a two-dimensional model with a blunt trailing edge and fitted with splitter plates. *J. Fluid Mech.* **21**, 241–255.

Bearman, P. W. 1967 The effect of base bleed on the flow behind a two-dimensional model with a blunt trailing-edge. *Aeronaut. Q.* **18**, 207–224.

Bearman, P. W. & Zdravkovich, M. M. 1978 Flow around circular cylinder near a plane boundary. *J. Fluid Mech.* **89**, 33–47.

Beaudet, L. 2014 Etude expérimentale et numérique du décrochage dynamique sur une éolienne à axe vertical de forte solidité. PhD thesis, Université de Poitiers.

Beaudoin, J.F. 2004 Controle actif d'écoulement en aérodynamique automobile. PhD thesis, Ecole des Mines de Paris.

Berger, E., Scholz, D. & Schumm, M. 1990 Coherent vortex structures in the wake of a sphere and a circular disk at rest and under forced vibrations. *J. Fluids Struct.* **4**, 231–257.

Berk, T. & Ganapathisubramani, B. 2019 Effects of vortex-induced velocity on the development of a synthetic jet issuing into a turbulent boundary layer. *J. Fluid Mech.* **870**, 651–679.

Berk, T., Medjoun, T. & Ganapathisubramani, B. 2017 Entrainment effects in periodic forcing of the flow over a backward-facing step. *Phys. Rev. Fluids* **2** (074605).

Bohorquez, P., Sanmiguel-Rojas, E., Sevilla, A., Jiménez-González, J. I. & Martínez-Bazán, C. 2011 Stability and dynamics of the laminar wake past a slender blunt-based axisymmetric body. *J. Fluid Mech.* **676**, 110–144.

Bonnavion, G. 2018 Dynamics of the unstable wake modes in automotive aerodynamics : from simplified models to real vehicles. PhD thesis, Ecole Nationale Supérieure de Techniques Avancées (ENSTA), Université Paris-Saclay.

Bonnavion, G. & Cadot, O. 2018 Unstable wake dynamics of rectangular flat-backed bluff bodies with inclination and ground proximity. *J. Fluid Mech.* **854**, 196–232.

Bonnavion, G. & Cadot, O. 2019 Boat-tail effects on the global wake dynamics of a flat-backed body with rectangular section. *J. Fluid Struct.* .

Bonnavion, G., Cadot, O., Herbert, V., Parpais, S., Vigneron, R. & Délery, J. 2019 Asymmetry and global instability of real minivan's wake. *Journal of Wind Engineering and Industrial Aerodynamics* .

Boujo, E. & Cadot, O. 2019 Stochastic modelling of a freely rotating disk facing a uniform flow. *J. Fluids Struct.* **86**, 34–43.

Brackston, R. D., de la Cruz, J. M. G., Wynn, A., Rigas, G. & Morrison, J. F. 2016 Stochastic modelling and feedback control of bistability in a turbulent bluff body wake. *J. Fluid Mech.* **802**, 726–749.

Brackston, R. D., Wynn, A. & Morrison, J. F. 2018 Modelling and feedback control of vortex shedding for drag reduction of a turbulent bluff body wake. *International Journal of Heat and Fluid Flow* **71**, 127–136.

Bradshaw, P. 1969 The analogy between streamline curvature and buoyancy in turbulent shear flow. *J. Fluid Mech.* **36**, 177–191.

Bradshaw, P. 1973 Effects of streamline curvature on turbulent flow. *Tech. Rep.*. DTIC Document.

Bridges, T. J. & Morris, P. J. 1984 Differential eigenvalue problems in which the parameter appears nonlinearly. *J. Comput. Phys.* **55**, 437–460.

Brillouin, M. 1910 Les surfaces de glissement d'helmholtz et la résistance des fluides. *Annales de chimie et de physique* **XXII**, 145–230.

Buren, T. Van, Whalen, E. & Amitay, M. 2016 Impact of orifice orientation on a finite-span synthetic jet interaction with a crossflow. *Phys. Fluids* **28** (037106).

Cabitza, S. 2015 Active control of the wake from a rectangular-sectioned body. PhD thesis, Imperial College London.

Cadot, O. 2016 Stochastic fluid structure interaction of three-dimensional plates facing a uniform flow. *J. Fluid Mech.* **794**, R1.

Cadot, O., Evrard, A. & Pastur, L. 2015 Imperfect supercritical bifurcation in a three-dimensional turbulent wake. *Phys. Rev. E* **91** (063005).

Castelain, T., Michard, M., Szmigiel, M., Chacaton, D. & Juvé, D. 2018 Identification of flow classes in the wake of a simplified truck model depending on the underbody velocity. *J. Wind Eng. Ind. Aerod.* **175**, 352–363.

Castro, I. P. & Bradshaw, P. 1976 The turbulence structure of a highly curved mixing layer. *J. Fluid Mech.* **73**, 265–304.

Cattafesta, L. N. & Sheplak, M. 2011 Actuators for active flow control. *Ann. Rev. Fluid Mech.* **43**, 247–272.

Chaligné, S. 2013 Contrôle du sillage d'un corps non profilé. application expérimentale à une maquette simplifiée de véhicule industriel. PhD thesis, Ecole Centrale de Lyon.

Chaligné, S., Castelain, T., Michard, M. & Juvé, D. 2013 Active control of the flow behind a two-dimensional bluff body in ground proximity. *Comptes Rendus Mécanique* **341** (3), 289–297.

Choi, H., Jeon, W.P. & Kim, J. 2008 Control of flow over a bluff body. *Ann. Rev. Fluid. Mech.* **40**, 113–139.

Choi, H., Lee, J. & Park, H. 2014 Aerodynamics of heavy vehicles. *Ann. Rev. Fluid. Mech.* **46**, 441–468.

Chrust, M., Goujon-Durand, S. & Wesfreid, J.E. 2013 Loss of a fixed plane of symmetry in the wake of a sphere. *J. Fluid Struct.* **41**, 51–56.

Courtine, S. 2006 Etude expérimentale des décollements provoqués par une paroi courbe : topologie et évolution spatio-temporelle. PhD thesis, Université de Poitiers.

Dahan, J. A., Morgans, A. S. & Lardeau, S. 2012 Feedback control for form-drag reduction on a bluff body with a blunt trailing edge. *J. Fluid Mech.* **704**, 360–387.

D'Alembert, J. 1752 Essai d'une nouvelle théorie de la résistance des fluides .

Dalla Longa, L., Evstafyeva, O. & Morgans, A. S. 2019 Simulations of the bi-modal wake past three-dimensional blunt bluff bodies. *J. Fluid Mech.* **866**, 791–809.

Dalla Longa, L., Morgans, A. S. & Dahan, J. A. 2017 Reducing the pressure drag of a d-shaped bluff body using linear feedback control. *Theoretical and Computational Fluid Dynamics* **31**, 567–577.

Darabi, A. & Wygnanski, I. 2004*a* Active management of naturally separated flow over a solid surface. part 1. the forced reattachment process. *J. Fluid Mech.* **510**, 105–129.

Darabi, A. & Wygnanski, I. 2004*b* Active management of naturally separated flow over a solid surface. part 2. the separation process. *J. Fluid Mech.* **510**, 131–144.

de la Cruz, J. M. G., Brackston, R. D. & Morrison, J. F. 2017*a* Adaptive base-flaps under variable cross-wind. *SAE Technical Paper* .

de la Cruz, J. M. G., Oxlade, A. R. & Morrison, J. F. 2017*b* Passive control of base pressure on an axisymmetric blunt body using a perimetric slit. *Phys. Rev. Fluids* **2** (043905).

Dimotakis, P. E. & Brown, G. L. 1976 The mixing layer at high reynolds number : large-structure dynamics and entrainment. *J. Fluid Mech.* **78**, 535–560.

Englar, R. J. 2001 Advanced aerodynamic devices to improve the performance, economics, handling and safety of heavy vehicles. *SAE Tech. Report. No. 2001-01-2072, Society of Automotive Engineers* .

Eulalie, Y. 2014 Etude aérodynamique et controle de la trainée sur un corps de ahmed culot droit. PhD thesis, Université de Bordeaux.

Evrard, A., Cadot, O., Herbert, V., Ricot, D., Vigneron, R. & Délery, J. 2016 Fluid force and symmetry breaking modes of a 3d bluff body with a base cavity. *J. Fluids Structures* **61**, 99–114.

Evstafyeva, O., Morgans, A. S. & Dalla Longa, L. 2017 Simulation and feedback control of the ahmed body flow exhibiting symmetry breaking behaviour. *J. Fluid Mech.* **817**, R2.

Fabre, D., Auguste, F. & Magnaudet, J. 2008 Bifurcations and symmetry breaking in the wake of axisymmetric bodies. *Phys. Fluids* **20**, 1–4.

Ford, C. W. Pitt & Babinsky, H. 2013 Lift and the leading-edge vortex. *J. Fluid Mech.* **720**, 280–313.

Freund, J.B. & Mungal, M.G. 1994 Drag and wake modification of axisymmetric bluff bodies using coanda blowing. *J. Aircraft* **31** (3), 572–578.

Gentile, V., Van Oudheusden, B., Schrijer, F. & Scarano, F. 2017 The effect of angular misalignment on low-frequency axisymmetric wake instability. *J. Fluid Mech.* **813**.

Gerrard, J. H. 1966 The mechanics of the formation region of vortices behind bluff bodies. *J. Fluid Mech.* **25**, 401–413.

Gharib, M., Rambod, E. & Shariff, K. 1998 A universal time scale for vortex ring formation. *J. Fluid Mech.* **360**, 121–140.

Glezer, A. & Amitay, M. 2002 Synthetic jets. *Ann. Rev. Fluid. Mech.* **34** (1), 503–529.

Glezer, A., Amitay, M. & Honohan, A. M. 2005 Aspects of low-and high-frequency actuation for aerodynamic flow control. *AIAA journal* **43** (7), 1501–1511.

Grandemange, M. 2013 Analysis and control of three-dimensional turbulent wakes : from axisymmetric bodies to road vehicles. PhD thesis, Ecole Nationale Superieure des Techniques Avancées (ENSTA).

Grandemange, M., Gohlke, M. & Cadot, O. 2012 Reflectional symmetry breaking of the separated flow over three-dimensional bluff bodies. *Phys. Rev. E* **86** (035302(R)).

Grandemange, M., Gohlke, M. & Cadot, O. 2013*a* Bi-stability in the wake past parallelepiped bodies with various aspect ratios and wall effects. *Phys. Fluids* **25** (9), 095103.

Grandemange, M., Gohlke, M. & Cadot, O. 2013*b* Turbulent wake past a three-dimensional blunt body. part 1. global modes and bi-stability. *J. Fluid Mech.* **722**, 51–84.

Grandemange, M., Gohlke, M. & Cadot, O. 2014*a* Statistical axisymmetry of the turbulent sphere wake. *Exp. Fluids* **55** (1838).

Grandemange, M., Gohlke, M. & Cadot, O. 2014*b* Turbulent wake past a three-dimensional blunt body. part 2. experimental sensitivity analysis. *J. Fluid Mech.* **752**, 439–461.

Grandemange, M., Mary, A., Gohlke, M. & Cadot, O. 2013*c* Effect on drag of the flow orientation at the base separation of a simplified blunt road vehicle. *Exp. Fluids* **54** (1529).

Greenblatt, D. & Wygnanski, I.J. 2000 The control of flow separation by periodic excitation. *Progress in Aerospace science* **36**, 487–545.

Haffner, Y., Borée, J., Spohn, A. & Castelain, T. 2020*a* Mechanics of bluff body drag reduction during transient near wake reversals. *J. Fluid Mech.* **894**, A14.

Haffner, Y., Borée, J., Spohn, A. & Castelain, T. 2020*b* Unsteady coanda effect and drag reduction of a turbulent wake. *J. Fluid Mech.* **899**, A.

Haffner, Y., Castelain, T., Borée, J. & Spohn, A. 2020*c* Manipulation of three-dimensional asymmetries of a turbulent wake for drag reduction. *Submitted to J. Fluid Mech.* .

Haffner, Y., Mariette, K., Bideaux, E., Borée, J., Eberard, D., Castelain, T., Bribiesca-Argomedo, F., Spohn, A., Michard, M. & Sesmat, S. 2020*d* Large-scale asymmetries of a turbulent wake : insights and closed-loop control for drag reduction. *55th 3AF International Conference on Applied Aerodynamics* .

Ho, C. M. & Huerre, P. 1984 Perturbed free shear layers. *Ann. Rev. Fluid. Mech.* **16** (1), 365–422.

Hucho, W. H. & Sovran, G. 1993 Aerodynamics of road vehicles. *Ann. Rev. Fluid. Mech.* **25**, 485–537.

Huerre, P. & Monkewitz, P. A. 1990 Local and global instabilities in spatially developing flows. *Ann. Rev. Fluid. Mech.* **22**, 473–537.

Kadosch, M. 1958 Déviation des jets par adhérence à une paroi convexe. *J. Phys. Phys. Appl.* **19** (S4), 1–12.

de Kat, R. & van Oudheusden, B.W. 2012 Instantaneous planar pressure deternination from piv in turbulent flow. *Exp. Fluids* **52**.

Khalighi, B., Zhang, S., Koromilas, C., Balkanyi, S. R., Bernal, L. P., Iaccarino, G. & Moin, P. 2001 Experimental and computational study of unsteady wake flow behind a bluff body with a drag reduction device. *SAE Paper* .

Kinsler, L.E., Frey, A.R., Coppens, A.B. & Sanders, J.V. 1999 *Fundamentals of Acoustics, 4th Edition*.

Kirchhoff, G. 1869 Zur theorie freier flüssigkeitsstrahlen. *Journal für die reine und angewandte Mathematik* **LXX** (4).

Klotz, L., Goujon-Durand, S., Rokicki, J. & Wesfreid, J. E. 2014 Experimental investigation of the flow behind a cube for moderate reynolds numbers. *J. Fluid Mech.* **750**, 73–98.

Krueger, P.S., Dabiri, J.O. & Gharib, M. 2003 Vortex ring pinch-off in the presence of simultaneously initiated uniform background co-flow. *Phys. Fluids* **15** (7).

Krueger, P.S., Dabiri, J.O. & Gharib, M. 2006 The formation number of vortex rings formed in unifrom background co-flow. *J. Fluid Mech.* **556**, 147–166.

Lambert, T.J., Vukasinovic, B. & Glezer, A. 2019 A freely yawing axisymmetric bluff body controlled by near-wake flow coupling. *J. Fluid Mech.* **863**, 1123–1156.

Li, R., Barros, D., Borée, J., Cadot, O., Noack, B.R. & Cordier, L. 2016 Feedback control of bimodal wake dynamics. *Exp. Fluids* **57** (158).

Li, R., Borée, J., Noack, B.R., Cordier, L. & Harambat, F. 2019 Drag reduction mechanisms of a car model at moderate yaw by bi-frequency forcing. *Phys. Rev. Fluids* **4** (034604).

Li, R., Noack, B.R., Cordier, L., Borée, J. & Harambat, F. 2017 Drag reduction of a car model by linear genetic programming control. *Exp. Fluids* **58** (8).

Li, Y., Bai, H. & Gao, N. 2015 Drag of a d-shaped bluff body under small amplitude harmonic actuation. *Theor. Appl. Mech. Letters* **5** (1).

Liu, X. & Katz, J. 2006 Instantaneous pressure and material acceleration measurements using a four-exposure piv system. *Exp. Fluids* **41** (2).

Lo, K.H. & Kontis, K. 2017 Flow around an articulated lorry model. *Experimental Thermal and Fluid Science* **82**.

Lorite-Díez, M., Jimenéz-González, J. I., Gutiérrez-Montes, C. & Martńez-Bazán, C. 2017 Drag reduction of slender blunt-based bodies using optimized rear cavities. *J. Fluids Struct.* **74**, 158–177.

Lorite-Díez, M., Jimenéz-González, J. I., Gutiérrez-Montes, C. & Martńez-Bazán, C. 2018 Effects of rear cavities on the wake behind an accelerating d-shaped bluff body. *Phys. Fluids* **30** (044103).

Lorite-Díez, M., Jimenéz-González, J. I., Pastur, L., Martńez-Bazán, C. & Cadot, 0. 2020 Experimental analysis of the effect of local base blowing on three-dimensional wake modes. *J. Fluid Mech.* **883**, A53.

Lucas, J.-M., Cadot, O., Herbert, V., Parpais, S. & Délery, J. 2017 A numerical investigation of the asymmetric wake mode of a squareback ahmed body – effect of a base cavity. *J. Fluid Mech.* **831**, 675–697.

Lumley, J. L. 1970 *Stochastic tools in turbulence*. Academic press.

Mair, W.A. 1969 Reduction of base drag by boat-tailed afterbodies in low-speed flow. *Aeronautical quarterly* **20** (4), 307–320.

Manesh, K. 2013 The interaction of jets with crossflow. *Annu. Rev. Fluid Mech.* **45** (1), 379–407.

Mariette, K. 2020 Phd k. mariette. PhD thesis, Institut National des Sciences Appliquées (INSA) de Lyon.

Mariotti, A., Buresti, G., Gaggini, G. & Salvetti, M.V. 2017 Separation control and drag reduction for boat-tailed axisymmetric bodies through contoured transverse grooves. *J. Fluid Mech.* **832**, 514–549.

Mariotti, A., Buresti, G. & Salvetti, M.V. 2015 Connection between base drag, separating boundary layer characteristics and wake mean recirculation length of an axisymmetric blunt-based body. *J. Fluids Struct.* **55**, 191–203.

Mariotti, A., Buresti, G. & Salvetti, M.V. 2019 Separation delay through contoured transverse grooves on a 2d boat-tailed bluff body : effects on drag reduction and wake flow features. *Eur. J. Mech. B/Fluids* **74**, 351–362.

Marquet, O. & Larsson, M. 2015 Global wake instabilities of low aspect-ratio flat-plates. *Eur. J. Mech. B-Fluid* **49**, 400–412.

Marquet, O., Sipp, D. & Jacquin, L. 2008 Sensitivity analysis and passive control of cylinder flow. *J. Fluid Mech.* **615**, 221–252.

Maull, D. & Hoole, B. 1967 The effect of boat-tailing on the flow round a two-dimensional blunt-based aerofoil at zero incidence. *The Journal of the Royal Aeronautical Society* **71** (684), 854–858.

Meliga, P., Chomaz, J.-M. & Sipp, D. 2009 Global mode interaction and pattern selection in the wake of a disk : a weakly non-linear expansion. *J. Fluid Mech.* **633**, 159–189.

Michalke, A. 1965 On spatially growing disturbances in an inviscid shear layer. *J. Fluid Mech.* **23**, 521–544.

Michard, M., Sesmat, S., Castelain, T., Jondeau, E., Bideaux, E. & Bourgeois, A. 2017 Unsteady pulsed jets using pneumatic valves for separation control : effect of internal acoustic waves on external flow structure. *Symposium GDR 2502 Contrôle des décollements* .

Morel, T. 1978 Aerodynamic drag of bluff body shapes characteristic of hatch-back cars. *SAE Technical Paper* **780267**.

Morris, S. C. & Foss, J. F. 2003 Turbulent boundary layer to single-stream shear layer : the transition region. *J. Fluid Mech.* **494**, 187–221.

Natarajan, R. & Acrivos, A. 1993 The instability of steady flows past spheres and disks. *J. Fluid Mech.* **254**, 323–344.

van Oudheusden, B. 2013 Piv-based pressure measurements. *Meas. Sci. Technol.* **24** (3).

Oxlade, A. 2013 High-frequency pulsed jet forcing of an axisymmetric bluff body wake. PhD thesis, Imperial College London.

Oxlade, A. R., Morrison, J. F., Qubain, A. & Rigas, G. 2015 High-frequency forcing of a turbulent axisymmetric wake. *J. Fluid Mech.* **770**, 305–318.

Parezanovic, V., Laurentie, J. C., Fourment, C., Delville, J., Bonnet, J. P., Spohn, A., Duriez, T., Cordier, L., Noack, B. R., Abel, M., Segond, M., Shaqarin, T. & Brunton, S. L. 2015 Mixing layer manipulation experiment. *Flow Turbulence Combust.* **94**, 155–173.

Park, H., Lee, D., Jeon, W. P., Hahn, S., Kim, J., Kim, J., Choi, J. & Choi, H. 2006 Drag reduction in flow over a two-dimensional bluff body with a blunt trailing edge using a new passive device. *J. Fluid Mech.* **563**, 389–414.

Parkinson, G. V. & Jandall, T. 1970 A wake source model for bluff body potential flow. *J. Fluid Mech.* **40**.

Pastoor, M., Henning, L., Noack, B. R., King, R. & Tadmor, G. 2006 Drag reduction in flow over a two-dimensional bluff body with a blunt trailing edge using a new passive device. *J. Fluid Mech.* **563**, 389–414.

Pavia, G., Varney, M., Passmore, M. & Almond, M. 2019 Three dimensional structure of the unsteady wake of an axisymmetric body. *Phys. Fluids* **31** (2).

Pfeiffer, J. & King, R. 2012 Multivariable closed-loop flow control of drag and yaw moment for a 3d bluff body. *6th AIAA Flow control conference* .

Pfeiffer, J. & King, R. 2018 Robust control of drag and lateral dynamic response for road vehicles exposed to cross-wind gusts. *Exp. Fluids* **59** (45).

Philip, J. & Marusic, I. 2012 Large-scale eddies and their role in entrainment in turbulent jets and wakes. *Phys. Fluids* **24** (055108).

Pier, B. 2008 Local and global instabilities in the wake of a sphere. *J. Fluid Mech.* **603**, 39–61.

Pineau, P. & Bogey, C. 2019 Steepened mach waves near supersonic jets : study of azimuthal structure and generation process using conditional averages. *J. Fluid Mech.* **880**, 594–619.

Plumejeau, B., Delprat, S., Keirsbulck, L., Lippert, M. & Abassi, W. 2019 Ultra-local model-based control of the square-back ahmed body wake. *Phys. Fluids* **31** (085103).

Provansal, M., Mathis, C. & Boyer, L. 1987 Bénard-von kármán instability : transient and forced regimes. *J. Fluid Mech.* **182**, 1–22.

Qubain, A. 2009 Active control of a turbulent bluff body wake. PhD thesis, Imperial College London.

Rigas, G., Morgans, A. S., Brackston, R. D. & Morrison, J. F. 2015 Diffusive dynamics and stochastic models of turbulent axisymmetric wakes. *J. Fluid Mech.* **778**, R2.

Rigas, G., Oxlade, A. R., Morgans, A. S. & Morrison, J. F. 2014 Low-dimensional dynamics of a turbulent axisymmetric wake. *J. Fluid Mech.* **755**, R5.

Roshko, A. 1954 On the drag and shedding frequency of two-dimensional bluff bodies. *NACA TN* **3169**.

Roshko, A. 1955 On the wake and drag of bluff bodies. *J. Aeronautical Sciences* **22** (2).

Roshko, A. 1961 Experiments on the flow past a circular cylinder at very high reynolds number. *J. Fluid Mech.* **10**, 345–356.

Roshko, A. 1993 Free shear layers, base pressure and bluff-body drag. *Tech. Rep.*. DTIC Document.

Rouméas, M., Gilliéron, P. & Kourta, A. 2009 Analysis and control of the near-wake flow over a square-back geometry. *Computers & Fluids* **38** (1), 60–70.

Ruiz, T., Sicot, C., Brizzi, L.E., Laumonier, J., Borée, J. & Gervais, Y. 2009 Unsteady near wake of a flat disk normal to a wall. *Exp. Fluids* **47** (4-5).

Saffman, P.G. 1992 *Vortex dynamics*. Cambridge Univ. Press.

Sau, R. & Mahesh, K. 2008 Dynamics and mixing of vortex rings in crossflow. *J. Fluid Mech.* **604**, 389–409.

Schlatter, P. & Örlü, R. 2010 Assessment of direct numerical simulation data of turbulent boundary layers. *J. Fluid Mech.* **659**, 116–126.

Schmidt, H.J., Woszidlo, R., Nayeri, C.N. & Paschereit, C.O. 2015 Drag reduction on a rectangular bluff body with base flaps and fluidic oscillators. *Exp. Fluids* **56** (151).

Schmidt, O. T. & Schmid, P. 2019 A conditional space-time pod formalism for intermittent and rare events : example of acoustic bursts in turbulent jets. *J. Fluid Mech.* **867**, R2.

Sevilla, A. & Martínez-Bazán, C. 2004 Vortex-shedding in high renolds number axisymmetric bluff-body wakes : local linear instability and global bleed control. *Phys. Fluids* **16**, 3460–3469.

Shariff, K. & Leonard, A. 1992 Vortex rings. *Annu. Rev. Fluid Mech.* **24** (1), 235–279.

Smith, B.L & Glezer, A. 1998 The formation and evolution of synthetic jets. *Phys. Fluids* **10** (9), 2281–2297.

Smits, A. J. & Lim, T. 2000 *Flow visualization, Techniques and Examples*. Imperial College Press.

Spohn, A. & Gilliéron, P. 2002 Flow separations generated by a simplified geometry of an automotive vehicle. *IUTAM Symposium: Unsteady Separated Flows* .

Steiros, K. & Hultmark, M. 2018 Drag on flat plates of arbitrary porosity. *J. Fluid Mech.* **853**, R3.

Stella, F., Mazellier, N., Joseph, P. & Kourta, A. 2018 Mass entrainment-based model for separating flows. *Phys. Rev. Fluids* **3** (114702).

Stella, F., Mazellier, N. & Kourta, A. 2017 Scaling of separated shear layers : an investigation of mass entrainment. *J. Fluid Mech.* **826**, 851–887.

Sujar-Garrido, P., Michard, M., Castelain, T. & Haffner, Y. 2019 Identification of efficient flow control strategies for truck model drag reduction. *11th International Symposium on Turbulence and Shear Flow Phenomena (TSFP11)* .

Sychev, V.V., Ruban, A.I., Sychev, V.V. & Korolev, G.L. 1998 *Asymptotic theory of separated flows*. Cambridge Univ. Press.

Szmigiel, M. 2017 Effet du flux de soubassement sur la dynamique du sillage d'un corps non profilé à culot droit : Application du contrôle actif pour la réduction de traînée de véhicule industriel. PhD thesis, Ecole Centrale de Lyon.

Taneda, S. 1956*a* Experimental investigation of the wake behind a sphere at low reynolds numbers. *J. Phys. Soc. Jpn.* **11**, 1104–1108.

Taneda, S. 1956*b* Experimental investigation of the wakes behind cylinders and plates at low reynolds numbers. *J. Phys. Soc. Jpn.* **11**, 302–307.

Thompson, M.C., Leweke, T. & Provansal, M. 2001 Kinematics and dynamics of sphere wake transition. *J. Fluid Struct.* **15**, 575–585.

Towne, A., Schmidt, O. T. & Colonius, T. 2018 Spectral proper orthogonal decomposition and its relationship to dynamic mode decomposition and resolvent analysis. *J. Fluid Mech.* **847**, 821–867.

Trip, R. & Fransson, J.H.M. 2017 Bluff body boundary-layer modification and its effect on the near-wake topology. *Phys. Fluids* **29** (095105).

Van Dyke, M. 1969 Higher-order boundary-layer theory. *Annu. Rev. Fluid Mech.* **1**, 265–292.

Van Dyke, M. 1982 *An album of fluid motion*. The parabolic press.

Varon, E., Aider, J.-L., Eulalie, Y., Edwige, S. & Gilotte, P. 2019 Adaptive control of the dynamics of a fully turbulent bimodal wake using real-time piv. *Exp. Fluids* (60:124).

Varon, E., Eulalie, Y., Edwige, S., Gilotte, P. & Aider, J.-L. 2017 Chaotic dynamics of large-scale structures in a turbulent wake. *Phys. Rev. Fluids* **2** (034604).

Volpe, R., Devinant, P. & Kourta, A. 2015 Experimental characterization of the unsteady natural wake of the full-scale square back ahmed body: flow bi-stability and spectral analysis. *Exp. Fluids* **56** (5), 1–22.

Waldon, M., Peacock, T., Jacobs, G.B., Helu, M. & Haller, G. 2008 Experimental and numerical investigation of the kinematic theory of unsteady separation. *J. Fluid Mech.* **611**, 1–11.

Wang, J., Zhang, C. & Katz, J. 2019 Gpu-based, parallel-line, omni-directional integration of measured pressure gradient field to obtain the 3d pressure distribution. *Exp. Fluids* **60** (4).

Wille, R. & Fernholz, H. 1965 Report on the first european mechanics colloquium, on the coanda effect. *J. Fluid Mech.* **23**, 801–819.

Williamson, C. H. K. 1996 Vortex dynamics in the cylinder wake. *Ann. Rev. Fluid Mech.* **28**, 477–539.

Wong, D.T.-M. & Mair, W.A. 1983 Boat-tailed afterbodies of square section as drag-reduction devices. *J. Wind Eng. Ind. Aerod.* **611**, 1–11.

Yeung, W. W. H. & Parkinson, G. V. 2000 Base pressure prediction in bluff-body potential-flow models. *J. Fluid Mech.* **423**, 381–394.

Zaman, K.B.M. & Hussain, A.K.M.F. 1981 Turbulence suppression in free shear flows by controlled excitation. *J. Fluid Mech.* **103**, 133–159.

Zdravkovich, M. M. 1985 Forces on a circular cylinder near a plane wall. *Applied ocean research* **7**, 197–201.

Zdravkovich, M. M. 1997 *Flow around circular cylinders : fundamentals*. Oxford Univiversity Press.

Zhang, B. F., Liu, K., Zhou, Y., To, S. & Tu, J. Y. 2018 Active drag reduction of a high-drag ahmed body based on steady blowing. *J. Fluid Mech.* **856**, 351–396.

Zhang, B. F., Zhou, Y. & To, S. 2015 Unsteady flow structures around a high-drag ahmed body. *J. Fluid Mech.* **777**, 291–326.

Zhou, J., Adrian, R.J., Balachandar, S. & Kendall, T.M. 1999 Mechanisms for generating coherent packets of hairpin vortices in channel flow. *J. Fluid Mech.* **387**, 353–396.

Manipulation of three-dimensional turbulent wakes for aerodynamic drag reduction

Combination of passive and active flow control are used to experimentally reduce the aerodynamic drag produced by the turbulent wake past a simplified vehicle geometry with a blunt base. Such wakes are characterized by two main features: important pressure drag linked to the massive flow separation, and large-scale asymmetries. The latter, manifesting as bi-modal dynamics or permanent symmetry-breaking, are shown to contribute for around 10 % of the pressure drag. The study of the transient wake reversals occurring in bi-modal dynamics though symmetric states enables to isolate the flow mechanism responsible for increased drag in symmetry-breaking states. An interaction and coupling between the recirculating flow from one side and the shear-layer from opposite side peculiar to symmetry-breaking states triggers shear-layer instabilities and their amplification leading to increased flow entrainment and drag. This mechanism is shown to be characteristic of the wakes of blunt bodies. An active flow control strategy combining tangential pulsed jets along the trailing-edges and small flush-mounted curved surfaces is used to reduce the pressure drag of the geometry. The flow reattachment and separation on the curved surfaces results in a fluidic boat-tailing of the wake leading to drag reductions up to 12 %, independently of the unforced large-scale asymmetry of the wake, and is noticeably influenced by the time-scale of unsteadiness of the forcing. Careful combination between forcing time-scale and size of the curved surfaces is needed to achieve all the potential of this unsteady Coanda effect in drag reduction as shown from a simple flow model providing scaling laws of the phenomenon. The model provided allows for an extension of the flow control mechanism to separated flows more generally. Furthermore, forcing along only selected edges enables to interact with the large-scale wake asymmetries and has very different impact on the drag depending on the unforced wake equilibrium. Symmetrisation of the wake through asymmetric forcing leads to 7 % drag reduction at a reduced energetic cost. Key ingredients are provided to adapt forcing strategies for drag reduction in presence of various wake asymmetries. As global wake equilibrium changes result from minor geometric and flow conditions changes, adaptive and robust flow control strategies are essential for industrial automotive applications.

Keywords : Automobiles – Aerodynamics, Wake, Drag, Base flow, Separated flows – Flow separation, Shear flow, Boundary layer control

Manipulation de sillages turbulents tridimensionnels pour la réduction de traînée aérodynamique

Une combinaison de moyens passifs et actifs de contrôle d'écoulement est utilisée pour réduire la traînée aérodynamique produite par le sillage turbulent d'une géométrie simplifiée de véhicule à culot droit. Ces sillages sont caractérisés par deux aspects principaux : une traînée de pression importante liée à la séparation massive de l'écoulement, et des asymétries à grande échelle. Ces dernières, se manifestant sous forme de dynamique bimodale ou de brisure de symétrie permanente, contribuent pour environ 10 % de la traînée de pression. L'étude des basculements de sillage transitoires en dynamique bimodale s'opérant au travers d'états symétriques du sillage permet d'isoler le mécanisme responsable de l'augmentation de traînée des états à brisure de symétrie. Une interaction et un couplage entre l'écoulement de recirculation issu d'un côté et la couche cisaillée opposée propre aux états à brisure de symétrie déclenche et amplifie les instabilités de couche cisaillée, ce qui conduit à une augmentation de l'écoulement d'entraînement et de la traînée. Il est montré que ce mécanisme est caractéristique des sillages de corps à culot droit. Une stratégie de contrôle actif de l'écoulement combinant des jets pulsés émis tangentiellement aux bords de fuite et de surfaces courbées miniatures affleurantes est utilisée pour réduire la traînée de pression de la géométrie. Le recollement de l'écoulement sur les surfaces courbées résulte en un rétreint fluidique du sillage se traduisant par une réduction de trainée jusqu'à 12 %, indépendamment de l'asymétrie initiale du sillage, et est notablement influencé par l'échelle de temps caractéristique de l'instationnarité du forçage. Une combinaison minutieuse entre l'échelle de temps du forçage et la taille caractéristique des surfaces courbées permet d'exploiter tout le potentiel de réduction de traînée de cet effet Coanda instationnaire comme le montre un modèle simple d'écoulement permettant la mise en évidence de lois d'échelles caractérisant le phénomène. De plus, un forçage localisé selon certaines arêtes seulement permet d'interagir avec les asymétries à grande échelle du sillage et impacte de manière très différente la traînée selon l'équilibre su sillage non-forcé. La symétrisation du sillage résultant d'un forçage asymétrique permet une réduction de traînée d'environ 7 % à coût énergétique réduit. Des éléments clefs sont donnés concernant l'adaptation de la localisation du contrôle pour une réduction de traînée en présence de différentes asymétries du sillage. Comme le changement d'équilibre global du sillage résulte de changements géométriques et d'écoulement mineurs, des stratégies de contrôle adaptives et robustes sont essentielles pour les applications dans l'industrie automobile.

Mots clés : Automobiles – Aérodynamique, Sillage, Traînée, Ecoulement de culot, Décollement des écoulements, Ecoulement cisaillé, Couche limite – Contrôle